Novel CO₂ Foam Concepts and Injection Schemes for Improving CO₂ Sweep Efficiency in Sandstone and Carbonate Hydrocarbon Formations

Final Technical Report

Period Covered: October 1, 2010 – December 31, 2014

Report Date: February 5, 2015

DE-FE0005902

Principal Investigator:
Quoc P. Nguyen   Department of Petroleum & Geosystems Engineering
The University of Texas at Austin

Co-Investigators:
George J. Hirasaki   Department of Chemical Engineering
Rice University
Keith P. Johnston   Department of Chemical Engineering
The University of Texas at Austin

Email: quoc_p_nguyen@mail.utexas.edu
Tel: 512.471.1204
Fax: 512.471.9605

Department of Petroleum and Geosystems Engineering
The University of Texas at Austin
1 University Station C0304
Austin, TX 78712

Distribution Statement: Approved for public release; distribution is unlimited.

Participants

UT Austin
Yunshen Chen

Amro Elhag

Sujeewa Palayangoda

Guang Ren

Onur Balan

Hang Zhang

Ramesh Yerramilli

Quan Nguyen

Tyler Seay

Rice University
Sonia Liao

Lisa Biswal

Kun Ma

Leyu Cui

Maura Puerto

Amir Amini

Guoqing Jian

Industry
Hung Lung Chen (Marathon)

Andy Falls (Oxy)

Jim Skurner (Tabula Rasa)

Table of Contents

REFERENCES AND PUBLICATIONS

List of Figures & Tables

EXECUTIVE SUMMARY

We explored cationic, nonionic and zwitterionic surfactants to identify candidates that have the potential to satisfy all the key requirements for CO_2 foams in EOR. We have examined the formation, texture, rheology and stability of CO_2 foams as a function of the surfactant structure and formulation variables including temperature, pressure, water/CO_2 ratio, surfactant concentration, salinity and concentration of oil. Furthermore, the partitioning of surfactants between oil and water as well as CO_2 and water was examined in conjunction with adsorption measurements on limestone by the Hirasaki lab to develop strategies to optimize the transport of surfactants in reservoirs.

Our novel switchable amine surfactants satisfied simultaneously the requirements of high CO_2 solubility and formation of C/W foams in the presence of water. Moreover, these switchable surfactants showed low partitioning towards oil and favorable CO_2/brine partitioning. In addition to cationic surfactants, nonionic linear and branched ethoxylate surfactants with high EO number formed strong foams in sand/bead packs and remained highly viscous in a capillary tube as bulk foam. Foam texture was visualized in an optical high pressure cell.

Both switchable surfactants and nonionic surfactants formed unstable oil-water/brine (up to 9 wt% NaCl) emulsion at reservoir temperature. To further demonstrate this concept, we showed that carbon dioxide foams broke in the presence of injected oil as a function of the oil concentration. Thus these smart surfactants may be used to generate foam that can stabilize the displacement front in CO_2 flooding. In addition, the smart foam would break in the presence of residual oil, which encourages the contact between CO_2 and oil, and further improve mobilizing residual oil. For nonionic alkyl ethoxylate surfactant with high EO number, a maximum in viscosity is visible at a quality of ~90% in a 30 Darcy sand pack. Shear-thinning behavior was found at low velocity, which indicates lower viscosity in near well-bore area for high injectivity and higher viscosity far from the injection well.

We have formed C/W foams with up to 9% NaCl for a nonionic surfactant and up to 18% NaCl, and with high Ca levels for a cationic switchable surfactant. The C/W foam

still formed with only 0.1 wt% surfactant in the aqueous phase, which equals to ~0.02 wt% in the total C/W foam flow. This very low concentration is beneficial for the economics of EOR. We have identified both nonionic and cationic surfactants with high efficiencies for lowering the interfacial tension at 1% (w/w) between water and CO2 as a function of CO2 density and temperature up to 18 mN/m, and have found these to be effective for forming C/W foams.

Oil/brine partition coefficients of novel switchable surfactants and nonionic alkyl ethoxylate surfactants with proper EO chains were determined and found very low at reservoir temperature, salinity and pH conditions. These low oil/brine partition coefficient values are on the order 0.1, which suggests that these surfactants will have minimal retardation due to partitioning into oil in the EOR process. The CO_2/water partition coefficient for the switchable tertiary amine surfactants was found to be on the order 0.1, which is optimal for transport of surfactant in porous media.

We hypothesized that the presence of silica and/or clay may significantly affect the adsorption of cationic surfactants on carbonates. To verify this hypothesis, we analyzed the surface chemistry of four kinds of natural carbonates, including dolomite and limestone samples. X-ray photoelectron spectroscopy (XPS) revealed that a substantial amount of silicon and aluminum exist in natural carbonates but not in synthetic calcite. Energy-dispersive X-ray spectroscopy (EDX) shows that silicon is widely distributed on dolomite surface. We performed static adsorption experiments on various carbonates using hexadecylpyridinium chloride monohydrate (CPC) as a cationic surfactant and sodium dodecyl sulfate (SDS) as an anionic surfactant. The results show that CPC exhibited negligible adsorption on synthetic calcite compared with SDS, and the adsorption plateau ratio of CPC/SDS was highly dependent on the atomic ratio of (Si+Al)/(Ca+Mg) of the carbonate sample. This finding indicates that, in addition to nonionic surfactants, cationic surfactants may be good candidates for CO_2 foam EOR with low adsorption on carbonates if the silica and clay contents in the carbonate formation are low.

High-speed microscopy videos highlight tunable bubble generation via a flow-focusing microchannel geometry, bubble stability at the foam-oil interface, and dynamic foam behavior at the pore scale (including both fractures and model porous media). Foam sweep and oil displacement is studied as a function of foam quality, bubble size, surfactant type, and fracture-matrix permeability. Comparisons are made with pure gas and surfactant-free flooding, showing improved sweep and oil mobilization (up to 98% oil-in-place displaced) for foam systems.

The model oil used is a paraffin oil dyed red with a viscosity of ~25 cP, and the surfactant solution is a 1% betaine solution with a viscosity of ~1.04 cP. A porous media matrix is designed and saturated with the paraffin oil, and the oil saturation is monitored as a function of time at various conditions.

For control experiments, a gas injection, water injection, and a surfactant solution injection scheme are compared to the foam flooding experiment. The pressure of the gas injection is chosen to match the pressure of the gas used to generate foam, and the liquid flow rate of the water and surfactant solutions are chosen to match the flow rate of the foam's surfactant solution. In the air injection experiment, the gas simply floods the middle fracture, the high permeability region, and then the low permeability region of the porous media. For the DI water flooding, the pressure is below the capillary entry pressure for the porous media and simply sweeps oil from the matrix only. For the surfactant flooding, the behavior is similar to that of the DI water flooding. For the foam injection, a faster sweep and imbibition into the porous media occurs. In particular, 90% of the original oil-in-place was displaced in ~0.07 pore volumes with foam, compared to only ~12% (from the fracture only) using only surfactant flooding.

High pressure core floods were successfully conducted to evaluate the capacity of foam to divert CO_2 from high permeability zone (thief zone) into low permeability zone (upswept oil-rich zone). The permeability contrast (defined as the ratio of high permeability to low permeability) for the core floods was chosen based on typical reservoir permeability variations from both Tensleep and Hobbs fields.

3

One of the important findings was that at very low fluid rates (i.e. far field rate conditions), the mobility of CO_2 in foam is quite uniform in both high and low permeability rocks. This indicates that foam is stronger in higher permeability zone to resist preferential flow of CO_2 in this zone, resulting in higher sweep efficiency. For high flow rates (i.e. near wellbore rate conditions), the effective permeability of CO_2 increases with injection rates. Therefore, strong foam that reduces injectivity does not develop near the wellbore region. The core flood results are also useful for understanding of local foam rheological behaviors and empirical approach based foam modeling.

Several core floods were conducted to investigate the conditions for foam generation during transient foam flow. In particular, it was found that gas solubility is an important effect that influences the generation mechanism. This result suggests that foam injection strategy can be influenced by reservoir pressure. Another important finding from transient foam flow was that foam flow exhibits multiple quasi-steady states that occur during water desaturation by gas displacement. This behavior has not been described in the current state of the art in foam modeling.

The partition coefficient of the CO2 soluble surfactants is dependent on pressure at a fixed temperature. This functional relationship is strongly influenced by the CO2-philicity of these surfactants. The conventional CO_2 insoluble surfactant such as CD 1045 could generate strong foam in Silurian dolomite cores. However, strong foam propagation was substantially delayed due to the surfactant adsorption.

CO_2 soluble surfactants could reduce the delay of foam propagation, enhancing foam robustness. The level of foam robustness enhancement varies with surfactant partition coefficient and adsorption. As the partition coefficient of the foaming surfactant increases from zero (CD 1045) to above 1.5 (15S) at the core flood conditions, the rate of strong foam propagation appears to be highest at around 0.1 (S). The dependency of foam robustness on surfactant partition coefficient can be explained based on the effect of critical surfactant concentration on foam stability and the spreading of surfactant concentration distribution due to partitioning. Core-scale CO_2 displacement rate increased with decreasing surfactant partition coefficient for all

4

CO_2 soluble surfactants.

The CMG STARS^{TM} foam model is an empirical model that has been widely used for historical matching of lab and field foam process. The limitation of this model in its prediction of laboratory data has been evaluated. To improve this model, we developed a new method to determine foam model parameters based on experimental data. Several core flood experiments were conducted with simultaneous injection of gas and surfactant solution at different experimental conditions. At steady state, saturation of the aqueous phase is shown to be strongly dependent on foam strength. By superimposing contour plots of the transition foam quality and the foam apparent viscosity, one can estimate the reference mobility reduction factor ($fmmob$) and the critical water saturation ($fmdry$) using the empirical STARS^{TM} foam model.

The parameter $epdry$ which regulates how abrupt the foam dry-out effect occurs can be estimated by a transient foam experiment. The effect of surfactant concentration on foam strength is investigated. It is found that the critical surfactant concentration ($fmsurf$) in the STARS^{TM} foam model is at least one order of magnitude above the critical micelle concentration. A modified model is implemented to include the effect of surfactant concentration on critical water saturation. Additionally, typical shear-thinning behavior in foam flooding is observed and modeled using the STARS^{TM} foam model.

A 3D pore-network model of computer-generated sphere packs coupled with fluid models that represent a lamella flow through a pore throat has been successfully used to quantify two key rheological features of foam mobility (i.e. gas relative permeability and effective gas viscosity) and their influencing factors.

Flowing gas fraction increases as the overall lamella density in the pore network decreases at a constant pressure gradient. This results in a significant variation of the threshold pressure gradients at high overall lamella density. Relative gas permeability

is a strong non-linear function of flowing gas fraction. This observation disagrees with most of the existing theoretical models for the effect of gas trapping on relative gas permeability in which a linear relationship is commonly assumed. Moreover, the shape of the relative gas permeability curve is poorly sensitive to overall lamella density.

The findings on the dynamics of foam trapping and remobilization indicate that both flowing and trapped lamella densities vary with pressure gradient, but are not necessarily the same. This preliminary result provides insight into the least explored aspect of population balance based modeling approaches, that is the kinetics of gas trapping. It is also relevant to understanding phase trapping during multi-phase flow.

Empirical and mechanistic pore-scale apparent gas viscosity models are evaluated and compared. It is found that all the models give almost the same functional relationship between flowing gas fraction and pressure gradient. This would facilitate scaling of flow rate with pressure gradient and testing a range of shear-thinning and yield-stress behavior in a simple format.

Effective gas viscosity is a strong function of flowing lamella density. The nonlinearity of this function is opposed to the existing foam viscosity models developed for foam flow in porous media and reported here for the first time. In addition, shear thinning foam flow is more obvious at high flowing lamella density while Newtonian flow becomes significant at relatively low flowing lamella density.

Scaling of effective gas viscosity with flowing lamella density depends on how the later quantity is defined. Effective gas viscosity is a unique function of the number of flowing lamellas normalized to the total number of pore throats open to flow. However, it also scales with overall lamella density if the number of flowing lamellas is normalized to the flowing gas volume. This issue has not been addressed in the literature of modeling of foam in porous media because the dynamics of gas trapping and remobilization and its effect on foam mobility has been neglected.

Scaling of foam process to field has been conducted. Different injection strategies have been investigated, including conventional CO_2 insoluble surfactants and the influences of surfactant partitioning between CO_2 and water phases on field-scale foam performance. One of the significant findings was that higher surfactant partition coefficient results in lower gas production rate over a relatively short period time owing to deeper surfactant and foam propagation into the reservoir. However, this early-time production behavior dramatically changes at later time. An increase in surfactant partition coefficient leads to a more spreading of surfactant concentration distribution towards the producer, enhancing the significance of surfactant concentration effect. Therefore, surfactants with relatively lower partition coefficients can improve better vertical sweep efficiency. This particular effect of surfactant partitioning improves not only sweep efficiency but also well injectivity. The average well bottomhole pressure decreases with increasing surfactant partition coefficient regardless of cycle size. Increasing slug size improves vertical sweep efficiency only for the conventional CO_2 insoluble surfactant at the expense of well injectivity.

Furthermore, for the conventional foam, an increase in slug size significantly improves vertical sweep efficiency. However, foam is actually weaker as the water-CO2 cycle increases for all the CO2 soluble surfactants. Surfactant concentration gradient is dependent on the cycle size and the magnitude of partition coefficient. If the latter is fixed, an increase of water-CO2 cycle reduces surfactant concentration gradient that may impair the continuation of strong foam propagation. An increase in surfactant partitioning leads to spreading of surfactant concentration distribution. Regarding the injectivity, it was observed with the conventional surfactant that high pressure gradient is concentrated only within the near wellbore region and expands somewhat from the wellbore as the fluid cycle increases. However, it spreads much further into the reservoir for CO2 soluble surfactants with small cycle size or low surfactant partition coefficient.

Marathon has offered valuable data including well logs, geologic model, production and injection historical data for the Steamboat Butte reservoir. We have

worked closely with Marathon to reconstruct a reservoir model for Steamboat Butte in commercial CMG STARS^{TM} for the future pilot design. Steamboat crude oil samples and reservoir core plugs have been used in laboratory work. A thorough review of the characteristics of the Tensleep field has been conducted based on subsurface data. Unfortunately, Marathon has not been able to commit a foam pilot as the CO_2 flood program for some of their assets is still in a planning phase.

Recently, we have collaborated with Oxy and Tabula Rasa to identify a dolomite reservoir candidate for foam application. Hobbs reservoir operated by Oxy and East Seminole operated by Tabula Rasa have been recommended based on its heterogeneity, formation fluid properties, historical reservoir performance, and operational constraints. Tabula Rasa has planned to start water-alternating-gas injection for these patterns in early 2016 for about 9 months to establish the injection and production base lines for a foam trial. A foam pilot design will be developed based on the injection/production base lines the results of all lab tests from this project.

PART I- SURFACTANT FORMULATION FOR CO$_2$ FOAMING

1.1. Cationic Surfactants

It is reported that cationic surfactants may exhibit significantly less adsorption on carbonate minerals than that exhibited by anionic surfactants. For cationic alkyl amine surfactants formed from a variety of amines and HCl, the pH of surfactant solutions was adjusted to pH 3 or 4 to mimic the pH condition in CO$_2$ EOR in carbonate formations close to or away from CO$_2$ injection well. For protonated primary, secondary and tertiary amine, viscous foams (viscosity: 6.6-36.9 cp) formed at pH 3 and at 50 ^{o}C.

1.1.1. CO$_2$ solubility

1.1.1.1. Experimental Methods

The cloud point density of a CO$_2$–surfactant solution was measured with a stirred high-pressure variable-volume view cell (Lemert, R.M. et al. 1990) containing a piston as shown in **Figure 1-1**. A magnetic stir-bar coated with polytetrafluoroethylene (Fisher brand, 3 mm in diameter, 10 mm in length, Octagonal) was used for mixing surfactant and CO$_2$. The pressure on the backside of the piston in the cell was controlled by a computer-controlled syringe pump (Isco, model 260D), with CO$_2$ as the pressurizing fluid. The temperature of the system was controlled to within±0.1 ∘C by wrapping the cell with heating tape (Omegalux, model STH051-020) equipped with a voltage controller (Staco, model 3PN1010B) and a temperature controller (Omega, model CN76000). The pressure of the system was increased to 5000 psia where the contents in the cell became clear without excess un-dissolved surfactant. Upon reducing the pressure slowly with a computer-controlled syringe pump (Isco, model 260D) at a rate of 1 psi/second, the pressure, at which the solution became so hazy that the piston was no longer visible, was recorded. This procedure was repeated at least 3 times for every temperature

and the average pressure was assigned as the cloud point pressure. The typical uncertainty was 50–100 psi.
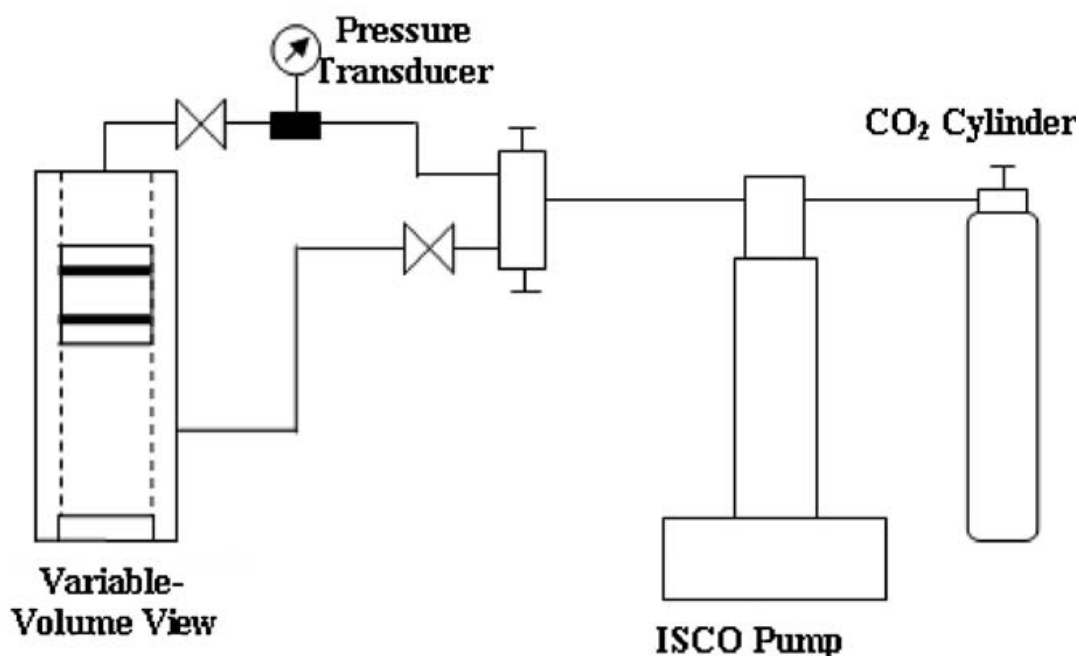
Figure 1-1. Schematic of the high-pressure apparatus for phase behavior.

1.1.1.2. Solubility of amines in CO_2

Many nonionic surfactants are known to be highly soluble in CO_2 including amines (without water present) as shown in **Table 1-i**

Table 1-i: CO_2 solubility of amines

Amine	Mole fraction solubility ($x10^6$)	T (K)	P (bar)
Di-n-dodecylamine	266	320	205
Di-phenylamine	6210	333.15	263
Tri-phenylamine	781	320	201
Tri-n-hexylamine (THA)	44000	320	155
Tri-n-octylamine	8000	320	235

The cloud point pressures of 0.2% (w/w) Ethoxylated (5EO) cocoamine in CO_2 at 25 up to 120 ^oC are listed in **Figure 1-2**. The cloud point density decreases with an increase in temperature. This lower critical solution temperature phase behaviour is well known for CO_2-based systems (O'Neill M.L. et al. 1998). At a given density of CO_2, the increase in the solubility of surfactant with increasing temperature is due primarily to weakened solute– solute interactions. The thermal energy overcomes the various attractive forces between surfactant molecules for both the head groups and tails.   The ethylene oxide group has moderate CO_2-philicity (Adkins S.S. et al. 2010). However, thermal energy is important for weakening hydrogen bonding between the terminal H atoms on the EO groups and the O and N atoms. It is possible that the Lewis acidity of CO_2 provides some degree of interaction with the basic nitrogen groups.   In EOR, the high solubility in CO_2 is beneficial for introducing the surfactant into the reservoir in the CO_2 phase and for favouring transport of the surfactant with the flowing CO_2.

For ethoxylated (5EO) tallowamine, the cloud point pressures of 0.2% (w/w) surfactant in CO_2 at 40 ^oC are 1547 and 1756 psia respectively.
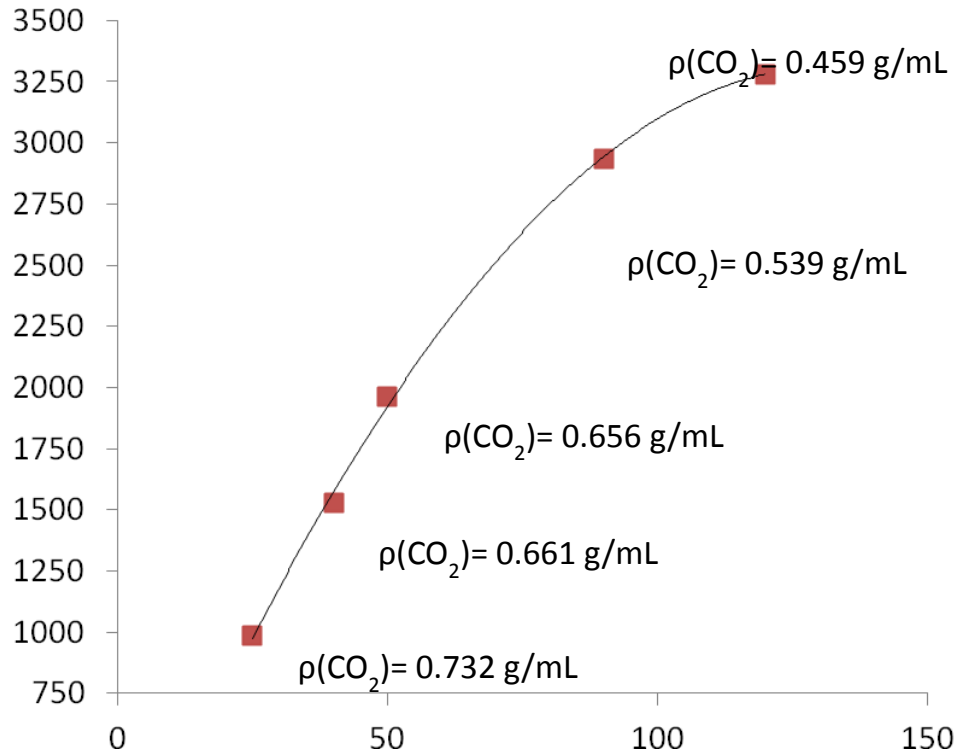
Figure 1-2: CO$_2$ solubility of 0.2 wt% Ethoxylated (2EO) cocoamine

1.1.2. Foam Viscosity

1.1.2.1. Experimental Methods

The apparatus to measure the foam viscosity up to 3400 psi is depicted in **Figure 1-3**. A forced convection air oven was used to control system temperature. For conventional foam generation, an ISCO syringe pump (model 260D) with a series D pump controller and an HPLC dual head pump (LDC/Milton Roy consta Metric III) were used to inject the CO$_2$ and aqueous solution, respectively, at set flow rates. The mixture of CO$_2$ and surfactant solution entered a sand pack with hydrophilic pores for foam generation. For co-injection foam generation, surfactant and CO$_2$ was loaded into the front part of an accumulator. After loading, the pressure inside the accumulator was around 1500 psi. Then end of the back part of the accumulator was heated by hot water for 2 hours up to 2500 psi to make natural flow inside the accumulator which helped the dissolving of surfactant in the CO$_2$ phase. Then CO$_2$ and surfactant was kept inside the accumulator for 1 or more days at 1500 psi to

12

reach the equilibrium surfactant concentration. Then CO_2 phase and water phase were co-injected at set flow rates and entered a sand pack with hydrophilic pores for foam generation. For both cases, the sand pack was a 14.7 cm long, 0.76 cm inner diameter tube packed with pre-washed 20-40 Mesh non-spherical sand (420-840 µm in diameter) that gives 50 µm pores. Sand was held in place by wire screens affixed to tubing ends. Sand packs were rinsed with 200 ml of isopropanol/water 1:1 (v/v) mixture and several liters of pH2 HCl solution and DI water until the effluent was surfactant-free. For conventional foam generation, the surfactant pre-adsorption was accomplished by running a sufficient volume of surfactant solution (60 mL) through the sand pack.
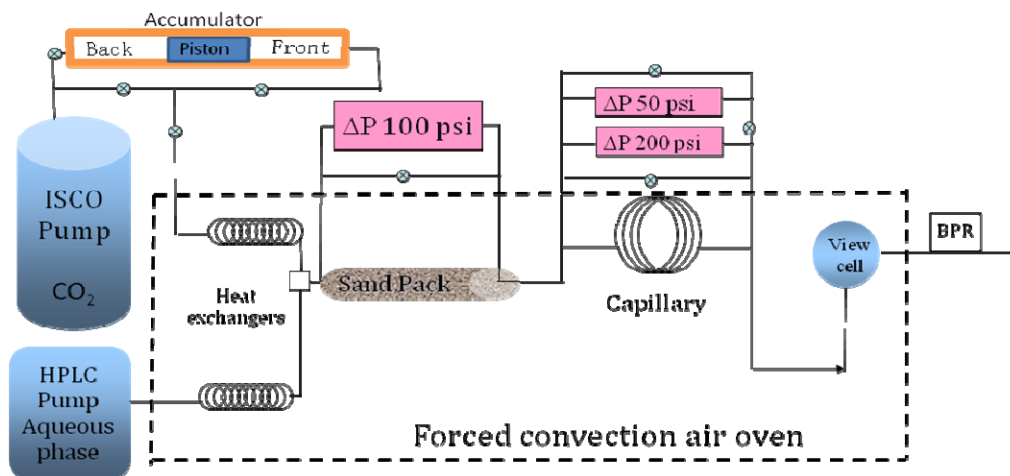
Figure 1-3: *Schematic of equipment used for CO_2-water foam viscosity measurements. BPR means back pressure regulator. The sand pack is used as the foam generator.*

The apparent viscosity of a bulk foam (η_{foam}) is calculated by the Hagen-Poiseuille equation from the known shear rate ($\dot{\gamma}$) and measured pressure difference (ΔP) across the capillary with a length (L) of 195 cm. The wall shear stress (τ) and wall shear rate are calculated from $\Delta P R_{cap}/2L$ and the velocity gradient ($4U/R_{cap}$), respectively. The average velocity, U, is determined from the total volumetric flow rate of the foam (the sum of the flow rates for the

two phases, Q_{total}) divided by the cross sectional area of the capillary tube. R_{cap} is the capillary tube radius (0.0381 cm).

$$\eta_{foam} = \frac{\tau}{\dot{\gamma}} = \frac{\left(\dfrac{\Delta P \cdot R_{cap}}{2L}\right)}{\left(\dfrac{4U}{R_{cap}}\right)} = \frac{R_{cap}^{2}\Delta P}{8LU}$$

Viscosities of C/W foam generated by protonated alkyl amines were measured up to 70 ^{o}C and 3400 psia. Viscosities of C/W foam generated by TMN-6 and THA with co-injection method (dissolve surfactants in CO_2 phase first, then inject with aqueous phase) were measured up to 70 ^{o}C and 3400 psia.

1.1.2.2. Viscosity of CO_2/water foam generated by amine based surfactants

Considering the presence of carbonate formation and variations in CO_2 concentration, it is possible that a surfactant may need to be able to work at a pH 4. Therefore, oleyamine, tri-pentylamine and THA were tested in the capillary viscometer with a total flow rate of 6 mL/min, at 3400 psia, CO_2: 0.1 or 1 wt% surfactant aq. pH4 HCl solution (9:1 v/v ratio) at 50 and 70 ^{o}C. The viscosity results are presented in **Table 1-ii**. Oleylamine formed foam with a higher viscosity at pH4 compared to that at pH3 at the same testing temperature. However, for THA, foams with lower viscosity formed at pH4. And for tri-n-pentylamine, no foam formed when temperature was equal to 70 ^{o}C. There are two possible explanations for this. First, less amine is protonated in solution with the higher pH value, and unprotonated alkyl amine does not work as surfactant in foaming process. Second, amine may not be entirely soluble in water phase in high pH condition.   If it is not entirely soluble there will be a third phase, which is an amine rich, "oil" phase. This additional phase may destabilize foam. Also, amines may partition preferentially into the oil phase

14

which would result in surfactant loss at the water-CO_2 interface. This partitioning into the oil is a possible limitation of amines. Thus we started new experiments with more hydrophilic amines.

__Table 1-ii__: Bulk foam apparent viscosities at total flow rate of 6 mL/min, 3400 psia, CO_2: 0.1 or 1 wt%, pH 3-4 protonated amine aq. solution* (9:1 v/v ratio) at 50 and 70 ^oC

Sample	Composition	Surf. Conc. (wt%)	pH	Viscosity (cp	
				50 °C	70 °C
Oleylamine	$CH_3(CH_2)_7CH=CH(CH_2)_8NH_2$	1	3	-	30.0
		1	4	36.9	-
Tri-n-pentylamine	$(CH_3CH_2CH_2CH_2CH_2)_3N$	1	3	-	8.9
		1	4	4.0	-
THA	$(CH_3CH_2CH_2CH_2CH_2 CH_2)_3N$	0.1	3	-	11.8
		0.1	4	6.6	-

* pH was adjusted by adding concentrated HCl solution.

A quick method for determining solubility of surfactants including amines in water was also developed. 1 wt% tri-n-hexylaamine (THA) water mixtures/solutions were adjusted to pH2 -10 by adding concentrated HCl aqs. (for pH2), acetic acid aqs. (for pH4 and 6), $NaHCO_3$ (for pH8) and NaOH aqs. (for pH10). Then all mixtures were sonicated for 15 s. For THA, the mixtures from pH 4 to pH10 turned cloudy after sonication as shown in **Figure 1-4**, which indicates that the insoluble surfactant formed small dispersed droplets inside water. THA was not totally dissolved at pH4 -10.

Figure 1-4: Sonication method for determining amine water solubility: 1 wt% THA water mixtures (pH2 -10) sonicated for 15 s.
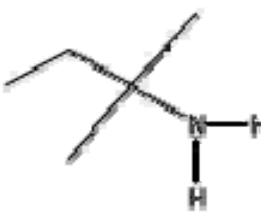
Three primary fatty amines were tested in the capillary viscometer with a total flow rate of 6 mL/min, at 3400 psia, CO_2: 1 wt% surfactant aq. solution (9:1 v/v ratio) at 70 ^{o}C. The viscosity results are presented in **Table 1-iii**.

For all Corsamine samples, C/W foam with viscosity higher than 26 cp was obtained at 70 ^{o}C.. For Corsamine PC (coco amine), PS (soya amine) and PT (tallow amine), the average number of carbon in alkyl groups are 12.7, 17.2 and 17.8 respectively. Similarly, as a consequence of van der Waals forces and hydrophobic effects, longer alkyl tails may increase the tendency to raise the interfacial viscosity and stabilize the aqueous lamellae and raise the foam viscosity. To our knowledge primary fatty amines have rarely been tested for C/W foams, and based on our result, they were good C/W foam stabilizers. Carbamate formation was not observed in any experiment, although it is not obvious if they will be visible in the presence of opaque foam.

It was found that reducing the contact between the phases by the molecular design of the surfactant was particularly important at the CO_2-water versus oil-water interfaces. Contact might be reduced by increasing the interfacial adsorption of the surfactant or by blocking more interface for a given surfactant adsorption with tail branching or double tails. Branching of the surfactant tail with methyl, propylene oxide or larger alkyl units reduces the contact of the CO_2 and water phases relative to a linear tail and raises surfactant efficiency. Therefore, a highly branched surfactant, tert-amylamine was also tested. Unfortunately, there was no C/W foam formed as the alkyl tail

of tert-amylamine is too short.   Further testing of longer chain branched primary amines will be considered.

Table 1-iii: Bulk foam apparent viscosities at total flow rate of 6 mL/min, 3400 psia, CO_2: 1 wt% pH3 protonated primary amine aq. solution (9:1 v/v ratio) at 70 $^{\circ}$C.

Sample	Composition	Viscosity (cp)
Corsamine PC	Coco amines (Coco alkyl group: C8-18)	26.1
Corsamine PS	Soya amine (Soya alkyl group: C14-C18)	33.7
Corsamine PT	Tallow alkyl amines (Tallow alkyl group: C16-C18)	33.4
Tert-amylamine		No foam
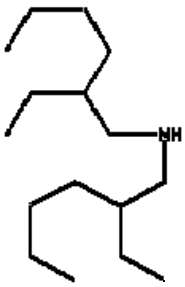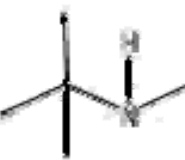
Three kinds of secondary amines were tested in the flow viscosity measurement apparatus with total flow rates of 6 mL/min, 3400 psia, CO_2: 1 wt% surfactant aq. solution (9:1 v/v ratio) at 70 $^{\circ}$C.

The viscosity result for secondary amines is presented in **Table 2-iv**. It was found that stable C/W foam was formed at 70 $^{\circ}$C. The longer the alkyl group was, the higher the foam viscosity was. Longer alkyl groups not only helped to stabilize C/W foam for a low CO_2 density, but also lead to a higher viscosity at the same shear rate and surfactant concentration. In all cases, texture of carbamate was not distinguishable in view cell.

17

Although n-tert-butylisopropylamine had two highly branched tails, neither tail was long enough to stabilize C/W foam at. 70 ^{o}C.

To our knowledge, secondary amines have received little attention as surfactants in generating C/W foam. Stable C/W foam formed when the number of carbons was 6 or more in each alkyl tail of the secondary amines at 70 ^{o}C.

Table 1-iv: *Bulk foam apparent viscosities at total flow rate of 6 mL/min, 3400 psia, CO$_2$: 1 wt% pH3 protonated secondary amine aq. solution (9:1 v/v ratio) at 70°C.*

Sample	Composition	Viscosity (cp)
Di-n-hexylamine (DHA)	(CH$_3$CH$_2$ CH$_2$ CH$_2$CH$_2$CH$_2$)$_2$NH	8.8
Di-2-ethylhexylamine		6.9
N-tert-butylisopropylamine		No foam

1.1.2.3. Viscosity of CO$_2$/water foam generated by ethoxylated coco and tallow amine based surfactants

Ethoxylated (5EO) coco and tallow amines were gifts from Akzo Nobel and used without any further purification. The structure of ethoxylated amines are presented in **Table 1-v.**

Surfactant	Composition	Activity
Ethoxylated (5 EO) Cocoamine	$R-N(CH_2CH_2O)_mH (CH_2CH_2O)_nH$ R=Coco ($N_{average}$ of Carbon=~13), m+n=5	98-100%
Ethoxylated (5 EO) tallowamine	$R-N(CH_2CH_2O)_mH (CH_2CH_2O)_nH$ R=tallow ($N_{average}$ of Carbon=~17), m+n=5	98-100%

The ethoxylation of the amine functionality modifies the hydrophilic-lipophilic balance (HLB) relative to alkyl amines. The pK_a for tetraoxyethylene dodecylamine ($C_{12}NH(EO)_4$) is 9.3, while that of dodecylamine is 10.6.[2] Soluble ethoxylated alkyl amines are highly protonated at pH 3 to 6 in the presence of high pressure CO_2. Ethoxylated alkyl amines are highly cationic in nature with EO numbers less than about 5. For higher EO numbers the surfactant behaves more like a nonionic surfactant,[2] as the effect of the protonated nitrogen group is screened by the surrounding EO groups.

The cloud points of ethoxylated cocoamines at pH 4 to 10 in DI water, with 30 g/L or 120 g/L are listed in **Table 1-vi**. At pH4, all the cloud points for the two ethoxylated cocoamines with 2 or 5 EO groups in water and up to 120 g/L NaCl brine are higher than 120 ^{o}C. For the case with 15 EO groups, the cloud point dropped slightly for 120 g/L NaCl at pH 6. These cloud points are significantly higher than those of most ethoxylated nonionic surfactants.[3] At higher salinity, the cloud points of ethoxylated non-ionic surfactants may be expected to be even lower.[4] The cloud point of ethoxylated cocoamine surfactant decreased with increasing of EO number from 5 to 15 EO groups. At first, this may seem counterintuitive given the increase in hydrophilicity with EO number. However a second important factor must be considered at low pH. The EO hydrophilic group may screen the protonated nitrogen and thus lower the contribution from hydration of the cation. At pH 10 where the amine is

not protonated, the cloud point is much lower at high salinity, and decreases with decreasing of EO number.

Thus, the ethoxylated cocoamine surfactant exhibits both non-ionic and ionic character that may be tuned by varying the EO length to achieve high cloud point of > 120 $^{\circ}$C in the presence of 120 g/L NaCl brine with optimal EO number of 2 and up to 5 at pH 4. The high cloud points of ethoxylated cocoamines are an important milestone for designing a successful surfactant candidate for CO_2 foam generation in high temperature and high salinity conditions.

Table 1-vi: _Cloud point temperature of 1 % (w/w) ethoxylated cocoamine aqueous solution with different NaCl concentrations and pH (adjusted by HCl) at atmospheric pressure_

Surfactant	pH	Salinity		
		0	30 g/L NaCl	120 g/L NaCl
$C_{12-14}N(EO)_2$	4	>120	>120	>120
	6	90	-	-
	10	<25	-	-
$C_{12-14}N(EO)_5$	4	>120	>120	>120
$C_{12-14}N(EO)_{15}$	4	>120	>120	>120
	6	-	>120	116
	10	>120	116	89

Based on composition analysis of an actual formation brine provided by Oxy, a brine made of 4.49 g/L NaCl, 2.03 g/L $MgCl_2 \cdot 6H_2O$, 2.02 g/L $NaHCO_3$, 1.18 g/L $CaCl_2 \cdot 2H_2O$ and 0.495 g/L $Na_2SO_4 \cdot 10H_2O$ was prepared and shown a small amount of precipitation. The precipitation was most probably $CaSO_4$ and $CaHCO_3$. We replaced SO_4^{2-} and HCO_3^- with Cl^-. No precipitation was found in the new brine. This brine (5.98 g/L NaCl, 2.03 g/L $MgCl_2 \cdot 6H_2O$ and 1.18 g/L $CaCl_2 \cdot 2H_2O$) was used in further investigation.

Foams were formed at 40 ^{o}C and 1700 psia for all three tested surfactants with a total flow rate of 6 mL/min, CO_2: 1 wt% surfactant brine solution (9:1 v/v ratio). The viscosity results are presented in **Table 1-vii**. All three surfactants formed foam that was more than one hundred times more viscous than pure CO_2.

As a consequence of van de Waals forces and hydrophobic effects, longer alkyl tails may increase the tendency to raise the interfacial viscosity and stabilize the aqueous lamellae and raise the foam viscosity. This factor may explain why ethoxylated tallow amine (average carbon number: 17) provides even higher viscosity than ehtoxylated coco amine (average carbon number: 13) with identical EO number. To our knowledge ethoxylated amines have rarely been tested for C/W foams. Ethoxylated amines with the proper alkyl group could be good C/W foam stabilizers.

Table 1-vii: Bulk foam apparent viscosities at total flow rate of 6 mL/min, 1700 psia, CO_2: 1 wt% surfactant South Hobbs brine (5.98 g/L NaCl, 2.03 g/L $MgCl_2 \cdot 6H_2O$ and 1.18 g/L $CaCl_2 \cdot 2H_2O$) solution (9:1 v/v ratio) at 40 ^{o}C

Sample name	Viscosity (cP)	Foam viscosity/CO_2 viscosity*
Ethoxylated (5EO) cocoamine**	10.8	189
Ethoxylated (5EO) tallowamine**	11.2	196

* CO_2 viscosity: 0.057 cP (40 ^{o}C, 1700 Psia) (Fenghour, A. et al. 1998)

** Concentrated and diluted HCl was added into surfactant brine solution to adjust the pH of the solution to 4.
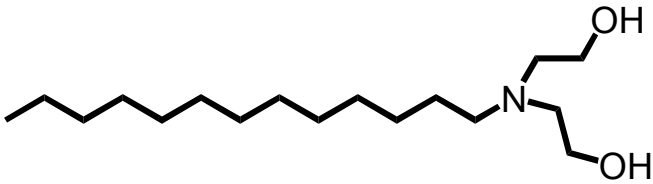
Bis(2-hydroxyethyl) cocoalkylamine ($C_{12-14}N(EO)_2$), polyoxyethylene (5) cocoalkylamine ($C_{12-14}N(EO)_5$) and polyoxyethylene (15) cocoalkylamine ($C_{12-14}N(EO)_{15}$) were gifts from Akzo Nobel and used without further

purification.(**Table 1-vii**). Research-grade carbon dioxide was used as received.

Sodium chloride (NaCl, certified ACS, Fisher), calcium chloride dehydrate ($CaCl_2 \cdot 2H_2O$, 99+% Acros), glacial acetic acid (HOAc, certified ACS plus, Fisher), hydrochloric acid (HCl, technical, Fisher) and isopropanol (certified ACS plus, Fisher) were used as received.

Brine was composed of deionized (DI) water (Nanopure II, Barnstead, Dubuque, IA), and NaCl in which the concentration of NaCl was varied from 30 g/L to 120 g/L.

Composition of surfactants

Surfactant	Composition and comments
$C_{12-14}N(EO)_2$	

Hydroxyl groups   added hydrophilicity

Raised solubility in water

C$_{12\text{-}14}$N(EO)$_5$
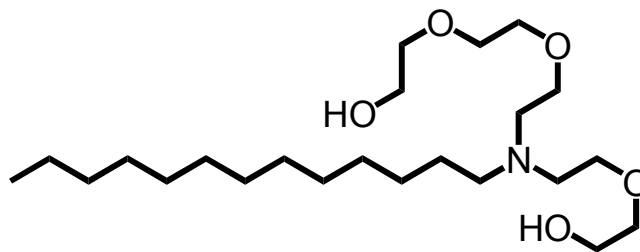
Significant character of nonionic and ionic surfactants

C$_{12\text{-}14}$N(EO)$_{15}$
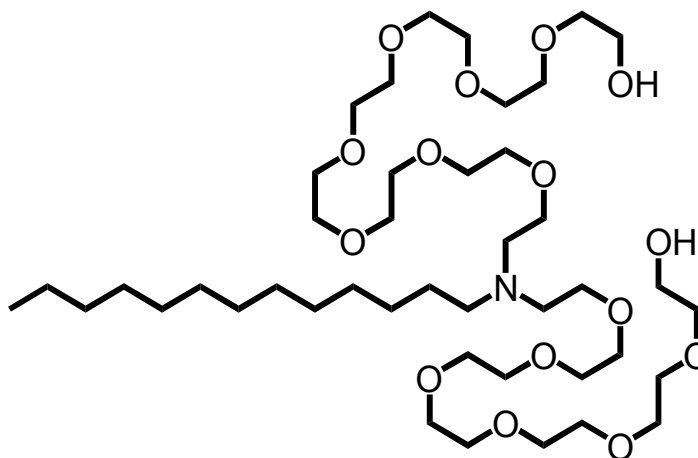
Strong character of nonionic surfactant from EO groups and steric hindrance. H bonding to EO becomes weak at high T and thus lowered cloud points.

Effect of Salinity and number of EO at a Given Temperature

The effect of salinity and number of EO groups are showed in **Table 1-viii**. At 50 $^{\circ}$C, and for 2 EO substitution in the amine head, as salinity increased from 30 to 120 g/L NaCl, the apparent viscosity decreased from 58 to 46 cP.

The apparent viscosity of C/W foams decreased with the increase in the number of EO. With fewer EO groups, the hydrophilic head group of ethoxylated cocoamine behaves more like a cationic surfactant than a nonionic

surfactant.   The greater aqueous solvation of the cation appeared to improve the stability of the lamellae for a favorable foam formation.

Table 1-viii: *Apparent viscosities of CO_2 foams. Surfactants were injected from aqueous phase. pH of aqueous phase was adjusted to 4 by HOAc or HCl initially*

Total flow rate of 6 mL/min, 50 °C, 3400 psia, CO_2: 1 % (w/w), ethoxylated cocoamine brine solutions (9:1 v/v ratio)

Surfactant	Salinity (g/L NaCl)	Apparent viscosity in sand pack (cP)	Apparent viscosity in capillary(cP)
$C_{12-14}N(EO)_2$	30	58	59
	120	46.4	41.9
$C_{12-14}N(EO)_5$	30	24	23
$C_{12-14}N(EO)_{15}$	30	12	12.8

Surfactant Injection in the CO_2 Phase

The surfactant $C_{12-14}N(EO)_2$ was dissolved in CO_2 and the solution was injected into the sand pack where it mixed with brine to form foam. Upon mixing the phases, the pH is lowered by formation of carbonic acid at high temperature, which may protonate the amine. As shown in **Table 1-ix**, this approach generated foam (apparent viscosity 62 cP) with an aqueous phase consisting of 120 g/L NaCl brine at a temperature of 50 ^oC. We are not aware of previous attempts to inject surfactants from the CO_2 phase with a switchable nonionic surfactant into a high salinity brine phase. The viscosities of foam generated by loading the surfactant from either the CO_2 phase or the aqueous phase were similar as shown in **Table 1-viii** and **Table 1-ix**. This equivalence demonstrates efficient mixing of the phase prior to entering and within the sand pack, resulting in good contact between phases and transport of surfactant to the interface from both phases. In heterogeneous reservoirs, options of

injecting surfactant in the CO_2 phase may simplify the flow path and increase sweep efficiency in certain scenarios, where the surfactant is more likely to be transported by the flowing CO_2.

Table 1-ix: *Apparent viscosities of CO_2 foams. Surfactant was injected from CO_2 phase*

Total flow rate of 6 mL/min, 3400 psia, 50 °C, 0.2 % (w/w) $C_{12-14}N(EO)_2$ CO_2 solution: 120 g/L NaCl solution (9:1 v/v ratio), 2 days surfactant dissolution time with agitation.

Apparent viscosity in sand pack (cP)	Apparent viscosity in capillary (cP)
62.3	60.4

Effect of Foam Quality

The effect of foam quality on apparent foam viscosity in the sand pack is shown in **Figure 1-5**. As the quality increased from 60% v/v, apparent foam viscosity increased gradually and then markedly above 80%, until it reached the transition foam quality. This transition takes place between the high foam quality regime (where the foam obeys the limiting capillary pressure model) and low foam quality regime (where foam behaviour is described by the bubble trapping model) as described in Rossen's unified model for steady-state foam behaviour. Often, the apparent viscosity of foams is highest at the transition foam quality.) The maximum viscosity was reached at qualities near 90% for a total flow rate of 1.5 mL/min.
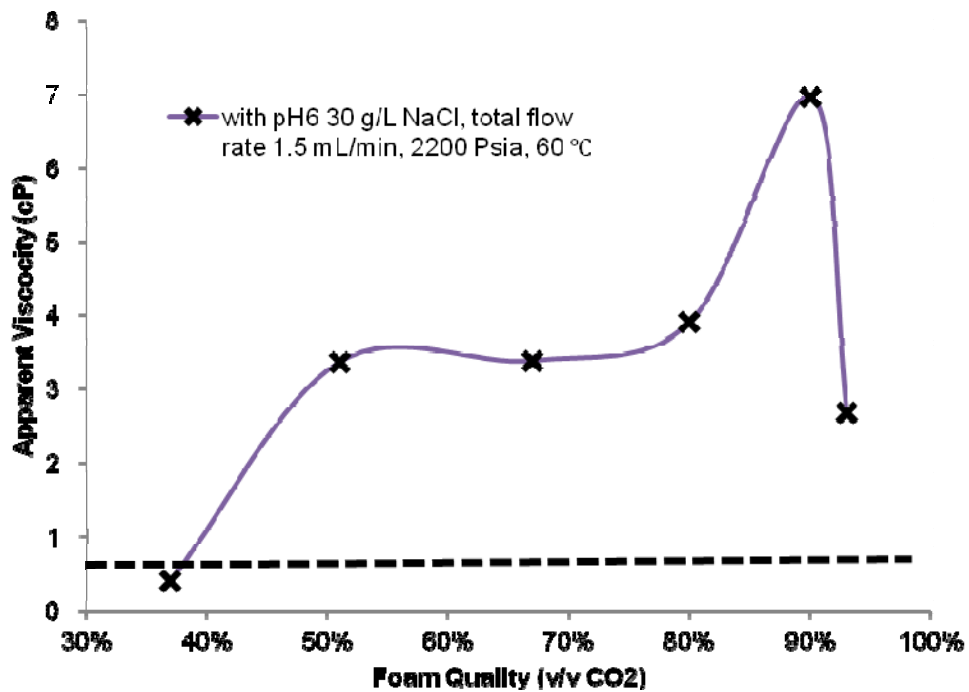
Figure 1-5: Foam apparent viscosity in sand pack of C/W foam stabilized with 1 % (w/w) $C_{12-14}N(EO)_2$ versus foam quality

The ability to increase or decrease foam viscosity via quality changes may provide control of the EOR process. Friedmann et al. found that higher quality foams (90%) were more stable than wet foams (40%) in porous media. A formulation with a high transition foam quality will require injection of less surfactant solution and will have less shielding of oil by water.

1.1.2.4. Viscosity of CO_2/water foam generated by quaternary ammonium bromide

Decyl trimethylammonium bromide (DTAB, CH3(CH2)9N(CH3)3Br, 99%) and cetyl trimethylammonium bromide (CTAB, CH3(CH2)15N(CH3)3Br, 99%) were purchased from Acros and used as received. Research-grade carbon dioxide was used as received.

The viscosity results of DTAB and CTAB are presented in **Figure 1-6** and **Figure 1-7**, respectively. For DTAB, high viscosity C/W foam was obtained in the presence of up to 3 wt% NaCl to total surfactant solution at 70 ^{o}C. Viscosity decreased when the salinity of surfactant solution increased.

It was possible that several Cl$^-$ ions were attracted to the positive charge on the trimethylammonium head group, and decreased the thickness of the double layer. With a smaller charge, the DTAB did not stabilize the aqueous lamellae between CO_2 cells as effectively.
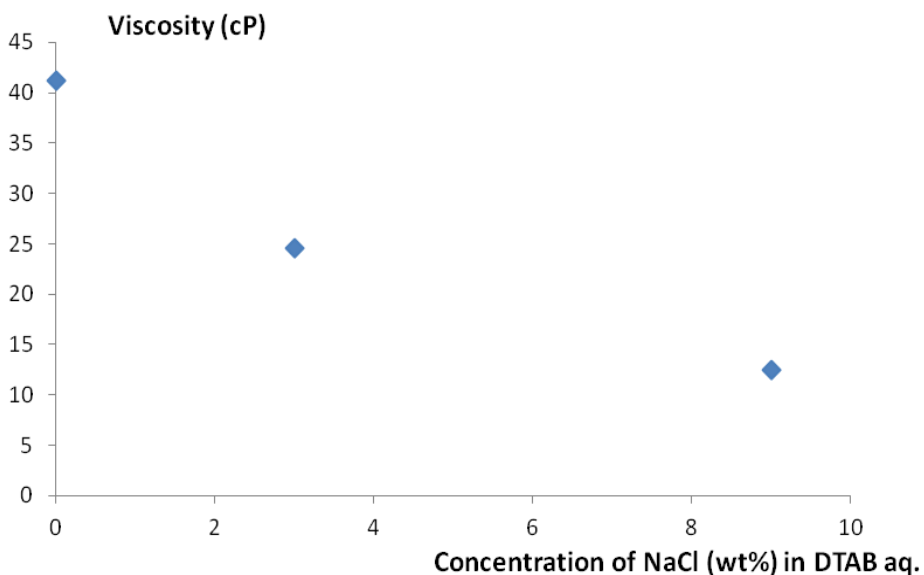
Viscosity (cP)

Figure 1-6: *Bulk foam apparent viscosities at total flow rate of 6 mL/min, 70 ^{o}C, 3400 psia, CO_2: 1 wt% DTAB aq. solution (9:1 v/v ratio) at different salinities*

For CTAB, high viscosity C/W foam was obtained at 70 ^{o}C in the presence of up to 9 wt% NaCl in surfactant solution. Viscosity increased when the salinity of surfactant solution increased, the opposite of the behavior for DTAB. A good surfactant which can form high viscosity C/W foam usually has a certain hydrophilic/lipophilic balance, or HLB. When salts are added into system, the HLB will change.
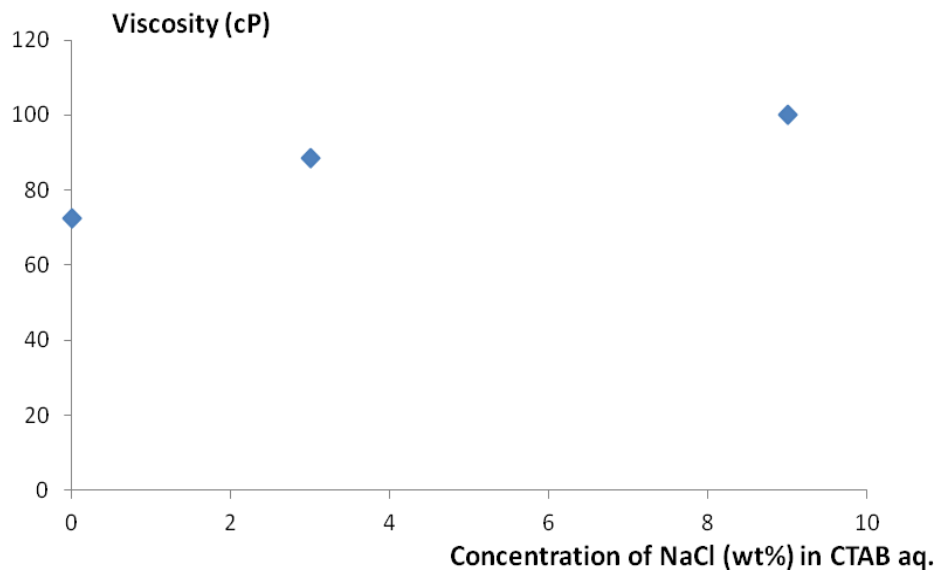
Figure 1-7: Bulk foam apparent viscosities at total flow rate of 6 mL/min, 70 ^{o}C, 3400 psia, CO_2: 1 wt% CTAB aq. solution (9:1 v/v ratio) at different salinities

1.1.3. Dodecane/brine Emulsion Stability

Initial images of the emulsions made using gentle hand mixing for 1 wt% pH4 ethoxylated (5EO) cocoamine in pH4 brine solution (5.98 g/L NaCl, 2.03 g/L $MgCl_2 \cdot 6H_2O$ and 1.18 g/L $CaCl_2 \cdot 2H_2O$) mixed with dodecane are shown in **Figure 1-8 (a)** The mixtures were put into an oven at 40 ^{o}C right after mixing. It is noticeable that it took tens of minutes for the emulsions made for an oil/water ratio near unity to totally separate into two clear lays than for emulsions made by mixing low aqueous surfactant solution with dodecane(1:9 and 2:8 v:v), which underwent phase separation immediately. After 30 minutes, all emulsions broke down to clear water and oil phases. Furthermore, similar results were observed up to 48 hours as shown in **Figure 1-8 (b**) Thus, at low shear, the emulsions generated for South Hobbs brine were all highly unstable. Similar result was found for ethoxylated (5EO) tallowamine. These results suggest ethoxylated (5EO) coco and tallow amine are successful candidates at low shear conditions for avoiding stable oil/water emulsions. The ability to form

C/W foams, without forming stable O/W foams would be highly beneficial in EOR to lower CO_2 permeability selectively in regions where oil is not present.

(A)

| 1:9 | 2:8 | 3:7 | 4:6 | 5:5 | 6:4 | 7:3 | 8:2 | 9:1 |

(B)
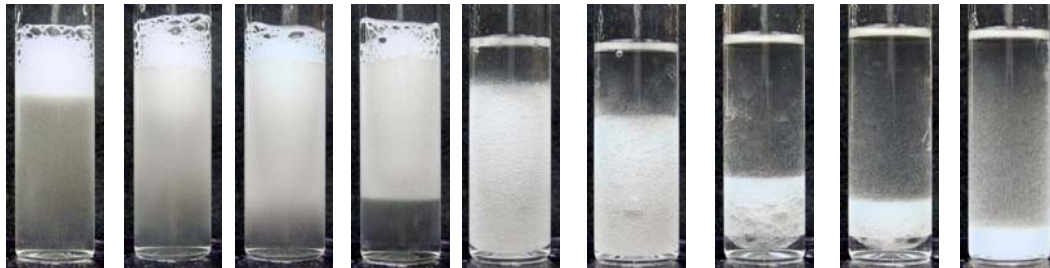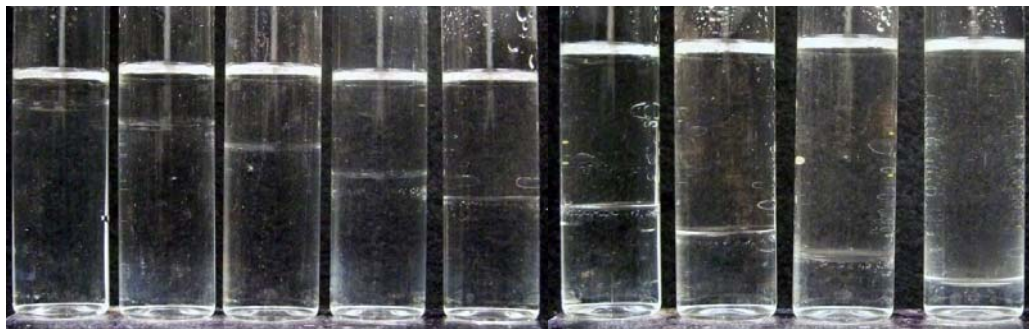
| 1:9 | 2:8 | 3:7 | 4:6 | 5:5 | 6:4 | 7:3 | 8:2 | 9:1 |

__Figure 1-8 A&B:__. Initial (A) and 48 hours (B) images of emulsion of different volumetric ratios of dodecane and 1% (w/w) ethoxylated (5EO) cocoamine pH4 South Hobbs brine solution at 40 °C. (The emulsions were prepared by hand mixing.)

1.2. Zwitterionic Surfactants

Amphosol CG and Amphosol CS-50 were gifts from Stepan and used without any further purification. Structures and nomanclature for Stepan surfactants were presented in **Figure 1-9**. Zwitterionic surfactants, BW-139, LAB and CB-35 were gifts from Rhodia Inc. and used without any further purification. Structures and nomenclature of Rhodia surfactants are presented in **Figure 1-10**.
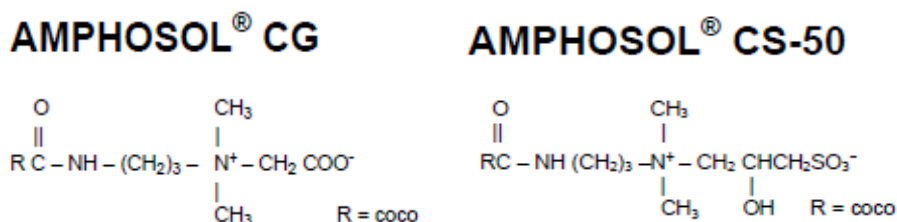
Figure 1-9: Schematics and naming scheme of Stepan surfactants.
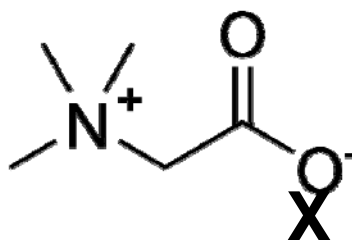
BW-139: X = $CH_3(CH_2)_7$-

CB-35:   X= COCO ALKYL GROUP (C8-C18 MIXER)

LAB: X = $CH_3(CH_2)_{11}$-

Figure 1-10: Structures of Rhodia surfactants.

1.2.1. Foam viscosity

C/W foams were formed at 50 ^{o}C and 2000 psia for amidobetaine and amido sultaine zwiterionics surfactants. Both alkyl betaine and alkyl amido betaine have a hydrophilic betaine head group and a hydrophobic alkyl group, which give them similar amphiphilicity. In addition, the thermal stability of alkyl betaines is higher than that of alkyl amido betaines, due to the absence of the amido group, which is beneficial for the high temperatures investigated. Therefore, three alkyl betaine surfactants from Rhodia were also tested in the capillary viscometer with a total flow rate of 6 mL/min, 3400 psia, CO_2: 1 wt% surfactant aq. solution (9:1 v/v ratio) at 70 ^{o}C. The viscosity results for all betaine surfactants are presented in **Table 1-x**.

For BW-139, C/W foam was obtained at 70 ^{o}C. CB-35 is coco-betaine. Coco alkyl group is a mixture of C8-C18 alkyl chains in which about 50% are dodecyl (C12) groups. As a consequence of van de Waals forces and hydrophobic effects, longer alkyl tails may increase the tendency to raise the interfacial viscosity and stabilize the aqueous lamellae and raise the foam viscosity.   This factor may explain why CB-35 provides even higher viscosity than LAB (Lauryl group is 12 carbons).   The other factors that influence the stability are the adsorption of the surfactant at the interface and the role of the surfactant on the interfacial elasticity.

To our knowledge betaines have rarely been tested for C/W foams. Alkyl betaines with the proper alkyl group could be good C/W foam stabilizers. It was also found that length of alkyl group in alkyl betaine surfactant had a significant influence on the viscosity of C/W foam. When the number of carbons was more than 8, high viscosity (foam viscosity/ CO_2 viscosity > 200) were formed at 70 ^{o}C.

Table 1-x: *Bulk foam apparent viscosities at total flow rate of 6 mL/min, 3400 psia, CO$_2$: 1 wt% alkyl betaine aq. solution (9:1 v/v ratio) at 70 ^{o}C*

Sample name	Composition	Pressure (Psia)	Viscosity (cP)	Foam viscosity/CO$_2$ viscosity
CG	Cocoamidopropyl betaine	2000	12.0	364
CS-50	Cocoamidopropyl hydroxysultaine	2000	8.2	248
BW-139	Octyl betaine	3400	1.4	23.7
CB-35	Coco-betaine	3400	15.2	258
LAB	Lauryl betaine	3400	14.4	244

Mackam CB-35 not only formed viscous (15.2 cP, more than 250 times higher than the viscosity of pure CO$_2$ at the same condition) C/W foam at 70 ^{o}C, 3400 psia, but also is more thermally stable than alkyl amido betaines, due to the absence of the amido group.   Thus this surfactant is a promising candidate for selective mobility control as a function of the amount of residual oil present. Therefore, effect of salinity, surfactant concentration, shear rate as well as foam quality on the viscosity of CB-35 foam was investigated.

1.2.2.   Effect of salinity on foam viscosity for Mackam CB-35

The effect of salinity on foam viscosity for Mackam CB-35 is presented in **Figure 1-11**. C/W foam was obtained in the presence of up to 9 wt% NaCl in surfactant solution. At 50 ^{o}C, viscosity was slightly higher in the presence of 3 wt% or 9 wt% of NaCl, compared to that at no salt condition. The ability to form foams at high salinities is highly beneficial for applying EOR for a wide variety of brine containing reservoirs.
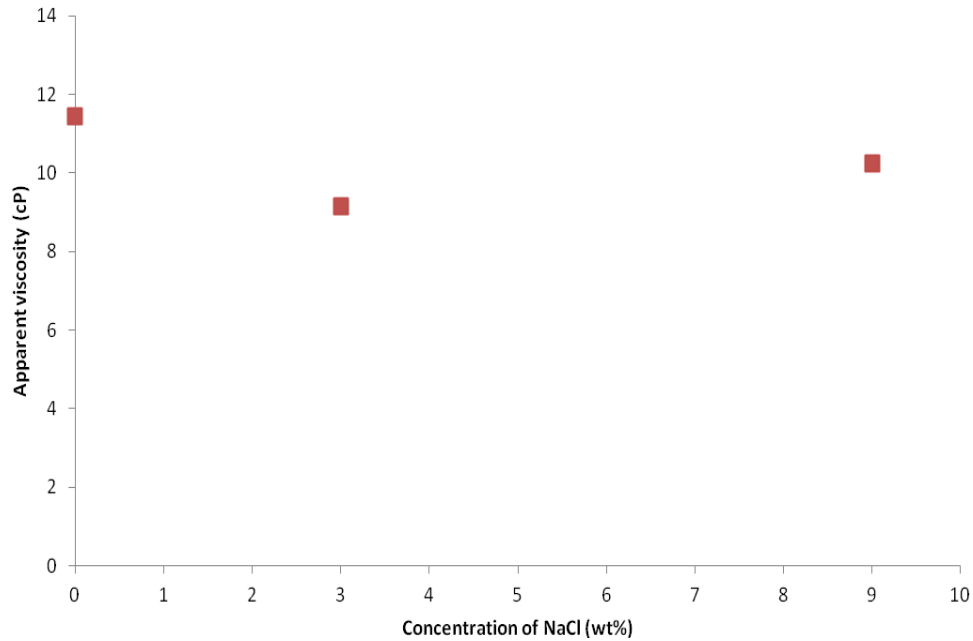
Figure 1-11: The foam viscosity of C/W foam stabilized with 1 wt% active CB-35 at total flow rate of 6 mL/min, 90% v/v CO_2, 50 °C, and 2000 psia as a function of the NaCl concentration (wt% to surfactant solution).

1.2.3. Effect of surfactant concentration on foam viscosity for Mackam CB-35

Figure 1-12 presents the foam viscosity of C/W foam stabilized with CB-35 at total flow rate of 6 mL/min, 50 °C, and 2000 psia as a function of the CB-35 concentration (active wt% to surfactant solution). It was found that CB-35 was still active to increase the viscosity of C/W mixture at 50 ^{o}C even at 0.1 wt% to surfactant solution, which equals to 0.02 wt% in total C/W foam flow. This concentration is 1/10 of the concentration (1 wt%, active) in basic cases, which indicates that CB-35 is a high efficient surfactant for CO_2 EOR.

Viscosity slightly increased with the concentration of CB-35 increased in the surfactant concentration range of 0.1-1 wt% active. At 0.01 wt%, no foam formed at 50 ^{o}C.
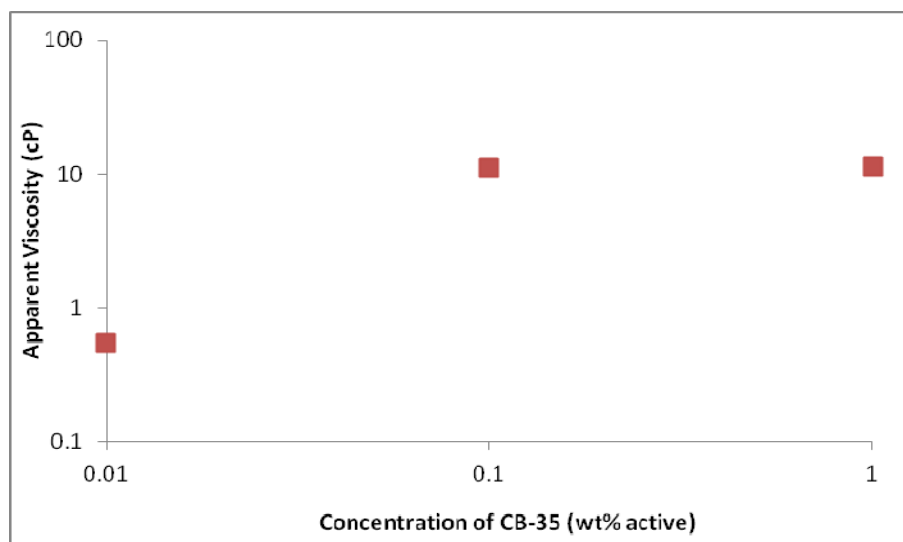
Figure 1-12: The foam viscosity of C/W foam stabilized with CB-35 at total flow rate of 6 mL/min, 50 °C, 2000 psia, 90% v/v CO_2, and 2000 psia as a function of the CB-35 concentration (wt% active to surfactant solution).

1.2.4. Effect of shear rate on foam viscosity for Mackam CB-35

A plot of shear stress versus shear rate (calculated from ΔPR/2L and 4U/R, respectively) was generated for an 1 wt% active CB-35 foam with 90% v/v CO_2 at 50 °C and 2000 psia, as shown in **Figure 1-13 (a)**.

Figure 1-13 (b) gives the viscosity as a function of shear rate. For a non-Newtonian foam a yield stress is often found.[3] . In the case of CB-35, Newtonian behavior is not observed at low shear rates and the curve in **Figure 1-13 (a)** does not intersect the origin. At low shear rates the elasticity of the foam structure produced a yield stress, that is non-Newtonian behavior. It was also found that no foam formed, when the shear rate was 192 s^{-1} or lower.   As the shear rate was increased, the foam filled a larger volume of the view cell, indicating greater foam formation and/or higher foam stability. For the base case of our viscosity measurement (total flow rate 6 ml/min), the shear rate is 2302 s^{-1}.
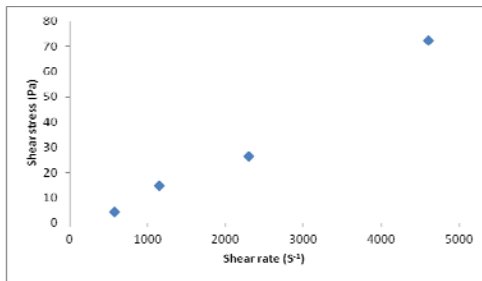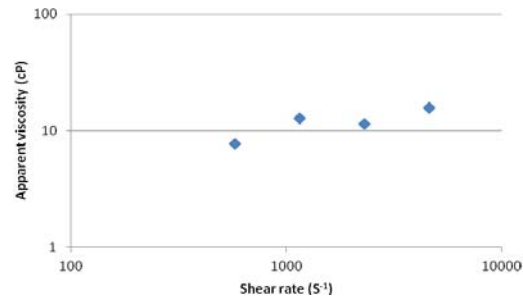
2.4(A)	**2.4 (B)**

Figure 1-13 1&2: *Shear stress (1) and viscosity (2) as a function of shear rate for the C/W foam stabilized with 1 wt% active CB-35 and 90% v/v CO_2 at 50 °C and 2000 psia*

1.2.5. Effect of foam quality on foam viscosity for Mackam CB-35

The quality of foam often has a large influence on foam viscosity.[4] As the quality is increased from 60% v/v, foam viscosity increases as well, due to the increase in the number of bubbles and lamellae in the foam from the additional volume of dispersed phase. As the quality is continually increased, a maximum viscosity is reached at qualities near approximately 95%, followed by a drop in viscosity. Foams with very high qualities have little aqueous solution, thus the liquid lamellae are very thin and cannot prevent bubble coalescence. Viscosity decreases as the lamella stability is reduced due to a drop in the number of lamellae. The effect of foam quality on foam viscosity is shown in **Figure 1-14** at a total flow rate of 6 ml/min with 1 wt% CB-35 at 50 °C and 2000 psia. A maximum in viscosity is visible at a quality of 95% and the foam lamella stability drops when the quality is increased further. The ability to vary foam viscosity via quality changes allows for some control of the foam in EOR uses, as the gas injection strategy can be altered to either increase or decrease foam viscosity. Friedmann et al. found that higher quality foams (90%) propagated better than wet foams (40%) in porous media, thus it is anticipated that high qualities with high foam viscosity may work best for CO_2 EOR.

Figure 1-14: *The foam viscosity of C/W foam stabilized with 1 wt% active CB-35 at total flow rate of 6 mL/min, 50 °C, and 2000 psia as a function of the foam quality (% v/v CO_2)*

1.3. Non-ionic surfactants

Tergitol 15-S-20 and TMN-6 were gifts from Dow and used without any further purification. Tergitol 15-S-30, 15-S-40 and NP-15 were purchased from Dow and used as received. The subscripts of Dow Tergitol surfactants denote the average number of repeat units per molecule based on the relative mass during synthesis. Structures and naming scheme of Dow surfactants were presented in **Figure 1-15**. Makon TD-18 and Bio-soft N91-8 were gifts from Stepan. The subscripts of Makon TD and Bio-soft N91 surfactants denote the average number of repeat units per molecule based on the relative mass during synthesis. Structures and naming nomenclature for Stepan surfactants are presented in **Figure 1-16** Several primary and secondary alkyl ethoxylate surfactants provided by Shell (Neodol series) and Huntsman (Surfonic series) were also tested.

TERGITOL® 15-S Series

$(CH_2CH_2O)_xH$

TERGITOL NP Series

C_9H_{19} —(OCH$_2$CH$_2$)xOH

TMN-6 ($n_{average}$= 8.33, 90% aqs.)

MAKON TD SERIES

BIO-SOFT® N91 SERIES

$CH_3(CH_2)_n$-O(CH$_2$CH$_2$O)$_y$H

n = 8-10
y = average moles of ethoxylation

__Figure 1-15__: Schematics and naming scheme of Stepan and Dow surfactants

1.3.1. Cloud Point

The cloud points of 1 % v/v nonionic ethoxylate surfactants with NaCl concentration 3 wt% or 9 wt% solutions are listed in **Table 1-xi**. The cloud point of surfactant solution increased with increasing the number of EO group of surfactant molecules and decreased with increasing salinity. In the presence of 9 wt% NaCl, the cloud points of all tested surfactants are still higher than 59 $^\circ$C, which indicates nonionic alkyl ethoxylate and alkyl phenol ethoxylate surfactants are promising surfactant candidates for CO_2 EOR.

Surfactant	Composition	No salt	3 wt% NaCl	9 wt% NaCl
15-S-20	Branched C(12-14)-EO20	>90°C	>90°C	78°C
15-S-30	Branched C(12-14)-EO31	>90°C	>90°C	81°C
15-S-40	Branched C(12-14)-EO41	>90°C	>90°C	80°C
N91-8	C(9-11)-EO8	82°C	72°C	60°C
NP-15	Nonylphenol Ethoxylate (EO15)	>90°C	88°C	68°C
TD-18	C13-EO18	>90°C	>90°C	72°C

For alkyl ethoxylate nonionic surfactants, the cloud point usually increases with increasing EO number as the surfactant becomes more hydrophilic due to an increase in hydrogen bonding of the head groups with water. Above the cloud point temperature, precipitation of the surfactant from water limits the ability of the nonionic surfactant to stabilize water lamellae in CO_2/water foams.(Adkins et al., 2010a)The cloud point temperatures for the surfactants in water and brine are listed in **Table 1-xii**. As the temperature is increased, the surfactants become less hydrophilic (**Figure 1-15**) and eventually precipitate from the water. For a given surfactant series, it is seen that an increase in the number of EO groups leads to an increase in the cloud point temperature as the hydrophilicity of the surfactant is raised when the size of the head is increased. A higher temperature is required to drive the surfactant from water as the hydrophilicity of the surfactant is increased. The addition of salt and divalent ions to the water decreases the cloud point temperature of the aqueous surfactant solution, as bonding between the water and the EO head groups is disrupted by the ions.(Bourrel and Schechter, 1988) As seen in the schematic of **Figure 1-15**, the salt pushes the nonionic surfactant away from the water phase.

Table 1-xii: Effect of salinity on cloud points of nonionic surfactants

Surfactant	Structure	HLB	DI water	South Hobbs brine	g/L NaCl			
					30	90	100	120
Neodol N25-9	linear C(12-15)-EO9	13.2	72°C		63°C	58°C		45°C
Bio-soft N91-8	linear C(9-11)-EO8	13.9	81°C					
Neodol N25-12	linear C(12-15)-EO12	14.4	>90°C		89°C	75°C		67°C
Surfonic L24-12	linear C(12-14)-EO12	14.4					68°C	
Surfonic L68-20	linear C(16-18)-EO20	15.5		>95°				
Surfonic L24-22	linear C(12-14)-EO22	16.6		>95°C	>90°C	83°C		76°C
Surfonic N-300	nonylphenol-EO30	17.1		>95°C			78°C	
Surfonic N-400	nonylphenol-EO40	17.8		>95°C				

a: 1% in di water

b: 1% in 10% NaCl aqs.

c: 1% (w/w) in south hobbs brine

The cloud point in a synthetic formation brine (5.98 g/L NaCl, 2.03 g/L $MgCl_2 \cdot 6H_2O$ and 1.18 g/L $CaCl_2 \cdot 2H_2O$) for several non-ionic surfactants is listed in **Table 1-xiii.**

Table 1-xiii: *Structures, HLB and cloud points of nonionic surfactants*

Surfactant	Structure	Supplier	HLB	Cloud point ($^{\circ}$C)
Surfonic L24-12	linear C(12-14)-EO12	Huntsman	14.4	68[b*]
Surfonic L24-22	linear C(12-14)-EO22	Huntsman	16.6	>95[c]
Surfonic L68-20	linear C(16-18)-EO20	Huntsman	15.5	>95[c]
Surfonic N-300	nonylphenol-EO30	Huntsman	17.1	78[b*], >95[c]
Surfonic N-400	nonylphenol-EO40	Huntsman	17.8	>95[c]
Neodol N25-9	linear C(12-15)-EO9	Shell	13.2	74[a*]
Neodol N25-12	linear C(12-15)-EO12	Shell	14.4	-
Bio-soft N91-8	linear C(9-11)-EO8	Stepan	13.9	81[a]

a: 1% in di water

b: 1% in 10% NaCl aqs.

c: 1% (w/w) in south hobbs brine

*: obtained from product brochures from suppliers

1.3.2. Interfacial Tension between CO_2 and aqueous surfactant solutions

1.3.2.1. Experimental methods

The interfacial tension between CO_2 and aqueous surfactant solutions is determined from axisymmetric drop shape analysis of a captive bubble. The captive bubble apparatus consists of a light source, a variable-volume view cell with two side windows, an optical rail for alignment, a CCD video camera (Sony, XC73CE), and a computer, as shown in **Figure 1-16**. The chamber on the front side of the view cell was initially filled with an aqueous surfactant solution of specified concentration. A stage with a glass lens (9 mm in diameter, Edmund Optics Inc., NJ) was then immersed into the solution from the top and sealed. The glass lens had one flat and one concave surface, and was used as a ceiling to capture rising bubbles. A known volume (and thus mass) of CO_2 was introduced with a manual syringe pump (Ruska) into the chamber from the bottom to saturate the water and leave a small amount of excess CO_2 visible at

the top of the pressurized cell. CO_2 bubbles were introduced to the cell directly below the glass lens via stainless steel tubing (0.01 inch in inner diameter) with a manual high-pressure syringe pump (Ruska). The pressure of the syringe pump was typically set 200 to 300 psia higher than that of the view cell to allow CO_2 to flow slowly until a single CO_2 bubble was formed on the glass lens. The typical size of the captive bubble was 2-4 mm in diameter, as shown in the inset in **Figure 1-17**. The cell was thermostatic to within ±0.1 °C by using a temperature controller (CN76000, Omega), and two cartridge heaters (1/4 inch I.D., 3 inches in length, CIR-1030/120V/16C/36, Omega) inserted within the stainless steel wall, and fiberglass insulation on the external surface of the cell. Copper tubing around the view cell was also used with flowing water to facilitate cooling. The pressure of the system was controlled on the backside of the pressurized cell by a computer-controlled syringe pump (Isco, model 100DX).

The bubbles were illuminated with a monochromatic light source and the digital images were recorded. The coordinates of the profiles were then analyzed through a computer program imbedded in a software package CAM200 (KSV Ltd., Finland) according to the Laplace equation.

$$\Delta P = 2\gamma \left(\frac{1}{H_0} + \frac{1}{H_1} \right) = \frac{2\gamma}{R_0} + (\Delta\rho)gz$$
[2.1]

Where ΔP is the pressure difference across the C-W interface, R_0 is the radius of curvature at the apex of the drop, H_0 and H_1 are the principle radii of curvature and z is the vertical distance from the apex. The density difference between the two phases (water and CO_2) was calculated from an equation state for pure CO_2 [3] and steam tables for pure water. The change of the density of water was negligible since a CO_2 solubility of 5 wt% only causes a 0.45% change in the density of water, as a consequence of the low partial molar volume of CO_2 in water (33 cm^3/mol) [4]. The interfacial tension measurements

41

in this study were obtained by averaging at least 10 measurements that were acquired every 10 seconds. When the pressure or temperature was changed, a minimum of 3 minutes or 30 minutes, respectively, was allowed to achieve equilibrium. An equilibrium value was assured by examining the standard deviation of the measurements for every condition. When the standard deviation became less than 2% of the mean value, the averaged interfacial tension was assumed to be the equilibrium value. Surfactant adsorption could be measured much more efficiently with this technique versus the pendant drop technique, as it was not necessary to prepare surfactant solutions of varying concentration in CO_2.
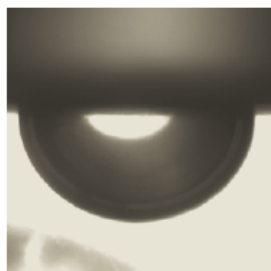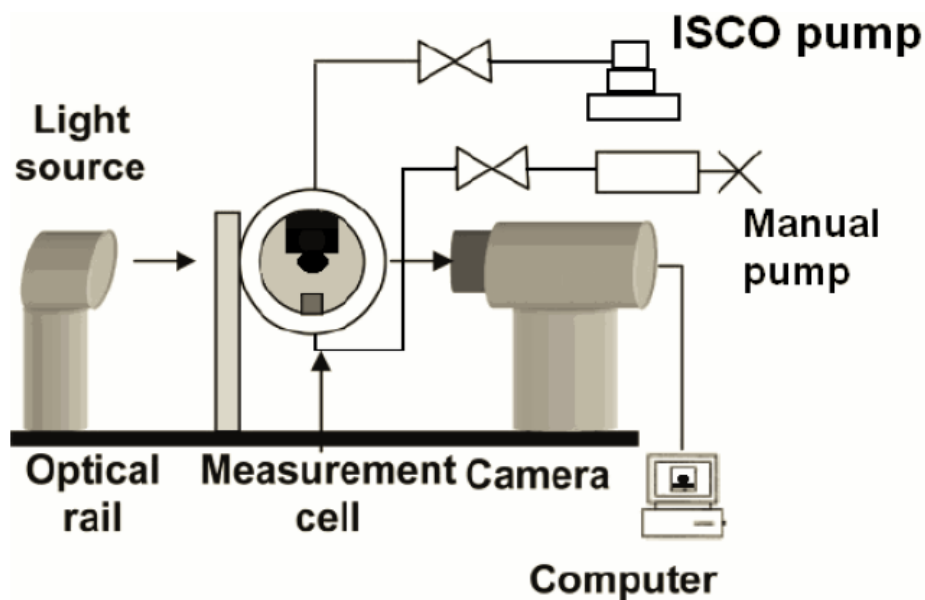
Figure 1-17: *Schematic of captive bubble experimental apparatus used to measure interfacial tension (above) and a photograph of a captive CO_2 bubble on the glass lens (below).*

1.3.2.2. CO$_2$-Brine linterfacial tension for TMN-6, Surfonic, and Neodol surfactants

The interfacial tension between CO$_2$ and 0.1 wt% TMN-6 aqueous solution is presented with results from previous research [6] in our group in **Figure 1-18**. Experimental results fit the trend of IFT results from previous work, which indicates the apparatus is ready for further test of other surfactants.
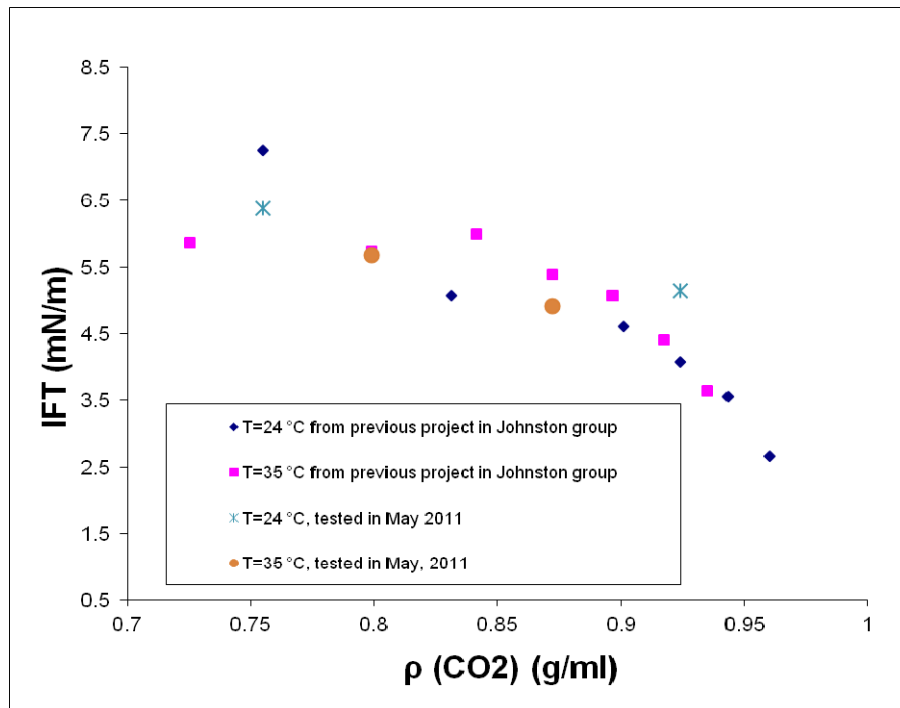
Figure 1-18: *Interfacial tension (IFT) between CO$_2$ and 0.1 wt% TMN-6 aqs. vs CO$_2$ density (ρ) at 24 and 35 ^{o}C*

Surfonic L24-22, Neodol 25-9 and Neodol 25-12 reduced the interfacial tension between CO$_2$ and South Hobbs Brine from ~28 mN/m (without surfactant) to 5-8 mN/m at 22 ^{o}C, 950 psia as shown in **Table 1-xv**. With a shorter EO chain, these non-ionic surfactants tend to have a lower interfacial tension at C/W interface. Also, these nonionic surfactants partitioned more towards CO$_2$ phase with less EO groups. The higher CO$_2$/water partition

43

coefficients may be beneficial to limit gravity override to improve the sweep efficiency. We will continue to use our knowledge and experience on surfactant interfacial property to explore and design surfactants with desirable foam stability, high adsorption on C/W interface and preference to stabilize CO_2/water foam over oil/water emulsion.

Table 1-xv: CO_2-water/brine interfacial tension for Suronic and Neodol surfactants

Surfactant	Salinity	Temperature (°C)	Pressure (psia)	IFT (mN/m)
None	0	22	950	28.3
Surfonic L24-22	5.98 g/L NaCl, 2.03 g/L	22	950	8.17
	$MgCl_2 \cdot 6H_2O$ and 1.18 g/L $CaCl_2 \cdot 2H_2O$	22	1700	7.32
Neodol 25-12	5.98 g/L NaCl, 2.03 g/L	22	950	5.95
	$MgCl_2 \cdot 6H_2O$ and 1.18 g/L $CaCl_2 \cdot 2H_2O$	22	1700	5.19
Neodol 25-9	5.98 g/L NaCl, 2.03 g/L	22	950	4.72
	$MgCl_2 \cdot 6H_2O$ and 1.18 g/L $CaCl_2 \cdot 2H_2O$	22	1700	4.49

The interfacial tension of 1% (w/w) L24-22 at the C/W interface as a function of CO_2 density is presented in **Figure 1-16** at 24 to 60 $^{\circ}$C. The interfacial tension between CO_2 and pure water or low salinity brine is 25-35 mN/m at 24 to 60 $^{\circ}$C, 1700 psia.(Chalbaud et al., 2010; Szulczewski et al., 2009)The interfacial tension decreases as the density of CO_2 is increased, which is also the case for binary systems without surfactant. As the density of CO_2 increases, the tail–CO_2 interactions become more attractive, which helps surfactant molecules to move from water to the C/W interface. At CO_2 density ~0.8 g/mL, the interfacial tension of 1% (w/w) L24-22 is ~7 mN/m. This indicates that although there is a longer alkyl carbon chain and a longer

44

hydrophilic head, L24-22 can lower interfacial tension between CO_2 and water as well as nonionic surfactants with a relatively short EO head group.
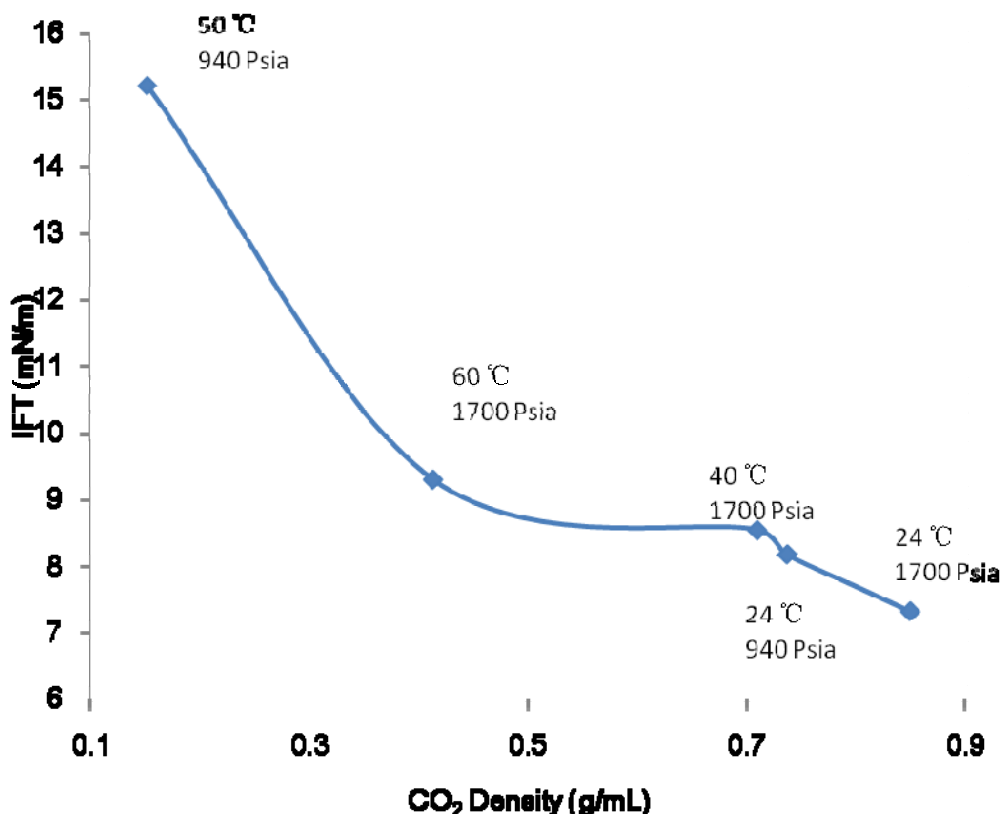
Figure 1-16: Interfacial tension (IFT) between CO_2 and 1 % (w/w) L24-22 South Hobbs brine vs CO_2 density (ρ) at 24- 60 ^{o}C

1.3.3. Partitioning of surfactant between water and CO_2

1.3.3.1. Experimental methods

To observe surfactant phase behavior, 5 g CO_2 and 5 g water plus 0.25% (v/w) surfactant, relative to the total weight, were loaded in the front part of the cell shown in **Figure 1-19**. A magnetic stir-bar coated with polytetrafluoroethylene (Fisherbrand, 3mm in diameter, 10mm in length, Octagonal) was used for gentle mixing to minimize emulsification. The pressure on the backside of the cell was controlled by a computer-controlled syringe pump (Isco, model 260D), with CO_2 as the pressurizing fluid. The temperature of the system was controlled to within±0.1 ◦C by submerging the cell into a

45

water bath equipped with a temperature controller (MP-BASIS, Julabo). To measure the equilibrium partitioning of the surfactant between the CO_2 and water phases, samples of the upper phase were extracted via a 6- port valve (Valco Instrument Co., Inc.) and a 50 μL stainless steel loop (Valco Instrument Co., Inc.). The first sample was discarded and three samples were obtained by discharging the loop into a vial with DI water of known volume, typically 7ml. The loop was flushed 3 times with a total of 3ml of DI water to recover all of the surfactant. The concentration of surfactant in the solution was then determined by pendant-drop surface tension measurement, below the cmc, based on a calibration made for known surfactant concentrations. If the surface tension obtained was near the CMC value (cmc), the original solution was diluted until the obtained surface tension was much larger than cmc. For each sample, the surface tension was measured at least 10 times and the average value was used to calculate the concentration.

1.3.3.2. Partition coefficient for Surfonic and Neodol surfactants

The partition coefficients of Surfonic L24-22, Neodol 25-12 and Neodol 25-9 between CO_2 and South Hobbs brine at 1700 psia, 24 and 40 $^{\circ}$C, are presented in **Table 1-xiv**. It was found that all three surfactants favor water over CO_2 with fewer EO groups, the surfactants partitioned more towards CO_2 phase. This series of surfactants may be utilized to design surfactant with favorable CO_2 partition coefficients for good vertical sweep efficiency while also producing high viscosity foams.(Ren *et al.*, 2011)

Surfactant	Structure	°C	CO$_2$ g/mL	Partition coefficient wt% in CO2/wt% in aqueous
Surfonic L24-22	C12-14 EO22	24	0.849	0.020
		40	0.709	<0.006
Neodol 25-12	C12-15 EO12	40	0.709	0.035
Neodol 25-9	C12-15 EO9	24	0.849	0.226
		40	0.709	0.077

Table 1-xiv: *Partition coefficients of Surfonic L24-22, Neodol 25-12 and Neodol 25-9 between CO$_2$ and South Hobbs brine at 1700 psia, 24 and 40 ^{o}C.*

1.3.4. Partition coefficient of surfactant between brine and dodecane

1.3.4.1. Experimental methods

5 mL dodecane (99%, Acros) was gently poured into a 20 mL vessel with 5mL 1 % (w/w) surfactant brine solution inside. Mixing was avoided during the addition process to eliminate emulsion formation between the two phases. The mixture was then put into an oven at 40°C for 72 h to equilibrate. The concentration of surfactant in the aqueous phase of the mixture was then determined by pendant-drop surface tension measurement, below the CMC (critical micellar concentration), based on a calibration made for known surfactant concentrations. If the surface tension obtained was near the CMC, the original solution was diluted until the obtained surface tension was much larger than the CMC. For each sample, the surface tension was measured at least 20 times and the average value was used to calculate the concentration. The partition coefficient was calculated by the equation below.

$$oil/brine\ partition\ coefficient = \frac{m_{surfactant\ in\ oil}/(m_{surfactant\ in\ oil} + m_{oil})}{m_{surfactant\ in\ brine}/(m_{surfactant\ in\ brine} + m_{brine})}$$
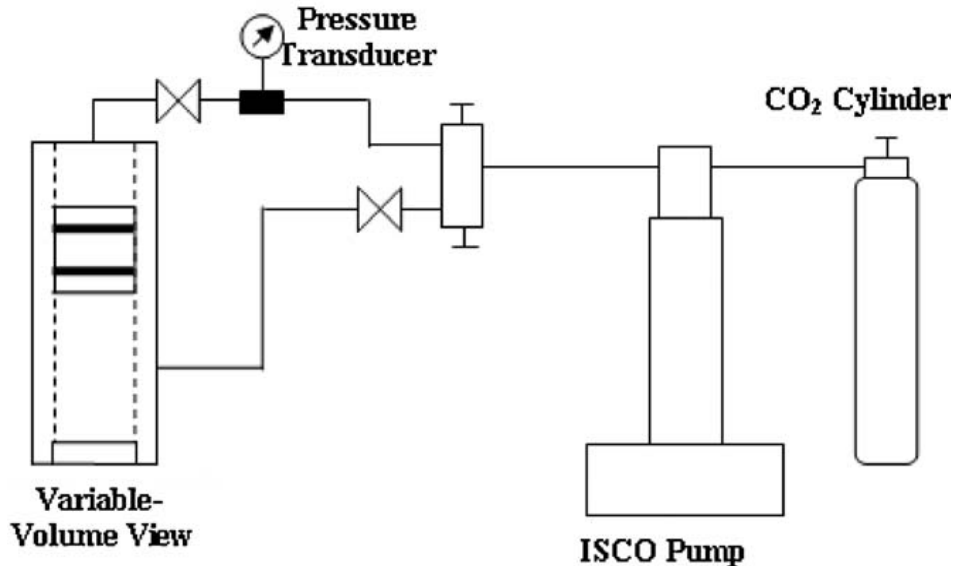
**Figure 1-19:** _Schematic of partitioning of surfactant into CO₂ with gentle stirring._

1.3.4.2. Surfactant partition coefficient with formation brine

Figure 1-20 shows the dodecane/brine partitioning results for nonionic surfactants with HLB ranging from 13 to 18 at 40°C and 1atm. The partition coefficient for Surfonic L24-22, Surfonic L68-20, Surfonic N-300 and Surfonic N-400, was below 0.1. These surfactant candidates are either with HLB higher than 16.5 or with 20 or more EOs.   The low partition coefficient values suggest that these surfactants will have minimal retardation due to partitioning into oil in the EOR process. The samples with partitioning coefficients between 0.1 and 0.5 will probably have small retardation.
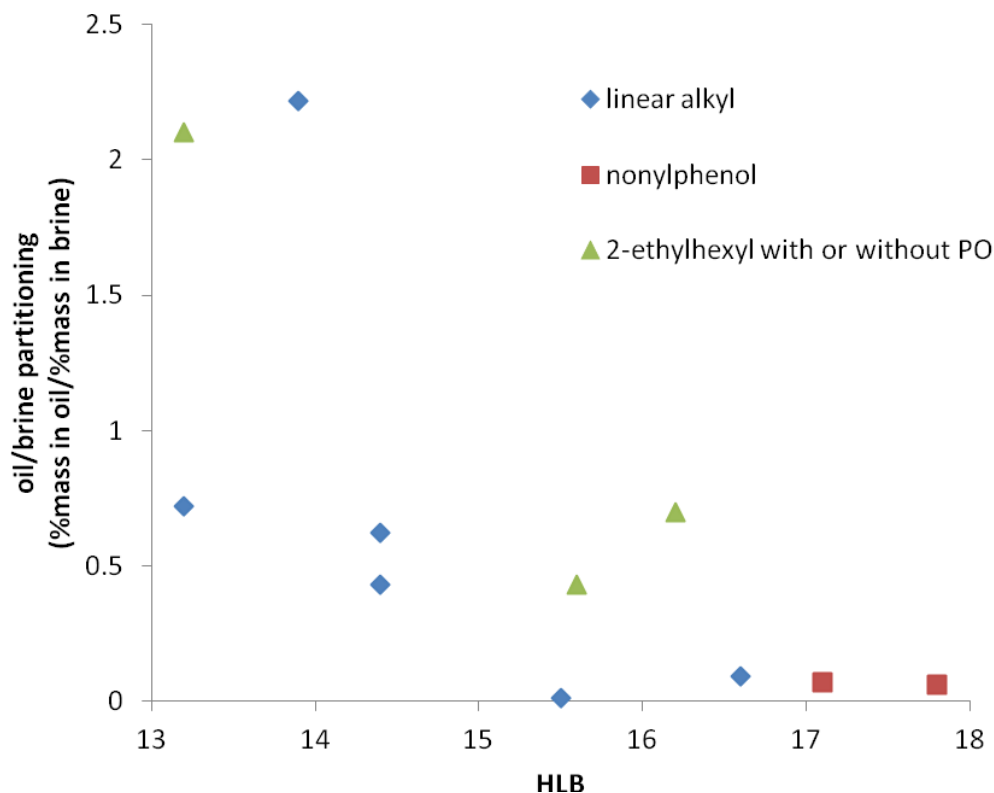
Figure 1-20: *Dodecane/brine partition coefficients of nonionic surfactants at 40 ^{o}C, 1 atm vs HLB. Brine composition: 5.98 g/L NaCl, 2.03 g/L MgCl$_2$·6H$_2$O and 1.18 g/L CaCl$_2$·2H$_2$O.*

The partition coefficients of nonionic surfactant between brine solution (5.98 g/L NaCl, 2.03 g/L MgCl$_2$ ·6H$_2$O and 1.18 g/L CaCl$_2$ ·2H$_2$O) and dodecane at 40 ^{o}C, 1 atm are presented in **Table 1-xvi**. Generally, the partition coefficient decreased with increasing of the HLB value of surfactant. For linear alkyl ethoxylate surfactant, when HLB is higher than 14.5, the partition coefficient is less than 0.1, which indicates the surfactant highly favors aqueous phase over oil phase. For non-linear alkyl nonionic surfactant, when HLB higher than 16.5, the partition coefficient is below 0.1. It indicates that it requires a higher HLB value for non-linear alkyl ethoxylate for the same low partitioning coefficient than linear alkyl ethoxylate surfactant. All oil-water partitioning results contained an error below ±0.02 in partition coefficients.

Table 1-xvi: *Structures, HLB and partition coefficients of nonionic surfactants between dodecane and synthetic formation brine at 40 ^{o}C, 1 atm*

Surfactant	Structure	Supplier	HLB	Partition coefficient
Neodol N25-9	linear C(12-15)-EO9	Shell	13.2	0.72
Bio-soft N91-8	linear C(9-11)-EO8	Stepan	13.9	2.22
Neodol N25-12	linear C(12-15)-EO12	Shell	14.4	0.62
Surfonic L24-12	linear C(12-14)-EO12	Huntsman	14.4	0.43
Surfonic L68-20	linear C(16-18)-EO20	Huntsman	15.5	0.01
Surfonic L24-22	linear C(12-14)-EO22	Huntsman	16.6	0.09
Surfonic N-300	nonylphenol-EO30	Huntsman	17.1	0.07
Surfonic N-400	nonylphenol-EO40	Huntsman	17.8	0.06

1.3.5. Foam viscosity

1.3.5.1. TERGITOL, MAKON, and BIO-SOFT surfactants

The viscosities of C/W foam generated at total flow rate of 6 mL/min, 2000 psia, CO_2: 1% v/v nonionic alkyl ethoxylate or alkyl phenol ethoxylate surfactant aq. solution (9:1 v/v ratio) at 24 and 70 ^{o}C are presented in **Table 1-xvii**.   It was found that highly viscous CO_2/Water foams with viscosities 50 to 500 times higher than that of pure CO_2 were formed at 24 ^{o}C and 70 ^{o}C. (viscosity of CO_2 at 2000 psi: 0.085 cP for 24 ^{o}C; 0.033 cP for 70 ^{o}C [5]) by using alkyl phenol ethoxylate or alkyl ethoxylates with varying EO numbers from 15 to 41. When the number of EO groups in the ethoxylate surfactants was less than 10, foam with viscosity over 15 times higher than that of pure CO_2 was generated.

Table 1-xvii: *Bulk foam apparent viscosities at total flow rate of 6 mL/min, 2000 psia, CO_2: 1% v/v nonionic surfactant aq. solution (9:1 v/v ratio) at 24 and 70 ^{o}C.*

Sample name	Composition	Temperature (^{o}C)	Apparent viscosity (cP)	Apparent viscosity/ viscosity of pure CO_2
TERGITOL 15-S-20	Branched C(12-14)-EO20	24	29.2	344
		70	8.3	251
TERGITOL 15-S-30	Branched C(12-14)-EO31	70	10.7	324
TERGITOL 15-S-40	Branched C(12-14)-EO41	70	8.4	254
TERGITOL NP-15	Nonophenol Eethoxylate (EO15)	70	2.1	63
MAKON TD-18	C13-EO18	70	17.1	518
BIO-SOFT N91-8	C(9-11)-EO8	70	0.5	15

Tergitol 15-S-20 and Tergitol 15-S-40 not only formed C/W foam at 24 and 70 ^{o}C, but also formed unstable O/W emulsion, which makes a promising surfactant candidate for selective mobility control. Therefore, effect of salinity, surfactant concentration, shear rate as well as foam quality on the viscosity of foams stabilized with 15-S-20 and Tergitol 15-S-40 was investigated, respectively.

Effect of salinity on foam viscosity

The effect of salinity on foam viscosity for Tergitol 15-S-20 is presented in **Figure 1-21**. C/W foam was obtained in the presence of up to 9 wt% NaCl in surfactant solution. At 24 and 50 ^{o}C, viscosity slightly increased when the salinity of surfactant solution increased. At 70 ^{o}C, no foam formed when 9 wt% NaCl brine was in present in the surfactant solution. The ability to form foams at

high salinities is highly beneficial for applying EOR for a wide variety of brine containing reservoirs.
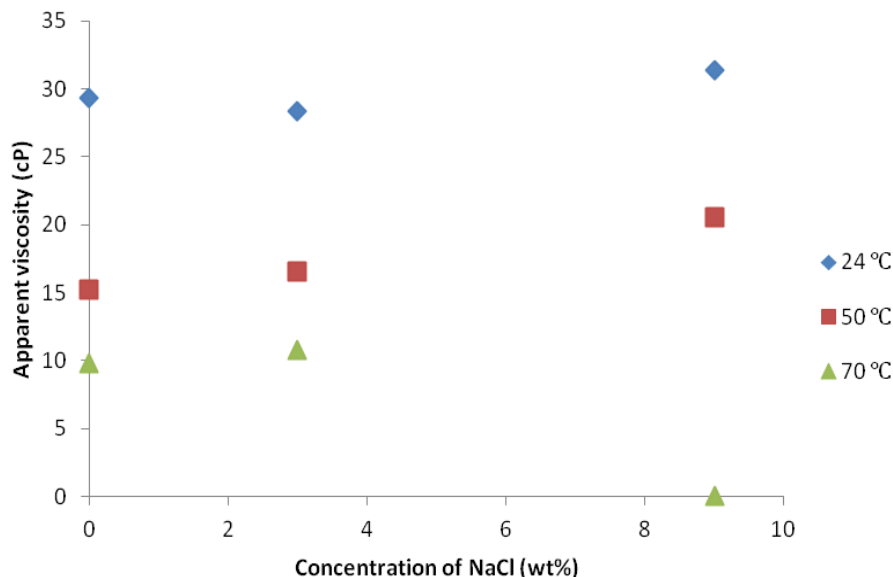
Figure 1-21: *The foam viscosity of C/W foam stabilized with 1 wt% 15-S-20 at total flow rate of 6 mL/min, 90% v/v CO$_2$, 24, 50, 70 °C, and 2000 psia as a function of the NaCl concentration (wt% to surfactant solution).*

The effect of salinity on foam viscosity for Tergitol 15-S-40 is presented in **Figure 1-22**. C/W foam was obtained in the presence of up to 9 wt% NaCl in surfactant solution. At both 50 and 70 $^{\circ}$C, viscosity of C/W foam increased with salinity. We reported that Tergitol !5-S-20 was not able to stabilize C/W foam in the presence of 9 wt% NaCl in aqs. at 70 $^{\circ}$C. (Yunshen, Chen et al. 2011) There are 20 more ethoxylate group in 15-S-40 than 15-S-20. Those ethoxylate groups may provide extra aqueous solubility for 15-S-40 and let it stabilize C/W in high salinity condition. The ability to form foams at high salinities is highly beneficial for applying EOR for a wide variety of brine containing reservoirs.
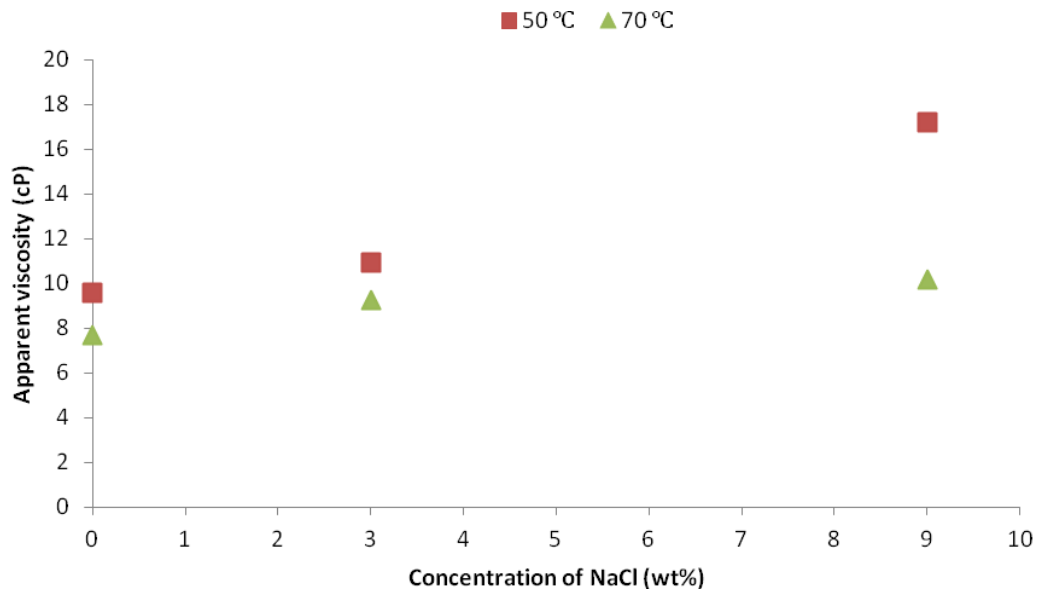
Figure 1-22. The foam viscosity of C/W foam stabilized with 1 wt% active 15-S-40 at total flow rate of 6 mL/min, 90% v/v CO_2, 50 and 70 °C, and 2000 psia as a function of the NaCl concentration (wt% to surfactant solution).

Effect of surfactant concentration on foam viscosity

Figure 1-23 presents the foam viscosity of C/W foam stabilized with 15-S-20 at total flow rate of 6 mL/min, 24, 50 and 70 °C, and 2000 psia as a function of the 15-S-20 concentration (wt% to surfactant solution). It was found that 15-S-20 was still active to increase the viscosity of C/W mixture at 70 ^{o}C even at 0.01 wt% to surfactant solution, which equals to 0.002 wt% in total C/W foam flow. This concentration is 1/100 of the concentration (1 wt%) in basic cases, which indicates that protonated 15-S-20 is a high efficient surfactant for CO_2 EOR.

At 0.001 wt%, no foam formed at 24, 50 or 70 ^{o}C. Viscosity increased with the concentration of 15-S-20 increased in the surfactant concentration range of 0.001-1 wt%.
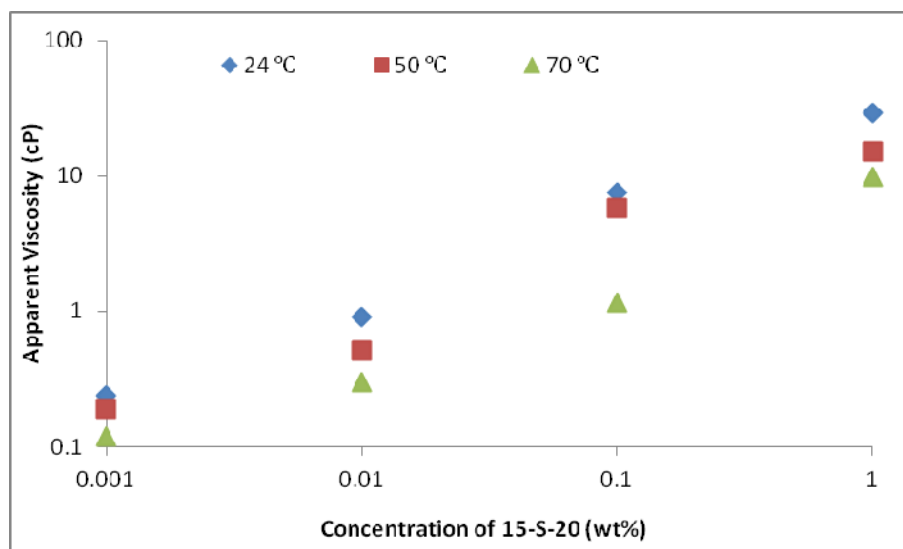
Figure 1-23: *The foam viscosity of C/W foam stabilized with 15-S-20 at total flow rate of 6 mL/min, 24, 50, 70 °C, 90% v/v CO_2, and 2000 psia as a function of the 15-S-20 concentration (wt% to surfactant solution).*

Figure 1-24 presents the foam viscosity of C/W foam stabilized with 15-S-40 at total flow rate of 6 mL/min, 50 °C, and 2000 psia as a function of the 15-S-40 concentration (active wt% to surfactant solution). It was found that 15-S-40 was still active to increase the viscosity of C/W mixture at 50 °C even at 0.1 wt% to surfactant solution, which equals to 0.014 wt% in total C/W foam flow. This concentration is 1/10 of the concentration (1 wt%, active) in basic cases, which indicates that 15-S-40 is a high efficient surfactant for CO_2 EOR.

Viscosity slightly increased with the concentration of 15-S-40 increased in the surfactant concentration range of 0.001-1 wt% active. At 0.01 wt%, no foam formed at 50 °C.
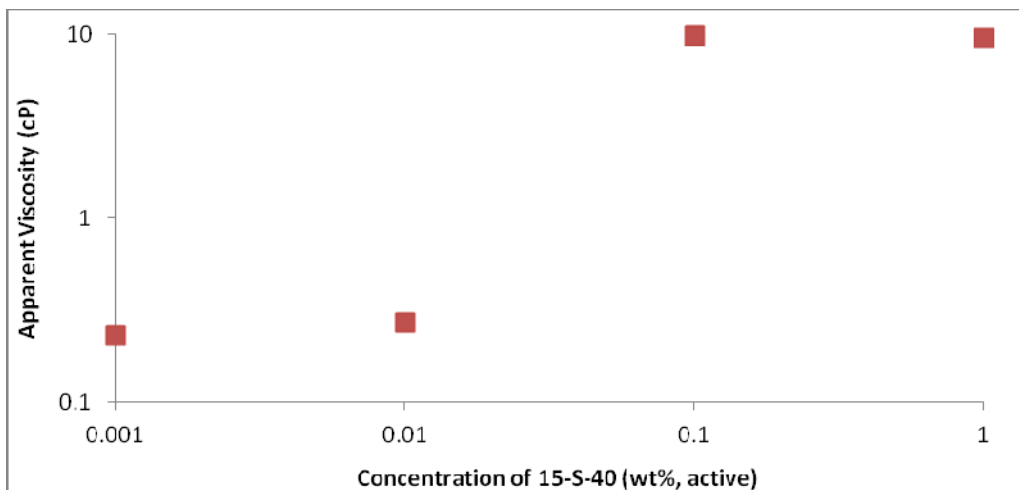
Figure 1-24: *The foam viscosity of C/W foam stabilized with 15-S-40 at total flow rate of 6 mL/min, 50 °C, 2000 psia, 90% v/v CO_2, and 2000 psia as a function of the 15-S-40 concentration (wt% active to surfactant solution).*

Effect of shear rate on foam viscosity for Tergitol 15-S-20

A plot of shear stress versus shear rate (calculated from ΔPR/2L and 4U/R, respectively) was generated for an 1 wt% 15-S-20 foam with 90% v/v CO_2 at 50 °C and 2000 psia, and is presented in **Figure 1-25 (a)**. The ratio of shear stress to shear rate gives a constant value equal to the viscosity, which indicates that 15-S-20 foam was a Newtonian fluid at 50 °C and 2000 psia with a shear rate from 576-4604 s^{-1}.

Figure 1-25 (b) gives the viscosity as a function of shear rate. For a non-Newtonian foam a yield stress is often found (Verbist et al. 1999). In the case of 15-S-20 in **Figure 1-26**, Newtonian behavior is not expected to occur for all shear rates and thus the slope does not intersect the origin. At low shear rates the elasticity of the foam structure and yield stress illustrate non-Newtonian behavior. It was also found that no foam formed, when the shear rate was 192 s^{-1} or lower.   As the shear rate was increased, the foam filled a larger volume of the view cell, indicating greater foam formation and/or higher foam stability. . For the base case of our viscosity measurement (total flow rate 6 ml/min), the shear rate is 2302 s^{-1}.
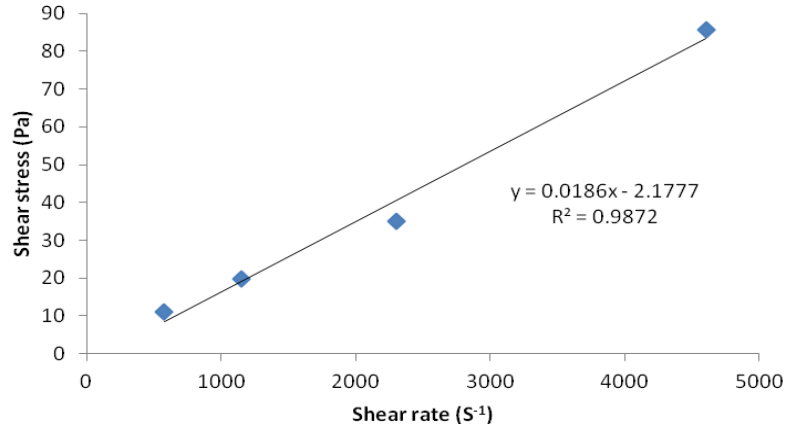
(A)
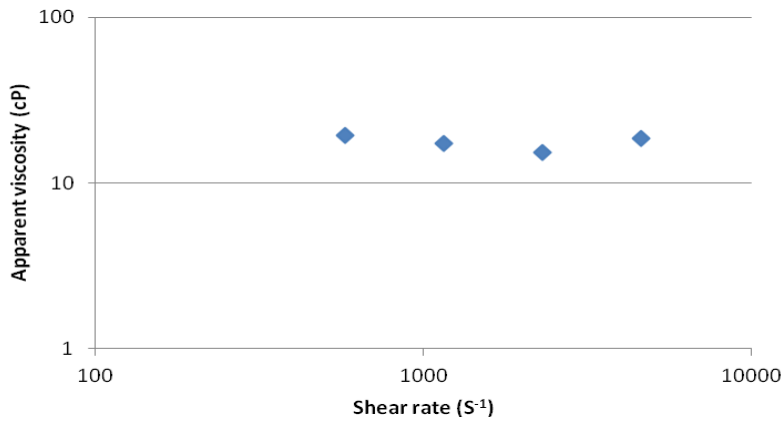
(B)

<u>Figure 1-25 A&B:</u> Shear stress (A) and viscosity (B) as a function of shear rate for the C/W foam stabilized with 1 wt% 15-S-20 and 90% v/v CO2 at 50 °C and 2000 psia .

A plot of shear stress versus shear rate (calculated from $\Delta PR/2L$ and $4U/R$, respectively) was generated for an 1 wt% active 15-S-40 foam with 90% v/v CO_2 at 50 °C and 2000 psia, as shown in **Figure 1-26 (a)**.

Figure 1-26 (b) gives the viscosity as a function of shear rate. For a non-Newtonian foam a yield stress is often found.(Verbist, G. et al. 1999) In the case of 15-S-40, Newtonian behavior is not observed at low shear rates and the curve in **Figure 1-26 (a)** does not intersect the origin. At low shear rates the elasticity of the foam structure produced a yield stress that is non-Newtonian behavior. It was found that foam formed, when the shear rate was 422 s^{-1}.   As

the shear rate was increased, the foam filled a larger volume of the view cell, indicating greater foam formation and/or higher foam stability. For the base case of our viscosity measurement (total flow rate 6 ml/min), the shear rate is 2302 s^{-1}.

(A)
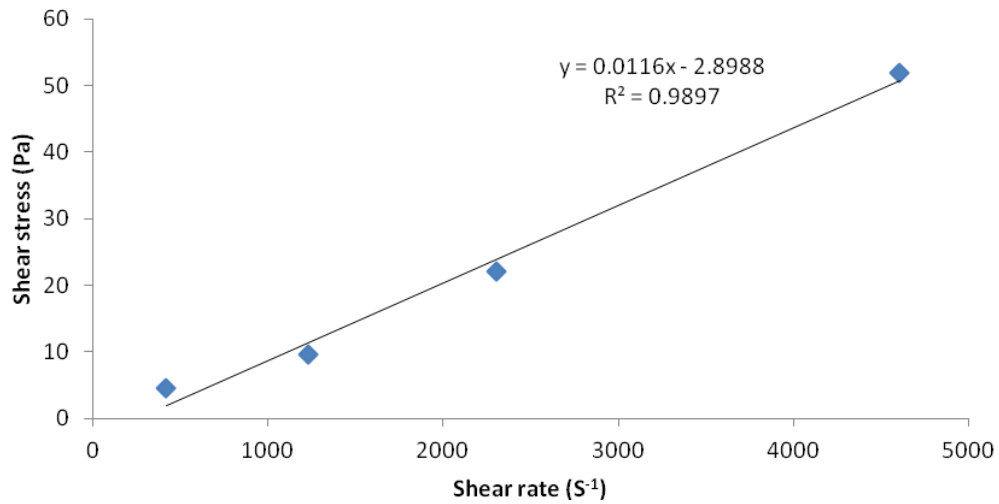
(B)
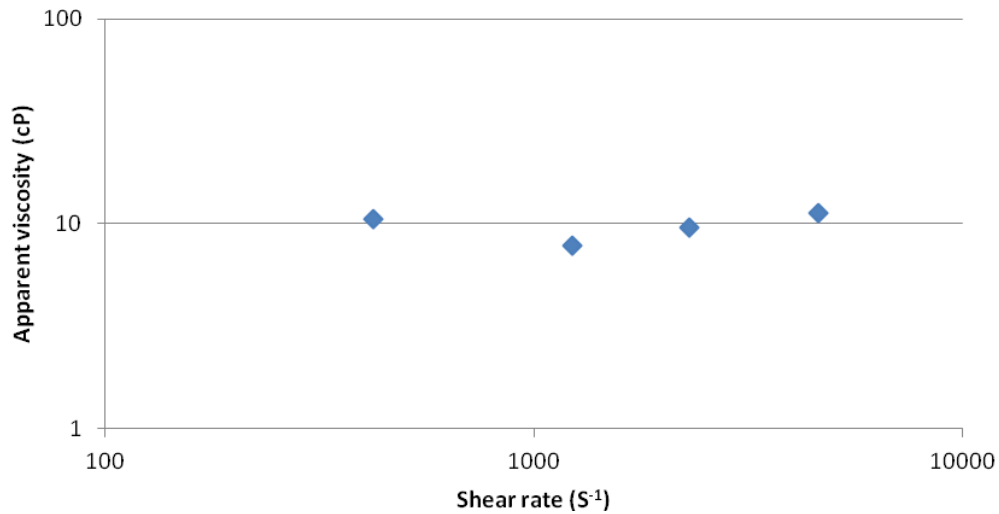
Figure 1-26 A&B: *Shear stress (A) and viscosity (B) as a function of shear rate for the C/W foam stabilized with 1 wt% active 15-S-40 and 90% v/v CO$_2$ at 50 °C and 2000 psia*

Effect of foam quality on foam viscosity

The quality of foam often has a large influence on foam viscosity (Harris 1989). As the quality is increased from 40% v/v, foam viscosity increases as well, due to the increase in the number of bubbles and lamellae in the foam from the additional volume of dispersed phase (Asghari and Khalil 2005, Smith and Johnston 1988, Patton et al. 1983, Enzendorfer et al. 1995, Otsubo and Prud'homme 1994). As the quality is continually increased, a maximum viscosity is reached at qualities near approximately 95%, followed by a drop in viscosity. Foams with very high qualities have little aqueous solution, thus the liquid lamellae are very thin and cannot prevent bubble coalescence. Viscosity decreases as the lamella stability is reduced due to a drop in the number of lamellae. The effect of foam quality on foam viscosity is shown in **Figure 1-27** at a total flow rate of 6 ml/min with 1 wt% 15-S-20 at 50 °C and 2000 psia. A maximum in viscosity is visible at a quality of 95% and the foam lamella stability drops when the quality is increased further. No foam formed, when the quality was less than 40%. The ability to vary foam viscosity via quality changes allows for some control of the foam in EOR uses, as the gas injection strategy can be altered to either increase or decrease foam viscosity. Friedmann et al. found that higher quality foams (90%) propagated better than wet foams (40%) in porous media (Friedmann and Jensen 1986), thus it is anticipated that qualities producing the greatest foam viscosity may work best for CO_2 EOR.
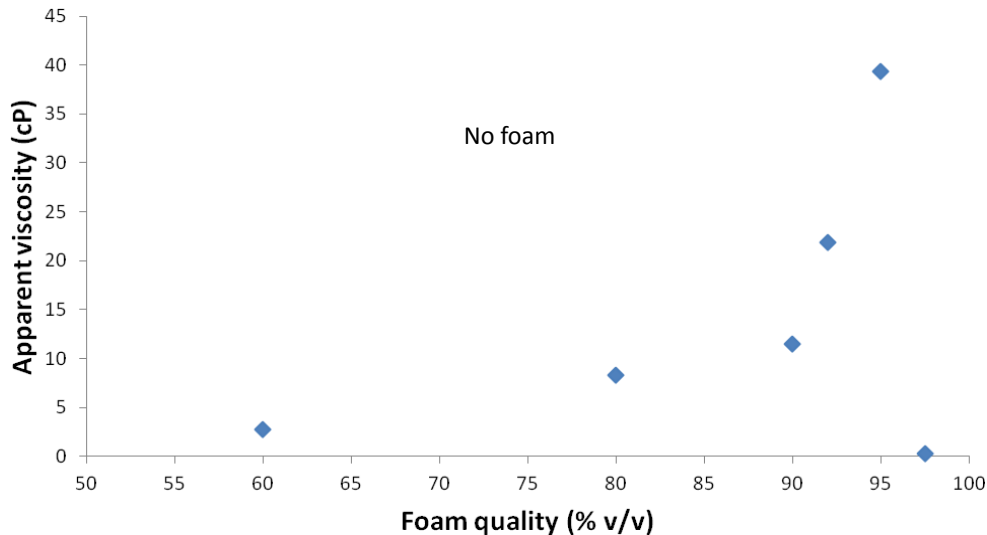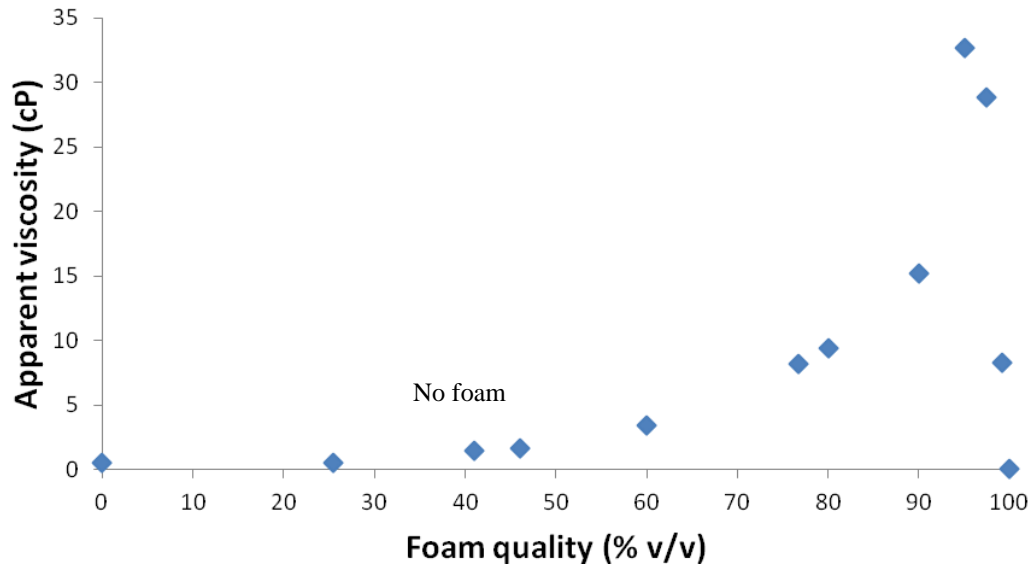
Figure 1-27: *The foam viscosity of C/W foam stabilized with 1 wt% 15-S-20 at total flow rate of 6 mL/min, 50 °C, and 2000 psia as a function of the foam quality (% v/v CO_2).*

The quality of foam often has a large influence on foam viscosity.(Harris, P.C. 1989) As the quality is increased from 60% v/v, foam viscosity increases as well, due to the increase in the number of bubbles and lamellae in the foam from the additional volume of dispersed phase. As the quality is continually increased, a maximum viscosity is reached at qualities near approximately 92%, followed by a drop in viscosity. Foams with very high qualities (~98%) have little aqueous solution, thus the liquid lamellae are very thin and cannot prevent bubble coalescence. Viscosity decreases as the lamella stability is reduced due to a drop in the number of lamellae. The effect of foam quality on foam viscosity is shown in **Figure 1-28** at a total flow rate of 6 ml/min with 1 wt% 15-S-40 at 50 °C and 2000 psia. A maximum in viscosity is visible at a quality of 92% and the foam lamella stability drops when the quality is increased further. The ability to vary foam viscosity via quality changes allows for some control of the foam in EOR uses, as the gas injection strategy can be altered to either increase or decrease foam viscosity. Friedmann et al. found that higher quality foams (90%) propagated better than wet foams (40%) in porous media

59

(Friedmann, F. et al. 1986), thus it is anticipated that high qualities with high foam viscosity may work best for CO_2 EOR.
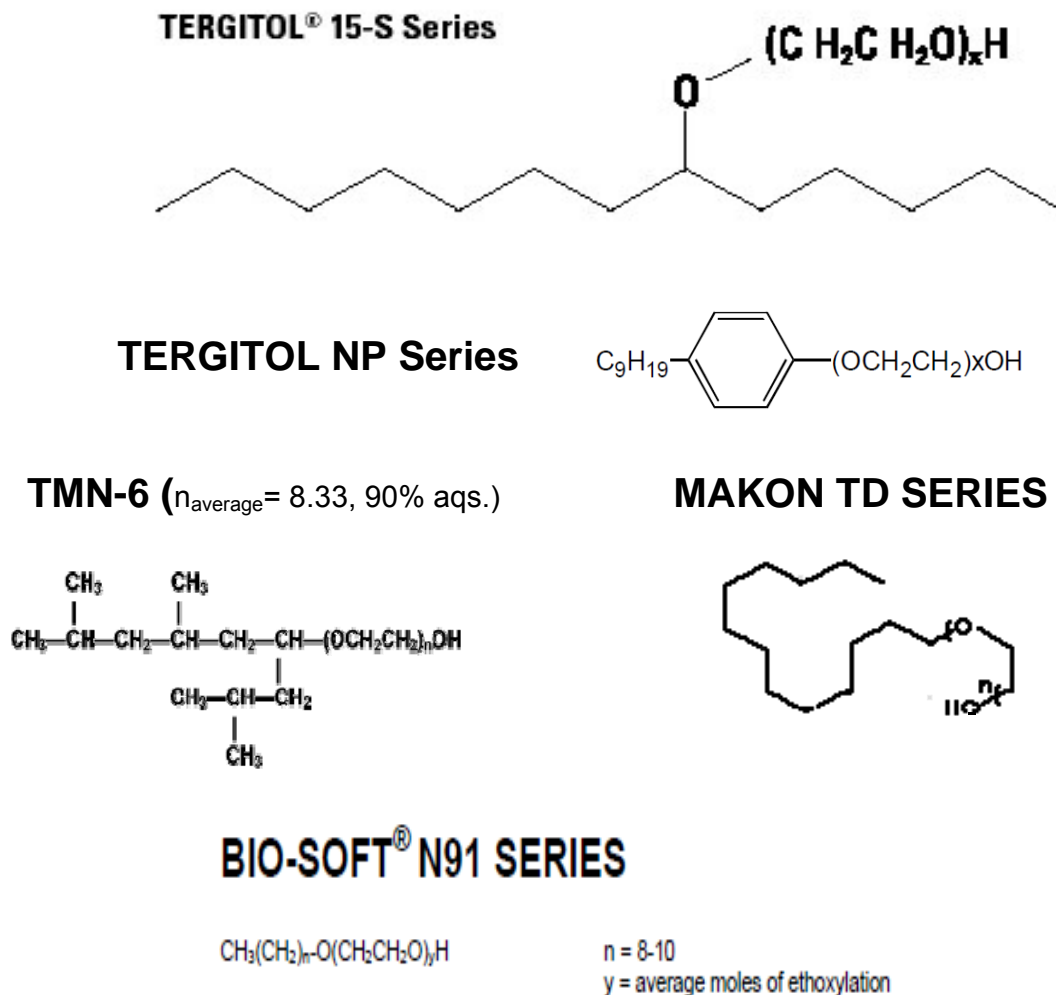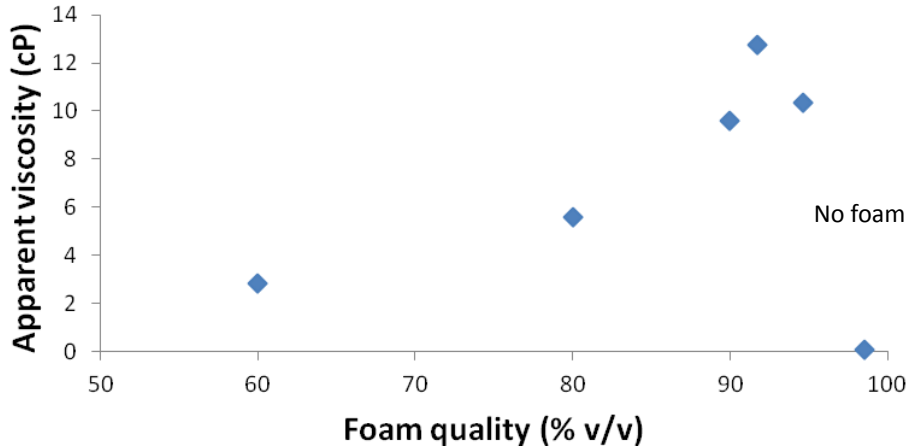

Figure 1-28: The foam viscosity of C/W foam stabilized with 1 wt% active 15-S-40 at total flow rate of 6 mL/min, 50 °C, and 2000 psia as a function of the foam quality (% v/v CO_2)

1.3.5.2. SURFONIC and Neodol surfactants

Nonionic linear alkyl ethoxylate and alkylphenol ethoxylate surfactants formed highly viscous CO_2/Water foams with viscosities orders of magnitude higher than pure CO_2 at 24 ^{o}C to 70 ^{o}C. Furthermore, these surfactants formed unstable O/W emulsions, which indicates that these surfactants are selective for forming stable C/W foams rather than O/W emulsions.[1] They also showed favorable oil/brine partitioning, and their adsorption should be low on both positive charged carbonate surface and negative charged sand stone surface, which further supports that they are promising surfactant candidates for CO_2 EOR. With the interest of exploring suitable alkyl ethoxylate surfactant candidates for south hobbs field test and investigating the relationship between surfactant structures and foaming ability (viscosity, ability of foaming at different temperature, foam quality and shear rate), Surfonic L24-22 was investigated in this report. It formed C/W foam that is two orders of magnitude higher than the viscosity of pure CO_2 from 24 to 60 ^{o}C in the presence of south hobbs brine at

1700 psia. The effect of temperature, surfactant concentration, shear rate as well as foam quality on the viscosity of L24-22 foam was also investigated.

Effect of temperature on foam viscosity for Surfonic L24-22

The effect of temperature on the foam viscosity of C/W foam stabilized with 1% (w/w) Surfonic L24-22 south hobbs brine solution, 90% (v/v) CO_2 at total flow rate of 6 mL/min, 40 °C, 1700 psia is presented in **Figure 1-29**. Surfonic L24-22 generated foam whose viscosity is 100-200 times higher than that of pure CO_2 from 24 to 60 ^{o}C at 1700 psia. The viscosity of foam stabilized with Surfonic L24-22 at 40 ^{o}C in capillary is higher than that of Tergitol 15-S-9, ethoxylated coco and tallow amines. **Figure 1-29** shows a decrease in the viscosity of the foam with increasing temperature. This decline can be owed to the decrease in CO_2 density with increasing temperature which leads to a decrease in the solvation of surfactant tails. Another factor that contributes to the reduction in viscosity is the effect of cloud point temperature. As the test temperature approaches the cloud point surfactants become less effectively solvated by water and may precipitate in the foam lamellae. At this point, various mechanisms may lead to rupture of the lamellae including film drainage and opening of holes in the films.
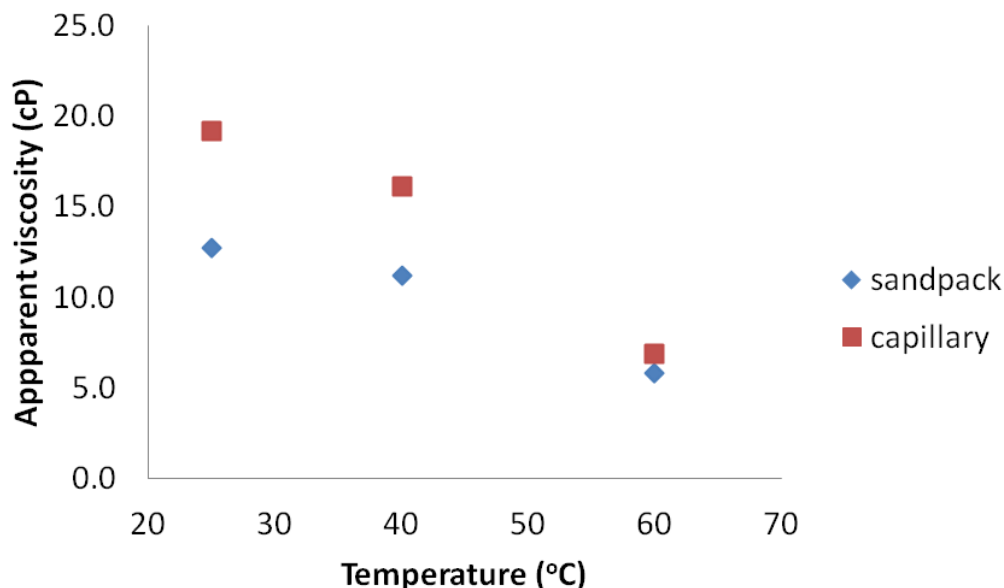
Figure 1-29: Temperature effect on the foam viscosity of C/W foam stabilized with 1% (w/w) Surfonic L24-22 south hobbs brine solution, 90% v/v CO_2, at total flow rate of 6.0 mL/min, 40 °C, 1700 psia

Note that foam formed in all tested salinity and foam viscosity was independent of salinity. For most of traditional nonionic surfactants with relative shorter EO chain[8], its cloud point at high salinity is usually moderate, which limits the applicable temperature and salinity condition. Also, in the real field trial, surfactant may be injected at a different salinity from the salinity inside reservoir. The ability to form viscous C/W foam over a wide range of salinity will offer means to reduce CO_2 mobility throughout an oil displacement process.

Effect of shear rate on foam viscosity for Surfonic L24-22

Figure 1-30 gives the viscosity as a function of shear rate. For a non-Newtonian foam a yield stress is often found. (Verbist, G. et al. 1999) In the case of L24-22, non-Newtonian behavior was observed at low shear rates. The elasticity of the foam structure produced a yield stress that is non-Newtonian behavior. In addition, it was found that foam started to form when the shear rate in the sand pack was ~150 s^{-1}. As the shear rate increased, the foam filled a larger volume of the view cell, indicating greater foam formation and/or higher

foam stability. Also, maximum foam apparent viscosity of 16 cP (~300 times as the viscosity of pure CO_2 at the same condition) was observed at a shear rate of $250s^{-1}$.
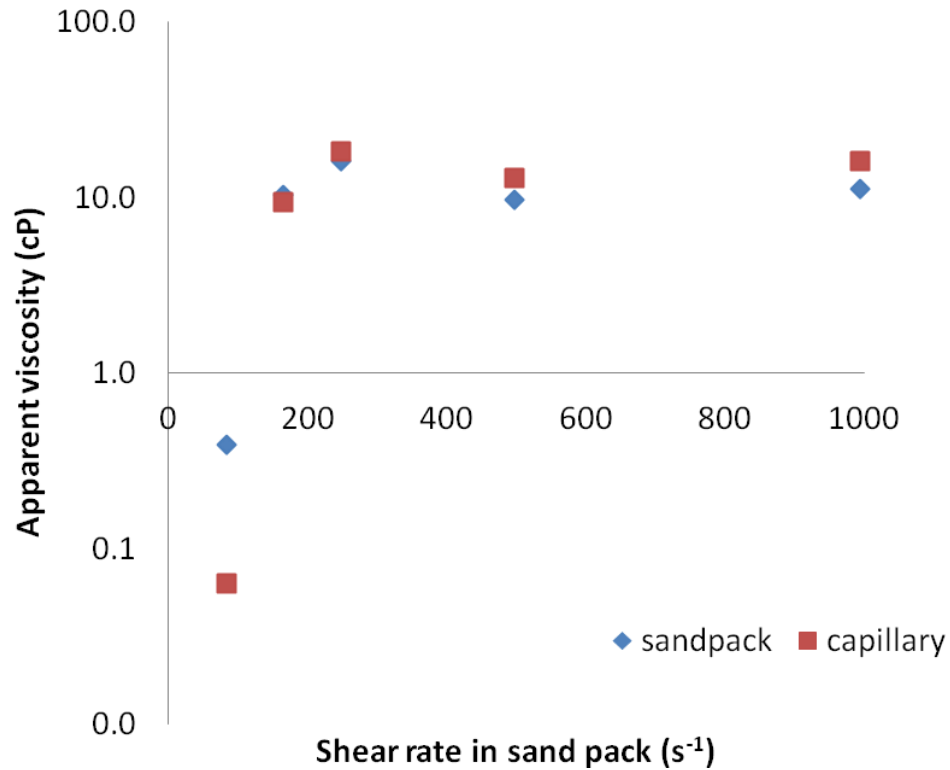
Figure 1-30: *Apparent viscosity in sand pack and capillary as a function of shear rate in sand pack for the C/W foam stabilized with 1% (w/w) Surfonic L24-22 south hobbs brine and 90% v/v CO_2 at 40 °C and 1700 psia*

Figure 1-31 gives the pressure gradient as a function of superficial velocity in the sand pack. The minimum pressure gradient required to generate foam was found to be 5 psi/ft for L24-22 at 1% (w/w) in aqueous.
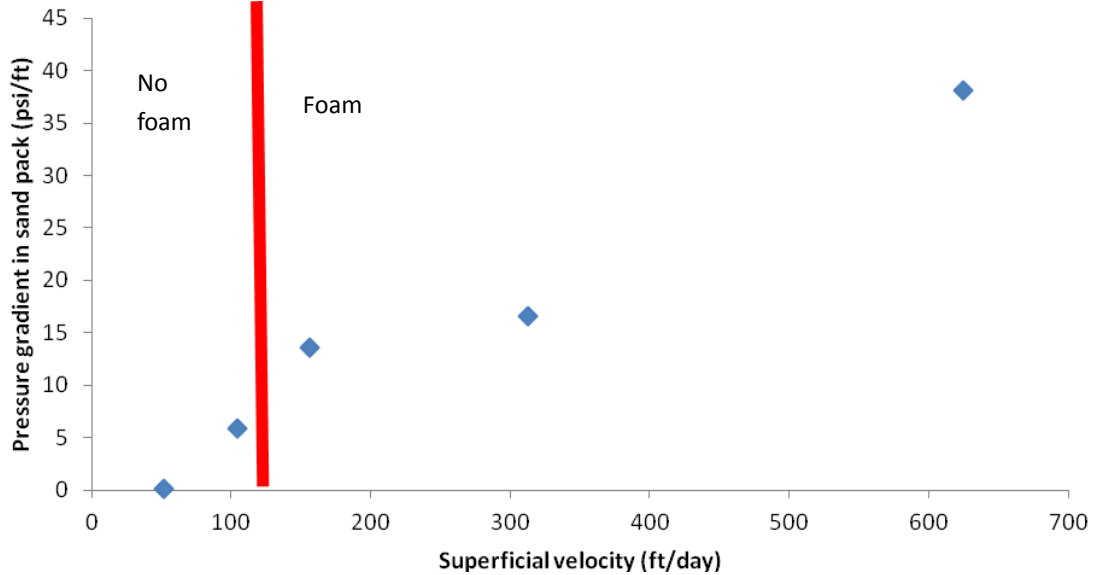
Figure 1-31: _Effect of superficial velocity in the sand pack on the pressure gradient in the sand pack for the C/W foam stabilized with 1% (w/w) Surfonic L24-22 south hobbs brine and 90% v/v CO_2 at 40 °C and 1700 psia_

Effect of surfactant concentration on foam viscosity for Surfonic L24-22

Figure 1-32 presents the foam viscosity of C/W foam stabilized with 1% (w/w) L24-22 south hobbs brine solution with 90% v/v CO_2 at total flow rate of 1.5 and 6 mL/min, 40 °C, and 1700 psia as a function of the surfactant concentration. It was found that L24-22 was still active to increase the viscosity of C/W mixture at 40 ^{o}C even at 0.1% (w/w) to surfactant solution at total flow rate of 6 mL/min, which equals to 0.016% (w/w) in total C/W foam flow. This indicates that L24-22 is a highly efficient surfactant for CO_2 EOR. However, at 1.5 ml/min, the lowest concentration of surfactant in brine that can stabilize foam is 0.5% (w/w).

At 6.0 ml/min the viscosity in the sand pack slightly increases as the surfactant concentration of L24-22 increases in the range of 0.1-1% (w/w) active. On the other hand, at 1.5 ml/min, the viscosity in the sand pack continued to increase in the range from 0.1-1% (w/w).
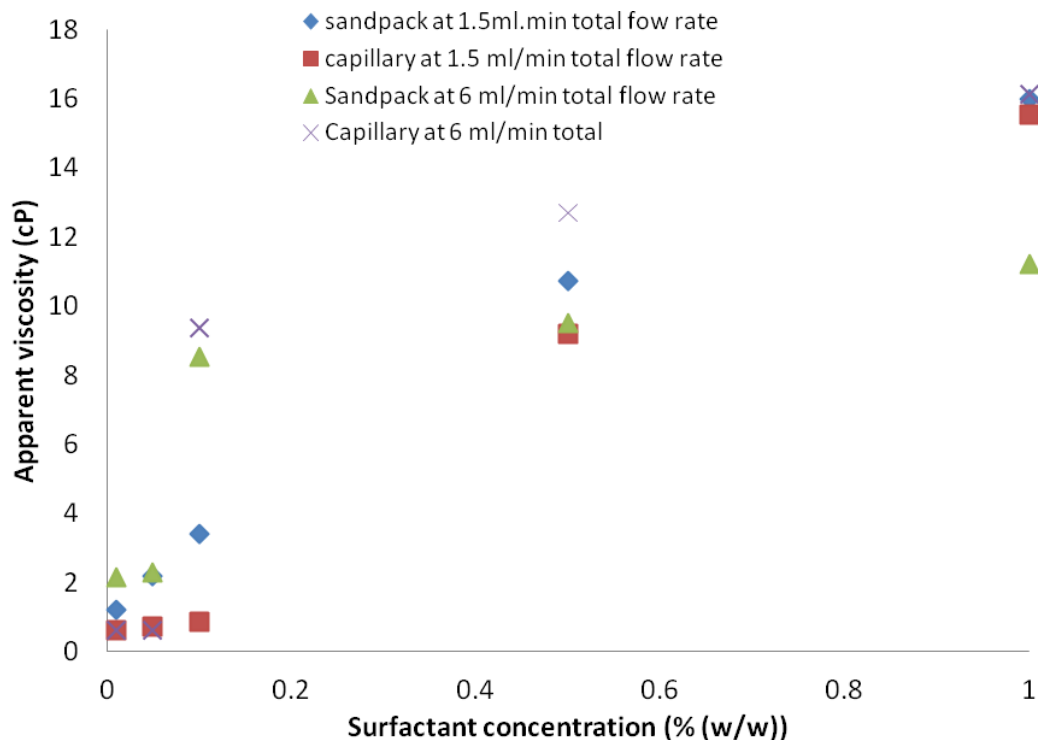
Figure 1-32: _Effect of surfactant concentration on the apparent viscosity in sand pack and capillary for the C/W foam stabilized with 1% (w/w) Surfonic L24-22 south hobbs brine solution and 90% v/v CO_2 at 40 °C and 1700 psia_

Effect of foam quality on foam viscosity for Surfonic L24-22

The quality of foam often has a large influence on foam viscosity. As the quality is increased from 60% v/v, foam viscosity increases as well, due to the increase in the number of bubbles and lamellae in the foam from the additional volume of dispersed phase. As the quality is continually increased, a maximum viscosity is reached at qualities near 70- 90%, followed by a drop in viscosity. For foams with very high qualities the liquid lamellae are very thin and cannot prevent bubble coalescence. As the lamella become too thin and rupture the foams become unstable. The effect of foam quality on foam viscosity is shown in **Figure 1-33** at a total flow rate of 1.5 ml/min (superficial velocity: 156 ft/day) with 0.1% and 1% (w/w) L24-22 south hobbs brine solution at 40 °C and 1700 psia. For 1% (w/w) surfactant in brine, a maximum in viscosity is visible at a quality of 90% for both the apparent viscosity in sand pack and capillary tube,

65

and the foam lamella stability drops when the quality is increased further. No foam was formed when the quality was below 50%. Here the number of lamellae was too small to produce a high viscosity. For 0.1% (w/w) surfactant in brine, foams with close viscosity were generated between 65% to 80% foam quality. Below 65% or higher than 80%, no foam was generated. It is noticeable that the optimal foam quality shifted to a lower range when injecting a lower surfactant concentration. The ability to vary foam viscosity via quality changes allows for some control of the foam in EOR uses, as the gas injection strategy can be altered to either increase or decrease foam viscosity. (Friedmann, F. et al. 1986) found that higher quality foams (90%) propagated better than wet foams (40%) in porous media (Friedmann, F. et al. 1986), thus it is anticipated that high qualities with high foam viscosity may work best for CO_2 EOR. We will further work on effect of permeability, superficial velocity as well as shear rate in porous media on optimal foam quality.
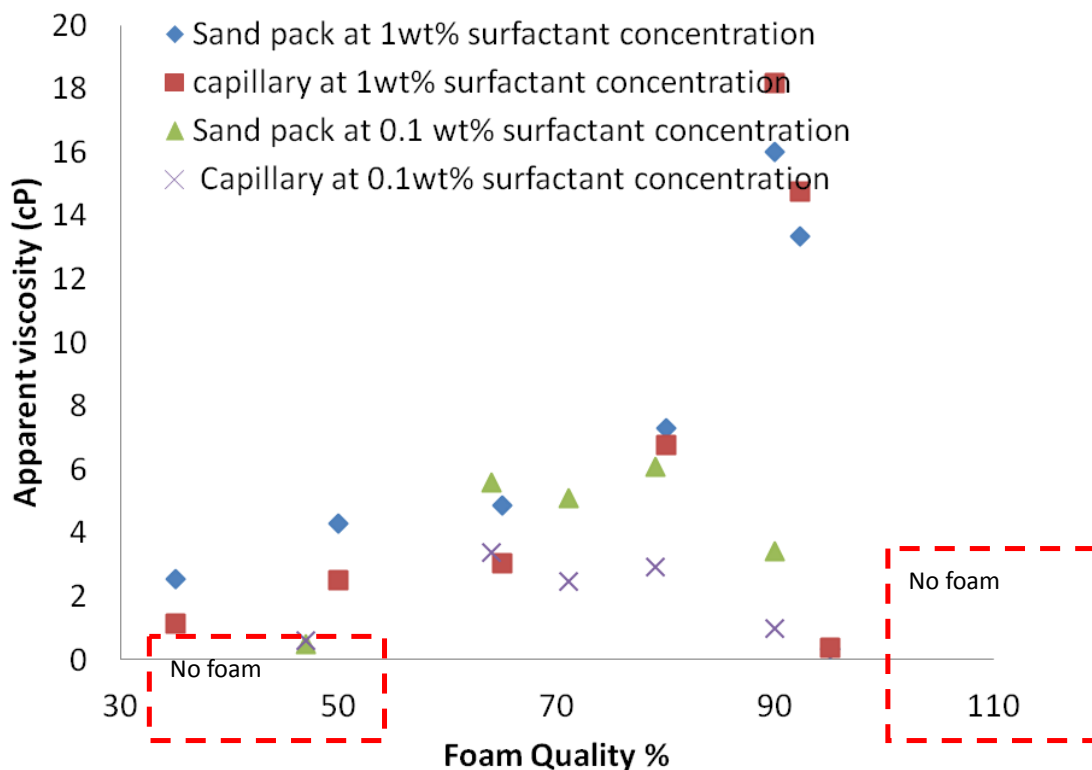
Figure 1-33: *The foam viscosity of C/W foam stabilized with 0.1% and 1% (w/w) Surfonic L24-22 at total flow rate of 1.5 mL/min, 40 °C, and 1700 psia as a function of the foam quality (% v/v CO_2)*

Figure 1-34 shows a comparison of foam viscosity for Surfonic L24-22, Neodol 25-9 and Neodol 25-12.
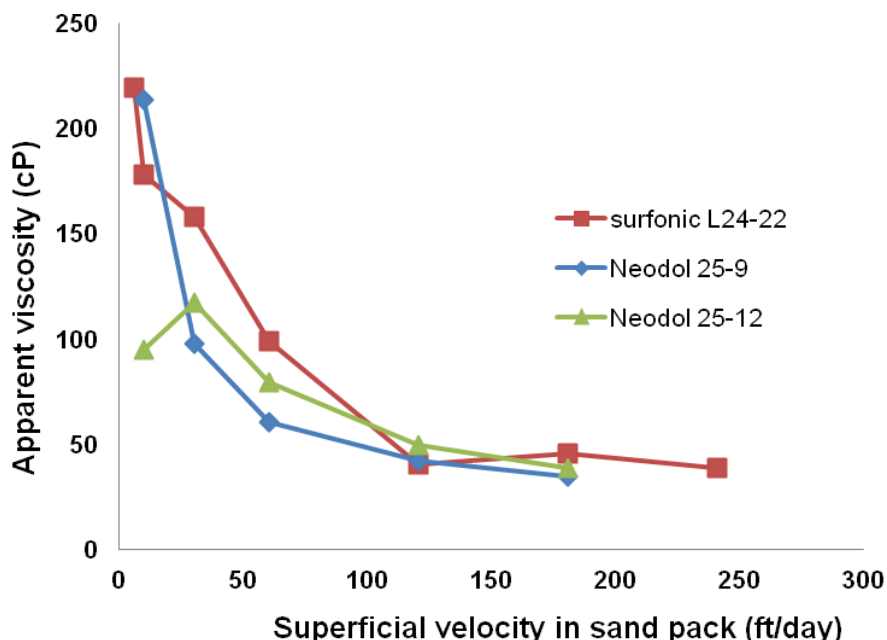
Figure 1-34: The foam viscosity of CO_2/WATER foam stabilized with 1% (w/w) Surfonic L24-22, Neodol 25-9 or Neodol 25-12 South Hobbs brine solution at different superficial velocity, 40 °C, and 1700 psia in 1-4arcy bead pack at 80% foam quality (v/v CO_2)

1.3.6. Dodecane/brine Emulsion Stability

Emulsions were prepared by mixing surfactant solution (1% v/v) and dodecane with an oil/water ratio of 9:1 v/v and then sonication for 1 min to mimic foams made with CO_2. Photographs were taken to record destabilization of emulsions.

Emulsion stability test for 15-S-20 at different salinities were carried out at 24 °C. Results are presented in **Table 1-35.** Coalescence took place and the upper phase became clearer from the top down. A water rich phase was observed at bottom about 1 min after sonication at 24 °C for all samples.

Unstable O/W emulsions indicate the water films between oil droplets break. Therefore, this may indicate that these surfactants are selective for stable C/W foams but form unstable O/W emulsions as desired for mobility control in CO2 EOR.

Salinity	0 min	1 min	5 min
0 wt% NaCl			
3 wt% NaCl			
9 wt% NaCl			

Figure 1-35: Destabilization of emulsions of dodecane and aq. 15-S-20 (1 wt%) brine solution with oil/water ratio of 9:1 v/v at 24 ^{o}C (Sonication for 1 min. to form white emulsion.)

Initial images of the emulsions made using gentle hand mixing for 1 wt% 15-S-40 9 wt% NaCl solution mixed with dodecane are shown in **Figure 1-36 (a)**. The mixtures were put into an oven at 60 ^{o}C right after mixing It is noticeable that it took less than 1 hour for the emulsions made for a high oil/water ratio (9/1, 8/2 and 7/3 v/v dodecane/aqs.) to separate into one clear oil

phase, one tiny emulsion layer and one slightly opaque aqueous layer. Others separated into one oil-in-water emulsion layer and one slightly opaque aqueous layer. Furthermore, similar results were observed up to 48 hours as shown in **Figure 1-36 (b)**. Thus, at low shear, the emulsions generated for 9wt% NaCl solutions at high oil ratio were unstable. These results suggest 15-S-40 is a successful candidate at low shear conditions for avoiding stable oil/water emulsions in the presence of large amount of surrounding oil. The ability to form C/W foams, without forming stable O/W foams would be highly beneficial in EOR to lower CO2 permeability selectively in regions where oil is not present. Similar result was found in emulsion stability test for 1 wt% 15-S-40 no salt solution mixed with dodecane

(A)

| 1/9 | 2/8 | 3/7 | 4/6 | 5/5 | 6/4 | 7/3 | 8/2 | 9/1 |

(B)

| 1/9 | 2/8 | 3/7 | 4/6 | 5/5 | 6/4 | 7/3 | 8/2 | 9/1 |
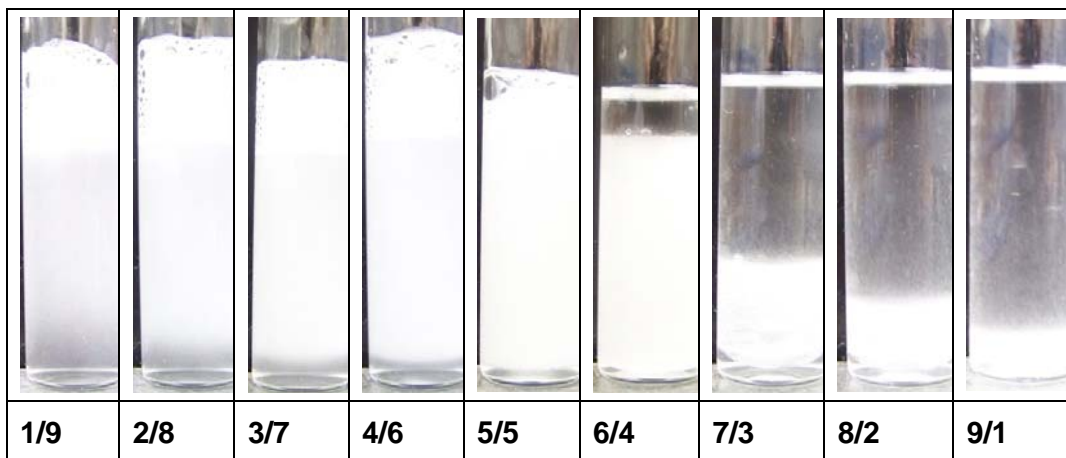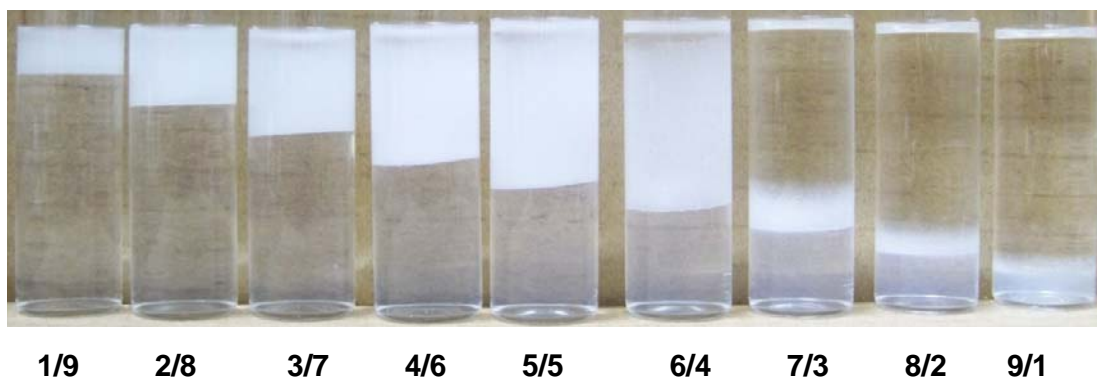
Figure 1-36 A&B:. *Initial (A) and 48 hours (B) images of emulsion of different volumetric ratios of dodecane and 1 wt% (w/w) Tergitol 15-S-40 9 wt% NaCl solution at 60 °C. (The Emulsions were prepared by hand mixing.)*

Initial images of the emulsions made using gentle hand mixing for 1% (w/w) L24-22 south hobbs brine solution mixed with dodecane are shown in **Figure 1-37 (a)**. The mixtures were put into an oven at 40 ^{o}C right after mixing and periodic pictures were taken to observe the phase behaviour. It was noticeable that it took less than 1 hour for the emulsions made at a high oil/water ratio (9/1 and 7/3 v/v dodecane/aqs.) to separate into one clear oil phase, one emulsion layer and one clear aqueous layer. Others separated into one oil-in-water emulsion layer and one clear aqueous layer. Furthermore, similar results were observed up to 72 hours as shown in **Figure 1-37 (b)**. Thus, at low shear, the emulsions generated for south hobbs brine solutions at high oil ratio were unstable. These results suggest that L24-22 is a successful candidate at low for avoiding stable oil/water emulsions at low shear in the presence of large amount of surrounding oil. The ability to form C/W foams, without forming stable O/W emulsions would be highly beneficial in EOR to lower CO_2 mobility selectively in regions where oil is present.

(A)
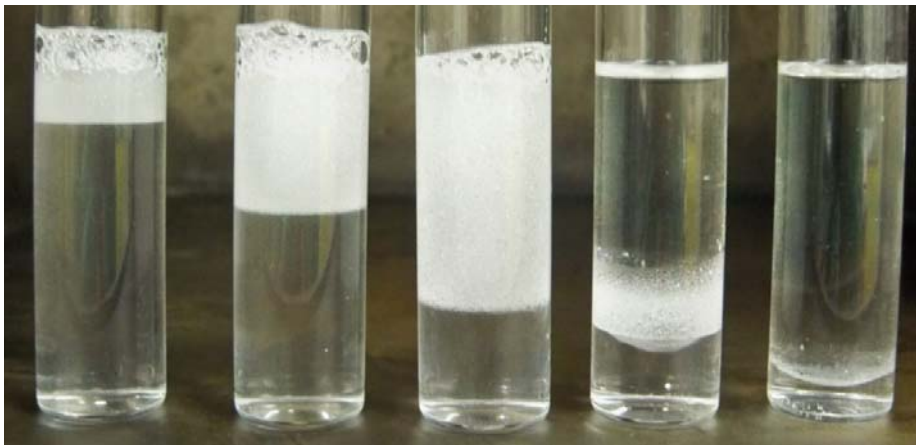
| 1/9 | 3/7 | 5/5 | 7/3 | 9/1 |

(B)
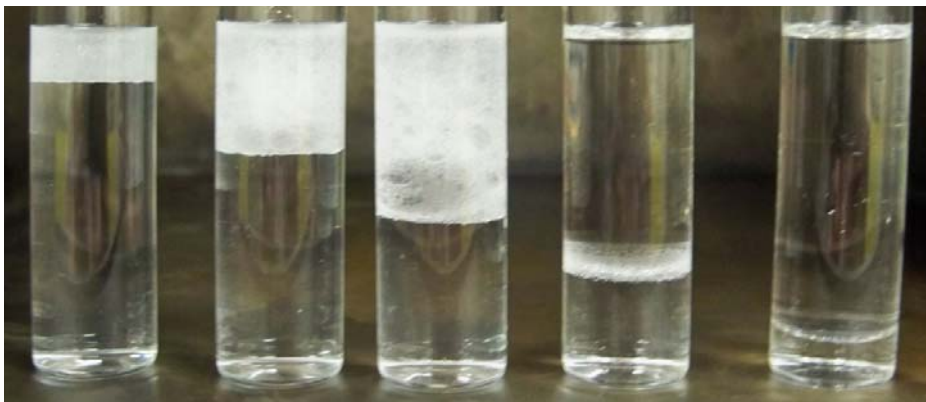
| 1/9 | 3/7 | 5/5 | 7/3 | 9/1 |

__Figure 1-37 1&2:__ Initial (A) and 72 hours (B) images of emulsion of different volumetric ratios of dodecane and 1 % (w/w) Surfonic L24-22 south hobbs brine solution at 40 ^{o}C. (The Emulsions were prepared by hand mixing.)

PART II- SURFACTANT AND FOAM TRANSPORT

2.1. Static adsorption of anionic and cationic surfactants

2.1.1. Materials

IOS1518 surfactant: Internal olefin sulfonate 1518 (19.42 wt%). This product was manufactured by Stepan (Lot# 18239-032708) with a trade name of Petrostep S-2A.

CS330 surfactant: Sodium laureth sulfate ethoxylated to an average of 3 moles. This product was manufactured by Stepan (Lot# 7378133) with a trade name of Steol CS-330.

CPC surfactant: hexadecylpyridinium chloride monohydrate, 358.00 g/mol, 99.0-102.0%, Sigma-Aldrich.
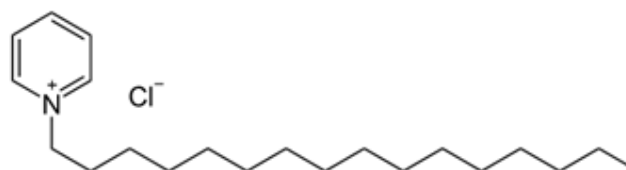
SDS surfactant: sodium dodecyl sulfate ($CH_3(CH_2)_{11}OSO_3Na$), 288.38 g/mol, ≥99.0%, Sigma-Aldrich.

TEGO trant A100: 1,3-didecyl-2-13ethyl imidazolinium chloride, 399.10 g/mol, Fisher Scientific.

Dolomite powder: the powder is sieved from the original pail and the one with size smaller than 75 micron (200 mesh) is collected for this experiment. The BET surface area for the sieved sample (200+ mesh) is 0.97 m^2/gram. This product was manufactured by Vital Earth / Carl Pool.

Limestone 20/40: limestone from Franklin Minerals, Nolanville TX. The carbonate sand was sieved from the original pail and that of 20/40 mesh was collected for this experiment. The BET surface area for the sieved sample (20/40 mesh) is 0.29 m^2/gram.

Calcite powder: synthetic calcium carbonate powder from Alfa Aesar Company, Ward Hill, MA. The powder has an average particle size of 5 μm, and a specific surface area of 1.67 m^2/gram (Seethepalli, Adibhatla et al. 2004;

Wu, Shuler et al. 2008).

CPC is measured with potentiometric titration using SDS as a titrant (Methohm 2011). SDS is measured with potentiometric titration using TEGO as a titrant (Methohm 2011).

2.1.2. Static adsorption on dolomite power and calcite sand

The comparison of adsorption of different anionic surfactants on dolomite powder in DI water is shown in **Figure 2-1**. Compared with AOS 1618, IOS 1518 shows a higher adsorption plateau (2.1 mg/m^2). However, the ethoxylated sulfate CS 330 shows much lower adsorption, with a plateau of only 1.1 mg/m^2. With ethoxylated groups on the structure of the surfactant, CS 330 is more water soluble and has a reduced adsorption at the water/dolomite interface.
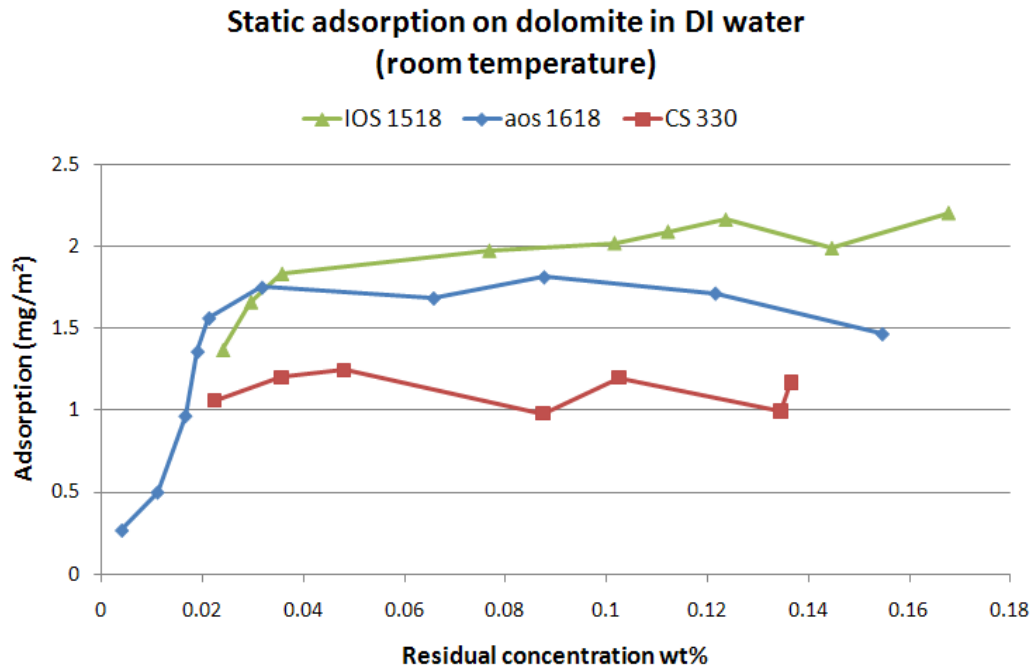
Figure 2-1: *Static adsorption of anionics on dolomite powder in DI water at room temperature.*

We evaluate the adsorption of CPC on both dolomite powder and carbonate sand (RT and 40˚C). The experiments at 40 ˚C are performed in the water bath without shaking. We examine the non-equilibrium effect in this report to make sure that the procedure at elevated temperatures also works for room temperature. **Figure 2-2** shows the results of our new procedure without shaking. At room temperature, the new results match well with our data of the old procedure in the shaker. Filtration of the sample does not significantly affect the results of adsorption. With the new procedure, we perform the experiments at 40 ˚C, as shown in the green curve in **Figure 2-2**. Adsorption reduction is observed at 40 ˚C with an adsorption plateau of around 2.8 mg/m^2, compared with that of 3.7 mg/m^2 at room temperature. A main reason for this reduction could be the effect of Krafft temperature.

CPC static adsorption on dolomite in DI water
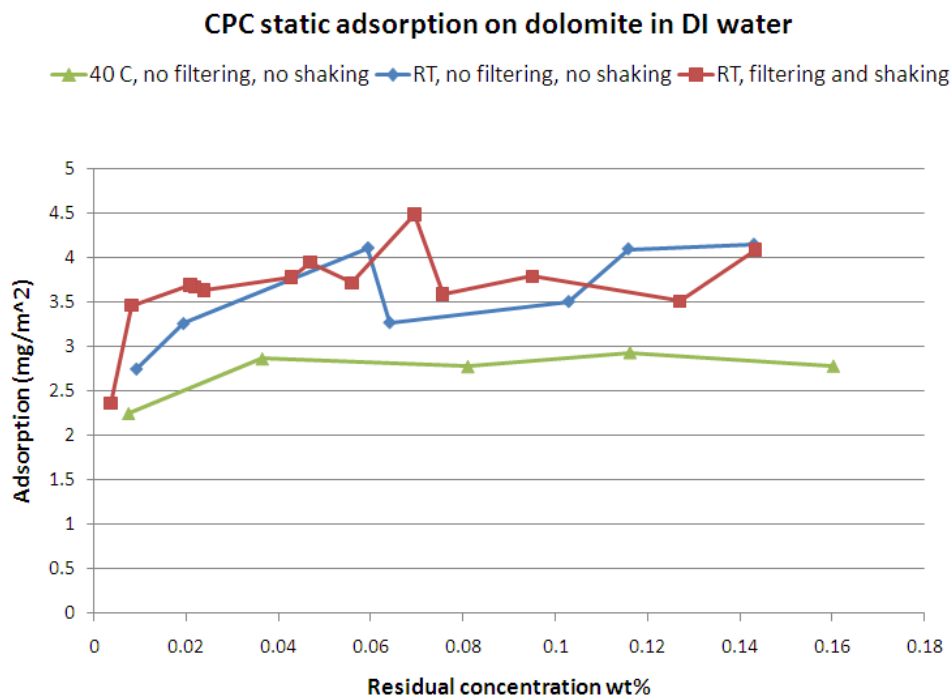
Figure 2-2: Static adsorption of CPC on dolomite powder in DI water. The equilibrium time is 24 hours.

We also performed the adsorption experiments on carbonate sand 20/40. In **Figure 2-3** we observe a big difference for the experimental results with

24-hour and 48-hour equilibrium time at room temperature, which means non-equilibrium effect is significant within 24 hours. Interestingly, it does not happen to the case with dolomite powder. A possible reason is that the limestone carbonate sand has microporous structure, which takes longer time for the diffusion of the surfactant onto the surfaces inside the grain than that on dolomite powder.

CPC adsorption on carbonate sand 20/40 in DI water
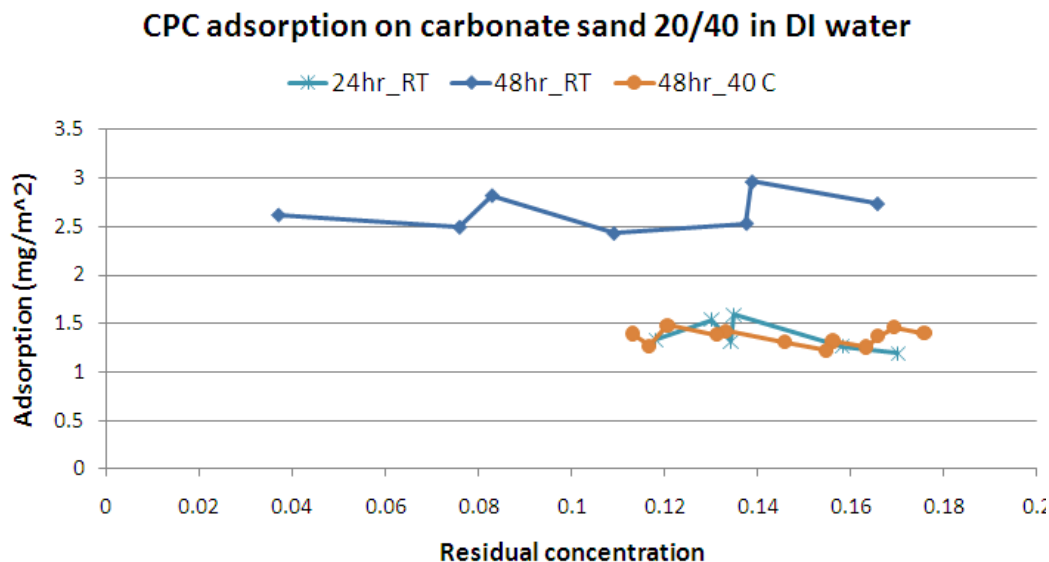
Figure 2-3: Static adsorption of CPC on carbonate 20/40 in DI water. The equilibrium time is shown in the legend. The samples are neither shaken nor filtered before measurement.

Again, we observe adsorption reduction at 40 ˚C than room temperature with 48-hour equilibrium. The adsorption results with carbonate sand 20/40 show the same trend as those with dolomite powder.

Ca^{2+} and Mg^{2+} are potential determining ions for the adsorption of cationics on carbonate minerals, as they react with CO_3^{2-} at the mineral surface and alter the surface charge. However, we do not observe significant reduction at room temperature as shown in **Figure 2-4**. By adding either 0.05 M $CaCl_2$ or 0.05 M $MgCl_2$, the adsorption plateaus do not change much for CPC on dolomite at room temperature. A possible explanation for the high

75

adsorption is that at room temperature the effect of Krafft temperature (phase transition) dominates over the effect of divalent ions. The effect of divalent ions is expected to be more significant at elevated temperatures, which are away from the Krafft temperature.
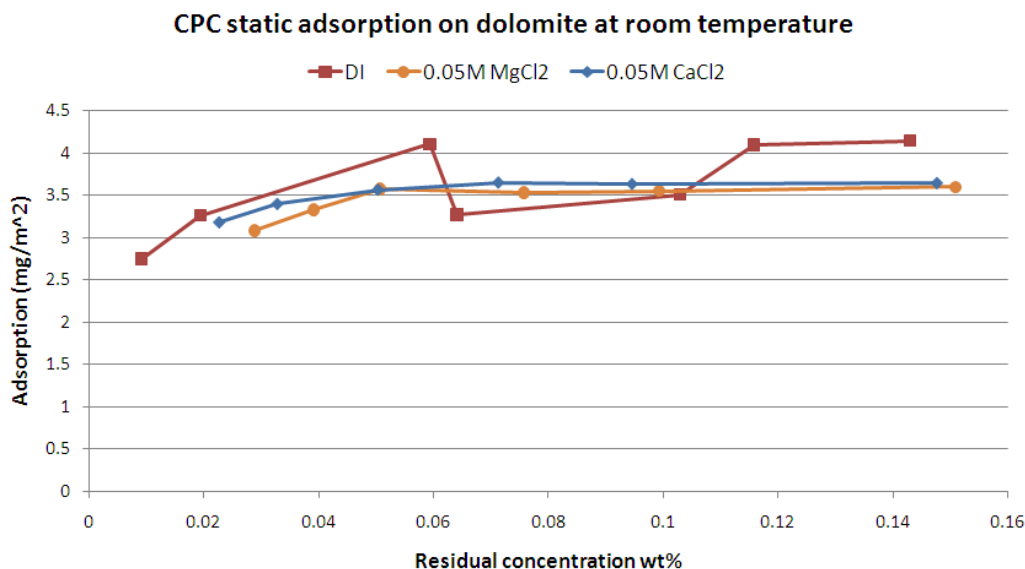
Figure 2-4:. *Static adsorption of CPC on dolomite powder. The samples are neither shaken nor filtered before measurement.*

2.1.3. Comparison of SDS and CPC adsorption on different minerals

The adsorption results are shown in **Figure 2-5** to **Figure 2-7**. SDS shows lower adsorption than CPC on either dolomite powder (**Figure 2-5**) or limestone 20/40 (**Figure 2-6**).

In DI water, the adsorption plateaus of CPC on dolomite powder and limestone 20/40 are 3.7 mg/m^2 and 3.0 mg/m^2, respectively. The adsorption plateau of SDS is not observed within our concentration range (0 - 0.2% wt), apparently because of the high critical micelle concentration of this surfactant (in pure water at 25 °C is 0.0082 M, or 0.24% wt (Mukerjee and Mysels 1971)).

The results on both dolomite powder and limestone are contradictory to those reported in the literature (Tabatabai, Gonzalez et al. 1993), which

76

showed that CPC exhibited significantly less adsorption on carbonate minerals than that exhibited by SDS. A possible explanation is that our natural materials (dolomite and limestone) may contain silica which spreads over the mineral surface, and silica has a strong negative charge which adsorbs cationic surfactant
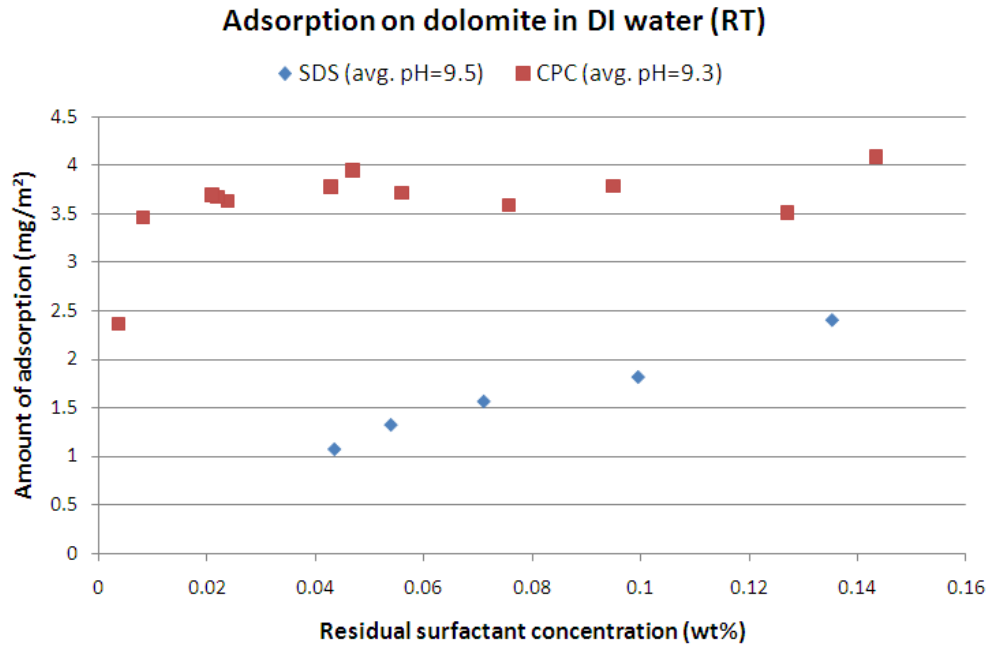
Figure 2-5: Comparison of static adsorption of SDS and CPC on dolomite powder in DI water at room temperature.
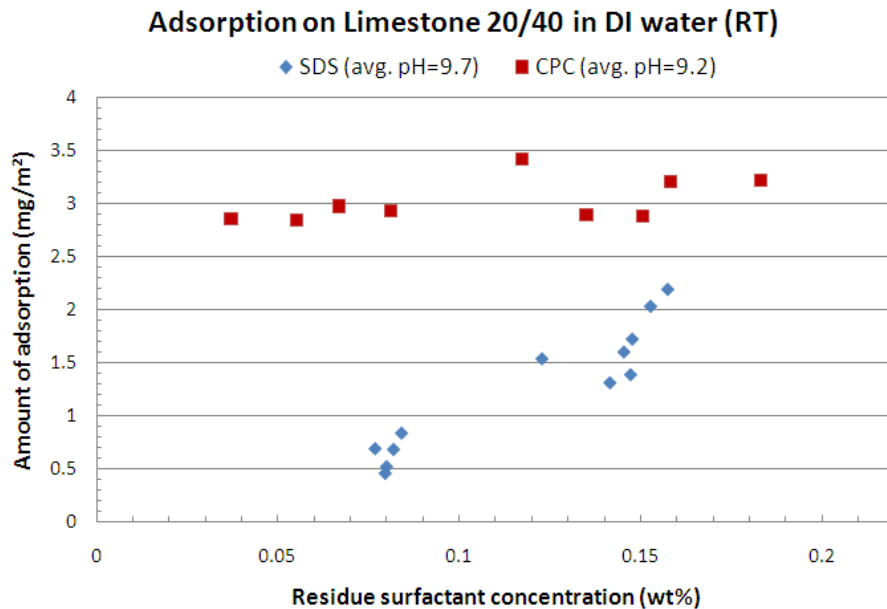
Figure 2-6: *Comparison of static adsorption of SDS and CPC on limestone 20/40 in DI water at room temperature.*

In **Figure 2-7**, we show that the adsorption on synthetic calcite powder of CPC is significantly lower than that of SDS, which agrees with the findings in the literature (Tabatabai, Gonzalez et al. 1993). The adsorption of CPC is negative on the surface of this material, due to the electrostatic repulsion between the positively charged head group of CPC and the positively charged carbonate surface.

Note that the average pH in the surfactant solutions which are equilibrated with the synthetic calcite powder is higher than those equilibrated with either dolomite powder or limestone 20/40. According to the MSDS of this material by Alfa Aesar, the pH of 100 g/l sample in water at 20 °C is 9.5 – 10.5, which is close to our measurements (10.8 and 10.9).
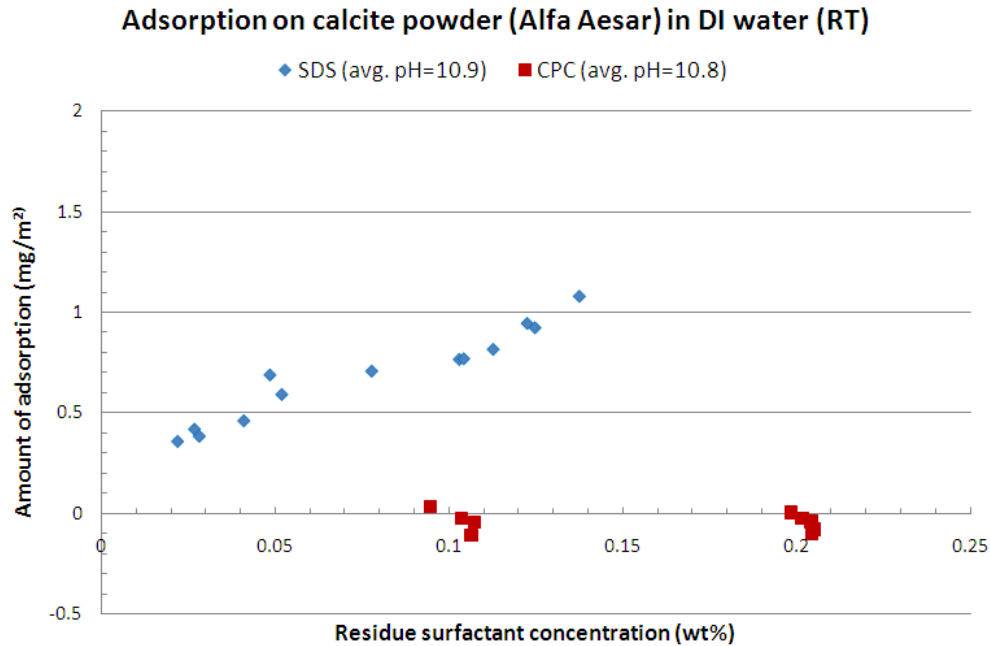
Figure 2-7: *Comparison of static adsorption of SDS and CPC on synthetic calcite powder in DI water at room temperature.*

2.2. Effect of CO2 on surfactant Adsorption

2.2.1. Calculation of pH and Ion Concentration

We have showed the calculation of pH for water in equilibrium with CO_2 and calcite. Here we make this method more general to calculate pH and aqueous composition with various CO_2 partial pressures. The equilibrium constants are listed in **Table 2-i** (Stumm and Morgan 1996):

Reaction	-log K at 25°C	Definition of K
$CaCO_3(s) = Ca^{2+} + CO_3^{2-}$	8.42	$K_{s0} = [Ca^{2+}][CO_3^{2-}]$
$H_2CO_3^* = H^+ + HCO_3^-$	6.35	$K_1 = [H^+][HCO_3^-]/[H_2CO_3^*]$
$CO_2(g) + H_2O(l) = H_2CO_3^*$	1.47	$K_H = [H_2CO_3^*]/P_{CO2}$
$HCO_3^- = H^+ + CO_3^{2-}$	10.33	$K_2 = [H^+][CO_3^{2-}]/[HCO_3^-]$
$H_2O = H^+ + OH^-$	14.0	$K_W = [H^+][OH^-]$

According to **Table 2-i** we have the following equations:

$\log [HCO_3^-]$

$= \log K_1 + pH + \log [H_2CO_3^*]$

$= pH + \log K_1 + \log K_H + \log P_{CO2}$………………………………………..……(3.4)

$\log [CO_3^{2-}]$

$= \log K_2 + \log [HCO_3^-] + pH$

$= 2pH + \log K_2 + \log K_1 + \log K_H + \log P_{CO2}$……………………………………………..……………..(3.5)

$\log [OH^-]$

$= pH + \log K_W$ ………………………………………......………..………………………………..(3.6)

$\log [Ca^{2+}]$

$= \log K_{s0} - \log [CO_3^{2-}]$

$= -2pH + \log K_{s0} - \log K_2 - \log K_1 - \log K_H - \log P_{CO2}$………..…..………………………………………………...…..(3.7)

Considering the charge balance, we have Equation (3.8) in the system:

$2[Ca^{2+}] + [H^+] = [HCO_3^-] + 2[CO_3^-] +$

80

$[OH^-]$……………………………………………………………………..………..(3.8)

Substituting Equations (3.4) ~ (3.7) into Equation (3.8) one can get:

$2*10^{-2pH + \log Ks0 - \log K2 - \log K1 - \log KH - \log PCO2} + 10^{-pH} = 10^{pH + \log K1 + \log KH + \log PCO2}$

$+2*10^{2pH + \log K2 + \log K1 + \log KH + \log PCO2} + 10^{pH + \log KW}$ …………….…………………………………………………………....……..(3.9)

Equation (3.9) can be solved by iteration methods once the partial pressure of CO_2 (P_{CO2}) is given. After getting the pH, the concentrations of calcium, carbonate and bicarbonate can be obtained through Equations (3.4), (3.5) and (3.7).

The results for 1 atm CO_2, 1 atm air with a CO_2 partial pressure of $10^{-3.5}$ (typical amount of CO_2 in air) and $10^{-4.5}$ atm are shown in **Table 2-ii**. The presence of 1 atm CO_2 can lower the pH of DI water to around 6 in equilibrium with calcite and increase $[Ca^{2+}]$ concentration by an order of magnitude.

Table 2-ii: *Calculation of pH and ion concentrations in DI water equilibrated with CO_2 and calcite.*

P_{CO2} in atm	1	$10^{-3.5}$	$10^{-4.5}$
pH	5.95	8.28	8.91
$[CO_3^{2-}]$ in mol/L	5.62E-07	8.13E-06	1.48E-05
$[HCO_3^-]$ in mol/L	1.35E-02	9.12E-04	3.89E-04
$[Ca^{2+}]$ in mol/L	6.76E-03	4.68E-04	2.57E-04

2.2.2. Adsorption on Different Minerals at 1 atm CO_2 pressure

The adsorption of the cationic surfactant CPC on limestone, calcite and dolomite in DI water at room temperature is shown from **Figure 2-8** to **Figure 2-11**. In all three cases, the presence of 1 atm CO_2 does not significantly alter the adsorption of CPC on various carbonate minerals, compared with the results equilibrated with 1 atm air. The pH of the aqueous phase is lowered to 6.1 in all three cases which is close to the prediction by **Table 2-ii** (pH=5.95 when P_{CO2} =1 atm).

81

These results suggest that even in acidic conditions CPC may still have negligible adsorption on synthetic calcite, but substantial amount of adsorption on natural carbonate materials such as limestone and dolomite.

CPC adsorption on limestone 20/40

◆ Equilibrated with 1 atm CO2 (avg. pH=6.1)　　■ Equilibrated with 1 atm air (avg. pH=9.2)
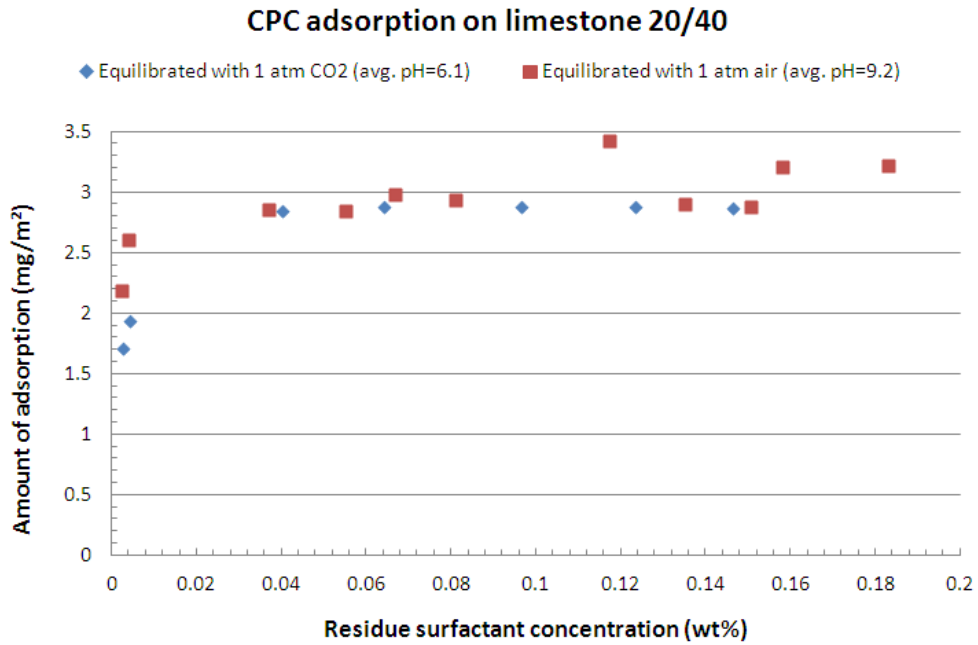
Figure 2-8: Comparison of static adsorption of CPC on limestone 20/40 in DI water at room temperature.

CPC adsorption on synthetic calcite powder
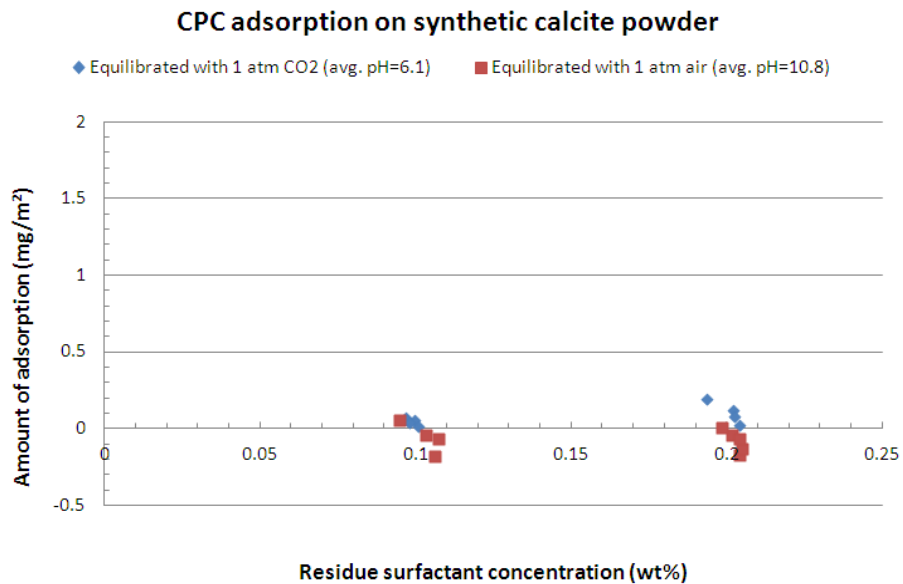
Figure 2-9: Comparison of static adsorption of CPC on synthetic calcite powder in DI water at room temperature.

CPC adsorption on new dolomite powder in DI water
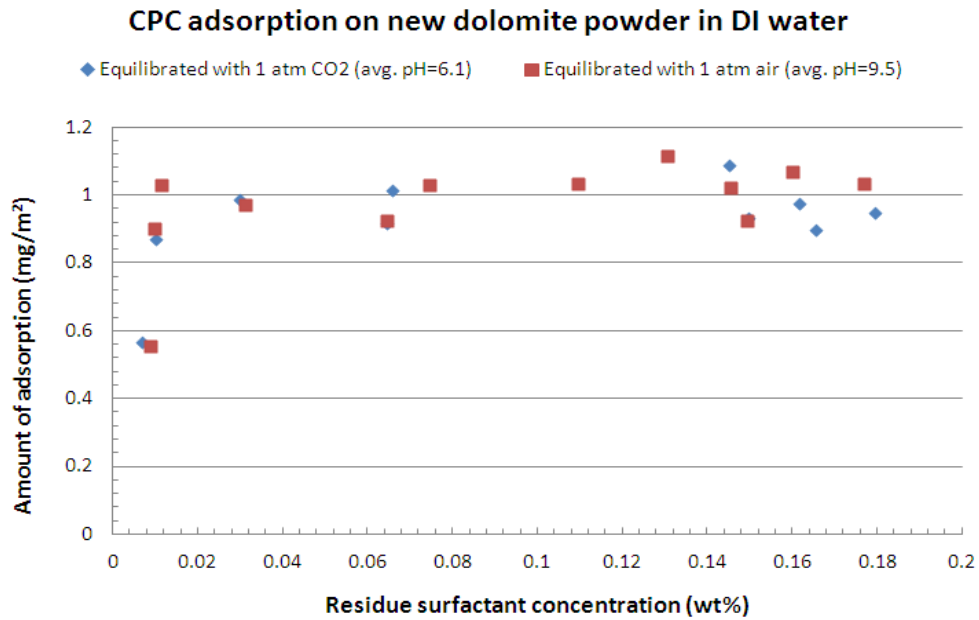
Figure 2-10: Comparison of static adsorption of CPC on new dolomite powder in DI water at room temperature.

Note that in **Figure 2-10** the adsorption plateau of CPC on new dolomite equilibrated with 1 atm air is 1.0 mg/m^2, which is much lower than the result we obtained from the old dolomite (3.7 mg/m^2). The difference between different

batches of dolomite suggests that the composition change of the impurities (silica or clay) in natural dolomite may dominate CPC adsorption, since CPC has negligible adsorption on synthetic calcite.

SDS adsorption on limestone 20/40
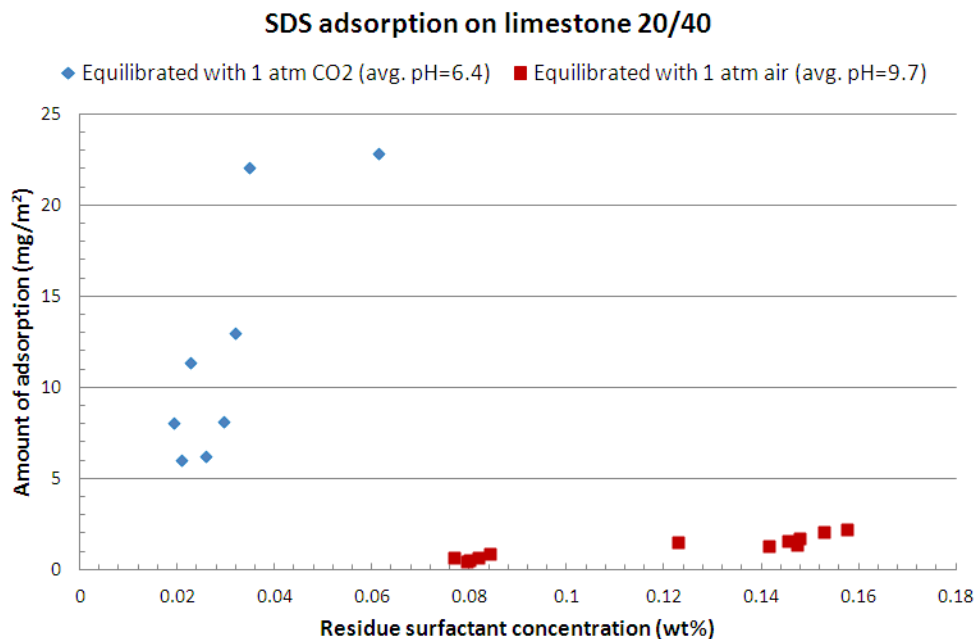
Figure 2-11: Comparison of static adsorption of SDS on limestone 20/40 in DI water at room temperature.

Figure 2-11 and 2-12 show the adsorption of the anionic surfactant SDS on acidified limestone and calcite with 1 atm CO_2. Compared with the results in 1 atm air, the presence of CO_2 causes very high amount of apparent adsorption on both carbonate materials. This behaviour usually suggests that phase separation of the surfactant occurs in the system, causing low aqueous concentration and high apparent adsorption. As indicated in **Table 2-vi**, the use of 1 atm CO_2 is able to increase calcium concentration to 6.76E-03 mol/L, compared with 4.68E-04 mol/L in the presence of 1 atm air ($P_{CO2} = 10^{-3.5}$ atm). In this case, the phase separation is due to the intolerance of SDS to divalent ions, and the surfactant precipitates out of the solution.

SDS adsorption on synthetic calcite powder
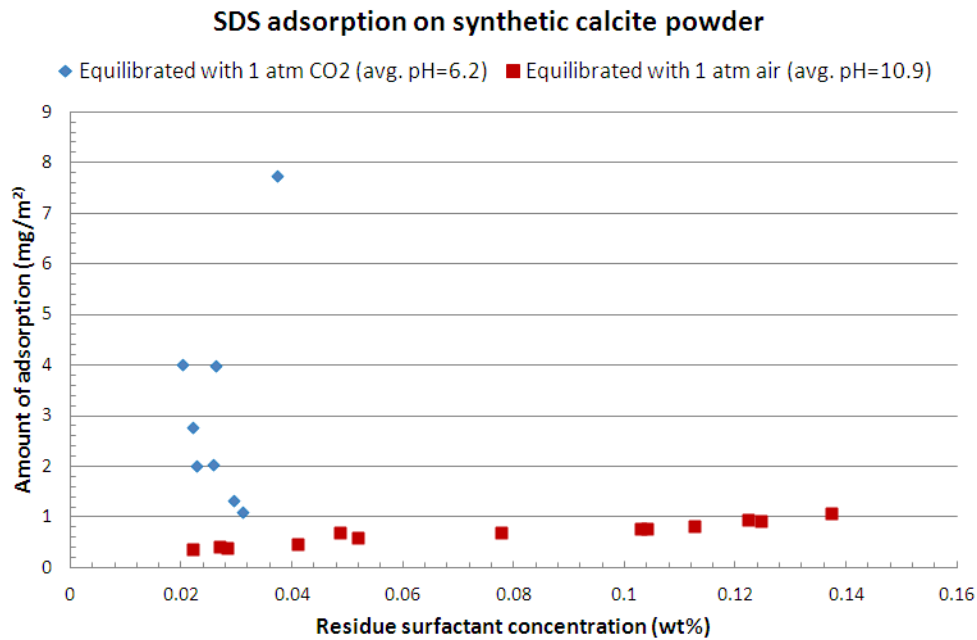
Figure 2-12: Comparison of static adsorption of CPC on synthetic calcite powder in DI water at room temperature.

The static adsorption results of CS-330 on dolomite are shown in **Figure 2-13**. The presence of 1 atm CO_2 lowers the pH to 6.3, which is slightly higher than predicted (pH around 6.0). Compared with the case without loading CO_2 (pH=8.8), we do not see significant change in the adsorption plateau as shown in **Figure 2-13**. The adsorption plateau values of CS-330 in the presence of both 1 atm air and 1 atm CO_2 are around 0.9 mg/m^2. This result indicates that ethoxylated anionic surfactants may be a good choice for CO_2 foam application from the standpoint of adsorption on formation minerals.
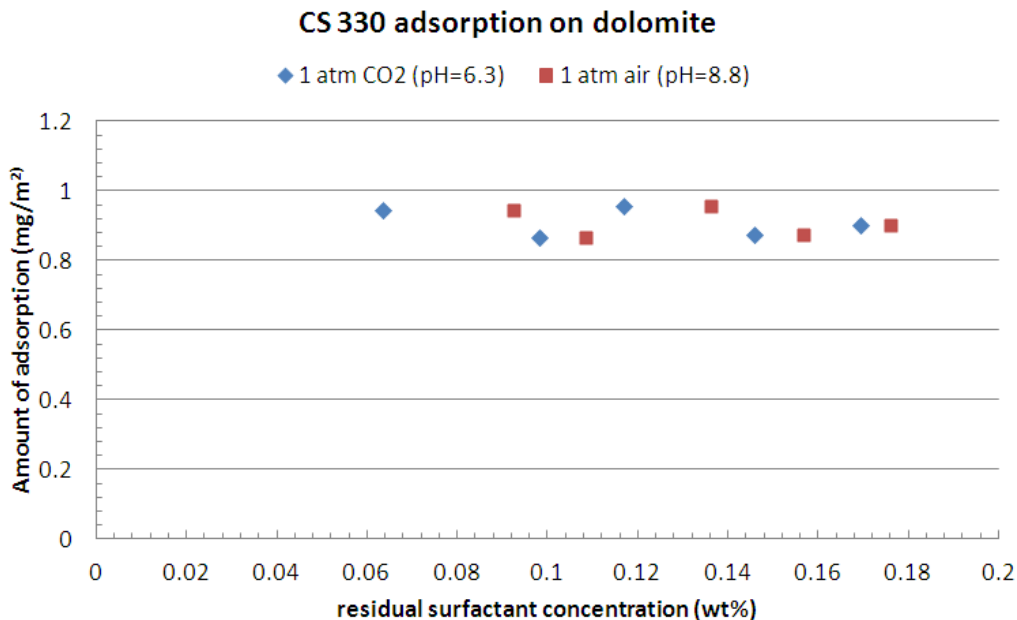
Figure 2-13: *Comparison of static adsorption of CS-330 on dolomite under 1 atm air and* CO_2 *conditions.*

2.3. Adsorption of cationic-nonionic switchable surfactant

2.3.1. ETHOMEEN C12'S CLOUD POINT TEST, ANALYSIS METHOD AND ADSORPTION EVALUATION

Ethomeen C12 (C12) was from AKZO NOBEL Co.

R = Coco group (≈ 8 to 16 carbon)
x + y = 2
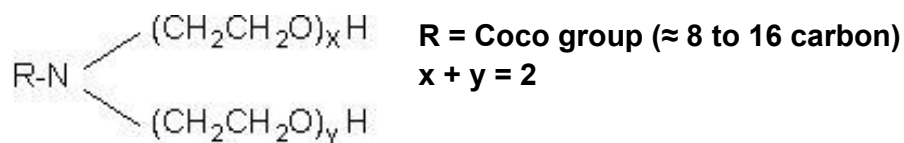
C12's molecule weight is 288 g/mol reported by AKZO NOBEL Co.

Ethomeen C12 is a good candidate for CO_2 foam. Its cloud point in DI water at original pH is smaller than room temperature, but higher than 130 ˚C at pH around 4. In order to investigate its adsorption and partition coefficient, methylene-blue two-phase titration with colorless endpoint is used to determine C12 concentration. The activity of C12 commercial product determined by above method is only 91.02%, compared to the activity

86

(97%-100%) reported in its MSDS. The cloud point of C12 is lower than room temperature at its original pH. Thus, a new adsorption procedure with two atmosphere partial pressure CO_2 is developed. With this new procedure, the pH of surfactant solution is lower than 6, which raises the cloud point of C12 much higher than room temperature. The average adsorptions of C12 in DI water after plateau are 2.21 mg/m^2 on dolomite sand and 0.47 mg/m^2 on calcite sand.

SDES: Sodium dodecyl ether sulfate with 3 EO from Stepan. Trade name is STEOL CS 330, lot # is 0-15021. MW=422 g/mol. Molecular formula is shown below. Contrary to SDS, SDES is divalent ion tolerant. The concentration of SDES used in this report is 1.018 mM, calibrated by standard cationic surfactant, i.e. TEGO, solution.
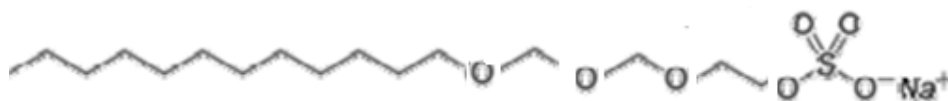
MB solution: Methylene blue solution, which contains 0.03g/L Methylene Blue, 50g/L Na_2SO_4, 6mL/L Sulfuric Acid (Fumic 20%), pH=1.25. The methylene blue structure is shown below:
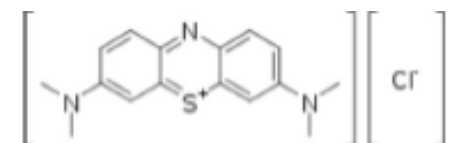
Chloroform: from Sigma-Aldrich Co., HPLC grade.

Dolomite Powder: Manufactured by Carl Pool. Composition is 20 % Ca^{2+}, 10 % Mg^{2+}. All dolomite powder used in this study was shaken through a NO. 200 mesh. A surface area of 0.97 m^2/g is assumed. But a different dolomite powder, with composition 7% Ca^{2+} and 10% Mg^{2+}, was used.

Calcite powder: synthetic calcium carbonate powder from Alfa Aesar Company, Ward Hill, MA. The powder has an average particle size of 5 μm, and a specific surface area of 1.67 m^2/gram (Seethepalli, Adibhatla et al. 2004;

87

Wu, Shuler et al. 2008).

2.3.2. Cloud Point Tests of Ethomeen C12

The cloud point of 1(wt)% C12 was tested in DI water at the pH values of 4, 6, and the original pH (pH = 9.88). The pH values were adjusted by adding 100% (by mass) acetic acid and measured at room temperature and the data is shown in **Table 2-iii.**

The C12 solution at the original pH of 9.88 was cloudy from room temperature to130°C while the pH 6 solution was clear at room temperature, but reached its cloud point at 90°C. The solution at pH 4 never reached its cloud point for the tested temperature range (between 23°C to 130°C), as shown in **Figure 2-14.**

Table 2-iii: C12 Solutions in DI water

NO.	Surfactant	Commercial product wt%	pH at room temperature	Solvent
1	C12	1.0001	4.05	DI water
2	C12	1.0003	5.84	DI water
3	C12	0.9987	9.88	DI water
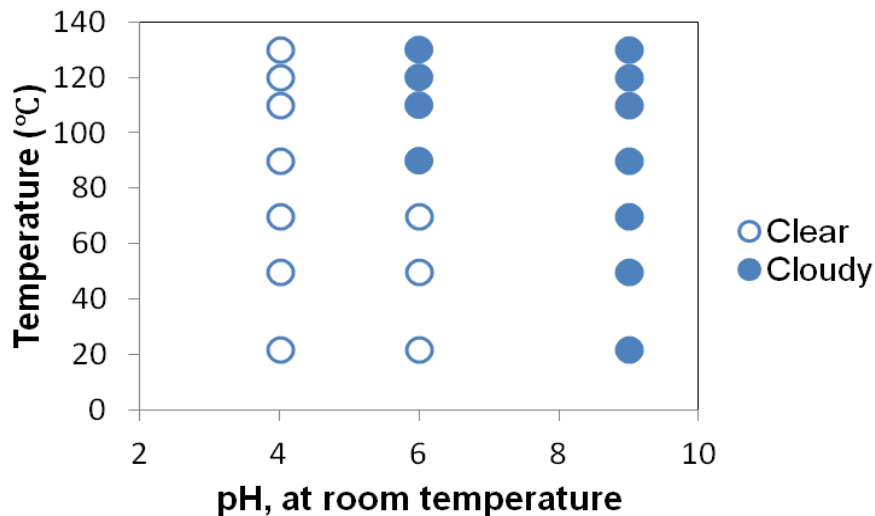
Figure 2-14: *Cloud Point Result of 1% C12 in DI Water.*

In CO_2 flooding process, the pH of solution should be around 4. Thus, C12 can be used as clear solution for CO_2 flooding.

2.3.3. ANALYSIS METHOD OF ETHOMEEN C12

2.3.3.1. MB Two-Phase Titration with Colorless Endpoint Procedure

SDES is the titrant, and methylene blue is the blue dye indicator.

1st step: Add 5 mL Choloroform and 2 mL methylene blue solution in a glass vial in a fume hood.

2nd step: Add a certain amount of C12 sample in the glass vial. All the methylene blue should stay in the upper aqueous phase, and the lower chloroform phase is colorless.

3rd step: Titrate the surfactant sample with SDES. After adding some SDES solution, vigorously shake the vial by hand, in order to partition all the ion-pairs into chloroform phase. If the color of upper aqueous phase just turns from slightly blue to colorless after one drop of SDES, the endpoint is reached. The endpoint can't be judged until two phases are completely separated due to the blue chloroform phase dispersed in aqueous phase. It takes a long time to completely separate two phases by gravity. So, centrifuge can be used to accelerate the phase separation process.

89

4th step: A blank need to be done to calibrate the titration results. Prepare a sample with 5 mL chloroform and 2 mL methylene blue solution without any C12 solution. Add DI water in the vial to reach the similar final aqueous volume of C12 titration case. Repeat 3rd step. The titrant consumed by blank should be subtracted from the sample titration, as shown in following equation:

$$C_{sample}\left(\frac{mole}{g}\right) = \frac{[V]_{titrant}(mL) - V_{blank}(mL)) \cdot C_{titrant}\left(\frac{mole}{mL}\right)}{m_{sample}(g)}$$

Each sample should be titrated three times with different amount. The plot: C12 amount vs. SDES volume should be linear. The R^2 of the linear regression should be greater than 0.9. The C12 sample concentration can be calculated from the slope of the linear regression and SDES titrant concentration, as shown in **Figure 2-15**.

2.3.3.2. Titration Results of C12

C12 is not water soluble at original pH. So, acetic acid is used to adjust the pH. C12 samples and SDES Titrant concentration used in this report are listed in **Table 2-iv**.

Table 2-iv: C12 samples and SDES titrant concentration

Surfactant Name	Surfactant mass / g	DI water / g	Acetic Acid /g	Theoretical wt% (Surfactant mass/totall mass)	pH
C12	0.125	46.8935	0.033	0.266%	4.91
C12	0.170	45.695	0.033	0.371%	5.31
C12	0.229	46.456	0.036	0.463%	5.71
SDES		SDES Concentration: 1.018 mM			

Take 0.266% C12 sample as an example to show the titration plot: surfactant mass vs. titrant volume and the calculation of C12 concentration, as

shown in **Figure 2-15**.

The titration results are shown in **Table 2-v**.
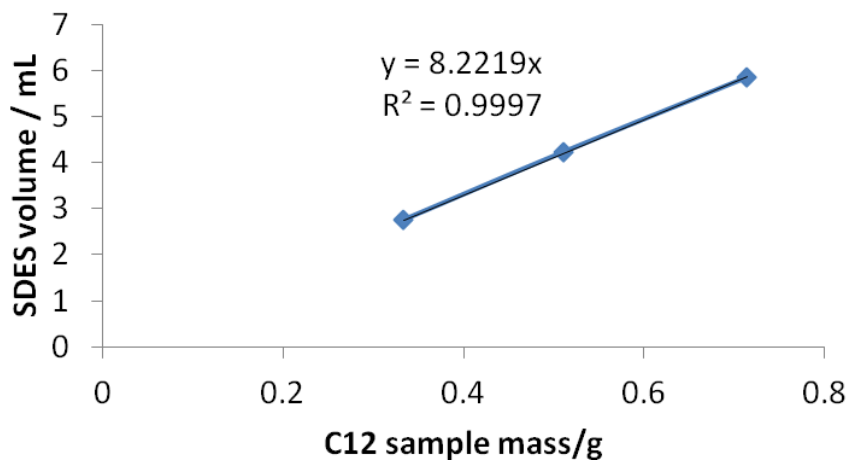
Figure 2-15: The titration plot: C12 sample mass vs. SDES volume. The C12 sample concentration=slope (8.2219 mL/g)xSDES concentration ($1.018x10^{-6}$ mol/mL)=$8.370x10^{-6}$ mol/g.

Table 2-v: Titration Results of C12 samples

C12 Theoretical wt% (Surfactant mass/totall mass)	Titrated Mole Concentration/ mol/g	Titrated wt% (mole Conc. x molecular weight)
0.266%	$8.370x10^{-6}$	0.241%
0.371%	$1.167x10^{-5}$	0.336%
0.463%	$1.564x10^{-5}$	0.450%

Draw the plot theoretical wt% vs. titrated wt%, the slope should be the activity (91.02%) of the C12 commercial product , as shown in **Figure 2-16**.
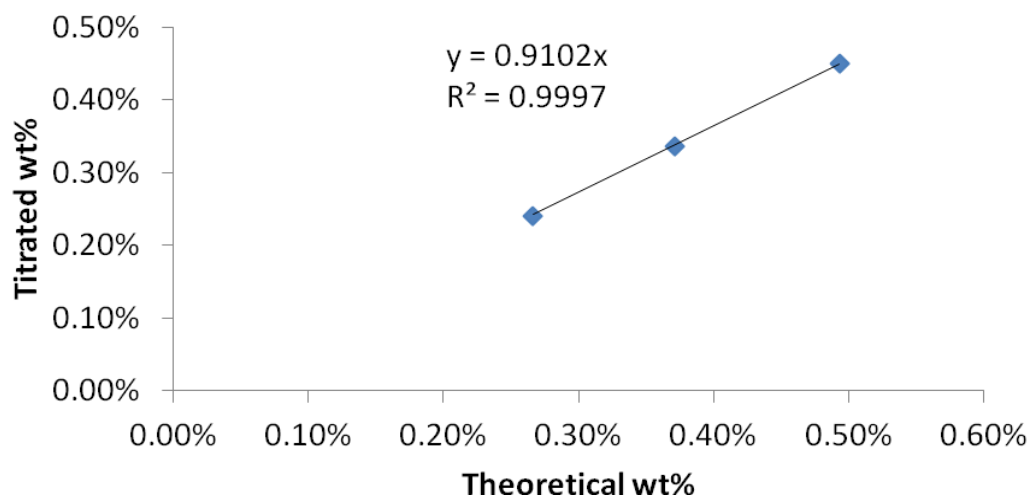
Figure 2-16: *The plot: theoretical wt% vs. Titrated wt%. The slope is the activity of C12, 91.02%.*

2.3.3.3. Discussion of Ethomeen C12 Analysis Method

The activity of C12 determined by two-phase titration is much lower than the activity (97%-100%) reported by MSDS. But the activities of C25A and T15 determined by same method is 96.0% and 98.3% respectively, which are very close to the activity (97%-100%) reported in their MSDS. There are several possible reasons for the low activity of C12.

1st reason: the activity reported in MSDS is not correct. The company titrates the total amine number in the surfactants with hydrochloric acid. Their titration method is based on acid-base reaction. If the surfactant contains other amine except C12, the activity will be over-estimated.

2nd reason: the average molecular weight of C12 is higher than 288 g/mol. The coco group is a mixture from C6 to C18, where C12 and C14 are the main components. The company reports that the weighted average molecular weight of C12 from C6 to C18 is 288 g/mol. But from the HPLC analysis, there are fewer peaks than expected, as shown in **Figure 2-17**. If the first highest

peak is the main component C12, the components from C6 to C10 don't exist in C12 solution. The weighted average molecular weight from C12 to C18 is 320 g/mol. The activity with the new molecular weight is around 100%, as shown in **Figure 2-18**.
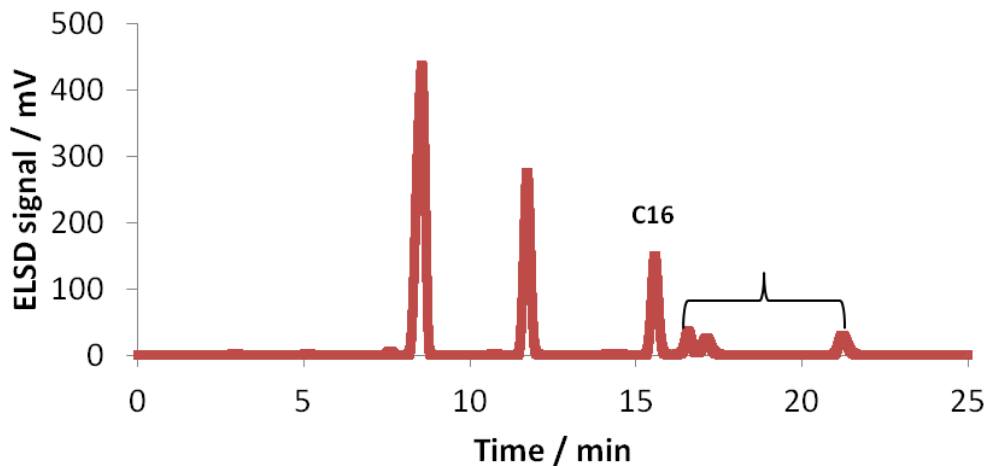
Figure 2-17: *HPLC analysis of 1% C12 at pH=4.*
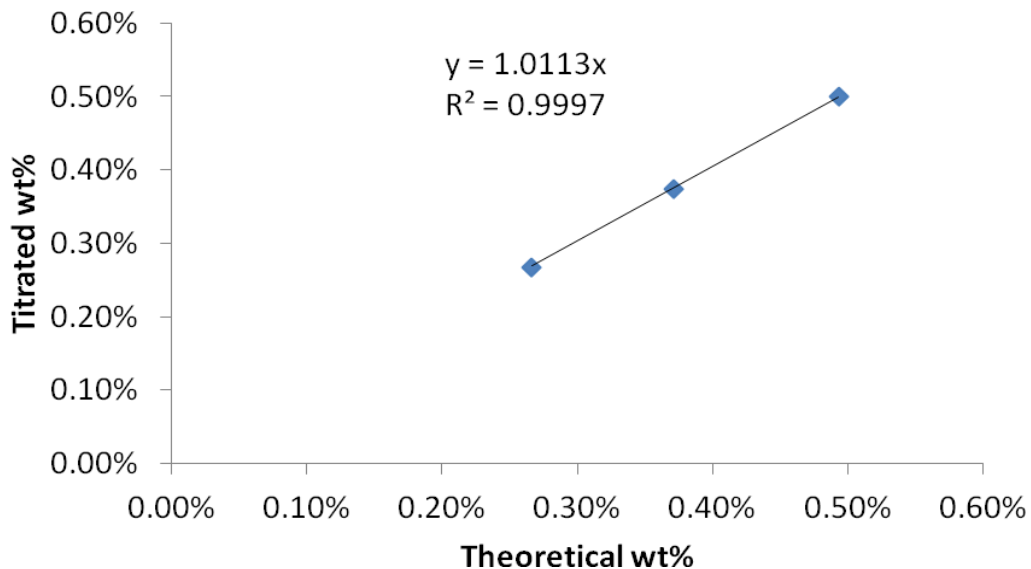
Figure 2-18: *the activity of C12 (101%) with new average molecular weight, 320 g/mol.*

3rd reason: Some components in C12 can't be titrated. If some active materials

in C12 can't form ion-pairs with SDES titrant, the titrated concentration should be less than real value. Thus, the calculated titrated wt% is less than the value reported by MSDS. Another analytical method should be found to verify our titration results. Elemental combustion analysis can get the C, H, O and N weight percentages in the sample. The apparent molecular formulation can be inferred from these weight percentages.

2.3.4. C12 Adsorption Test

2.3.4.1. New Procedure for the Adsorption Test under two atmosphere CO_2

The cloud points of C12 in DI water at original pH are lower than room temperature. Thus, the adsorption of C12 at original pH should be abnormally high (Verkruyse 1985). But at pH ≤ 6, the cloud point of C12 can be raised much higher than room temperature. In reservoir conditions, the solution pH should be around 4.

In order to get reasonable adsorption, the pH of surfactant solution should be reduced to at least 6. Acids, such as acetic acid and HCl, can't directly add into surfactant solution, because the acid can react with carbonate sands. Based on simulation results, two atmosphere partial pressure of CO_2 can maintain pH lower than 6 after equilibrium with carbonate sands in DI. Thus, a new procedure with two atmosphere CO_2 is developed.

2.3.4.2. Procedure of Ethomeen C12 Solution Preparation

Step 1.1 Add certain amount of C12 and DI water in a storage bottle

Step 1.2 Inject CO_2 above the water surface for 1 minute to dissolve C12; seal the cap and mix by hand vigorously for 0.5 minutes. Repeat this step until the pH is lower than 6.

Step 1.3 Stir the solution overnight, until the solution becomes clear. Repeat CO_2 injection step if the solution is still hazy.

Step 1.4 Take the supernatant and measure the concentration by two-phase

titration with Methylene blue solution (colorless endpoint).

2.3.4.3. Procedure of Ethomeen C12 Adsorption Tests

Step 2.1 Add certain amount of surfactant solution whose concentration has been known and dolomite powder or calcite powder into a pressure cell.

Step 2.2 Purge CO_2 into the pressure cell. The air in the pressure cell should be purged out with CO_2. Inject CO_2 into the cell to five atm absolute pressure and then release the pressure to one absolute atm. Repeat above purging process for 5 times. Thus, the volume ratio of air in the cell equals $\frac{1}{3125}$ which is negligible.

Step 2.3 Inject CO_2 to two atm pressure in the cell. Seal the pressure cell and observe the pressure change in the cell. Pressure will slowly decrease because of the dissolution of CO_2 in water and reaction of carbonate and CO_2. Repeat to inject CO_2 till the pressure get stable at two atm and equilibrium is reached.

Step 2.4 Shake the pressure cell by shaking machine for 24 hours.

Step 2.5 Stand the pressure cell for two days, so the sand deposits at the bottom by gravity. Pour the liquid out of cell. Measure the liquid's pH. Centrifuge the liquid by 8000 rpm for 30 minutes and take the supernatant. Measure the pH again.

Step 2.6 Determine the surfactant concentration in supernatant by two-phase titration with Methylene blue solution (colorless endpoint). So, the adsorption can be calculated by mass balance.

2.3.4.4. Adsorption of C12 in DI water

As discussed in section 2, the activity of commercial product of C12 is not 100%. Thus, active materials concentration is used for the adsorption tests and calculation, instead of commercial product concentration.

$$\text{Active material weight percent by titration} = \text{active material mole concentration by titration} \left(\frac{mole}{g}\right) * \text{molecular weight} \left(\frac{g}{mole}\right)$$

The C12 adsorption samples in DI water are listed in **Table 2-vi.**

Table 2-vi: C12 /DI water adsorption test samples

NO.	Sand type	Sand mass (g)	Solution Conc. (mole/g)	Surfactant Soln. Mass (g)
1	Dolomite	10.0205	4.4100E-06	20.0116
2	Dolomite	10.058	4.4100E-06	29.944
3	Dolomite	5.7862	4.4100E-06	33.1307
4	Dolomite	14.044	8.9112E-06	20.092
5	Dolomite	10.116	8.9112E-06	20.714
6	Dolomite	10.03	8.9112E-06	21.824
7	Dolomite	10.423	1.7504E-05	21.497
8	Calcite	11.275	4.4100E-06	19.992

The tests results are listed in **Table 2-vii** and **Figure 2-19**. The samples are arranged and numbered by increasing weight percent, corresponding to the points (from left to right) on the adsorption curve.

Table 2-vii: *C12/DI water adsorption on dolomite and calcite*

Number	Residual wt%	Adsorption (mg/m^2)	Clarity	pH before centrifuge
1	0.05%	1.53	clear	6.67-6.70
2	0.06%	2.16	clear	6.83
3	0.09%	2.47	clear	6.44-6.48
4	0.11%	2.09	clear	6.45-6.51
5	0.15%	2.19	clear	6.48-6.49
6	0.16%	2.15	clear	6.53
7	0.39%	2.42	clear	6.29-6.34
8	0.11%	0.26	clear	--
9	0.23%	0.56	clear	--
10	0.46%	0.61	clear	6.17-6.21
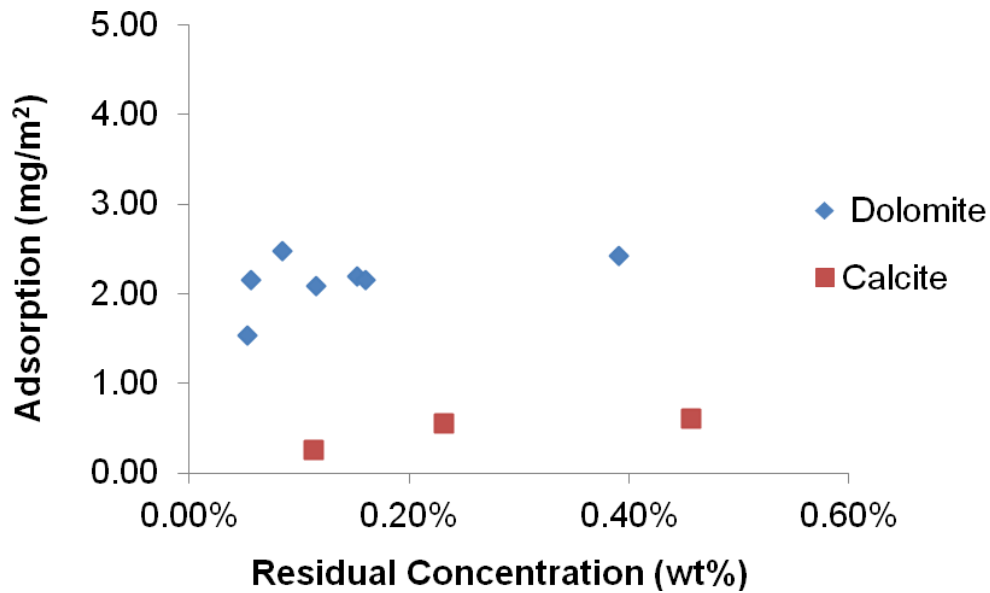
Figure 2-19:. *Adsorption curve of C12/DI water solution on carbonate sand.*

For dolomite, the adsorption values reach a plateau around 0.1% weight percent. After the plateau, the average adsorption on dolomite is 2.21 mg/m^2. For calcite, the adsorption is lower, with an average of 0.47 mg/m^2.

The adsorption on calcite is lower than that on dolomite because dolomite comes from natural source while calcium carbonate is pure chemical; dolomite sand carries impurity, like silica which is negative charges at tested pH. C12 is protonated at low pH and carries positive charge. The impurity in dolomite generates attraction towards C12, which results in higher adsorption on dolomite. Calcite is pure chemical which carries positive charge at tested pH. Thus C12 is repulsed from calcite surface due to the same positive charge, which results in the low adsorption of C12 on calcite.

2.3.4.5. Comparison of Adsorption of C12 and IOS 15-18 in DI Water on Dolomite

Dolomite sand is supposed to carry positive charge when pH < 9. Thus,

the adsorption of anionic surfactant, such as IOS 15-18 should be higher than that of cationic surfactant, such as C12. The adsorption curve of IOS 15-18 in DI water is shown in **Figure 2-20**. The IOS 15-18 adsorption samples are exposed to air rather than CO2 during tests. It is inferred that the adsorption of IOS 15-18 should be even higher if the adsorption samples are exposed to two atmosphere CO^2, because the dolomite surface area carries more positive charge at low pH.

The average adsorption after plateau is 3.18 mg/m^2, which is higher than C12/DI adsorption value (2.21 mg/m^2).
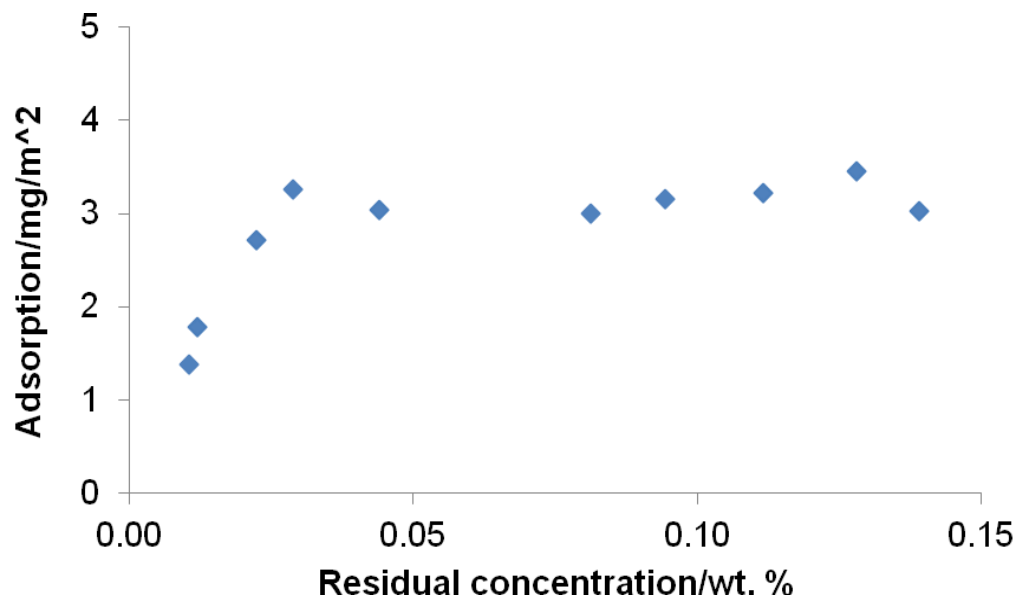
Figure 2-20: *The adsorption curve of IOS 15-18 in DI water exposed to Air.*

Thus, for the carbonate reservoirs, the surfactants which carry positive charge generally have lower adsorption than those surfactants which carry negative charge.

2.3.5. Effect of clay minerals on Ethomeen C12's Adsorption

2.3.5.1. Materials

Silica sand: silica sand from US Silica Company. Trade name is MINUSIL-10 with control #06030211. The BET surface area is 1.16 m^2/g.

Kaolin powder: kaolin powder from Sigma-Aldrich Company. The product number is K7375 with batch #048k0046. The BET surface area is 26.61 m^2/gram.

In order to get reasonable adsorption, the pH of surfactant solution should be reduced to at least 6. Acids, such as acetic acid and HCl, can't directly add into surfactant solution, because the acid can react with carbonate sands. Based on simulation results as shown in **Figure 2-24**, two atmosphere partial pressure of CO_2 can maintain pH lower than 6 after equilibrium with minerals in DI water.
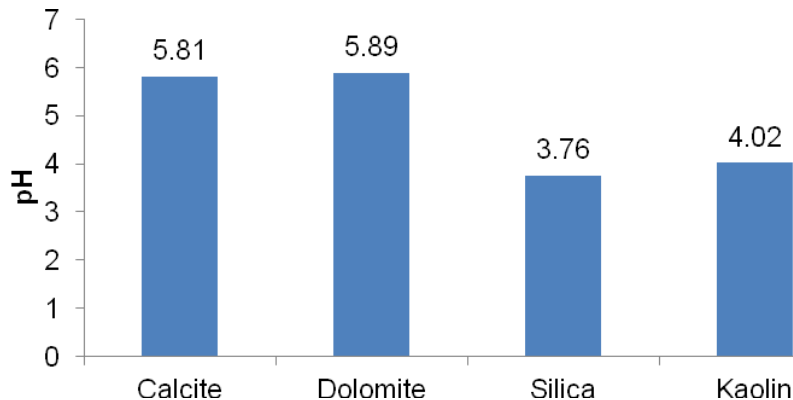
Figure 2-24: pH of DI water equilibrium with minerals under 2 atm CO_2 simulated by PHREEQC software.

The adsorptions of C12 are tested on synthetic calcite, natural dolomite, natural silica and natural kaolin. The adsorption results are shown in **Figure 2-25.**
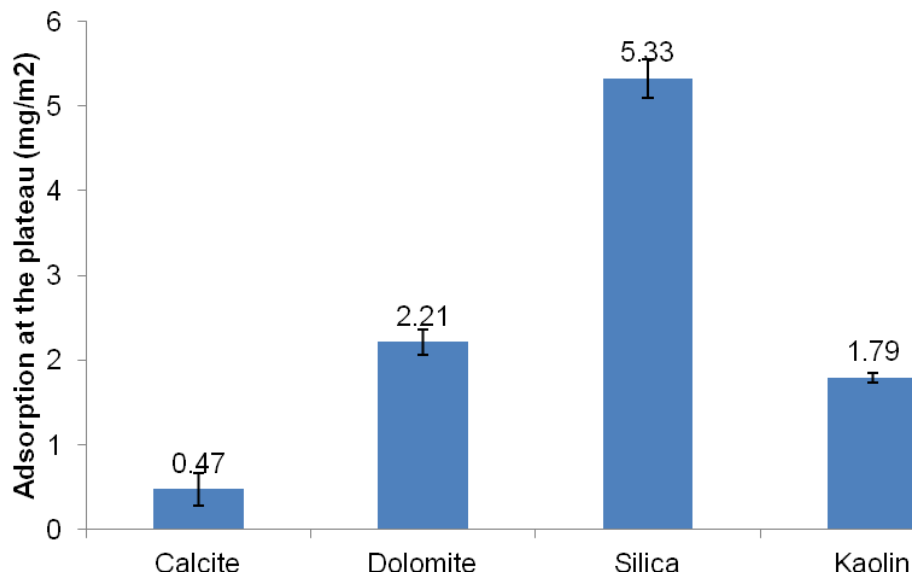
Figure 2-25: *the average adsorption of C12 after reaching the plateau on various minerals*

At pH from 4 to 6, the carbonate surfaces should carry positive charges and silica and kaolin surfaces should carry negative ones. Thus the adsorption of cationic surfactants should be low on carbonate surfaces and high on silica and kaolin surfaces because of the electric repulsion and attraction forces. The adsorption of C12 on synthetic calcite is only 0.47 mg/m^2 and on silica and kaolin surfaces are up to 5.33 and 1.79 mg/m^2 respectively, which follows above electric repulsion and attraction theory. But the adsorption of C12 on natural carbonate mineral (dolomite) is 2.21 mg/m^2, much higher than on calcite, which is against the above theory. That's because the natural dolomite surface carries silica and clay impurity, as shown in **Figure 2-21** and **Figure 2-22**. In **Figure 2-21**, for the synthetic calcite, only Ca exists in the mineral. But for natural dolomite, Si and Al are also found, which means there are silica and clay impurity in natural dolomite. In **Figure 2-22**, the silicon spots are found all over the dolomite surface.
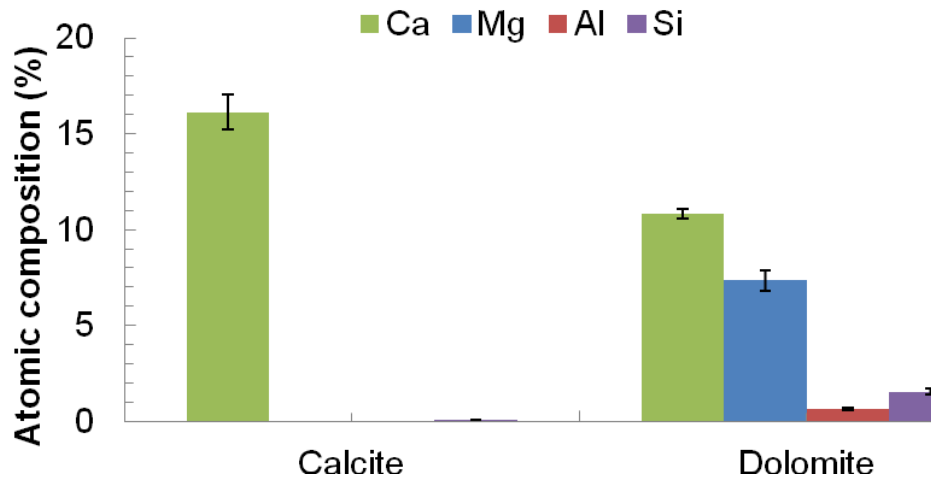
Figure 2-21: *XPS analysis for synthetic calcite and natural dolomite*
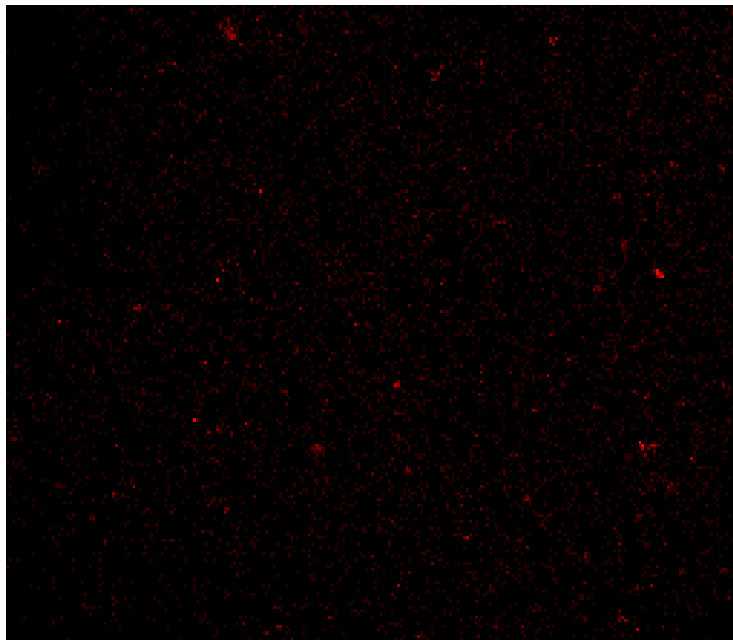
Figure 2-22: *Distribution of silicon on dolomite surface detected by EDAX. (The red spots are silicon)*

2.4. Adsorption of non-ionic surfactants

2.4.1. Materials and methods

SURFONIC® L24-22 Surfactant (L24-22): from Huntsman Co. Alkyl ethoxylated alcohol (m=12~14, n=22 in **Figure 2-26**). The activity is 100%.

Figure 2-23: Chemical structure of SURFONIC® L24-22 Surfactant

NaCl: Sodium Chloride, from J.T. Baker(ACS reagent grade). >=99.0% Assay. Molecule weight is 58.44 g/mol.

KCl: Potassium Chloride, from Sigma Aldrich (ACS reagent grade). 99.0~100.5% Assay. Molecule weight is 74.56 g/mol.

CaCl2·2H2O: Calcium Chloride Dihydrate, from EMD Chemicals (GR ACS grade). 99.0~102.0% Assay. Molecule weight is 147.01 g/mol.

MgCl2·6H2O: Magnesium Chloride Hexahydrate, from EMD Chemicals (GR ACS grade). 99.0~101.0% Assay. Molecule weight is 203.30 g/mol.

KHP: Potassium hydrogen phthalate, from Sigma Aldrich. >=99.95% Assay. Molecular Weight is 204.22 g/mol.

Figure 2-26: Ion composition of East Seminole brine

The ion composition of East Seminole(ES) brine was summarized in the Water Analysis Report by Backer Petrolite as shown in **Figure 2-26**. The Strontium, Barium, iron which are below (40mg/L) was neglected when calculating the East Seminole brine composition. The bicarbonate and sulfate anions was replaced by the same ion strength of chloride. The salt composition was calculated based on the ion composition in **Figure 2-26** and summarized in **Table 2-viii**.

Table 2-viii: Composition of East Seminole Brine

NaCl(g/L)	MgCl2·6H2O(g/L)	CaCl2·2H2O(g/L)	KCl(g/L)
30.27	4.88	6.69	0.50

The composition of East Seminole brine used in this report consists of 30.27g/L Sodium Chloride, 4.88g/L Magnesium Chloride Hexahydrate, 6.69g/L Calcium Chloride Dihydrate and 0.50 g/L Potassium Chloride. When investigate the effect of pH on the cloud point of L2422, 10mM potassium

104

hydrogen phthalate buffered ES brine was used (same ion strength as original ES brine).

Table 2-ix: *pH of different solutions at room temperature*

Solution	pH
1* ES brine	6.72
2* ES brine	6.92
10 mM KHP buffered 1*ES brine	3.56
20 mM KHP buffered 2*ES brine	3.38
1% L2422 in DI water	**6.24**
1% L2422 in 1*ES brine	**6.74**
1%L2422 in 10mM KHP buffered 1*ES brine	**3.67**

Note: 2 ES brine means double salinity of ES brine*

Energy-dispersive X-ray spectroscopy (EDS) and Scanning electron microscope (SEM)

The equipment FEI Quanta 400 ESEM FEG was used in this experiment. It has different modes and detectors. The spectrum and composition analysis is from EDS an detector whereas the SEM image is from an SE detector.

BET Surface area

The BET surface areas of dolomite were measured using a surface analyzer based on nitrogen adsorption (Quantachrome instruments Autosorb-3B). Samples are degassed at 200°C at vacuum pressure of 10 mTorr for 24 hours. The temperature of the liquid nitrogen bath, used during the BET test, was kept at 77.4 K, and an equilibrium time of 3 h was given for each point. The reported multi point BET surface area resulted from 11 points in adsorption isotherm.

High Performance Liquid Chromatography (HPLC)

The HPLC system used was purchased from Agilent Company (series 1100). It mainly consists of seven parts, including a solvent cabinet, vacuum degasser, binary pump, auto sampler, column compartment, Diode-Array Detector (DAD) and Evaporating Light Scattering Detector (ELSD). In this report, only ELSD detector (Agilent Technologies 1200 Series ELSD) was used to determine the surfactant concentration. The mobile phase consists of water and ACN. The column is a Dionex Acclaim C18 column, 4.6*250mm (Product No. 059149). The temperature of the column is set at 25°C. The temperature of the ELSD is set at 60°C and carrier gas with a purity of 99.995% industrial grade was used. The pressure of the carrier gas is set at 3.5 bar. **Figure 2-27** shows the details of the HPLC system.
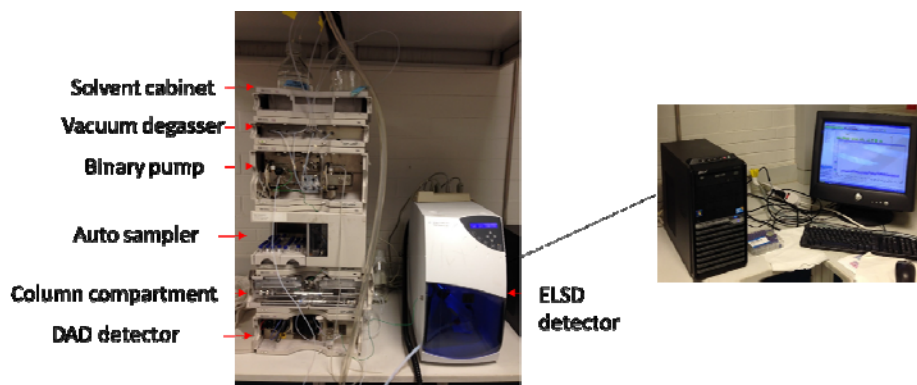
Figure 2-27: Setup of High Performance Liquid Chromatography

Adsorption test

For the adsorption test, a certain amount of surfactant solution and dolomite materials was mixed in a 50ml centrifuge tube and then was placed in the orbit shaker for at least 12 hours shaking. After that, the surfactant solution and dolomite mixture was centrifuged at 3000r/min for 30 min. The supernatant was used for HPLC analysis after filtered through a 0.22μm filter (filter should be wetted and saturated by sample first).

The adsorption could be calculated by the following equation,

$$\Gamma = (c_i - c_e) * \frac{M_{surf}}{M_{abs}\,c_s} * 10^1$$

Γ: Adsorption amount (mg/m^2)

c_i: Initial concentration of surfactant (wt%)

c_e: Equilibrium concentration of surfactant (wt%)

M_{surf}: Mass of surfactant solution (g)

M_{abs}: Mass of absorbent (g)

c_s: BET surface area (m^2/g)

2.4.2. Cloud point analysis

In order to ensure that the L2422 surfactant solution is clear under reservoir brine and temperature conditions, the cloud point test was conducted. First, 2ml samples was injected in to a glass vial (Fisherbrand, 5ml) and was sealed by flame. And then was put into a glass bottle with silicone oil inside as shown in **Figure 2-28**. Last, the sample was set into the heating box at a certain temperature.

95°C	**100°C**	**105°C**	**110°C**
115°C	**120°C**	**125°C**	**130°C**
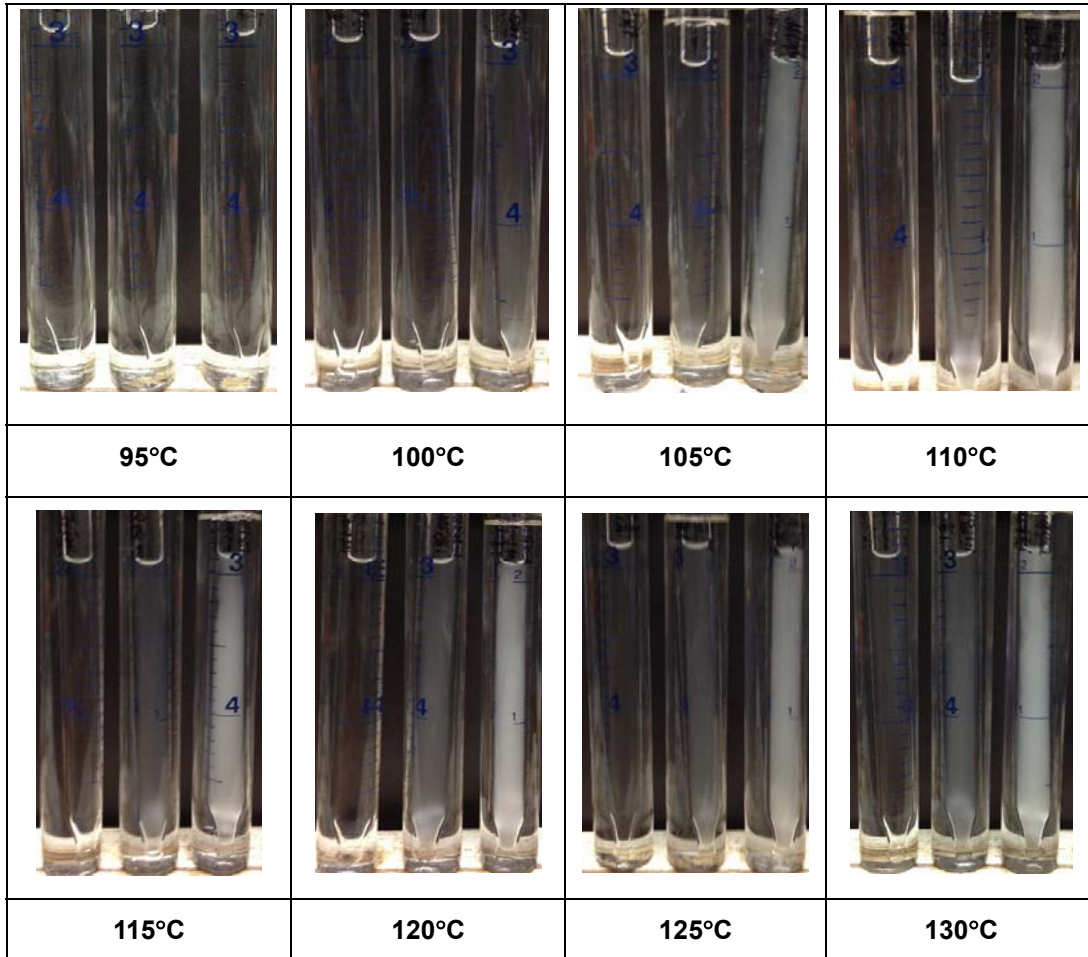
Figure 2-28: *Cloud point test of L2422*

Cloud point of 1% L2422 in different solutions
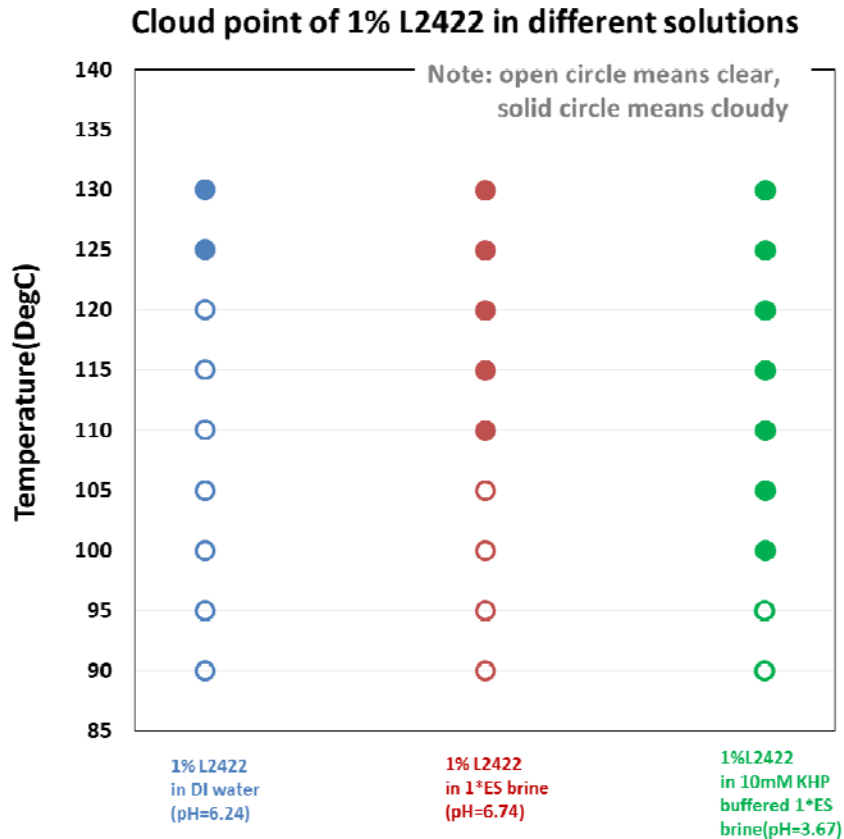
Figure 2-29: *Cloud point in different solutions*

From the cloud point test as shown in **Figure 2-28** and **Figure 2-29**, it could be found that the salinity has influence of decreasing the cloud point. The cloud point of 1wt% L2422 in DI water was about 125°C. However, the cloud point of 1wt% L2422 in ES Brine is only about 110°C. The solubility of L2422 in water highly depends on the hydrogen bond between the oxygen atom of EO group and water molecules. The salt weaken the hydrogen bond which caused the decrease of cloud point in brine conditions. The cloud point of 1wt% L2422 in KHP buffered ES brine is 100°C which is also lower than that (125°C) in ES Brine.

109

2.4.3. Silurian dolomite analysis
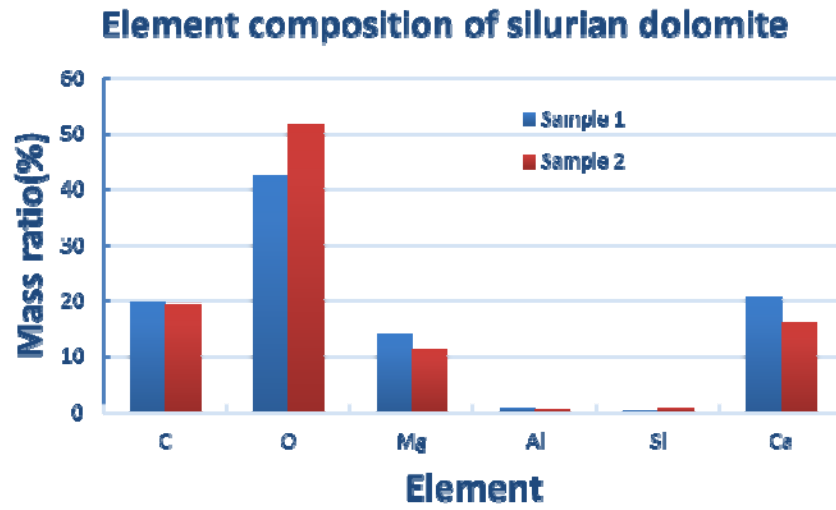
Figure 2-30: *Element composition of the dolomite*
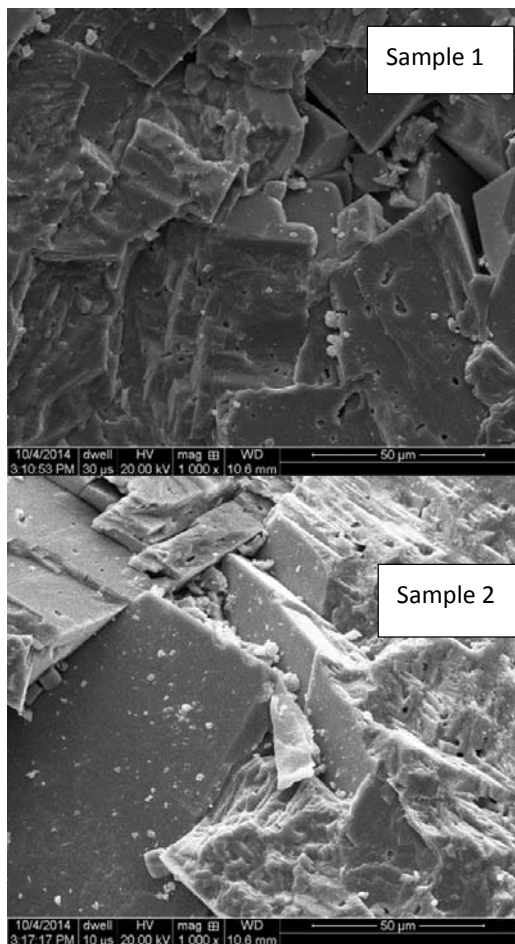
Figure 2-31: SEM of Silurian dolomite

EDS and SEM characterization of the Silurian dolomite are shown in **Figure**

2-30 and **Figure 2-31** respectively. Two sample pieces was used in the characterization. For sample 1, the composition was $Ca_{0.51}Mg_{0.58}C_{1.64}O_{2.65}$ and for sample 2 the composition was $Ca_{0.67}Mg_{0.46}C_{1.61}O_{3.23}$ which are typical element composition of dolomite.

2.4.4. L24-22 surfactant adsorption in DI water
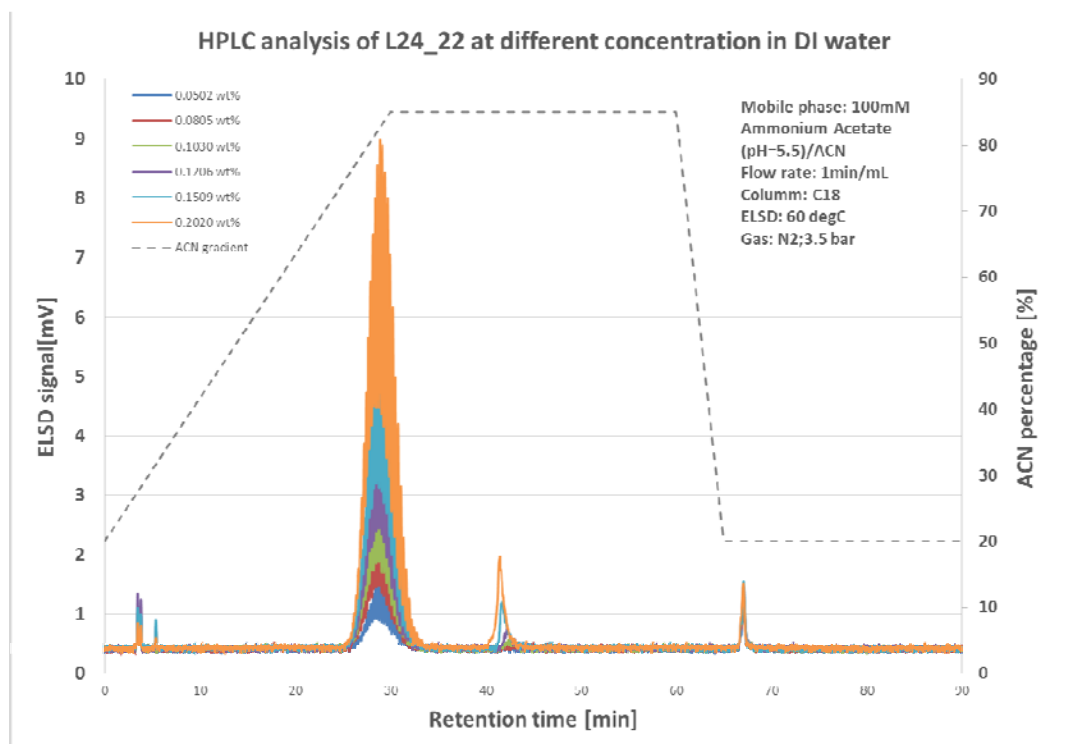
Figure 2-32: *HPLC analysis of L24_22 at different concentration in DI water*

Before doing adsorption experiment, a series of concentration of L24_22 in DI water was prepared and analyzed by HPLC. The mobile phase consists of 100mM Ammonium Acetate(pH=5.5) and ACN. The percentage of ACN is 20% at first and was gradually increased to 85% at 30 min and then was kept at 85% from 30min to 60min and gradually decreased to 20% at 65min and then kept at 20% as shown in **Figure 2-32**. The flow rate of total mobile phase is 1 ml/min. The ELSD was set at 60 °C and the injection pressure of N_2 was kept at 3.5 bar. The amount of sample injection for all experiment below is 50 μL. In **Figure**

2-32, the chromatography clearly shows the chromatographic separation of different components of the surfactant. As here an inversed phase chromatography was used, the more hydrophobic the component, the longer retention time. The first small peak may be the salt or alcohol left in the surfactant. The main two peaks collection(25min~45min) are the active components in the surfactant compound which is typically C12(EO)n for the first peak collection with retention time from 25min to 35 min and C14(EO)n for the second peak collection from 35min to 45min. The peak after 65min is assumed to be some hydrophilic components left in the column which is not surfactant.
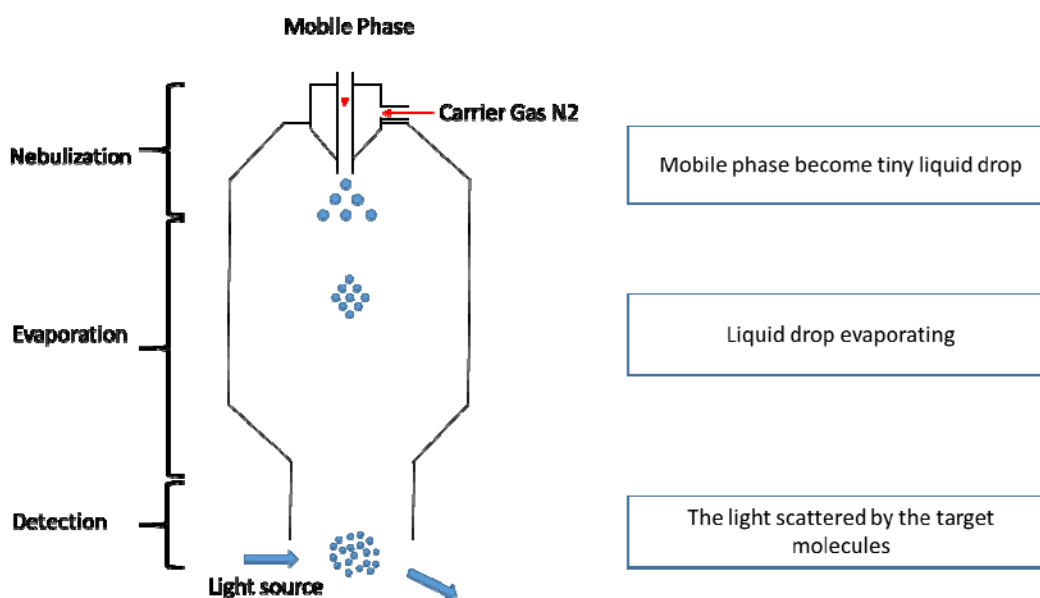
Figure 2-33: *Schematic diagram of ELSD detector*

The principle of ELSD detector is shown in **Figure 2-33**. The mobile phase was sent by the carrier nitrogen gas into the nebulizer and part of the mobile phase become tiny liquid drops and then liquid drops are sent to the drift tube and evaporate. Then the molecules was detected by the light source. The logarithm of intensity of the scattering light versus logarithm of mass of particles provides a linear response. In this report, the calibration curve based on a log10-log10 scale as shown in **Figure 2-34** is in good linear relationship. This

calibration line was used to calculate the concentration after adsorption.
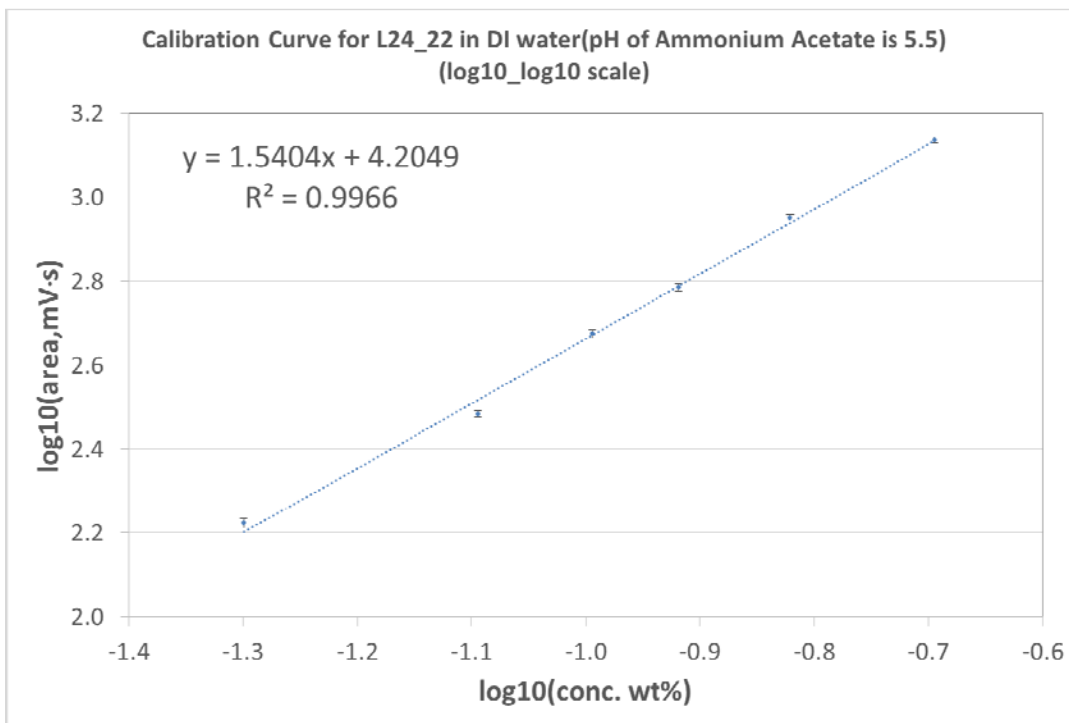
Figure 2-34: Calibration curve of L24_22 in DI water based on log10_log10 scale

Table 2-35: Properties of absorbent

Absorbent	Size	BET Surface area(m^2/g)
Silurian dolomite	6~9 mesh	0.33
Silurian dolomite	140~200 mesh	0.95

The basic properties including the size and BET surface area of the absorbent are summarized in **Table 2-35**. The absorbent pieces or particles were made from Silurian dolomite cores with diameters of 1.5 inch and length of 3 inches.   A ceramic mortar and pestle were used to crush the limestone cores into small pieces or powders. The BET surface area of 140~200 mesh Silurian dolomite is about three times that of 6~9 mesh ones.
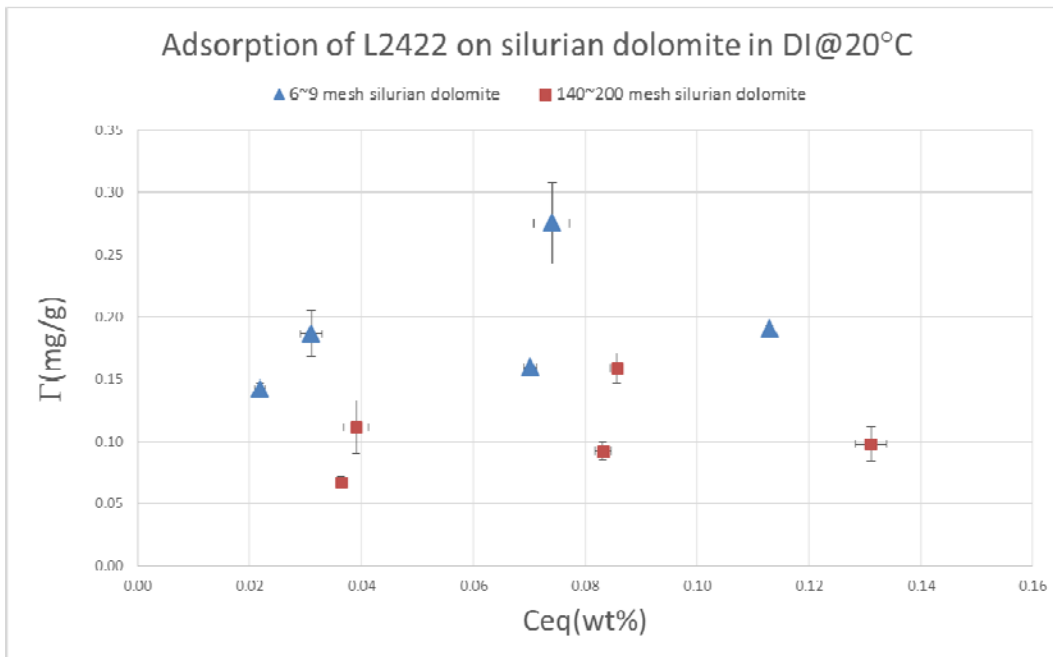
Figure 2-36: *Adsorption(mg/g) of L2422 on Silurian dolomite in DI water at 20°C*
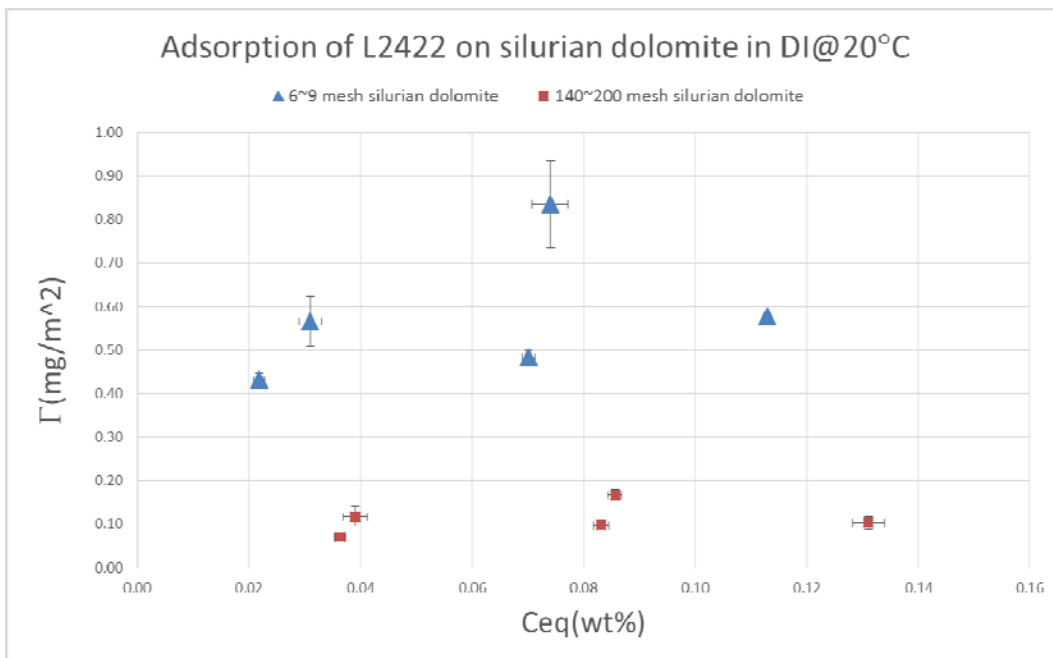
Figure 2-37: *Adsorption(mg/m^2) of L2422 on Silurian dolomite in DI water at 20°C*

For the adsorption test, the absorbent and surfactant solutions was put together in a 50ml plastic centrifuge tube and was shaken in an orbit shaker for

24 hours. Three times of HPLC analysis was taken for each sample. From **Figure 2-36**, the average equilibrium adsorption for 6/9 mesh and 140/200 mesh Silurian dolomite is about 0.18mg/g and 0.10mg/g under DI water condition. The **Figure 2-37** shows the adsorption amount in DI water condition by the expression of mg/m^2.

2.4.5. L24-22 surfactant adsorption in East Seminole Brine
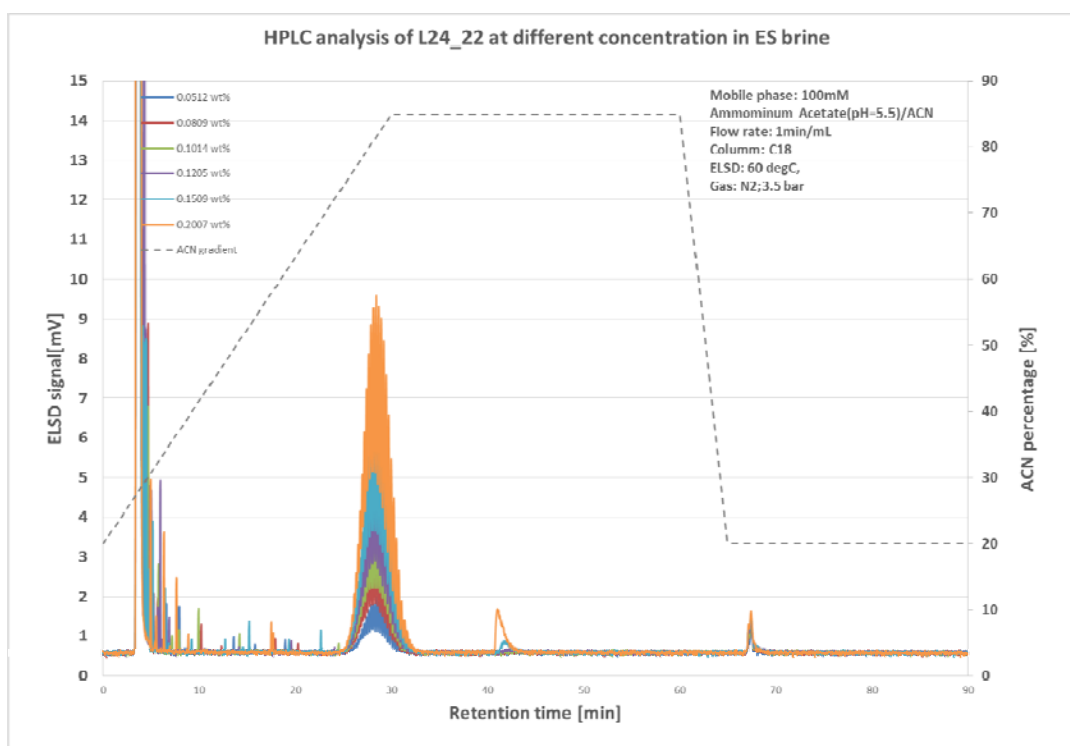
Figure 2-38: HPLC analysis of L24_22 at different concentration in East Seminole Brine

For L24_22 in East Seminole Brine, the ELSD signal are shown in **Figure 2-38**. The salt peaks eluted out first and followed with the two collections of surfactant peaks which are the same as the peaks of surfactant in DI water.
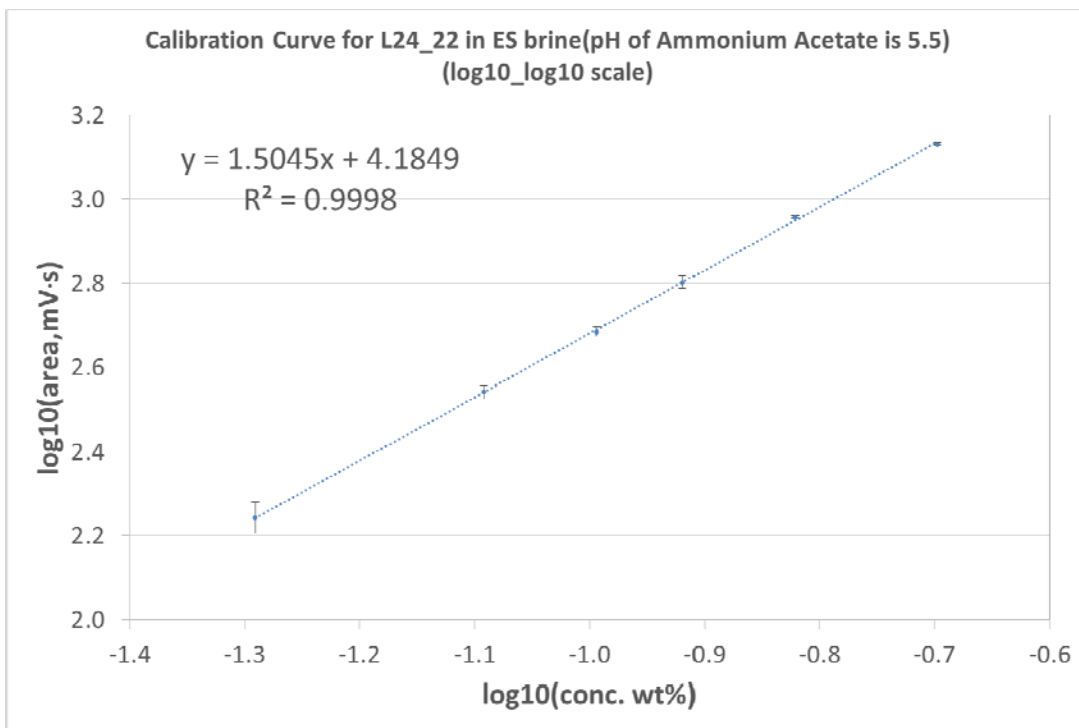
Figure 2-39: *Calibration curve of L24_22 in East Seminole Brine based on log10_log10 scale*
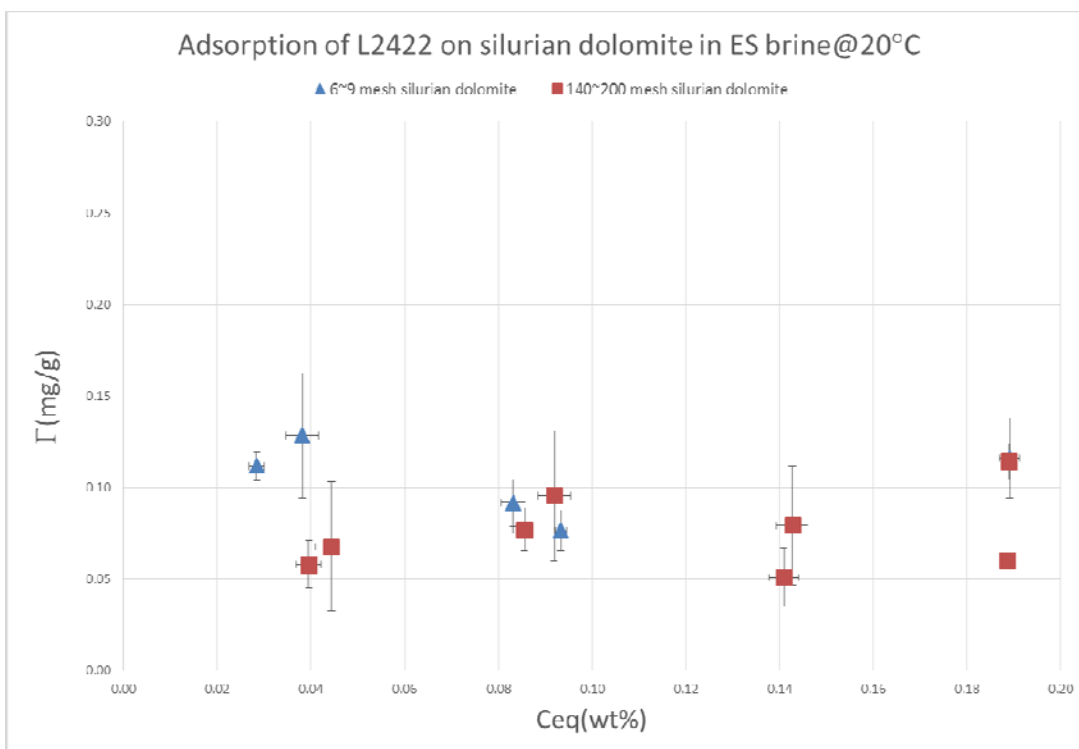
Figure 2-40: *Adsorption of L2422 (mg/g) on Silurian dolomite in East Seminole Brine at 20℃*
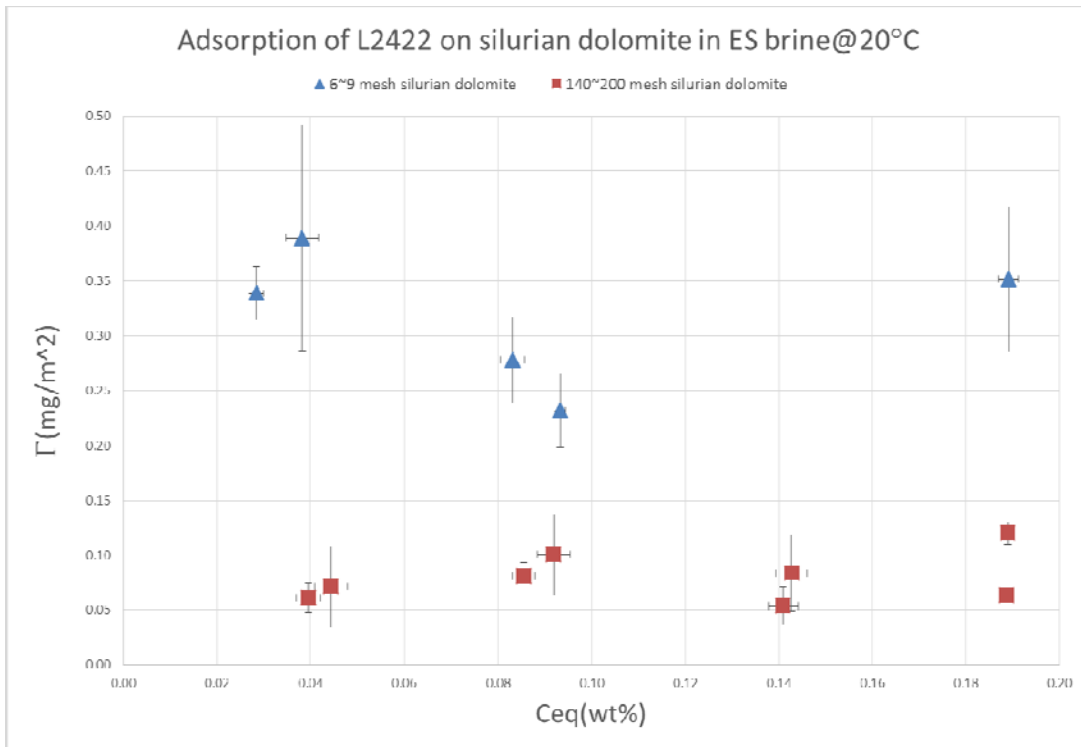
Figure 2-41: Adsorption (mg/m^2) of L2422 on Silurian dolomite in East Seminole Brine at 20℃

From **Figure 2-39**, the calibration curve also gives a good linear relationship for the area and the concentration based on the log10_log10 scale. From **Figure 2-40**, the average equilibrium adsorption amount for 6_9 mesh and 140_200 mesh Silurian dolomite under ES brine condition is about 0.10mg/g and 0.08mg/g which are lower than that in DI condition (0.18mg/g and 0.10mg/g). The **Figure 2-41** shows the adsorption amount in brine condition by the expression of mg/m^2.

2.5. Phase Behavior with ES crude oil

Crude oil from East Seminole field was used in the phase behavior test. The salinity scan was conducted for the 2wt% L24_22 and crude oil. The salinity changing from 1*ES brine to 0(DI water). Different salinities was prepared by different ratio of brine and DI water as shown in **Figure 2-42** and **Figure 2-43**. The total volume of brine and DI water is 0.5ml. Then 0.5ml 4wt% L24_22 (0.5ml) and crude oil (1ml) was injected in to a glass vial (Fisherbrand, 5ml)

and was sealed by flame. So the final surfactant concentration in the aqueous phase is 2wt%. The sample was shaken by hand to mix the crude oil and surfactant solution and then was put into a glass bottle with silicone oil inside. Then the sample was shaken and rotated [3] for 24hours and then was set at room temperature for 1 day for phase separation as shown in **Figure 2-42**. After that, the sample was set in a heating box to investigate the phase behavior under reservoir temperature (43°C) as shown in **Figure 2-43**. The result indicate that the 2wt% L24_22 doesn't have obvious emulsification ability at 20°C and 43°C.

(From Left to right) Brine, 9:1, 8:2, 7:3, 6:4, 5:5 ,4:6 , 3:7, 2:8 , 1:9, DI
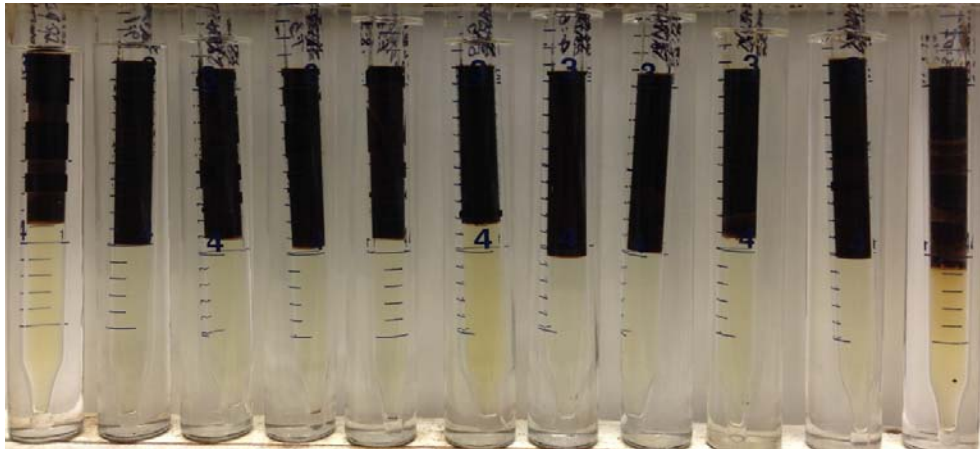
Figure 2-42: *Salinity scan of phase behavior for 2% L2422 under 20°C(after 1 day setting)*

(From Left to right) Brine, 9:1, 8:2, 7:3, 6:4, 5:5 ,4:6 , 3:7, 2:8 , 1:9, DI
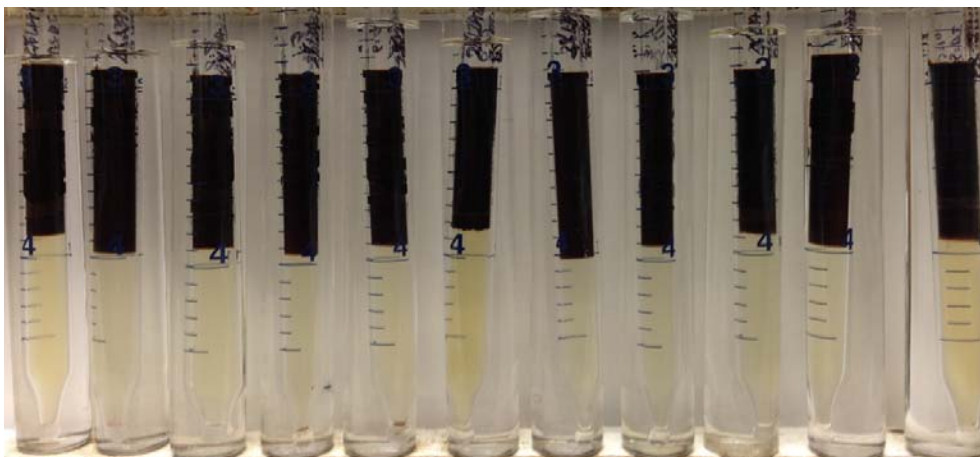
Figure 2-43: *Salinity scan of phase behavior for 2% L2422 under 43°C(after 4 days setting)*

2.6. Foam transport in microflow models

2.6.1. MATERIALS AND METHODS

We designed a PDMS-based micromodel to mimic heterogeneous porous media, as shown in **Figure 2-44**. The foam generator worked by injecting surfactant solution and air such that the surfactant solution pinched off the air to form bubbles, or foam. The heterogeneous porous medium contained a high permeable region with a larger grain radius, 150 μm, and pore throat, 60 μm, than the low permeability region, which had a grain radius of 50 μm and a pore throat of 20 μm. Both regions had the same porosity, 45.0%. The heterogeneous porous medium was the region of interest in investigating the foam flow.
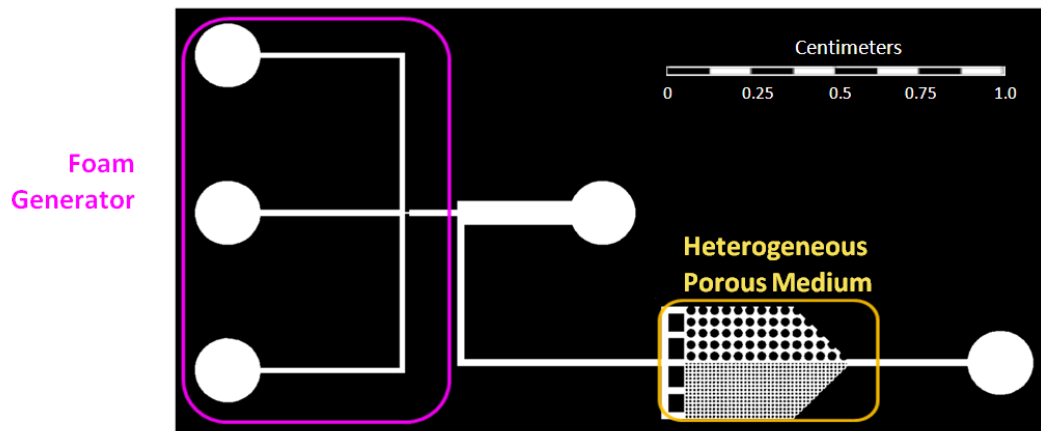
Figure 2-44: Design of the micromodel to mimic heterogeneous porous media.

To operate the micromodel, syringe pumps are used with tubing attached to the device. First dye is injected until the porous medium is completely saturated. Then surfactant solution (0.2% Mackam CB-35, Rhodia) and gas (air) are injected to generate bubbles. Once the bubbles are generated at a steady rate, the outflow end is tied to redirect the bubbles into the porous medium.

119

2.6.2. In-situ fluid distribution and foam generation without fracture

Following the above process, we took videos of the porous medium for 70% gas/30% surfactant injection, 80% gas/20% surfactant injection, 90% gas/10% surfactant injection, and 100% gas injection. For each of these fractional flows, the total flow rate (gas and surfactant) was set at a constant 5 mL/hr. The images from these videos were processed using MATLAB. We found that the 100% air injection resulted in a continuous gas phase that only entered the high permeable region of the heterogeneous porous medium, and the 70% gas/30% surfactant produced relatively small bubbles that did not effectively displace the aqueous phase in either the high permeable or low permeable regions. The 80% gas/20% surfactant injection and 90% gas/10% surfactant injection both demonstrated effective displacements in the high and low permeable regions, with the 90% gas/10% surfactant getting better results particularly in the low permeability region **(see Figure 2-44)**.
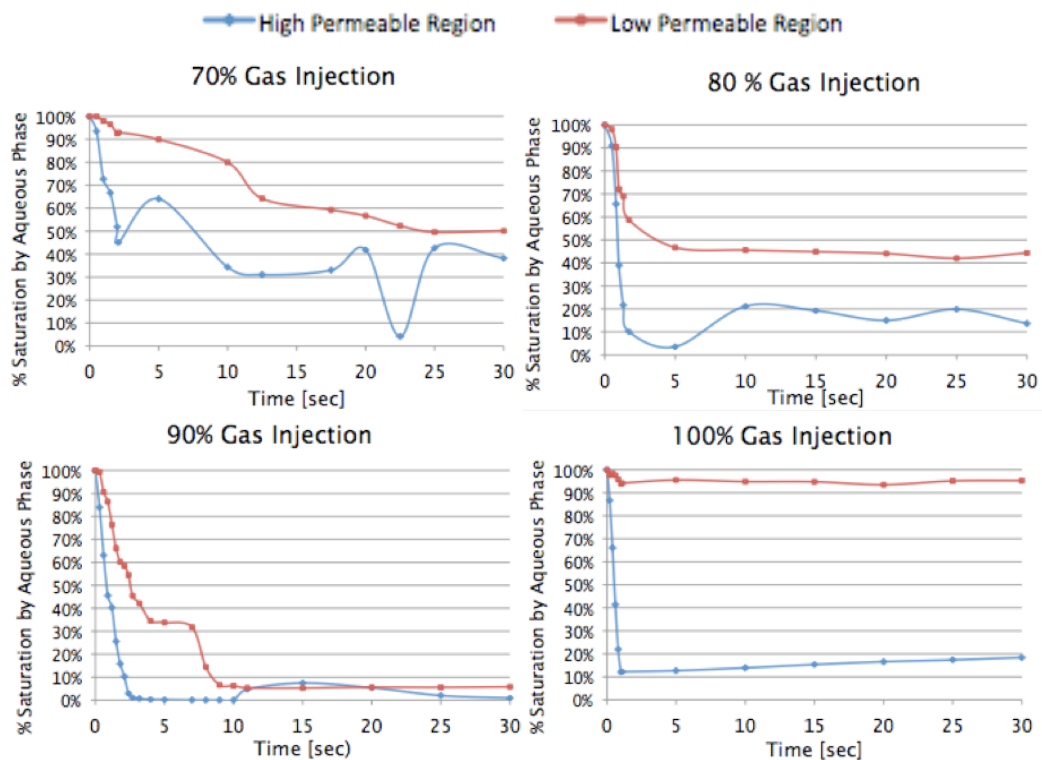
Figure 2-45: Displacement profiles with different gas fractional flow. The total flow rate (gas and surfactant) was set at a constant 5 mL/hr.

The results can also be compared by processing the images at gas breakthrough, when the first bubble exits the porous medium (see **Figures 2-46 and 2-47**). From **Figures 2-46 and 2-47**, we found similar results as with the displacement profiles: the 90% gas/10% surfactant solution combination had the greatest sweep, particularly in the low permeable region.

70% Gas/ 30% Surfactant
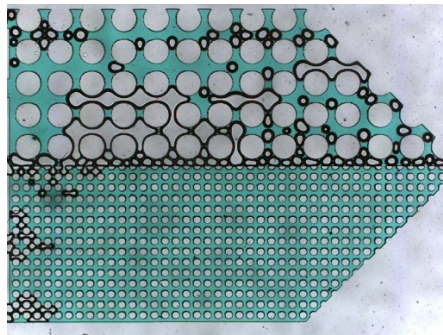
80% Gas/ 20% Surfactant
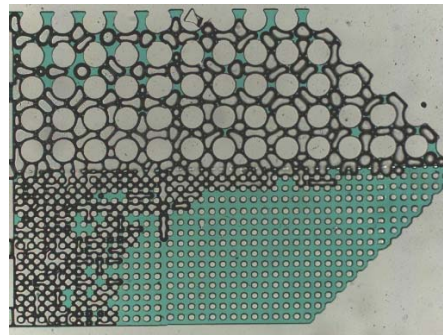
90% Gas/ 10% Surfactant
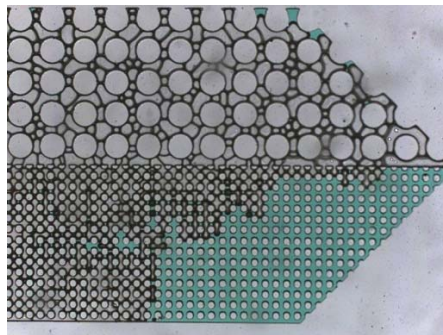
100% Gas
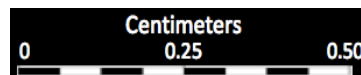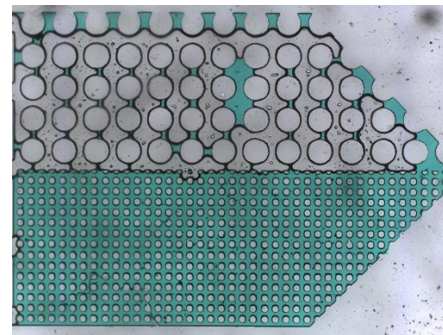
Figure 2-46: Snapshots of porous media at gas breakthrough.
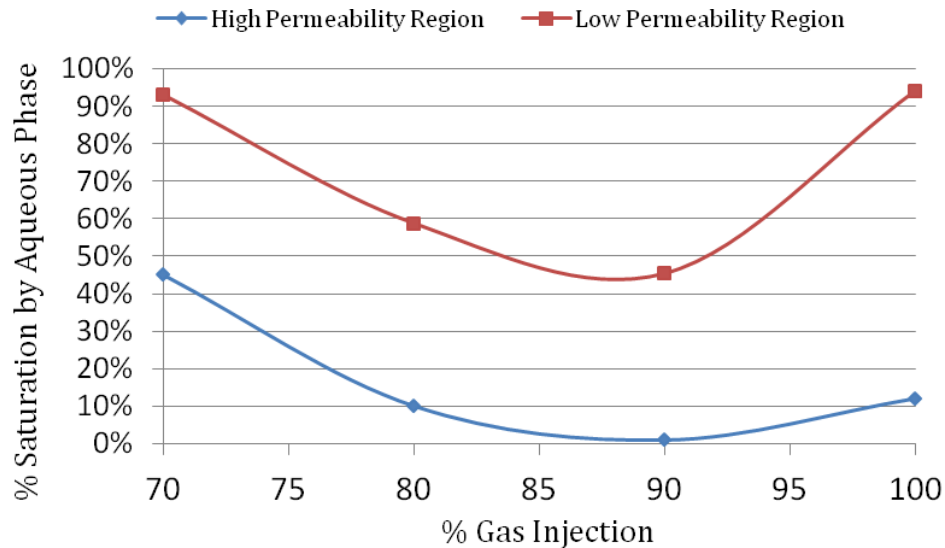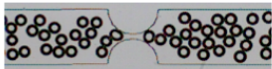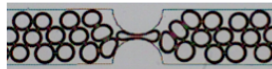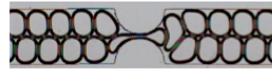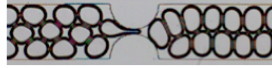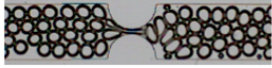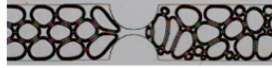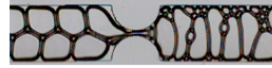
Figure 2-47: *Aqueous saturation at gas breakthrough.*

Based on these preliminary results, pre-generated foam is able to greatly improve sweep in the low permeable region of heterogeneous porous media. An issue in the current experimental setup is instability in the upstream foam generator. When the outflow end is tied to direct bubbles into the porous medium, steady state bubble formation is disturbed and non-uniform bubble size is observed. We will improve our design in the future work.

The behavior observed as the foam flows through the constriction is highly dependent upon the size and arrangement of the bubbles in the microchannel. Thus it is useful to consider the observed behaviors in terms of the bubble size.

It was expected that bubbles would snap-off when flowed through the constriction, but snap-off only occurs in our system under unstable conditions, when the foam is wet with a large bubble size. Instead, the following behaviors are observed as the stable foam passes through the constriction: no change, reorientation, and pinch-off via two newly observed mechanisms. These behaviors for each bubble size are pictured in **Figure 2-48**.

	> 3-bubble	3-bubble	2-bubble
No change			
Reorientation	N/A		
Pinch-off			

Figure 2-48: Categories of the observed behaviors (no change, reorientation, pinch-off) for each of the foam types (> 3-bubble, 3-bubble, and 2-bubble)

No change in the foam upon passing through the constriction is favored for small bubble volumes.   However no change happens at certain conditions, particularly low flow rates, for all types of foam: > 3-bubble, 3-bubble, and 2-bubble, as shown in **Figure 2-48**.

In reorientation, the foam exiting the constriction has a different arrangement than the foam entering the constriction, as shown in **Figure 2-48**. This reorientation via the constriction only occurs for 3-bubble and 2-bubble foams, because the volume of 3-bubble and 2-bubble foams can reach sizes such that upon passing through the constriction 3-bubble foam is reoriented to 2-bubble foam, and 2-bubble foam is reoriented to 1-bubble foam.

In addition, bubbles may break into additional smaller sized bubbles via their interactions with neighboring bubbles upon passing through the constriction.   This bubble breakage is a type of pinch-off, whereby a single bubble stretches and the width of the bubble narrows until that bubble is broken into two disconnected pieces.   The pinch-off we observe occurs via two different newly observed mechanisms: neighbor-wall pinch-off and neighbor-neighbor pinch-off.   Neighbor-wall pinch-off is observed for all categories of bubble size (> 3-bubble, 3-bubble, and 2-bubble), and happens when a bubble is pinched off between the hard surface of the constriction wall and the soft surface of a neighboring bubble, as shown in **Figure 2-49**.
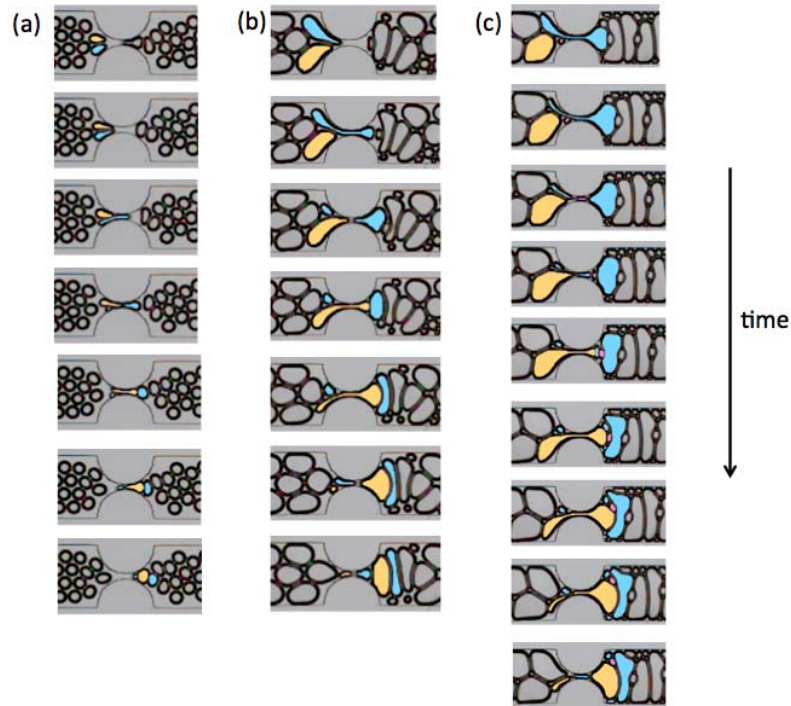
Figure 2-49: *Time series of images for neighbor-wall pinch-off with colors to emphasize contrast in the bubbles of interest. Mechanism of neighbor-wall pinch-off for: (a) > 3-bubble foam, (b) 3-bubble foam, (c) 2-bubble foam. The time interval between images is 61 μs for all cases shown.*

The other mechanism of pinch-off, neighbor-neighbor pinch-off only occurs for 3-bubble and > 3-bubble foam. In this mechanism, as three bubbles attempt to flow through the constriction simultaneously, the two outer bubbles flow into the middle bubble pinching off the middle bubble between their soft bubble surfaces, as shown in **Figure 2-50**. This mechanism requires very high flow rates to create enough shear stress for the soft surfaces of the outer bubbles to pinch-off the middle bubble. In order for neighbor-neighbor pinch-off to arise, three bubbles need to approach the constriction relatively simultaneously.

124
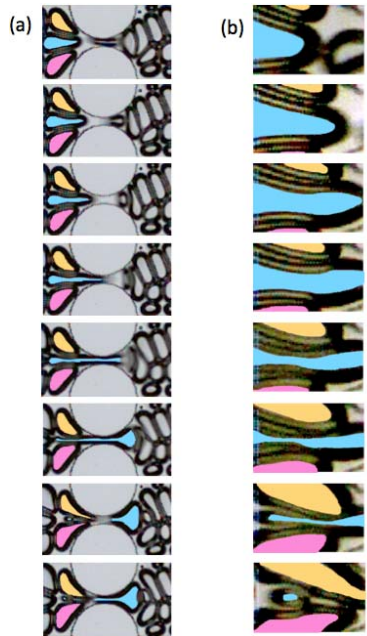
Figure 2-50: *Time series of images for neighbor-neighbor pinch-off with colors to emphasize contrast in the bubbles of interest. (a) Zoomed out view, time interval between images = 22 μs, (b) Zoomed in view, time interval between images = 13 μs,*

2.6.3. In-situ fluid distribution and foam generation with fracture

High-speed microscopy videos highlight tunable bubble generation via a flow-focusing microchannel geometry, bubble stability at the foam-oil interface, and dynamic foam behavior at the pore scale (including both fractures and model porous media). Foam sweep and oil displacement is studied as a function of foam quality, bubble size, surfactant type, and fracture-matrix permeability. Comparisons are made with pure gas and surfactant-free flooding, showing improved sweep and oil mobilization (up to 98% oil-in-place displaced) for foam systems.

Porous media micromodels have been redesigned to improve ease of fabrication, facilitate microscopy viewing, alter pressure drop, and increase permeability contrast between the high- and low-permeable regions and adjacent fracture. Both hexagonally close-packed and square lattice model porous media micromodels have been designed. The pressure field in the micromodel, especially near the entrance, is apparent when looking at the fluid front in relation to the pore channels' orientation. MATLAB code was improved to provide higher quality image processing, increased processing

125

speed, and ability to track bubbles from frame-to-frame.
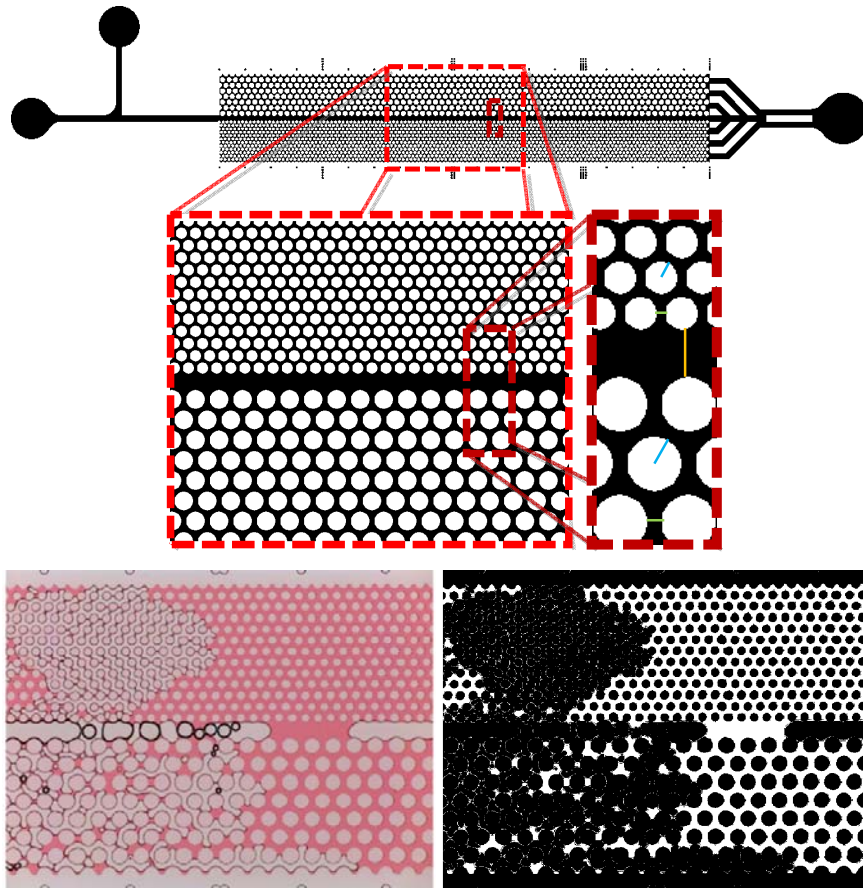
Viscosity and surface tension has been measured for both aqueous and oil phases. Paraffin oil dyed red with Oil Red O is indistinguishable from the stock paraffin oil (25 mN/m surface tension in water and 25 cP). Water and aqueous betaine surfactant solution both behave like pure water (1 cP). The measurements indicate the dimensionless capillary number for this system is directly proportional to fluid velocity. Calculations show flow is indeed laminar at low Reynolds number and surface-tension dominated with small capillary number.

Micromodel experiments included oil displacement via liquid-only, gas-only, and multi-phase (foam) sweeps. The surfactant used was a 1% betaine solution with ~10% NaCl. Experiments indicate several stages of fractured porous media flooding: flooding of the large central fracture, flooding of the high-permeable region, and flooding of the low-permeable region. Capillary

entry pressure is the dominant factor dictating whether gas or surfactant solution enters the porous matrix in foam floods. In some experiments o/w emulsions were visualized in the aqueous phase. Foam coarsening (bubble collapse/coalescence) is observed prior to and during micromodel flooding resulting in typical bubble sizes much larger than the pore throat size.

Comparing foam floods to water-only or surfactant solution-only floods, foam displaces the oil more efficiently, due to a higher established pressure gradient. Foams demonstrate the potential to reduce the volume of surfactant solution needed in EOR floods. We predict higher permeability contrast will result in enhanced phase separation.

2.6.4. Oil recovery foam flood

This work demonstrates improved displacement of paraffinic oil (long chain alkanes) with foam in an oil-wet micromodel with different parallel permeability layers. A rigorous understanding of the mechanisms which govern foam transport in porous media is still incomplete, hence the need for direct visual observation of relevant foam transport and oil displacement phenomena in porous media.
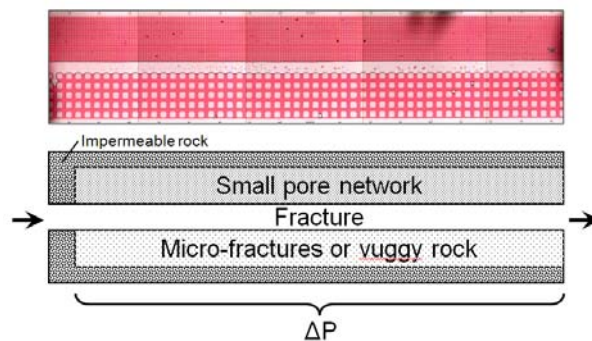
Porous media micromodels in silicon, glass, PDMS, and other polymers, are used to better understand fluid transport at the multi-pore scale. These 2-4 systems allow real-time, in-situ observation of relevant transport. In foam studies, the confined geometry of microfluidic devices allows for well-controlled

foam generation with tunable bubble-size, foam quality (gas fraction), and flow rates/pore-volume throughput.
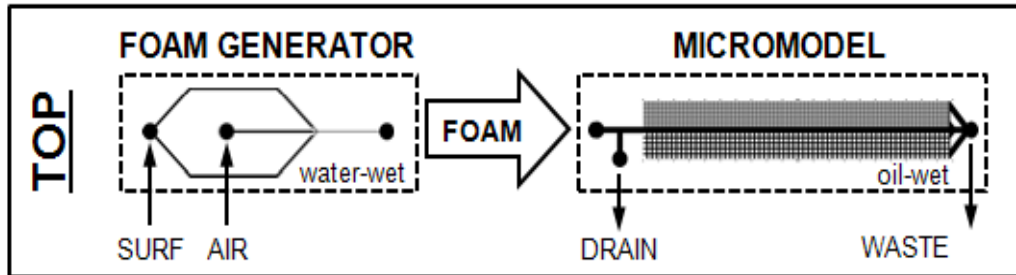
Foam was pre-generated via a flow-focusing microfluidic design which produces monodisperse bubbles in series prior to injection into porous media. Adjusting the supplied fluid flow rates (syringe pump or gas pressure regulator) allows for tunable foam quality and texture (volumetric gas:liquid ratio and bubble size). In a flow-focusing device, gas and surfactant solution is squeezed through an orifice at sufficient shear rates to pinch bubbles off the other side. These bubbles flow single-file to transfer tubing connecting the foam generator and micromodel devices. The diameter, length of tubing, and speed of pre-generated foam is designed so that minimal foam destruction occurs in the transfer tubing.

In this micromodel, the fracture's CEP is governed primarily by the smallest principal pore radius - the channel height (uniformly 50 µm z-dimension across the micromodel). This means the fracture is more akin to a thin slit and bubbles usually have a characteristic diameter larger than the channel height (squished). This makes bubbles easier to visualize and quantify, but comes with the caveat that this system cannot represent a true "bulk" foam as may be found in some large-aperture natural fractures. In the high-perm region the pore-throat gap is about twice the z-dimension, and in the low-perm region the pore-throat gap is about half the z-dimension. Both regions had tapered-corner square grains arrange in a square-lattice. The high- and

128

low-perm regions were designed to maximize the range of CEPs available in a single micromodel considering practical lithographical constraints in fabrication.

Gas and liquid flow rates are set low enough so that pressure drops are representative of those observed in reservoirs, fast enough so that foam does not collapse en route to the micromodel, and with a gas:liquid ratio high enough so that foam does not phase-separate in transfer tubing (liquid is carried along with bubbles in lamellae and does not noticeable drain). Injected fluids included single-phase water (waterflood), surfactant solution (control experiment), single-phase gas (control experiment), water/gas coinjection (analogous to WAG), and foam. We frame the water/gas co-injection as a WAG experiment because even at the microscale air and water would phase-separate into alternating slugs. Literature simulations show WAG injection performance approaches that of co-injection as WAG slug size decreases.

Pressure data was recorded by a Validyne Pressure transducer with a 0-3.2 psi diaphragm. Since trapped bubbles pressure tubing can result in signal lag, pressure tubing and transducer chambers were flushed with paraffin oil until air ceased to exit the bleed valve screw holes, then sealed. Pressure data was recorded via MATLAB script every 0.1 sec for the duration of the experiment. Total pressure drop across the 20 cm micromodel was typically between 0-1.8 psi, with foam floods exhibiting the highest pressure drops.

Oil saturation was determined via image processing of recorded video in MATLAB with the assumption of a 2D fluid system. Each pixel is assumed to represent a single-phase fluid volume (no vertical fluid overlap), with pink pixels representing oil. For each low-perm, high-perm, and fracture section, the fraction of oil present was calculated by dividing the current oil pixel-count by the original oil pixel count when completely oil-saturated (just prior to experimentation). "Pink" pixels representing oil were identified by subtracting the green from the red channel and applying a threshold cutoff. The appropriate threshold value was determined by comparing the original and

129

threshold images to best represent visual interpretation of remaining oil, and varies depending on experimental lighting conditions. Black-and-white images are 3x3 pixel Gaussian-blurred for presentation in figures to reduce single-pixel noise.

Experiments show that water, air, and WAG floods (without foam) were unable to displace oil from the low-permeable zone. Oil saturation was measured over time, with comparisons shown for the waterflood, WAG, and foam cases. Total oil saturation trends were similar to core and sandpack experiments in literature, however these micromodel experiments were able to resolve differences in where produced oil comes from in a heterogeneous system (oil was displaced differently from each permeability zone and depended on the injection strategy used). Compared to other micromodel studies which sweep a surfactant-saturated porous medium, this experiment represents a more realistic oil-saturated, oil-wet system and shows the fluid interactions when foam first contacts trapped oil.

In all experiments, the fracture was swept immediately and completely, as it was the most permeable zone and offered "the path of least resistance". In the waterflood control experiment only oil in the fracture was displaced. In some experiments after the initial waterfront passed through the fracture the trailing water stream would "thin" from the edges of the fracture as oil imbibed due to the micromodel's hydrophobicity (indicated by the increase in fracture oil saturation from 1 to 3 PV for the waterflood case). Spikes in the WAG fracture oil saturation are due to upstream slugs of oil entering the microscope's limited field of view. In general there was no oil in the fracture after the front passed, though oil did occasionally enter the fracture from the matrix as local pressure fluctuated (e.g. just downstream from a slow bubble train in the fracture there is a relatively lower pressure).

The high-perm region has a slightly higher capillary entry pressure than the fracture, and it is the next zone to flood. The capillary entry pressure for the high-perm region must be exceeded to displace any oil, and for the

waterflood experiments this meant relatively high flow rates. The WAG flood streamed gas through the fracture until an occasional slug of water passed through, which could then increase the local pressure high enough to divert fluids into the high-perm matrix. Though this technique ultimately improved the displacement of oil from the high-perm region, it came at the cost of wasting large volumes of injected fluid since water and air would phase-separate into streams which bypassed most of the oil. Lots of leave-behind oil lamellae were observed in the high-perm region.

The low-perm region represented the most-difficult region to sweep, and the most-interesting zone to investigate for EOR applications. In the waterflood control experiment (analogous to secondary recovery) *no* oil was displaced from the low-perm region, even at extremely high flow rates (unrealistic in an actual reservoir except perhaps near the injection well). WAG flooding occasionally pushed into the low-perm region, but was constrained to grids of slightly-wider pores (the result of a lithography overlap defect during fabrication) and the few pores immediately downstream from those defects. This phenomenon illustrates just how sensitive the non-wetting fluid path is to capillary effects – just a marginally wider pore-spacing can allow fluid to stream past trapped oil. Foam injection swept the most oil from the low-perm region, though phase-separation of foam was observed suggesting that the majority of low-perm displacement was by the liquid fraction of the foam. Foam left only 20% oil saturation remaining in the low-perm region after 5 minutes (~4 PV).

Overall, foam was shown to significantly mobilize more oil than both waterflood and gas-flood, consistent with similar micromodel and core studies. Additionally, we demonstrate superior foam performance compared to a water/air co-injection at the same conditions as the foam injection, but without surfactant (WAG analogous).
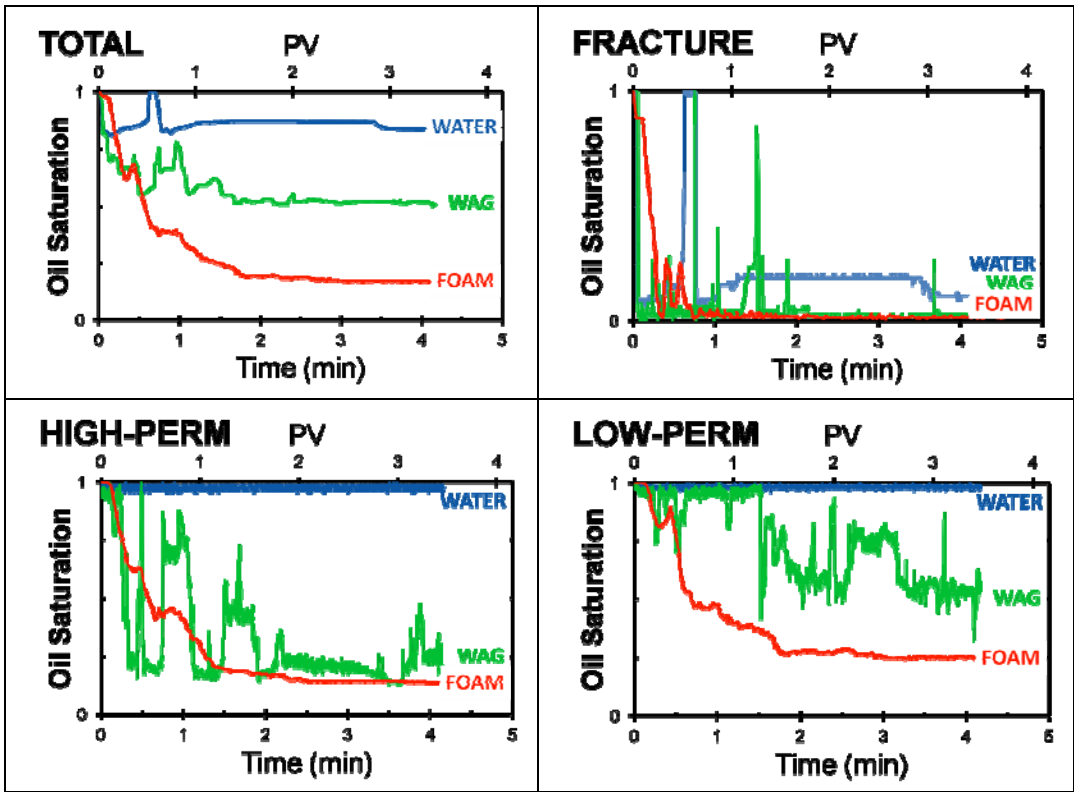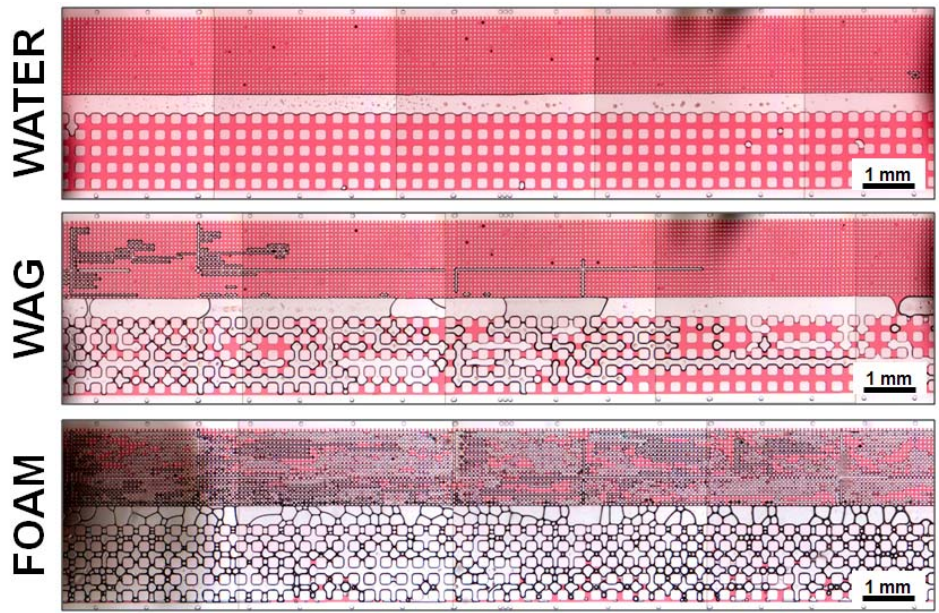
Literature suggests that fluid transport is this micromodel is dominated by the capillary entry pressure (CEP) – the critical pressure drop needed for fluid to move through a constriction (pore):

$$\delta P_C = 2\gamma \left(\frac{1}{R_2} - \frac{1}{R} \right)$$

Where δP_C is the pressure drop across the pore of interest, γ is the displacing fluid-displaced fluid interfacial tension, and R_1 and R_2 are the principal pore radii.

A control experiment with increasing water flow rates (increasing pressure drop across the micromodel) demonstrates critical capillary entry pressures intuitively: as an oil-filled micromodel is injected with water or air, the oil in the fracture is displaced first, followed closely by oil the high-perm region, and finally by oil in the low-perm region at extreme pressure drops. Air floods behaved similarly to water floods but with a higher capillary entry pressure. The sensitivity of fluid flow to capillary entry pressures is emphasized by observation of preferential fluid displacement occurred along a fabrication defect which resulted in lines of slightly wider low-perm region pore-throats in a repeating rectangular grid. Pore-throat size irregularities like this necessitate denoting critical displacement pressures as a range:

	Pore dimension	Measured CEP air	Measured CEP surf
Fracture	380 x 50 µm	<0.01 psi	<0.01 psi
High-perm	105 x 50 µm	0.13 psi	0.02 psi
Low-perm	20 x 50 µm	0.23-0.46 psi	0.03-0.60 psi

Relevant pore dimensions and experimentally measured pressures at which oil began to be displaced from each permeability region.

Foam promotes local pressure fluctuations in regions adjacent to a fracture, so that as bubble-trains in the fracture build up pressure[#], injected fluid can push into the low-perm regions previously inaccessible. Higher local

133

pressure gradients mean more pores' capillary entry pressures are exceeded and ultimately more trapped oil displaced from those pores.
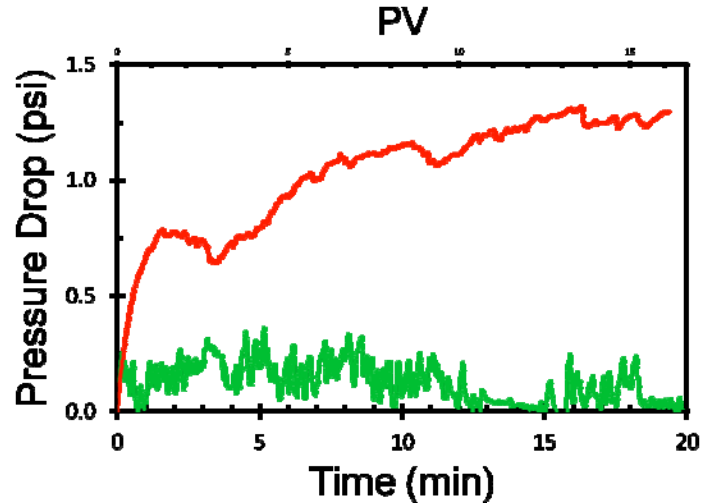
Measured pressure drop across the porous media micromodel for foam in red vs. water and air con-injection without surfactant (WAG) in green. Foam has a higher apparent viscosity than seen with the exact same injection conditions without surfactant.

Pressure drop across the entire micromodel shows increased pressure drop for foam flooding compared to waterflooding, gas flooding, and water-and-gas co-injection without surfactant (WAG). Continuous single-phase fluid spanning both pressure taps, even if flowing at high velocity, displays the lowest pressure drop. In general, the measured pressure drop increases as phase interfaces build up between pressure taps; even in single-phase flooding it is observed that measured pressure spikes when oil cuts into the continuous stream. In foam, gas trapped in bubbles reduces the gas phase relative permeability, and lamellae cause resistance which increases the apparent viscosity. The result is a decrease in mobility ratio, and a more efficient sweep and oil displacement.

A periodic, cyclical pressure behavior develops when long bubbles and small bubbles flow through the fracture: a bubble-train of small bubbles in the fracture increases resistance to flow (apparent gas viscosity) and slows-down the fluid velocity within the fracture to divert fluid just upstream of the bubble train into the matrix. It is here where localized pressure gradients are highest, and where the best chance that the critical capillary entry pressure needed to enter the matrix is offered. Video shows fluid movement in the matrix is often correlated with slow-moving bubble trains in the adjacent fracture.

In this system most oil in the matrix is displaced *through* the matrix (as opposed to being pushed into the fracture), but this may be due to the alignment of the fracture and porous media zones *parallel* to the dominant pressure gradient except at the entrance. Future experiments will address the importance of fracture orientation to pressure gradient when displacing oil.

Foam quality was seen to differ in the high- and low-perm zones. High-perm regions were more gas-rich with surfactant only present in thin lamellae between bubbles. Low-perm regions were more liquid-rich with gas occupying only the most permeable pores. Furthermore, initial sweep of the low-perm region was almost entirely by the surfactant phase and gas seemed to only invade pores previously swept by surfactant. We note two favorable conditions for gas preferring to enter only aqueous-filled pores: the gas-surfactant interfacial tension is lower than the gas-oil interfacial tension, and surfactant adsorption may (slightly) create a more favorable gas-surface contact angle. Near a given pore with a given pressure drop, if both liquid and gas are present (as in foam), the critical capillary entry pressure favors the surfactant solution entering the pore first because the surfactant-oil interfacial tension is much lower than gas-oil. This results in zones with only small pores becoming liquid-rich as gas is immobilized in bubbles that cannot invade the next pore until the local pressure gradient increases. Meanwhile, sub-critical gas-phase entry pressure gradients are sufficient enough to mobilize the liquid phase.

135

At the entrance to the micromodel foam phase-separates, with surfactant solution invading the low-perm zone, then continues through the low-perm region.   It is at this point the pressure gradient from the fracture into the matrix is highest.   Downstream the pressure gradients are parallel to the fracture and there is no driving force into the matrix unless a bubble train generates enough resistance that forces fluid around it (and into the matrix).

PART III- FOAM CORE FLOOD EXPERIMENTS

3.1. Steady-state foam behavior in sandstone

The main objective of steady-state foam coreflood experiments is to identify local-equilibrium foam flow regimes and to evaluate the effect of permeability on foam rheology.

Foam is generated in-situ by co-injection of surfactant and CO2 at different injection rates into a brine-saturated core. A schematic of foam coreflood setup is shown in **Figure 3-1**. It is comprised of three main modules: (a) fluids injection system, (b) coreholder and pressure transducers, and (c) backpressure and effluent collection system.

Fluid injection system. A TELEDYNE ISCO Model 500D syringe pump with maximum working pressure of 5000 psig was used to directly inject brine or surfactant solution into the core. CO2 was displaced into the core by deionized water through a high pressure accumulator that had a piston to separate water from CO2.

Core holder and pressure transducers. A Phoenix Hassler-type core holder was mounted in the vertical direction and fluids were injected from the top to the bottom. Hydraulic oil was used as an overburden fluid, which compressed and sealed the 0.25 inch thick rubber sleeve to assure the axial flow of the injection fluids and to prevent leakage. The core holder had two end caps, and the top one had an adjustable end plug length to accommodate different core lengths. There were five pressure taps along the side of the core holder in the vertical direction, which connected two absolute pressure transducers (channels 1 and 5) and three differential transducers (channels 2, 3 and 4). The differential transducers detected the pressure drops over sections along the core from the top, whose lengths were 2, 4, and 4-inches and denoted as sections 1, 2, and 3 respectively. Note that the pressure drop over a 2-inch section at the bottom was not measured due to a temporarily reduced capacity of our data acquisition system at the time that the core flood experiments were

conducted.

Backpressure regulator (BPR) and effluent collector. Two BPRs were used in a series to maintain a constant backpressure of 1500 psig during coreflooding. The first BPR was placed immediately at the outlet of the core holder and was set to 1500 psig and the second BPR was set at 1100 psig. The purpose of the second BBR was to prevent an undesired flash of $CO2$ immediately downstream from the first BBR as it could reduce the pressure control robustness of the first BBR.

Core preparation. The core was cleaned and dried in a convection oven at 110 °C for 48 hours. It was then wrapped in three layers of aluminum foil and a thin Teflon heat shrink tube. The wrapped core was placed in the core holder and vacuumed for 10 hours before saturating the core with brine in order to measure its porosity. The permeability of the brine saturated core was determined based on Darcy's law.
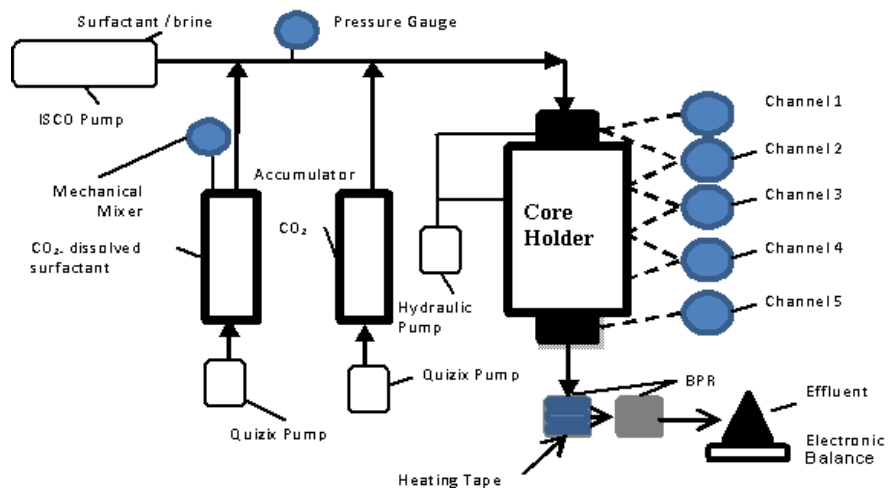
Figure 3-1: *Schematic of experimental setup for core flooding.*

Steady state foam core floods were performed on two separate cores that are different in permeability. Berea sandstone cores were used in all core floods. The core properties are shown in **Table 3-i.** Industrial-grade carbon

dioxide was purchased from Matheson Gas. CO2 was delivered in cylinders with about 800 psig initial pressure. All corefloods were conducted with 1500 psig backpressure.

The surfactant was a gift from Dow and used for coreflooding with 0.2 wt% as injected in a synthetic brine solution, respectively. The composition of the synthetic brine was 5.02 wt% sodium chloride (NaCl), 0.58 wt% calcium chloride (CaCl2), and 0.23 wt% magnesium chloride in deionized water. Gas and liquid injection rates for nine steady-state core floods conducted on each Berea sandstone core are shown in **Table 3-ii.**

Table. 3-i: Core properties

Rock Type	**Core Dimension** **(length - diameter, inch)**	**Average Permeability to Air (md)**	**Porosity (%)**
High perm	11.5 – 1.5	520	22
Low perm	11.5 – 1.5	57	21

Table 3-ii: Fluid injection rates

Superficial Gas Velocity (ft/day)	***Foam Quality***		
6.50	0.82	0.74	0.68
12.99	0.90	0.85	0.81
19.49	0.93	0.90	0.86
Superficial Liquid Velocity (ft/day)	**1.39**	**2.23**	**3.06**

The steady state pressure drops across the core were measured and used to determine the total effective permeability (k_e) during foam flow

$$k_e = \frac{\mu_g u_t}{\Delta P_{foam}}$$

where ΔP_{foam} is the pressure drop measured during steady state flow of surfactant solution and CO_2, μ_g is the CO_2 viscosity at core flood conditions, u_t is the total Darcy velocity.

In all corefloods, strong foam propagation was observed as indicated by high pressure gradients throughout the core. **Figure 3-2** shows the total effective foam permeability for both high and low permeability cores, which is about 100 times lower than the absolute core permeability.

For low permeability, foam strength (k_e) first increases and then decreases as foam quality increases for all liquid rates (**Table 3-ii**). While very wet foam is responsible for weak foam at low quality, high rate of foam coalescence due to high capillary pressure accounts for foam instability at high quality regime. However, foam strength appears to be much less sensitive to the variation of liquid rate at fixed high gas rate.
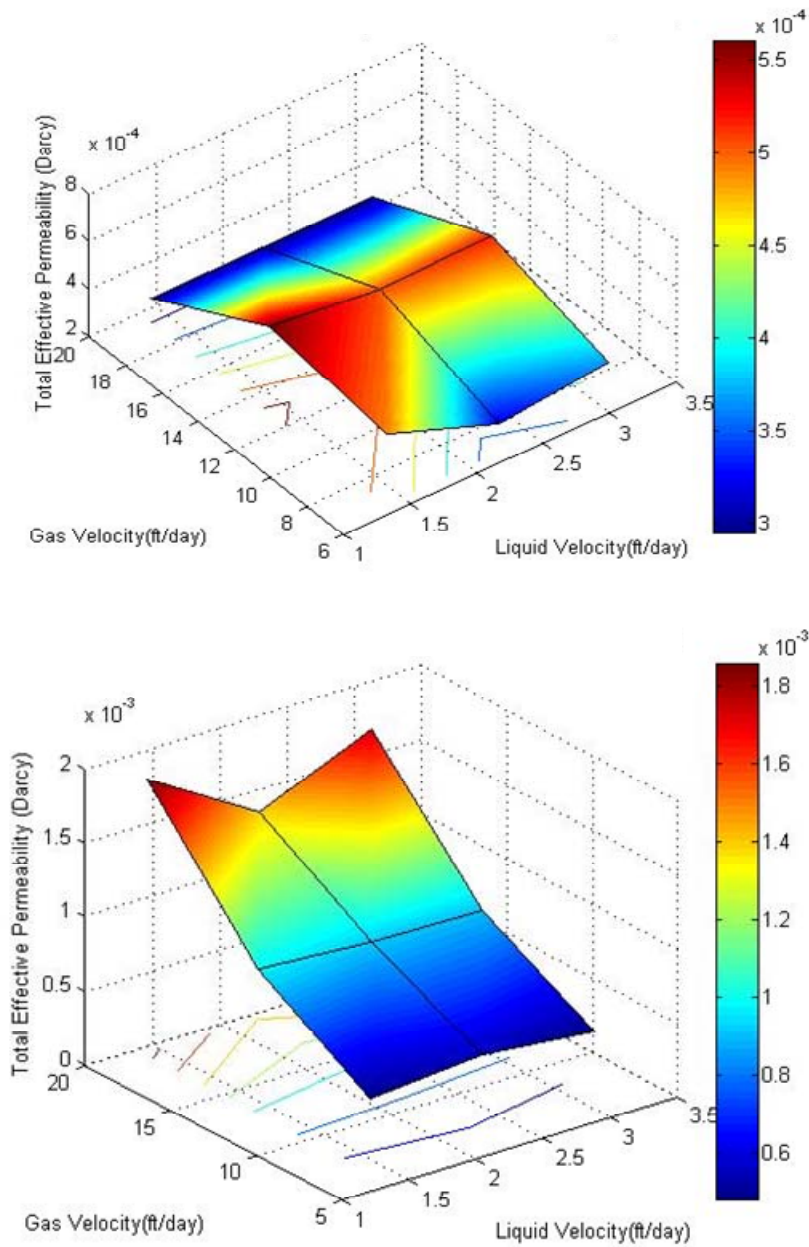
Figure 3-2: *Total effective foam permeability in (top) low and (bottom) high permeability Berea sandstone cores at 40°C*

For high permeability, two distinct differences from the low permeability are observed: Foam strength increases almost linearly with foam quality at a fixed liquid rate over the entire range of gas rates used in this study and it is not sensitive to liquid rate at low gas rate. Furthermore, comparing the

effective permeability of foam in both cores reveals that foamed gas mobility is more uniform in both cores regardless of their high absolute permeability contrast of about 10. This indicates that foam strength increases with permeability which is a favorable rheological feature for controlling gas mobility in high permeability thief zones. In addition, high quality foam in the high permeability core is stronger than low quality foam in the low permeability core. This flow behavior is important to maintain the foam induced diversion of gas from high permeability zone where foam quality is typically high to lower permeability zone.

3.2. Transient foam behavior in sandstone

3.2.1. Foam displacement-base case

Figure 3-3 shows a typical pressure drop profile for foam propagation process. Gas and liquid are co-injected through the foam generator to the porous medium. Foam starts to propagate and push the liquid out (desaturate) in the first section. Pressure drop across the first section rises while remaining very low in the subsequent sections. This trend is repeated in section 2 and 3, exhibiting a "cascading" buildup of the sectional pressure drop over time. The pressure drop is a good indicator of foam propagation. Therefore, as the core is divided into different sections, the pressure drop in a given section is expected to increase in response to foam invasion -- the higher the pressure drop, the stronger the foam develops (pressure drop is a macroscopic indicator).
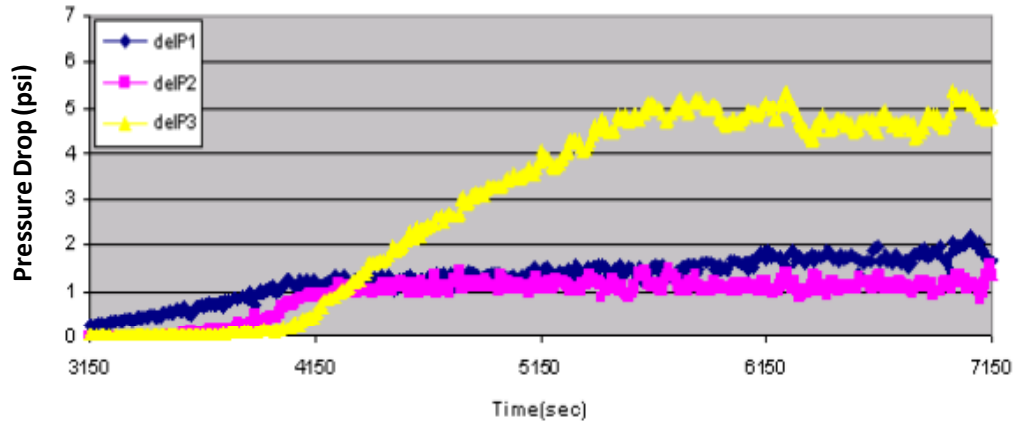
Figure 3-3: *A typical pressure drop curve at 2500 psi core backpressure*

In the first section, after 3150 sec, foam starts to develop, and after a short time (about 3900 sec), pressure drop in the second section starts to increase, indicating foam already propagates in this section. Note that during this time the pressure drop in the first section still has not yet reached the steady-state. This is not an ideal case where the pressure drop in the second section only increases when reaching the steady-state in the first section. However, this is not observed in the current case, as foam still develops behind the front.

Based on this observation, we believe that the liquid saturation behind the front continues to desaturate. As a result, foam generation mechanism by snap-off may be promoted because for snap-off, gas will invade the pore and displace the liquid out. Note the leave behind can also be a mechanism.

3.2.2. Effect of Backpressure on Foam Propagation

Figures 3-4 to **3-6** present the pressure drop profile from three foam coreflood experiments with different backpressures (750, 1250, and 2500 psi). The total flow rate is fixed at 1 ml/min. Let's consider the magnitudes of the pressure drop, real injection time, and the pressure gradient (slope of the profiles).
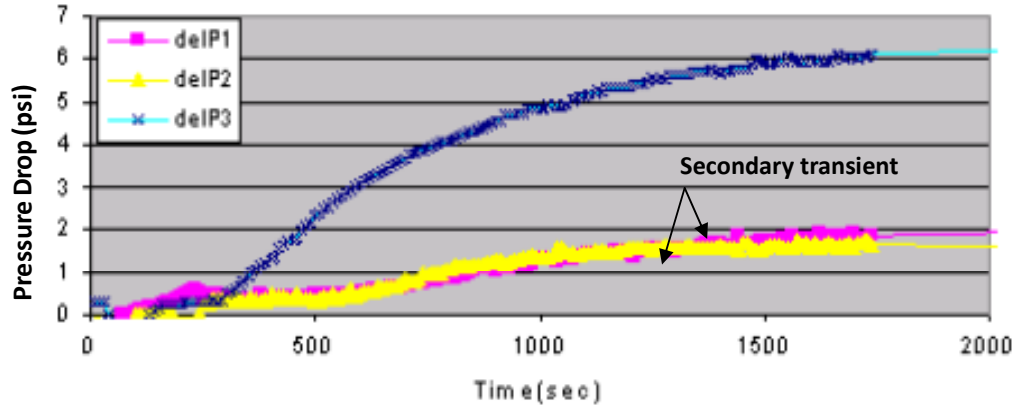
Figure 3-4: *Effect of Backpressure on foam propagation at 750 psi, secondary wave starts to develop after about 700 sec*
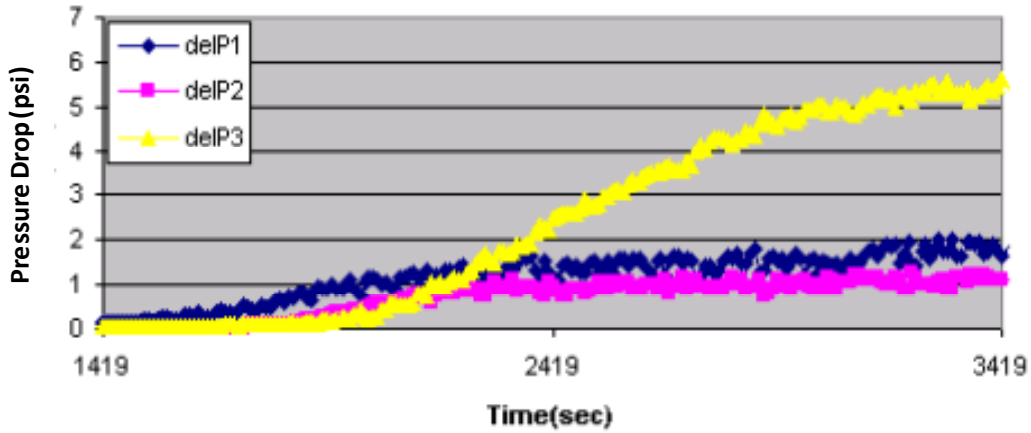
Figure 3-5: *Effect of Backpressure on foam propagation at 750 psi, secondary wave starts to develop after about 700 sec*
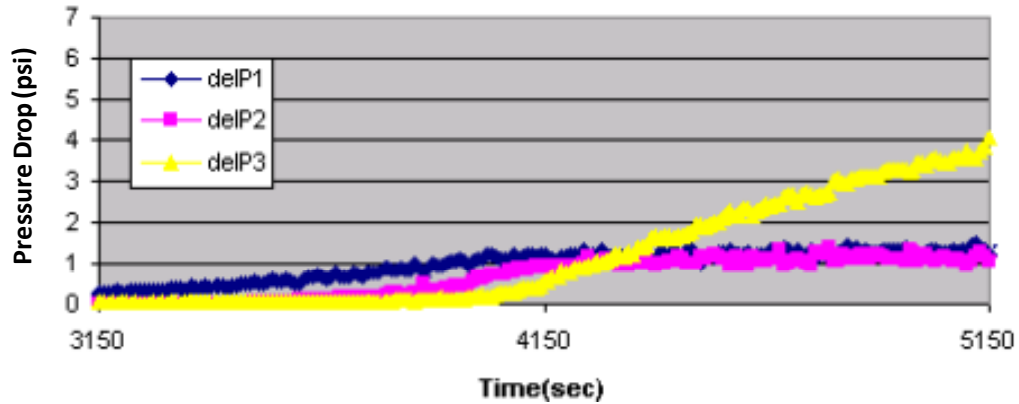
Figure 3-6: *Effect of Backpressure on foam propagation at 2500 psi, no evidence of secondary wave development*

At 750 psi backpressure, after foam breakthrough, the pressure in the third section continues to increase very steeply. Surprisingly, the pressure drop

144

in the second section starts to increase when about reaching the plateau in the third section. This trend (called secondary displacement) is repeated in section 2 and 1, similar to that observed before the foam front breakthrough (called primary displacement).

The two displacement stages above can be explained as follows. During the primary displacement, we simply have the displacement of liquid out of the core by foam. Only large pores are going to be displaced by foam during this period. We call it "primary liquid desaturation". After foam breakthrough, foam continues to develop. Particularly, foam develops strongly in the last section, leading to the buildup of the pressure drop in the last section and thus over the whole core. Consequently, the viscous force becomes dominant over the capillary force, enhancing displacement of liquid by foam in smaller pores. We call it "secondary liquid desaturation". After the secondary liquid desaturation reaches the steady-state, gas can no longer displace any further liquid. It means that the foam strength reaches a critical value.

At 1250 and 2500 psi backpressures (**Figures 3-5** and **3-6**), only primary liquid desaturation can be seen and there is no evidence of secondary liquid desaturation. We believe that the pressure drop over the whole core is not sufficient to push the liquid out of the smaller pores.

Looking at the primary wave for three backpressures, we can see immediately that for 750 psi backpressure, foam starts to develop very soon. At 1250 psi backpressure, after about 1419 sec, and for 2500 psi foam development starts after about 3150 sec. This difference in time for foam development will tell us how strong foam is going to develop. Since it can take a long time for foam to develop, but very strong, or it can take a short time for foam to develop, but very weak.

The first reason is that during the saturation process, the core is not saturated with surfactant solution at 1250 and 2500 backpressures. It means that surfactant solution stays in the core before foam injection in equilibrium

with gas at atmospheric pressure. When we inject foam into the core, a large fraction of gas is going to be dissolved into the liquid (surfactant solution) until it saturates the liquid. Then gas comes out of the liquid and free gas starts to make foam. We call it the "gas solubility" effect. As we increase the backpressure, it takes longer time for foam development, which means that solubility effect is more severe at higher backpressures. So if we already saturate the liquid, gas solubility is not the problem anymore. We expect it to behave like one bar.

The second reason is, according to the ideal gas law, pressure and volume are inversely proportional at constant temperature. When we inject 0.8 ml/min of gas into the core at 2500 psi, the volume flow rate is going to be 30 times lower than the time we inject the same amount of gas at 750 psi. Consequently, the interstitial gas velocity is going to be lower at higher backpressure, and it is probably going to influence the foam generation mechanism (since the generation rate by snap-off is a function of the gas rate). There exists an optimum range of gas velocity that increasing the gas rate cause generation to increase. Very high gas rate is going to destabilize the generation process mechanically. At very high gas rates generated lamellae stretching and contracting so fast, and it is easy to break. Gas preferably invades the large channels, and if the velocity of gas is high enough, may be the viscous pressure gradient going to help gas to invade the smaller pores.

A closer look at pressure drop profiles of three backpressures reveals another difference. At 2500 psi backpressure foam develops very gradually (slope of the pressure drop profile), while at 750 psi the pressure drop profile is very steep. As we increase the backpressure, pressure drop value decreases, and the slope of the pressure drop profile becomes very gradual. Foam apparently is very strong at 750 psi. If we base foam strength on pressure drop, it means that the pressure tends to make foam weaker. We believe that gas solubility is an important effect that influences the generation mechanism. To

evaluate this effect, we conducted two tests where the injected surfactant was equilibrated at 14.5 psia and 2500 psi, respectively, before injected into the core. The result is shown in **Figures 3-7** and **3-8**. Comparing the pressure drop profiles over sections 2 and 3 reveals that the pressure drop increases relatively faster when the injected surfactant solution is equilibrated at 2500 psi. This indicates that the effect of gas solubility is significantly reduced in this case.
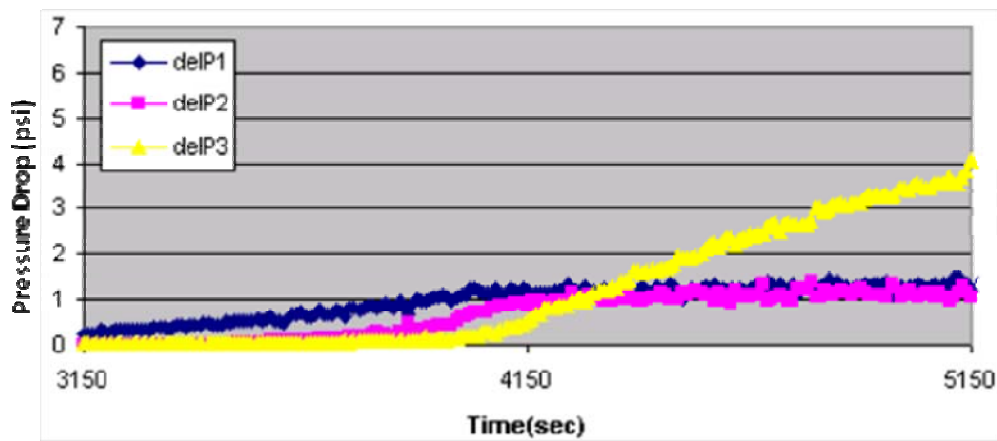
Figure 3-7: Pressure drop profile during injection of gas and surfactant solution equilibrated with CO_2 at 14.5 psia
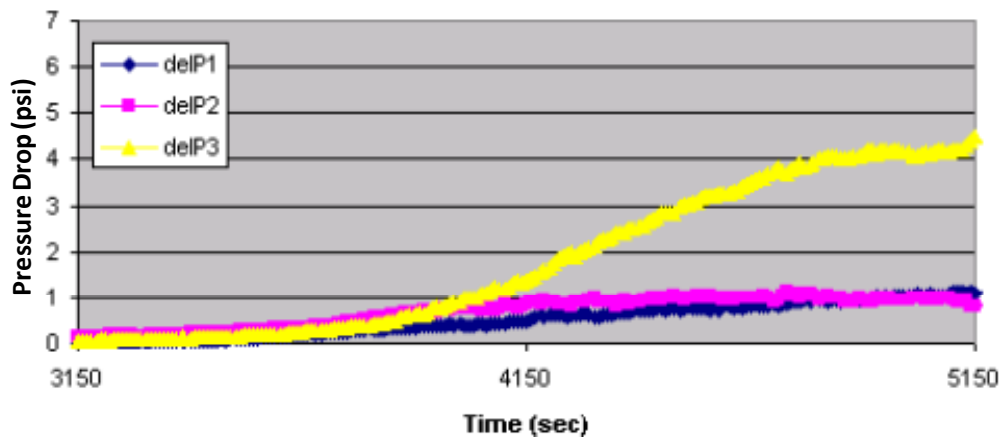
Figure 3-8: Pressure drop profile during injection of gas and surfactant solution equilibrated with CO_2 at 2500 psi

3.3. Foam propagation in dolomite cores with nonionic CO2 soluble surfactants

3.3.1. Materials and methods

Four different surfactants that represent a wide distribution of partitioning coefficients between CO2 and brine were used in this study. The commercially available anionic surfactant (CD 1045) is a proprietary mixture of surfactants. Enick and Olsen (2011) suggested that the light brown color of this surfactant mixture appears to be a water-based blend of anionic α-olefins sulfonates, non-ionic alkyl phenol ethoxylates, and amphoterics. If the CD 1045 does contain nonionics, a small portion of the CD 1045 may be dissolved in the scCO2. However, we believe that the CO2 soluble components in CD 1045 are not strong foaming agents and that their overall concentration is insignificant compared to the CO2 insoluble components because (a) CD 1045 is a strong foaming surfactant mixture, (b) the adsorption of CD 1045 in carbonate rock is significantly higher than that of the other non-ionic CO2 soluble surfactants (S, 4S, and 15S) used in this work as shown in Results and Discussion, (c) the adsorption of non-ionic surfactants is generally lower than anionic surfactants in carbonate rocks at pH < 9, and (d) foam propagation with CD 1045 is very different from that with the non-ionic CO2 soluble surfactants (S, 4S, and 15S) under the same coreflood conditions, as shown in Results and Discussion. Therefore, CD 1045 is considered a CO2 insoluble surfactant in this work.

The other three proprietary non-ionic surfactants (named S, 4S, and 15S) have different levels of solubility in supercritical CO2 at given pressure and temperature due to their CO2-philic hydrocarbon-based tails and different hydrophiles. The average solubility of these surfactants in CO2 is about 0.15 wt% at coreflood conditions (1500 psi and 35 °C), with 15S exhibiting the highest solubility and S the lowest solubility. In all core flood experiments, a surfactant solution containing 0.2 wt% surfactant and 3 wt % NaCl (analytical grade quality) was used to stabilize supercritical CO2 foam generated in

Silurian dolomite cores with a 1-foot length and 2-inch diameter. The same NaCl concentration was used for saturating the core with brine before injection of surfactant solution and CO2. The purity of liquid CO2 was 99.5%. The rock permeability to brine was around 300 md.

Surfactant adsorption test

The static surfactant adsorption experiments were conducted to evaluate the level of adsorption of the four surfactants (CD 1045, S, 4S, and 15S) on the Silurian carbonate surface at room temperature and pH of 8.2. The rock samples were first ground into fine particles and then passed through two sieves of 40 mesh and 100 mesh. The particles with a diameter between 0.15 mm and 0.425 mm were used for the adsorption experiments. In each experiment, 10 g of the rock particles were added to 20 g of aqueous solution containing 5 wt% NaCl and 1 wt% surfactant. After it was gently stirred for 1 hour, the sample was rested for 24 hours, and then centrifuged for 5 minutes to remove the rock particles. The surfactant concentration in the supernatant was analyzed using high performance liquid chromatography (HPLC).

Measurement of partition coefficient between CO2 and brine

The partition coefficient of the three CO2 soluble surfactants (S, 4S, and 15S) was directly measured as a function of pressure at 35 ^{o}C. The partitioning of each surfactant between free CO2 and brine was allowed to reach equilibrium at different pressures in a series of high pressure 300 ml cells using the following procedure. First, each cell is charged with pure CO2, and then chased with surfactant solution to bring the cell pressure to a set value. The surfactant solution filled about 30% of the volume of the cell. The cell pressure slightly decreased to a constant value due to the small amount of CO2 that was dissolved into the surfactant solution. It was determined through trial and error that 24 hours were sufficient for the system to reach equilibrium

at this pressure. A 5 ml sample of the aqueous phase was then taken to analyze its equilibrium surfactant concentration using HPLC, which was used to determine the partition coefficient k by the equation below.

$$k = \frac{m_{sCO2}/(m_{sCO2} + m_{fCO2})}{m_{sw}/(m_{sw} + m_w)}$$

where msCO2 is the mass of surfactant in the free CO2, which is the difference between the initial mass of surfactant injected in brine into the cell and the remaining mass of surfactant in the brine at equilibrium (msw); mfCO2 is the mass of free CO2 determined based on the initial mass of CO2 charged into the cell and the solubility of CO2 (Wiebe, 1941) in the brine at equilibrium pressure and temperature; mw is the initial mass of water injected into the cell. Note that the solubility of water in CO2 was neglected. It was found from literature data that the water solubility in supercritical CO2 was about 0.2 wt% at 35 °C and 3172 psi (Liu et al., 2001; Liu et al., 2002) or 0.16 g water/100 g CO2 at 670 psi and temperatures up to 50 °C (Adkins et al., 2010a), which is relatively small as compared to the solubility of CO2 in water under the same conditions.

Foam flooding

For the purpose of comparison, all the surfactants used in this work were injected during the aqueous phase. CO2 and the surfactant solution were simultaneously injected without the use of a foam pre-generator. To obtain a fixed injection foam quality of 75% for all core floods, the surfactant solution and CO2 injection rates were fixed at 0.1 cc/min (1.4 ft/d) and 0.3 cc/min (4.2 ft/d), respectively. Pressure drops over the three sections of the core were recorded. Water saturation was determined based on the pore volume (PV) and the difference in cumulative mass (Δm) between the injected and the produced waters (Sw = 100*(PV- Δm)/PV). All core floods were conducted at 35 °C and 1500 psi backpressure. These conditions were chosen to assure

that the rubber sleeve would not be damaged during prolonged core flood experimentation.

3.3.2. Surfactant partitioning between CO2 and brine

Figure 3-9.A shows the measured surfactant partition coefficients as a function of pressure for three different CO2 soluble surfactants (S, 4S, 15S). The average partition coefficient is highest for 15S (about 1.8) and lowest for S (about 0.13). This is primarily due to the fact that the average solubility of 15S in supercritical CO2 at 35 ^{o}C is about 1.25 times that of 4S and 1.89 times that of S. Note that we directly measured the solubility of these three surfactants in supercritical CO2 and found that the differences in solubility between the surfactants were not significantly influenced by pressure up to 2500 psi. The main reason of the observed solubility increase with pressure is that the hydrocarbon tail-CO2 interactions became more attractive, as described by a surface equation of state (Adkins, 2010b; O'Neil et al., 1998), when the density of CO2 increased with pressure, and thus the solvent power of supercritical CO2 was stronger at an elevated pressure. This is consistent with our observation (**Figure 3-9.A**) that the sensitivity of partition coefficient to pressure increases with CO2-philicity. For example, the partition coefficient of 4S increases significantly with pressure to a plateau value while it is much more gradual with S. Note that even though the increase in the CO2 density raises the solubility of CO2 in water modestly, it does not influence the solvation of the surfactant in the water phase as much as it does in the CO2 phase (Chen et al., 2010).

Figure 3-9.B shows the best fit of Eq. (2) in terms of mole fraction to the experimental data. The correlation matches the data for S quite well but shows significant deviations for 4S and 15S, particularly at elevated pressure. Therefore, we chose to use the experimental data interpolation method instead of the model fits for field-scale foam process simulation for all surfactants.

3.3.3. Surfactant adsorption in Silurian dolomite rock

Figure 3-10 shows the results of surfactant adsorption for Silurian dolomite rock. The adsorption of CD 1045 is highest among the four surfactants. This is due to the fact that CD 1045 and dolomite surfaces (positively charged at pH < 8.2, Schechter, 1992) are oppositely charged while the CO_2 soluble surfactants are non-ionic. However, within the series of CO_2 soluble surfactants, the results clearly show a gradual increase in adsorption with surfactant partition coefficient or CO_2-philicity. Quantitatively, an increase in the partition coefficient by a factor of 15 results in an increase in surfactant adsorption by a factor of 2.6. Since the polarity of CO_2 is much lower than that of water (O'Shea et al. 1991), the work of surfactant adsorption would reflect the importance of dispersive over polar interactions between the surfactants and the Silurian mineral surface. This result is consistent with the fact that surfactants with higher hydrophilicity exhibit lower adsorption on given mineral surfaces (Celik et al., 1988; Austad et al., 1987; Zhang and Somasundaran, 2006; Fjelde and Zuta, 2009; Zuta and Fjelde, 2008).

3.3.4. Foam flow behavior in Silurian dolomite cores

Figures 3-11.A and **3-11.B** show the sectional pressure drops and corresponding water saturation during simultaneous injection of CO_2 and CD 1045 solution. The pressure drop near the inlet (Section 1) was much lower than that in subsequent sections (Section 2 and 3), which has been well known as the "inlet effect" (Kovscek and Radke, 1994; Nguyen et al., 2003; Simjoo et al., 2012). Strong foam started to propagate into Section 2 after almost 2 injected pore volumes (PV) and then Section 3 after 5 PV. The pressure drop history corresponds with the water desaturation shown in **Figure 3-11.B**. The water saturation first decreases sharply to 50% after 1 PV, and then more gradually towards the residual water saturation (16%) after about 11 PV.

Closer examination of the water saturation reveals that it actually almost levels off between 1 and 2 PV before further gradual decreases. This is due to weak foam development throughout the core until 2 PV.

The pressure drops for the three different CO_2 soluble surfactants are shown in **Figures 3-12.A, B &C**, respectively. The most important observation from the pressure drop history is that an increase in surfactant partition coefficient causes further delay of strong foam propagation in all core sections. Indeed, a high pressure drop, as an indicator of strong foam, advanced towards the core outlet after about 1.3 PV for S, while it took more than 3 PV for 15S. As a consequence, the rate of displacement of water by foamed CO_2 (**Figure 3-13**) significantly decreased from 11.6 %/PV (for S) to 6.3 %/PV (for 15S) as the partition coefficient increased by a factor of 15. However, the respective residual water saturations for all the CO_2 soluble surfactants were quite close (around 5%, **Figure 3-13**) but slightly lower than that for CD 1045 (**Figure 3-11.B**).

Comparing the pressure drops for all four surfactants (**Figures 3-11** to **3-12**) reveals that surfactant partitioning between CO_2 and water does improve foam robustness (i.e. rate of foam development) and that an increase in partition coefficient delayed strong foam propagation. These observations can be explained by the fact that strong foam propagates with surfactant concentration above a critical value. A combination of CO_2 mobility being relatively higher than water mobility and the partitioning of surfactant into the mobile CO_2 phase enhances surfactant propagation, and thus foam robustness. This was observed in the cases of CD 1045 (zero partition coefficient) and S (non-zero partition coefficient). However, a further increase of partition coefficient would retard strong foam propagation. This is because it leads to severe spreading of surfactant concentration distribution along the main flow direction so that the effect of critical surfactant concentration mainly determines strong foam propagation. In other words, the rate of increase in

total surfactant concentration at a given position is reduced as surfactant partition coefficient increases. Hence, this effect is transient and becomes insignificant once surfactant concentration exceeds a critical value for foam stabilization. In addition, the presence of surfactant adsorption that increases with surfactant partition coefficient as observed with S, 4S, and 15S can retard further surfactant transport. The increase in spreading of surfactant concentration distribution and in surfactant adsorption is most likely responsible for the increasing delay of strong foam propagation between S, 4S and 15S. We did not analyze the effluent surfactant concentration, but performed a simple foaming test on the fluent samples by shaking the collection tubes. The test results show that good foaming was observed in the tube at around 1.15 PV for 15S, but delayed until almost 1.57 PV for S. Since the adsorption of S is relatively lower than that of 15S, these results suggest that the effect of surfactant spreading could be significant in our coreflood experiments.

(A)

(B)
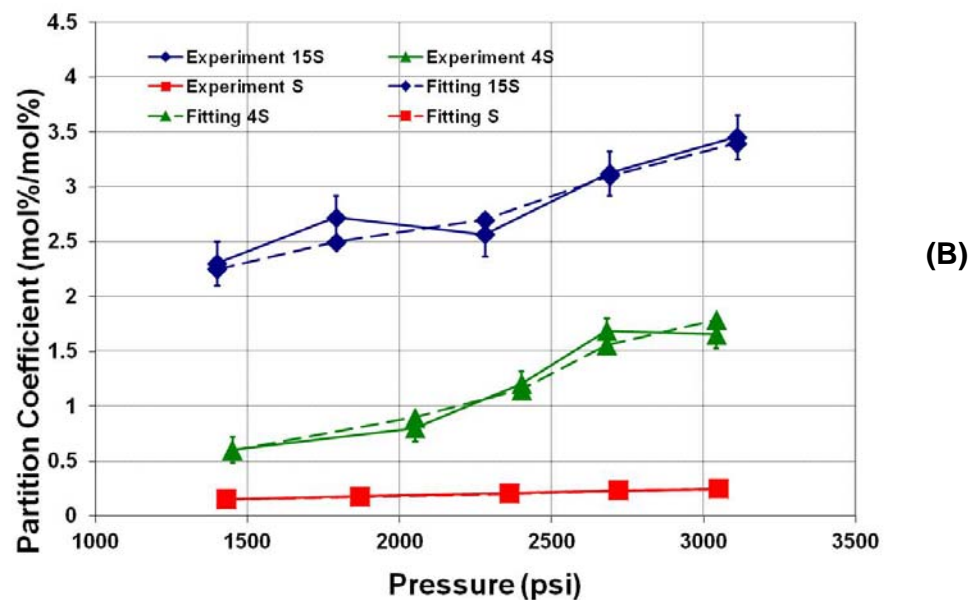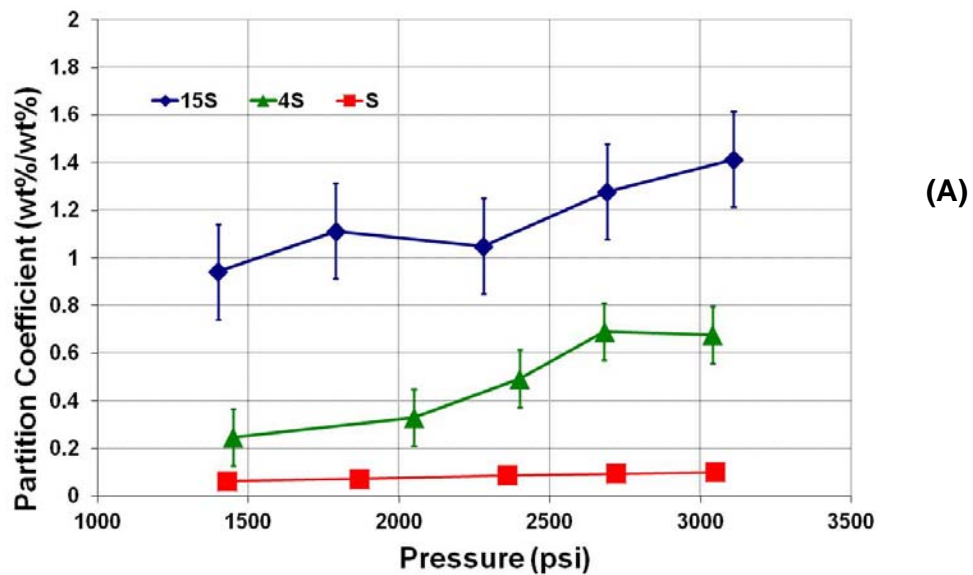
Figure 3-9:* Partition coefficients for S, 4S, and 15S at 35 OC: (top) measured data in terms of mass fraction (wt%surfactant in CO2/wt% surfactant in aqueous phase), (bottom) best fits of Eq. (B) to the measured data in terms of model fraction.*
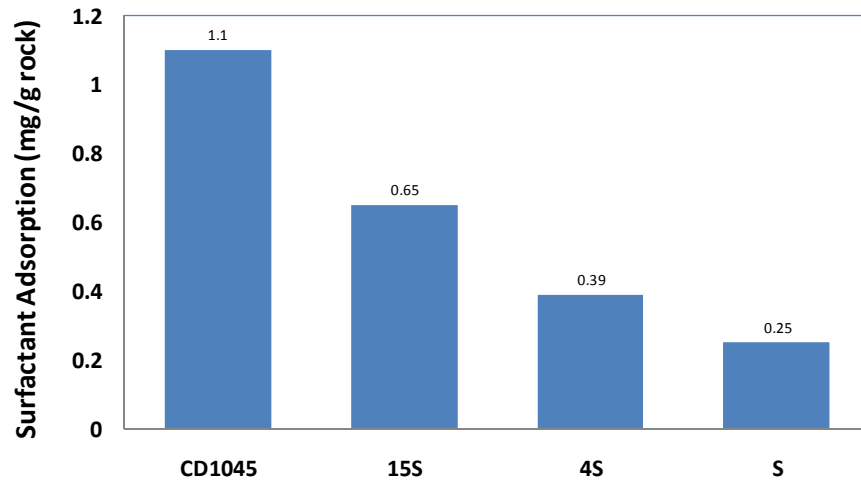
Figure 3-10: Adsorption of four surfactants on Silurian dolomite rock.
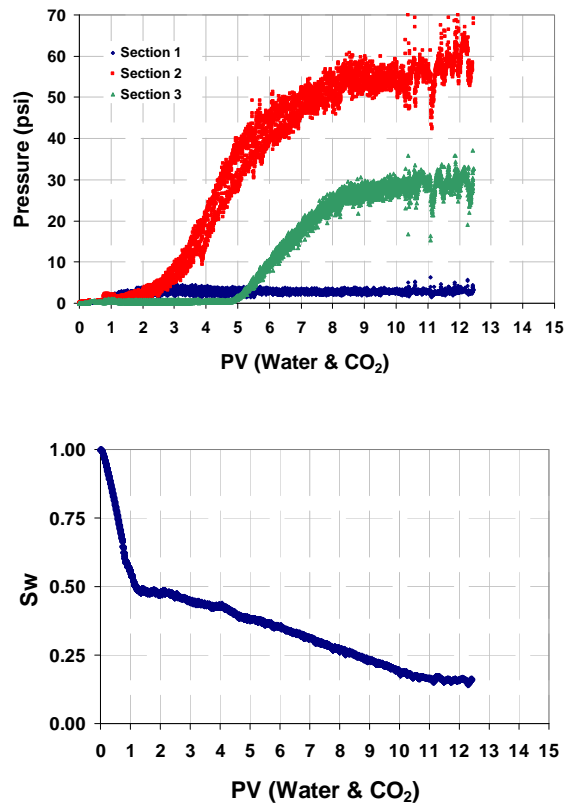
Figure 3-11: (top) Pressure drop and (bottom) water saturation during simultaneous injection of CO2 and CD 1045 solution.

156
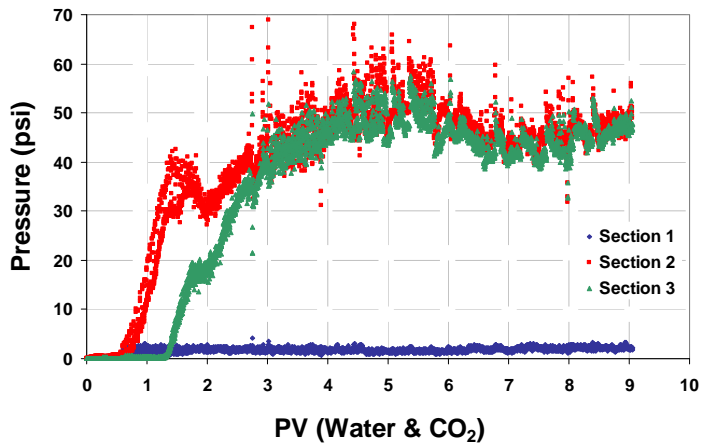
(a)
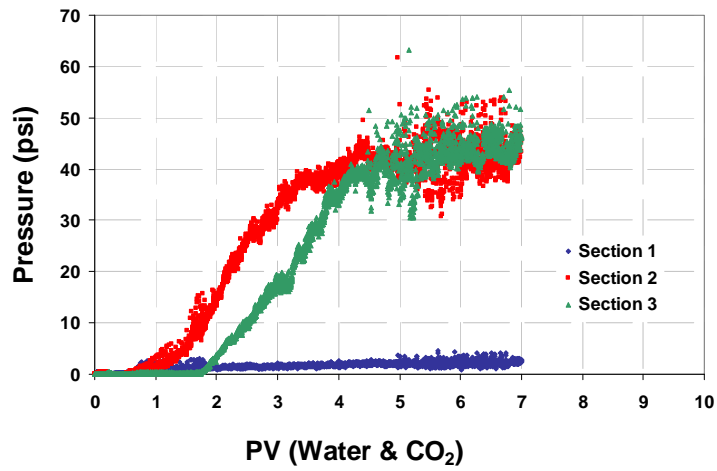
(b)
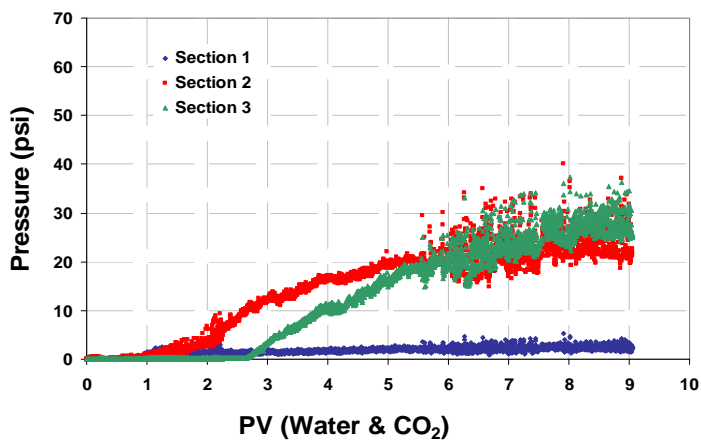
(c)

__Figure 3-12:__ Pressure drops during simultaneous injection of CO_2 and aqueous solution of (A) S, (B) 4S, and (C) 15S.

Table 3-iii: *The Parameters of Core Samples*

	Core 1	Core 2
Diameter / inch	1.50	1.50
Length / inch	2.99	2.99
Pore Volume (PV) / ml	13.0	15.5
Porosity / %	15.0	17.9
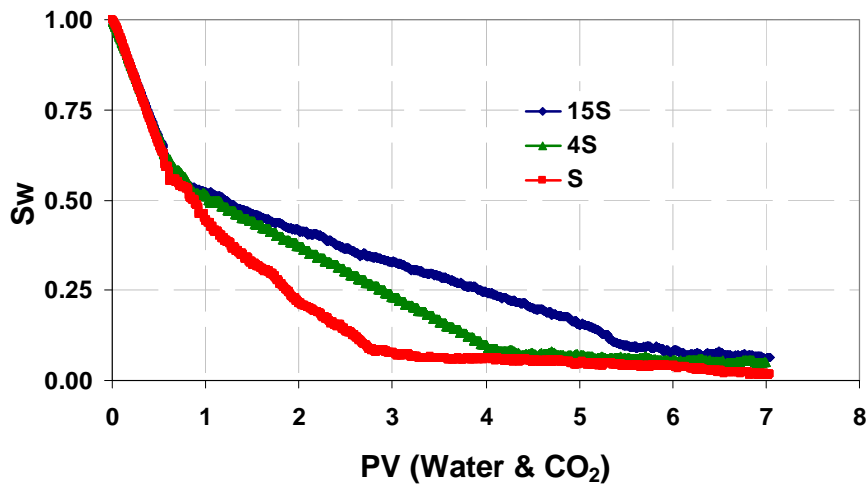
Figure 3-13: *Water saturation profiles for S, 4S, and 15S during simultaneous injection of CO_2 and surfactant solution.*

3.4. Foam propagation in dolomite cores with nonionic CO2 insoluble surfactant (Surfonic L24-22)

3.4.1. Experimental description

The core is vacuumed and injected DI water to measure the pore volume (PV). After the core is fully saturated with DI water, inject water at various flow rates to measure the corresponding pressure drop. Based on Darcy's law, the permeability of core can be calculated. The pore volume and permeability for the core samples are listed in **Table 3-iii**.

3.4.2. Reference core floods

Water and CO$_2$ Core Flooding

Water and CO$_2$ are injected into Core 1 sample as reference experiments. The injection schemes include co-injection, water alternated surfactant injection and 100% CO$_2$ continuous injection.

Water and CO$_2$ are injected at the same time. The total superficial velocity is 4 ft/day. The foam qualities (CO$_2$ volumetric percentage) are 70%, 80% and 90% respectively. The procedure is described below:

(1) Flush water at 2 ml/min for one hour at atmosphere pressure (Because the core is re-used, flush the core to dissolve the trapped CO$_2$).

(2) Pressurize the system to 3400 psi with DI water by adjusting relieve valves. Thus, the residual gas in the core can be dissolved into water.

(3) Shut down both inlet and outlet valves to isolate the core holder. The pressure in the core sample should be still at 3400 psi. If the pressure decreases, there must be leak somewhere. Keep the pressure transducer connecting with the core system to get zero flowrate pressure (ZFP) across the core sample. The ZFP is the gravity potential, i.e. the static hydro pressure in the core.

(4) Inject both CO$_2$ and water at the same time. The flow rates are shown in **table 3-iv**. Record the pressure reading across the core. The pressure drop equals (pressure reading – ZFP). Release the system pressure to atmosphere pressure.

(5) Convert the pressure drop into foam apparent viscosity by Darcy's law:

$$\mu = \frac{k \Delta P}{u\, L}$$

Table 3-iv: The Injection Parameters for Water and CO2 Co-Injection Flooding

Foam Quality	70%	80%	90%
Total superficial velocity / ft/day	4	4	4
Total flow rate / ml/min	0.97	0.97	0.97
CO2 flow rate / ml/min	0.679	0.776	0.873

Where μ is viscosity, k is the core's permeability (43.5 md), u is the total superficial velocity (4 ft/day), ΔP is the pressure drop= (pressure reading – ZFP), L is the length of core sample (2.99 inches).

The apparent viscosity histories of the co-injection are shown in **Figure 3-14.**
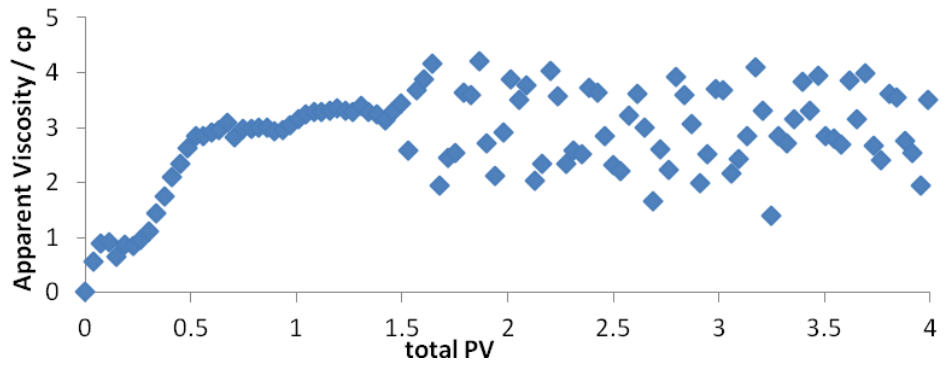
(a) 70% Foam Quality
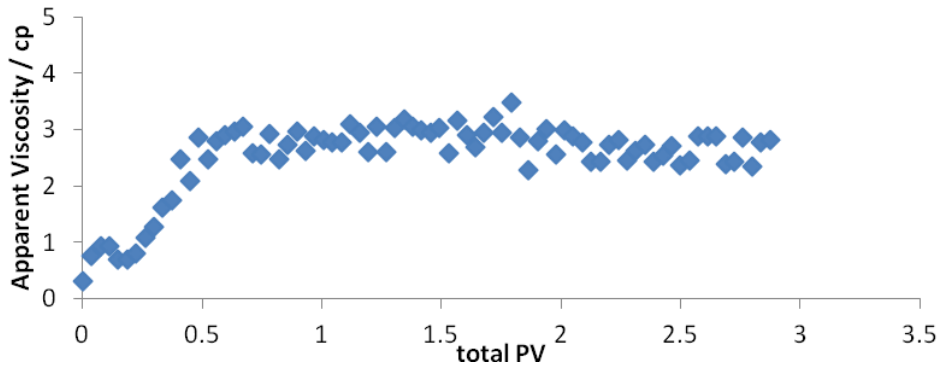
(b) 80% Foam Quality
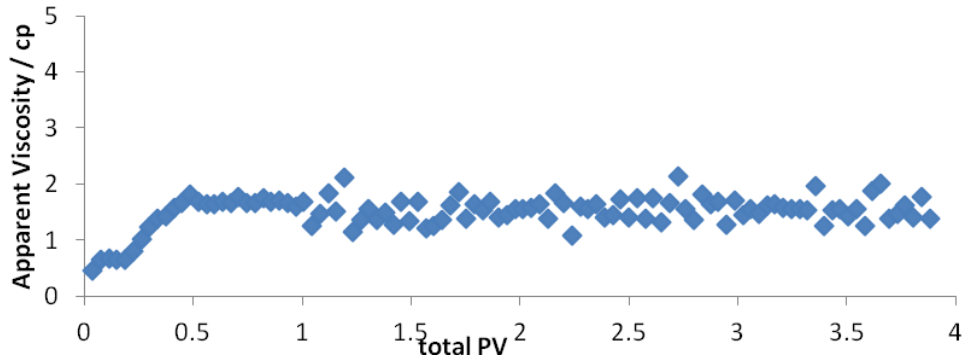
(c) 90% Foam Quality

Figure 3-14: *The apparent viscosity history for water and CO$_2$ co-injection flooding*

161

The steady apparent viscosity decreases with increasing foam quality as shown in **Figure 3-15**. Because of the capillary force in the core sample, the apparent viscosity of water foam is higher than the viscosities of both water (1 cp) and CO_2 (0.102 cp).
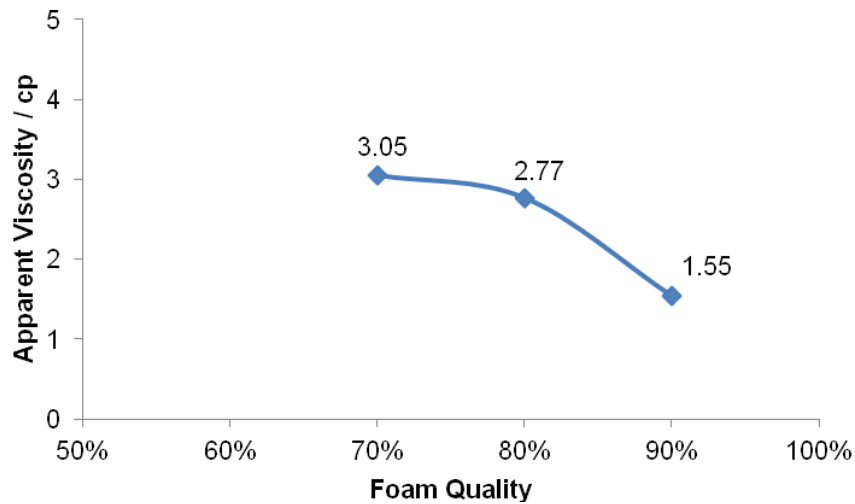
Figure 3-15: The steady apparent viscosity during water and CO_2 co-injection

Water Alternating Gas (WAG) Injection

During WAG injection, a slug of water is injected first and then followed by a slug of gas (CO_2). Water and CO_2 are alternated to inject. The procedure is described below:

The steps (1) to (3) are the same as in section 3.1.4.1.

(4) Inject a slug of water, and then inject a slug of CO_2. Repeat above injection cycle for 3 PV. The slug sizes for different foam qualities are shown in **Table 3-v**. Record the pressure reading across the core. The pressure drop equals (pressure reading – ZFP). Release the system pressure to atmosphere pressure.

Foam Quality	80%	90%
Total superficial velocity / ft/day	4	4
Total flow rate / ml/min	0.97	0.97
CO_2 flow rate / ml/min	0.97	0.97
Water flow rate / ml/min	0.97	0.97
Water slug size / PV	0.1	0.1

(5)   Convert the pressure drop to apparent viscosity as the same equation as in section 3.1.4.1

The results are shown in **Figure 3-16.**

Figure 3-16: The apparent viscosity history during WAG injection
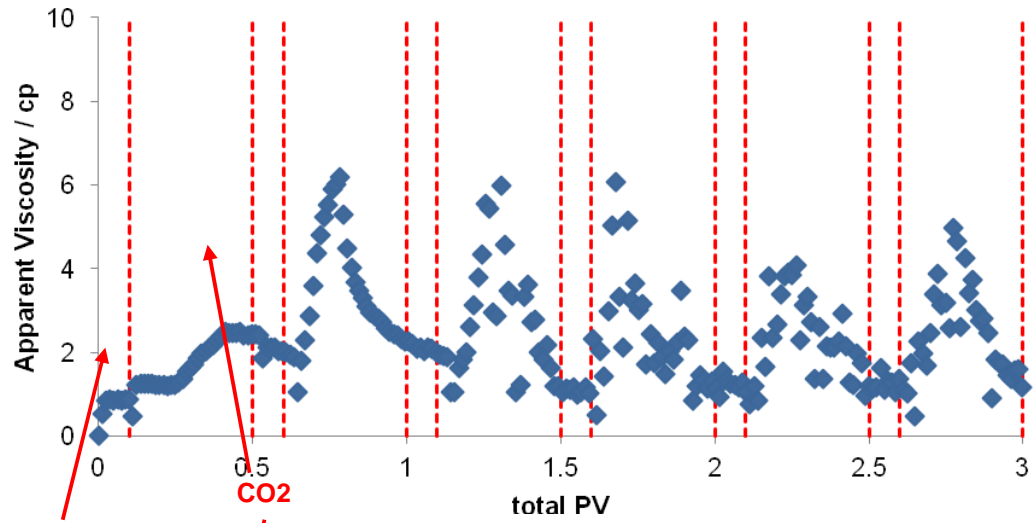
(a)   80% Foam Quaility: 0.1 PV water slug and 0.4 PV CO_2 slug
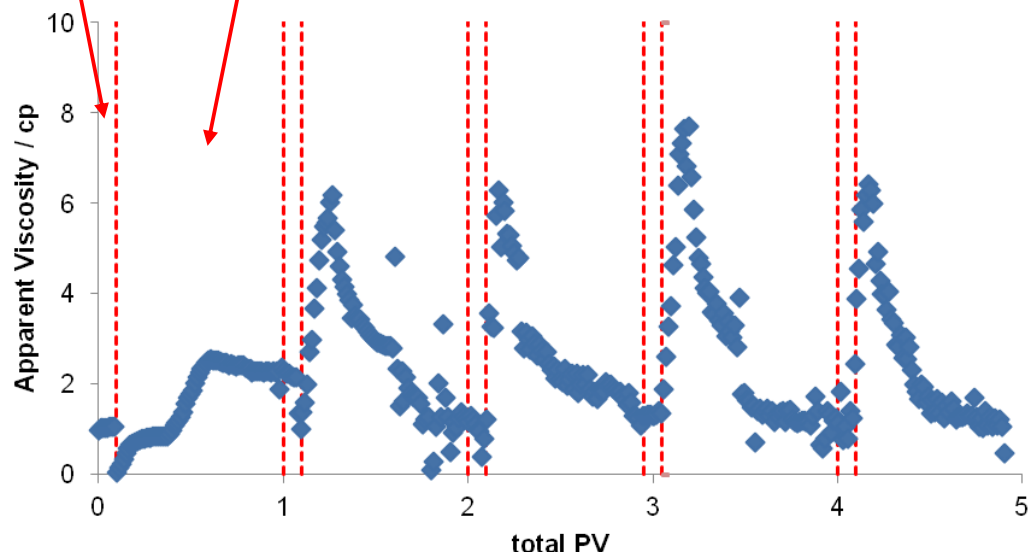
(b)   90% Foam Quaility: 0.1 PV water slug and 0.9 PV CO_2 slug

Figure 3-17: The apparent viscosity history during 100% CO_2 injection

100% CO_2 Continuous Injection

The core is fully saturated with water, and then 100% CO_2 is injected to

reach the steady state. The steps (1) to (3) are the same as in section 3.1.4.1.

(4) Inject 100% CO_2 at 4 ft/day (0.97 ml/min for this core sample) to reach the steady state. Record the pressure reading across the core. The pressure drop equals (pressure reading – ZFP). Release the system pressure to atmosphere pressure.

(5) Convert the pressure drop to apparent viscosity as the same equation as in section 3.1.4.1

The results are shown in **Figure 3-18.**
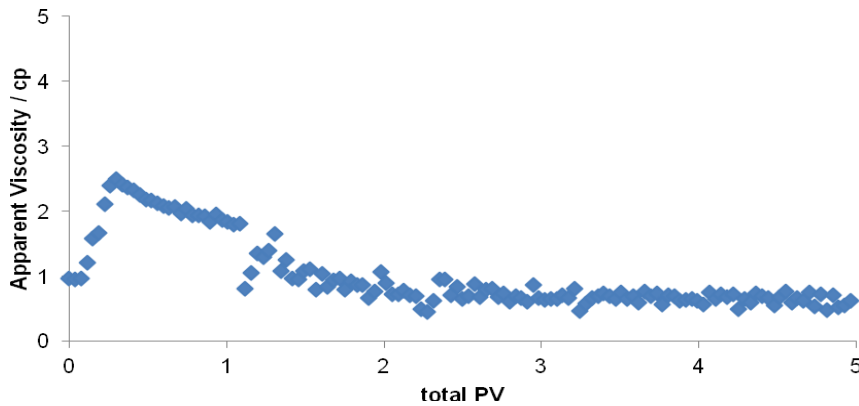
Figure 3-18: *The apparent viscosity history during 100% CO_2 injection*

3.4.3 Core flood with surfactant

The apparent viscosity histories of L24-22 CO_2 foam compared to that of water CO_2 foam are shown in figure 3.7. The L24-22 and CO_2 foam is much stronger than water and CO_2 foam.

The strongest L24-22 and CO_2 foam is generated at 80% foam quality, as shown in **Figure 3-20.** At 90% foam quality, the foam is too dry and capillary force reaches the limiting capillary pressure which results in the collapse of foam and lower apparent viscosity.

165
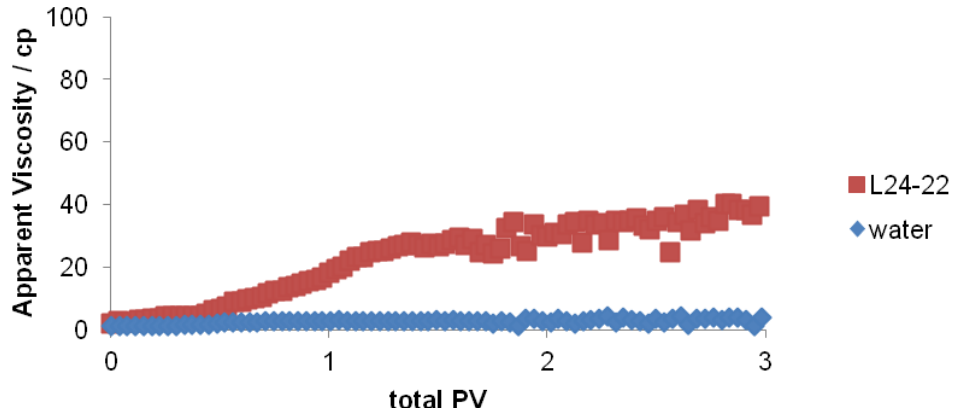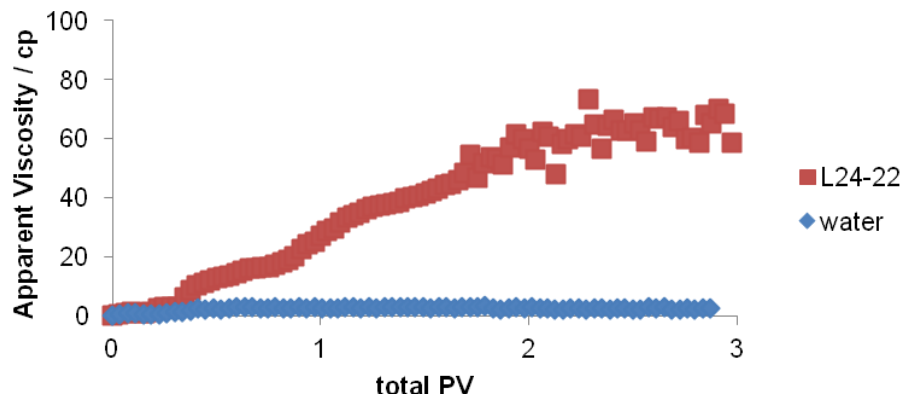
(a) 70% Foam Quality
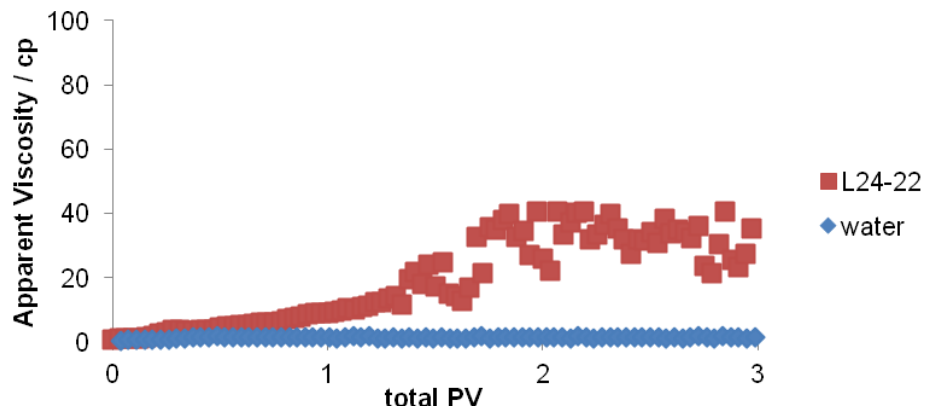
(b) 80% Foam Quality

(c) 90% Foam Quality

Figure 3-19: The Foam Apparent Viscosity History

166
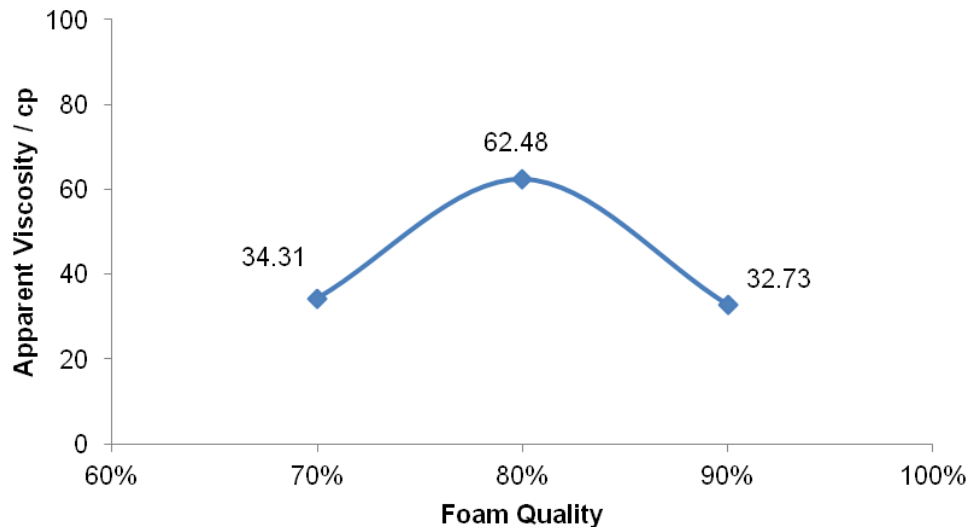
Figure 3-20: *The comparison of steady foam apparent viscosity for the co-injection foam flooding of L24-22 and CO_2*

SAG: L24-22 Alternating CO_2 Injection

The results are shown in **Figure 3-21**. L24-22 shows good mobility control in both foam qualities. During the CO_2 injection slug, the apparent viscosity always increases and then decreases. It's because that the apparent viscosity increase with decreasing the water saturation, but as long as the water saturation is lower than critical saturation, the capillary pressure reach the limiting value and the foam starts collapsing.
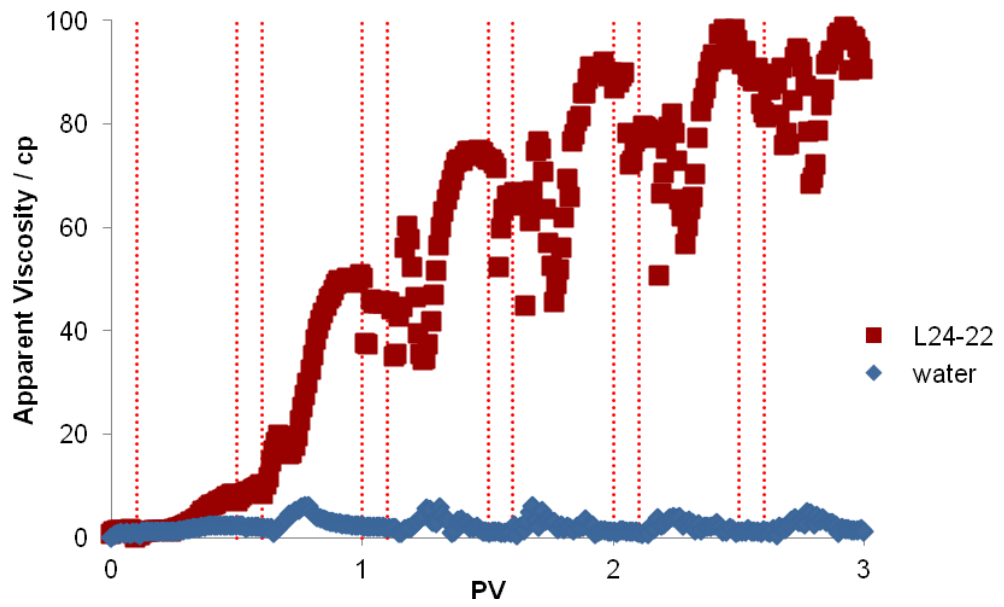
(a) 80% Foam Quality: 0.1 PV aqueous solution and 0.4 PV CO_2
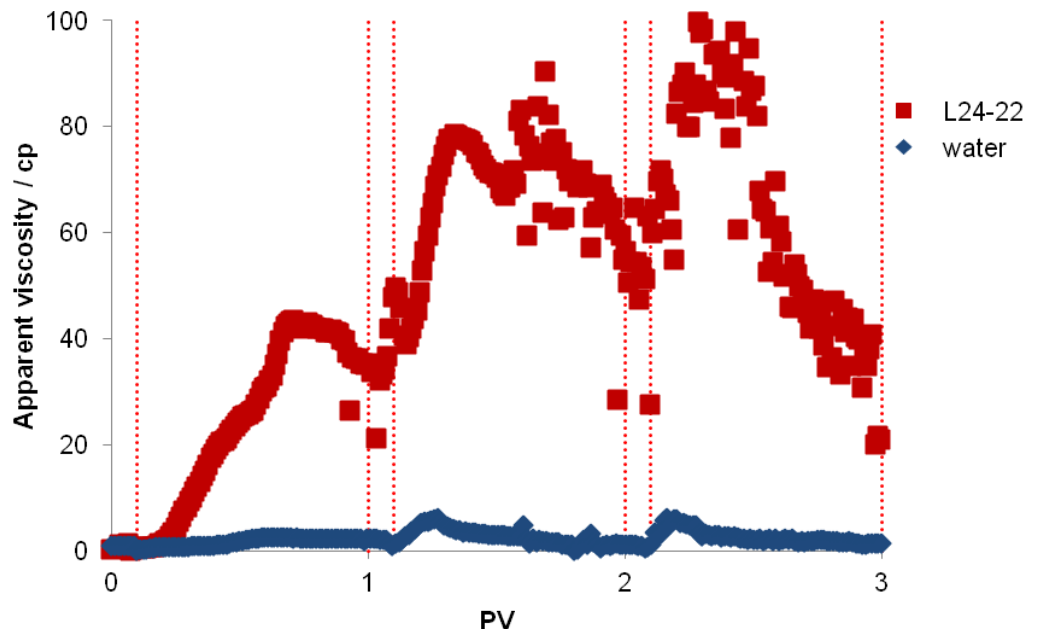
(b) 90% Foam Quality: 0.1 PV aqueous solution and 0.9 PV CO_2

Figure 3.21: *The Apparent Viscosity History during SAG Process*

100% CO₂ Continuous Injection

For the 100% CO_2 continuous injection, 4 pore volume of surfactant solution is injected into core at 4 ft/day before CO_2 is injected. The apparent viscosity of L24-22 compared to water CO_2 foam is shown in **Figure 3-22**.
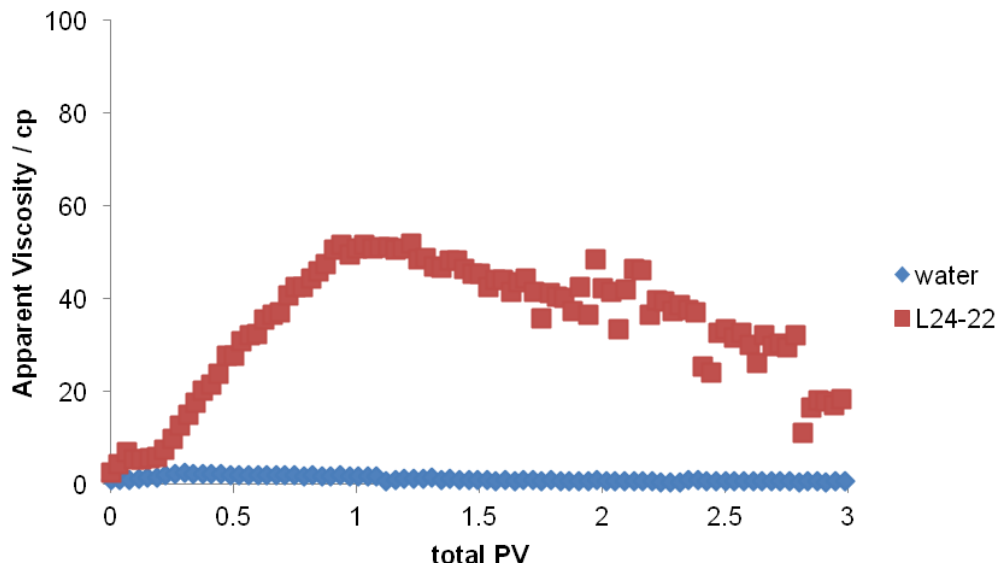
Figure 3-22: *The apparent viscosity history during 100% CO2 continuous injection*

The L24-22 and CO_2 foam is pretty stable. After 3 PV CO_2 injection, the apparent viscosity is still around 20 cp which is much higher than that of water and CO_2 foam.

3.5. Foam propagation in carbonate reservoir core with nonionic CO2 insoluble surfactant (Surfonic L24-22)

A foam core flood was conducted using the nonionic surfactant L24_22 and a reservoir core from San Andres field. The surfactant solution contain was prepared using the composition of East Seminole brine. The synthetic brine

was injected into the core at different flow rates to measure the permeability of the core to brine at 110 °F. The core properties are shown in **Table 3-vi**.

After brine saturation, 0.5 wt% surfactant solution and CO2 were simultaneously injected at 80% foam quality and 4 ft/day (total superficial velocity) for 3.9 injected pore volumes (IPVs). The surfactant injection was then stopped while gas was still injected at the same gas rate.

The core was divided into two equal-length sections for pressure drop monitoring and recording. The sectional pressure drops are shown in **Figure 3-23.** Strong foam developed mainly in the first section of the core (inlet section) over 2 IPVs before it propagate further into the second section (outlet section). Note that the pressure drop in section 2 was about 3 psi which is almost 8 times pressure drop induced by brine flow at 100% brine saturation. This indicates that even though foam in section 2 was weaker than in section 1 during the first 2 IPVs, but it could reduce gas mobility by a factor of 8. The mobility reduction sharply increases further in section 2 after 2 IPV as indicated by the pressure drop profile in **Figure 3-23**.

Surfactant injection was stopped after 3.9 IPVs, which results in a significant decrease in pressure drop over the two sections. However, the pressure drop after 4 IPVs levels off at around 18 psi and 8 psi in section 1 and 2, respectively. These high pressure drop values indicate that gas mobility was reduced several hundred times over several IPVs of pure CO_2 without surfactant due to strong foam flow resistance and blocking. The main conclusion from this core flood is that strong foam could propagate in 32 md reservoir core that represents high permeability zones in East Seminole formation. It is thus possible to improve volumetric sweep efficiency with foam in the formation. However, the observed pressure gradient may be too high for field foam application because it may cause a significant injectivity loss. Lower pressure gradient can be obtained by lowering surfactant concentration.

170

Table 3-vi: *Reservoir core properties*

Length	26.48	cm
Diameter	3.81	cm
Cross-sectional area	11.40	cm^2
Bulk volume	347.55	cm^3
Pore volume	80.34	cm^3
Porosity	23	%
Permeability	32	md
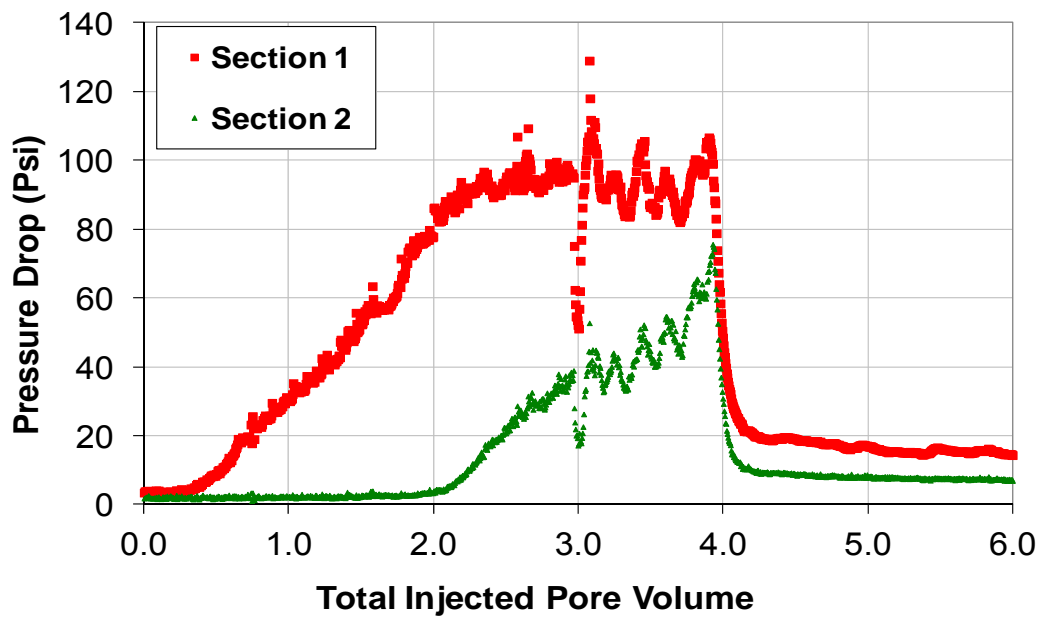
Figure 3-23: *Pressure drop during CO2-surfactant solution injection in San Andres reservoir core*

PART IV- FOAM MODELING AND PROCESS UPSCALING

4.1. Empirical Modeling Approach

4.1.1. Background

The foam model using the fractional flow theory (Cheng, Reme et al. 2000), or the STARS^{TM} foam model (Computer Modeling Group 2007), has been widely used to describe foam flow through porous media in the oil and gas industry. These applications include simulation of surfactant-alternating-gas processes (Renkema and Rossen 2007) and simultaneous injection of surfactant solution and gas (Masalmeh, Wei et al. 2011), simulation of oil displacement by foam (Ashoori, van der Heijden et al. 2010; Liu, Andrianov et al. 2011; Zanganeh, Kam et al. 2011), interpretation of experimental data of co-injection of gas and surfactant solution on the 10 m scale (Vassendan, Holt et al. 1999) and in Berea cores (Chalbaud, Moreno et al. 2002), and simulation of foam process at reservoir scale from the Snorre field in Norway (Skauge, Aarra et al. 2002).

The STARS^{TM} foam model is capable to simulate foam flow in both high-quality and low-quality foam regimes. Cheng and coworks (Cheng, Reme et al. 2000) showed how to fit the parameters to steady-state laboratory coreflood data. We briefly reiterate the procedure as follows. (1) Draw vertical ∇p contours through data in the high-quality regime and horizontal contours in through data in the low-quality regime; (2) Pick one representative ∇p contour in the high-quality regime and find *fmdry* using the equation

$\nabla p = u_w \dfrac{\mu_w}{kk_{rw}(fmdry)}$; (3) Determine $f_g^{\,*}$ (transition foam quality) by the ratio of flow rates at the transition region of high-quality and low-quality regimes; (4) Estimate *fmmob* by using $S_w = fmdry$ and applying the fractional flow equation at the transition foam quality $f_g^{\,*}$.

The above modelling process is physically clear, however, it requires the experimental ∇p data to be vertical in the high-quality regime and horizontal in the low-quality regime in order to draw the contours of ∇p, which is not easily obtained in some cases (Alvarez, Rivas et al. 2001; Kim, Dong et al. 2005). The ∇p contours generated by computer programs are limited to the measured experimental data points, and insufficient data points may cause inaccuracy of the ∇p contours.

Thus, we develop a method to implement the STARS^{TM} foam model without using ∇p contours. Our method is used to model foam flow with a fixed total flow rate of both gas and liquid. Furthermore, we investigate the effect of surfactant concentration on foam strength and verify the function of surfactant in the current foam model in STARS^{TM}. The model can then be used for prediction of foam apparent viscosity as a function of gas fraction and surfactant concentration, in the form of contour plot or 3D plot. This plot will be useful for practical applications to minimize surfactant cost and achieve the required foam strength.

4.1.2. Foam core floods for model verification and improvement

IOS1518: Internal olefin sulfonate 1518 (19.42% wt). This product was manufactured by Stepan (Lot# 18239-032708) with a trade name of Petrostep S-2A.

Silica sand 20/40 is used to pack the porous media in the 1-D glass column. The sand pack has a diameter of 2.58 cm and a length of 27.5 cm. We obtain the permeability of 158.0 darcy and the porosity of 36.0% for this system.

IOS1518 with various concentrations is dissolved in brine and the salinity is fixed at 1.0% wt NaCl. The apparatus is shown in **Figure 4-1**. Surfactant

solution is co-injected with air to the sand pack at a total superficial velocity of 20 ft/day. At the inflow end of the sand pack, a pressure transducer is used to monitor the pressure drop across the porous media. The outflow end of the sand pack is open to atmosphere.

The water saturation in porous media is measured by weighing the sand pack. 0 water saturation corresponds to the weight of fresh sand pack before water injection; 100% water saturation corresponds to the weight of water-saturated sand pack after water injection to the system which was previously filled with CO_2. A linear relationship of the water saturation and the weight of the sand pack is employed to determine the water saturation at a specific weight.
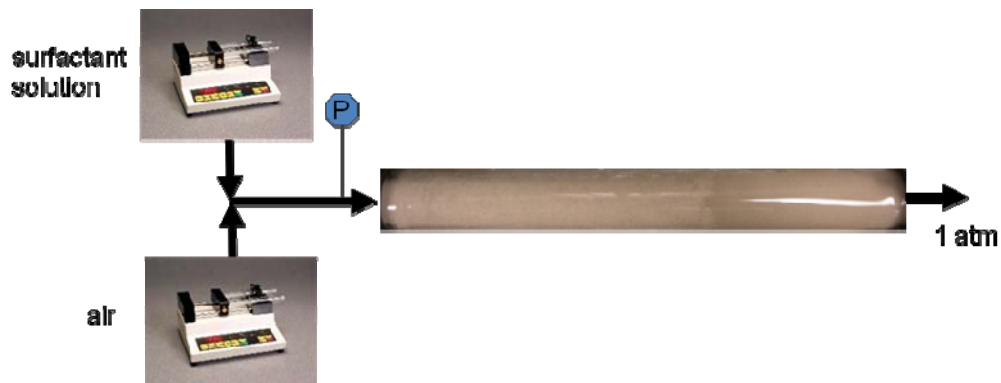
Figure 4-1: *Schematic of the apparatus for foam experiments in this report.*

Before each experiment, we clean the sand pack by alternately injecting 5 PV DI water and CO_2 (1 psi for 30 min) for 3 cycles. Subsequently, 2 PV of surfactant solution is injected to the porous media to minimize surfactant adsorption in our experiments. In each set of experiments with a certain surfactant concentration, the series of experiments start from 99% air injection and end up with 10% air injection. Each time when the surfactant concentration is changed, the cleaning procedure is performed as described in this paragraph.

To minimize the effect of previous flooding on foam strength, at least 4 total pore volumes of surfactant and air are injected in each experiment before we start observing the pressure drop for steady state. When a steady state is reached and the pressure drop is relatively stable, the pressure drop is averaged over the period of the steady state and the foam apparent viscosity is calculated through 1-D Darcy's law.

The effect of foam quality on foam apparent viscosity is shown in **Figure 4-2**. Within the concentration range investigated (0.02% to 0.2% wt), higher surfactant concentration provides higher foam apparent viscosity at the same foam quality. We also observe two distinctive foam regimes: high quality regimes and low quality regimes (Osterloh and Jante Jr 1992; Alvarez, Rivas et al. 2001). The foam apparent viscosity increases when injected gas fraction increases in the low quality regime, and decreases when injected gas fraction increases in the high quality regime. At the boundary of the two regimes, foam obtains maximal apparent viscosity at a given surfactant concentration and total superficial velocity.
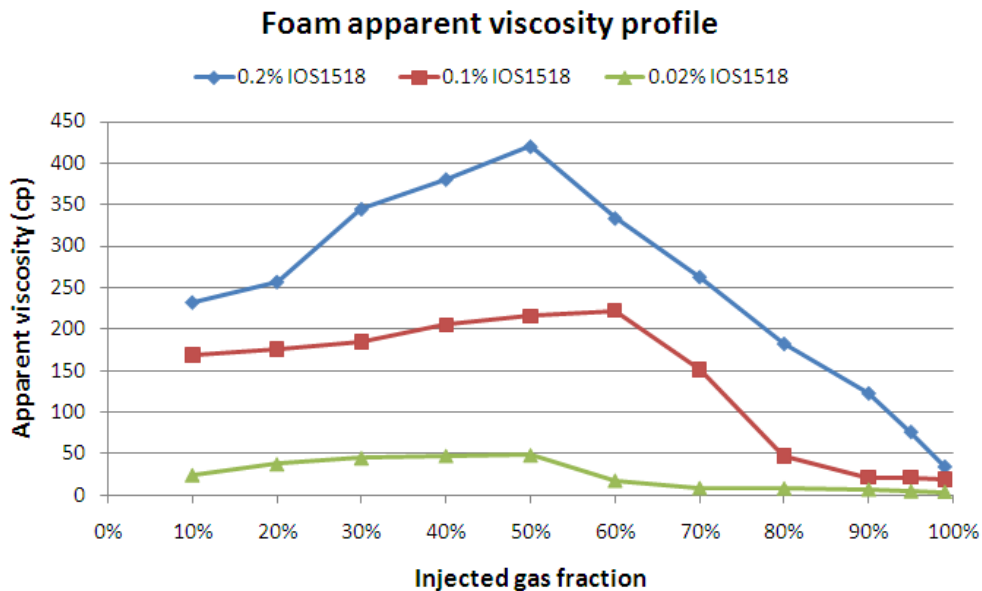
Figure 4-2: *The effect of foam quality on foam apparent viscosity with different surfactant concentrations.*

The effect of foam quality on the saturation of aqueous phase is shown in **Figure 4-3**. It is obvious that with 0.02% IOS1518 the saturation of aqueous phase is much higher than the case with 0.1% or 0.2% IOS1518, indicating that weak foam causes gas channeling and fingering through porous media and leads to high saturation of aqueous phase. Typical fraction flow curves show that higher injected gas fraction results in lower water saturation in the absence of foam. However, within the range of gas fractional flow (10% to 99%) we investigate in the presence of foam, we find that the saturation of aqueous phase is more dependent on foam strength other than gas fractional flow. Surfactant concentration is an important factor that alters foam strength. This result is consistent with the findings in previous studies (Kovscek and Apaydin 2001).
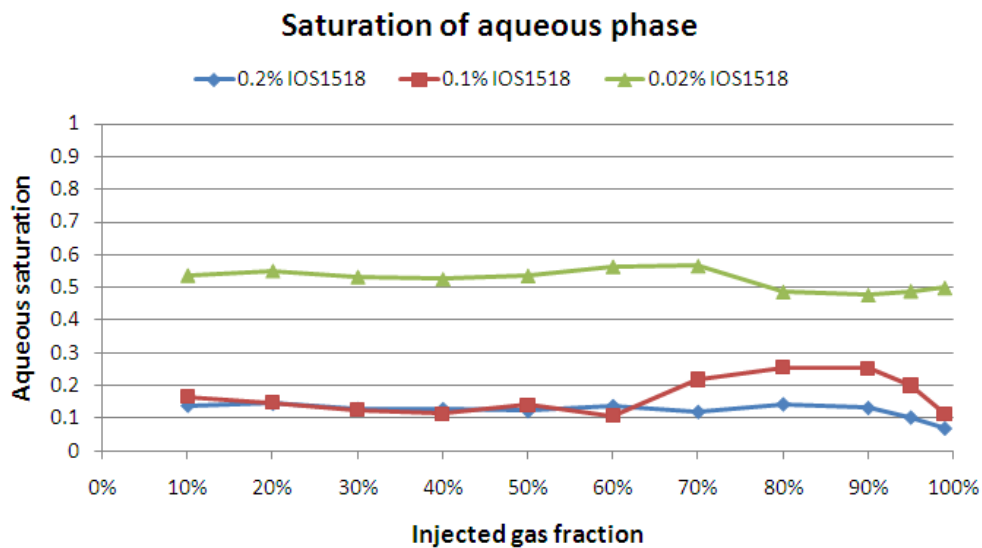
Figure 4-3: The effect of foam quality on aqueous saturation with different surfactant concentrations.

4.1.3. Matching of foam core flood with CMG/STARS foam simulator

We describe the STARS foam model in the following equations:

$$k_{rgD}^f = k_{rg}^f / k_{rg}^{f0} = (k_{rg}^{nf} / k_{rg}^0) \times FM = (\frac{1 - S_{gr} - S_w}{1 - S_{gr} - S_{wc}})^{epg} \times FM$$

where $FM = \dfrac{1}{1 + fmmob \times F_{water} \times F_{surf}}$

$$F_{water} = 0.5 + \frac{\arctan[epdry(S_w - fmdry)]}{\pi}$$

$$F_{surf} = \begin{cases} (\dfrac{C_{sw,inj} C_{swD}}{fmsurf})^{epsurf} & \text{for } C_{swD} < (fmsurf / C_{sw,inj}) \\ 1 & \text{for } C_{swD} \geq (fmsurf / C_{sw,inj}) \end{cases}$$

We realize that there are several parameters to fit and it is important to develop a strategy to perform this task. To fit the parameters in the model, the first step is to focus on the term F_{water} and lay aside the term F_{surf}. Now we only have three parameters to fit: $fmmob$ (reference mobility reduction factor), $fmdry$ (critical aqueous phase saturation) and $epdry$ (a parameter regulating the slope of F_{water} curve near $fmdry$).

If the application focuses on a fixed total superficial velocity, we propose a simple method to fit the parameters. Our process is shown below:

(1) For a fixed surfactant concentration at different foam qualities, identify the transition foam quality $f_g^* = A$ and the maximal foam apparent viscosity $\mu_{foam}^* = B$ from the experimental data.

(2) Draw the contour plot of f_g^* with respect to $fmmob$ and $fmdry$

using the equation $f_g^* = 1 - (1 + \dfrac{k_{rg}^{nf}(S_w = fmdry) \times FM(S_w = fmdry)}{k_{rw}(S_w = fmdry)} \times \dfrac{\mu_w}{\mu_g})^{-1}$.

(3) Draw the contour plot of μ_{foam}^* at $f_g = A$ with respect to $fmmob$ and $fmdry$ using the simulator.

(4) Make superposition of contour plots of f_g^* in Step (2) and μ_{foam}^* in Step (3), and identify $fmmob$ and $fmdry$ where $f_g^* = A$ and $\mu_{foam}^* = B$ cross over.

After getting $fmmob$ and $fmdry$, some fine tunings are needed to find the parameters that gives the best fit to the experimental data. This is mainly due to the fact that Step (2) uses an estimated equation to perform the contour plot rather than the simulator. However, using this estimated equation is time-saving and usually gives good estimate of the parameters.

We show the derivation of the equation in Step (2) for estimating f_g^* as follows. To simplify the derivation we show the case in the absence of capillary pressure ($p_w = p_g$).

$$f_g = \frac{u_g}{u_w + u_g} = \frac{-\dfrac{kk_{rg}(S)}{\mu_g}\dfrac{\partial p_g}{\partial x}}{-\dfrac{kk_{rw}(S)}{\mu_w}\dfrac{\partial p_w}{\partial x} - \dfrac{kk_{rg}(S)}{\mu_g}\dfrac{\partial p_g}{\partial x}} = \frac{k_{rg}(S)/\mu_g}{k_{rw}(S)/\mu_w + k_{rg}(S)/\mu_g}$$

$$= 1 - (1 + \frac{k_{rg}(S)/\mu_g}{k_{rw}(S)/\mu_w})^{-1}$$

$$k_{rw} = k_{rw}^0 \times (\frac{S_w - S_{wc}}{1 - S_{gr} - S_{wc}})^{n_w}$$

$$k_{rg}^f = k_{rg}^{nf} \times FM = k_{rg}^0 \times (1 - \frac{S_w - S_{wc}}{1 - S_{gr} - S_{wc}})^{n_g} \times \frac{1}{1 + fmmob \times F_{water} \times F_{surf}}$$

178

At $S_w = fmdry$

$$f_g^* = 1 - (1 + \frac{k_{rg}^{nf}(S_w = fmdry) \times FM(S_w = fmdry)}{k_{rw}(S_w = fmdry)} \times \frac{\mu_w}{\mu_g})^{-1} \quad …………..…………..(1)$$

We show an example of implementing the above procedure for the case of 0.1% IOS1518 below. In this case, we find $f_g^* = 0.6$ and $\mu_{foam}^* = 222$ cp from the experimental data in **Figure 4-2**. Contour plots of f_g^* and μ_{foam}^* are drawn in **Figure 4-4** and **Figure 4-5**, respectively. Superposition of these two plots results in $fmmob$ of around 18000 and $fmdry$ of around 0.34 where $f_g^* = 0.6$ and $\mu_{foam}^* = 222$ cp cross over. Further tunings of ($fmmob$, $fmdry$) around the region near (18000, 0.34) give the optimal pair of (12000, 0.34) as shown in **Figure 4-6**.
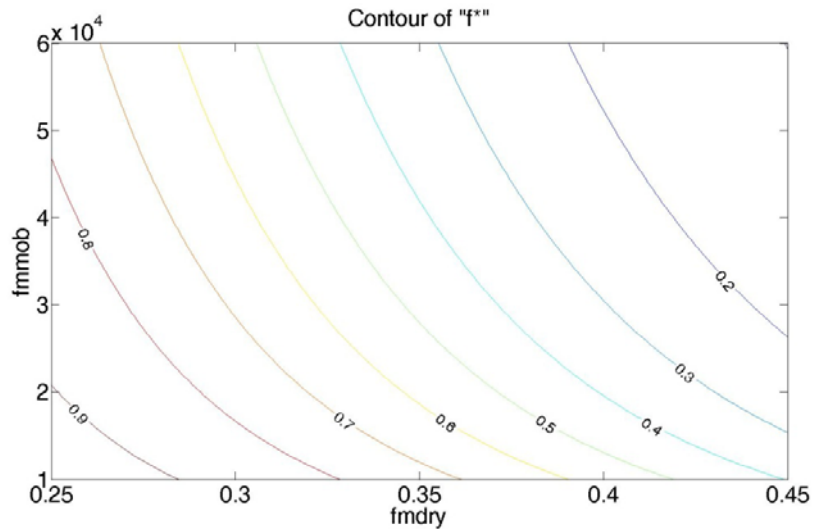
Figure 4-4: *Contour plot of f* as a function of fmmob and fmdry. The plot is based on Eq.(1) shown above.*
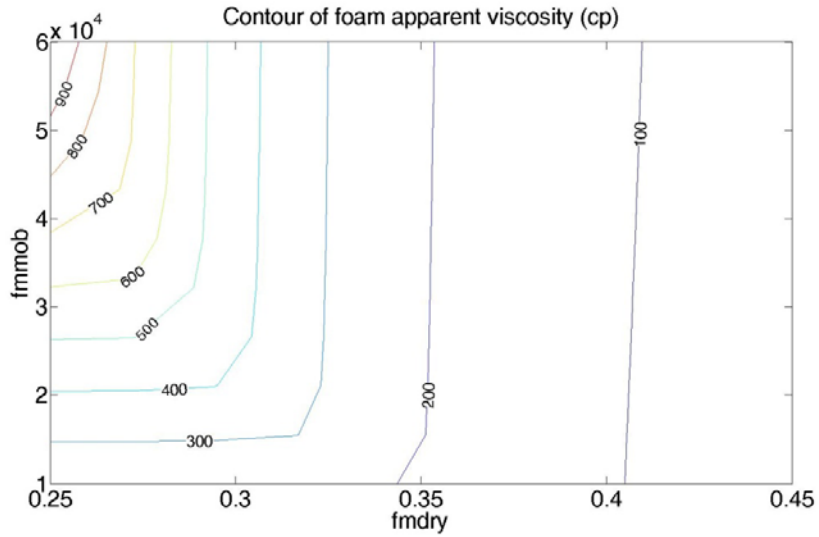
Figure 4-5: *Contour plot of foam apparent viscosity as a function of fmmob and fmdry. Injected gas fraction is set to be 60% and* F_{surf} *is set to be 1.*

The rest of the parameters are not tuned so far and are listed in **Table 4-i**. We use the relative permeability curves in the literature which demonstrated successful foam simulations with the above model (Ashoori, van der Heijden et al. 2010). We also use the value of $epdry$ in the literature (Ashoori, van der Heijden et al. 2010) and will tune it in the future as needed.
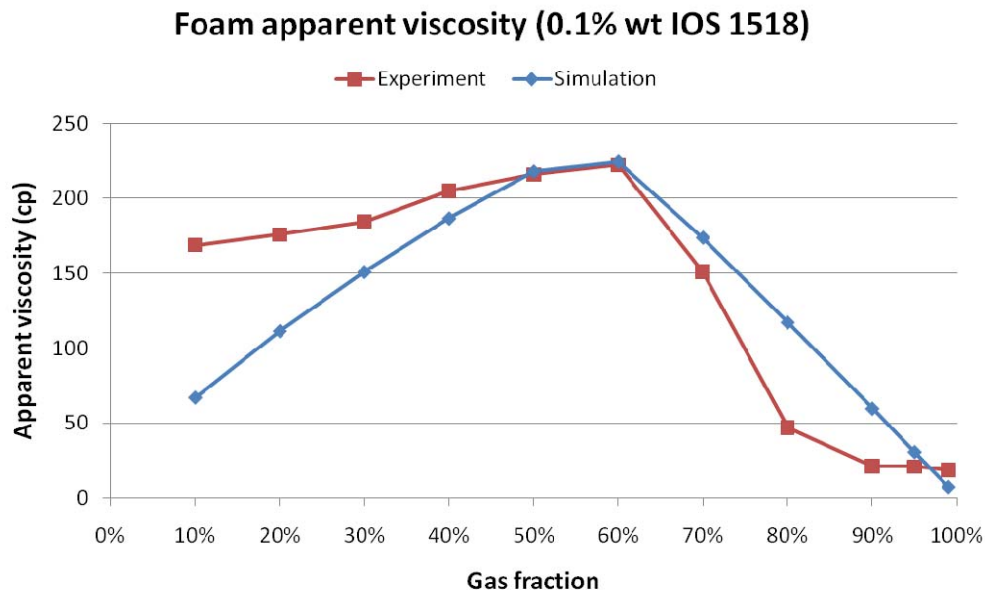
Figure 4-6: *Comparison of foam apparent viscosities between simulation and experiment.* $fmmob$ = 12000; $fmdry$ = 0.34.

The comparison of foam apparent viscosities between simulation and experiment for 0.1% IOS1518 is shown in **Figure 4-6**. The simulation shows good match to the experimental data at 50% and 60% gas fractional flow, and the same trend as the experimental data in both low-quality and high-quality regimes. However, deviations are seen in both regimes between simulation and experiment. A possible explanation in the high-quality regime is the requirement of minimum pressure gradient for strong foam generation is not involved in the foam model. In the low-quality regime, the experimental foam viscosity may be dependent on its previous flooding since we decrease injected gas fraction in the experiment. Hysteresis may be existent in the system if the experiment starts from low gas fractional flow to high gas fractional flow.
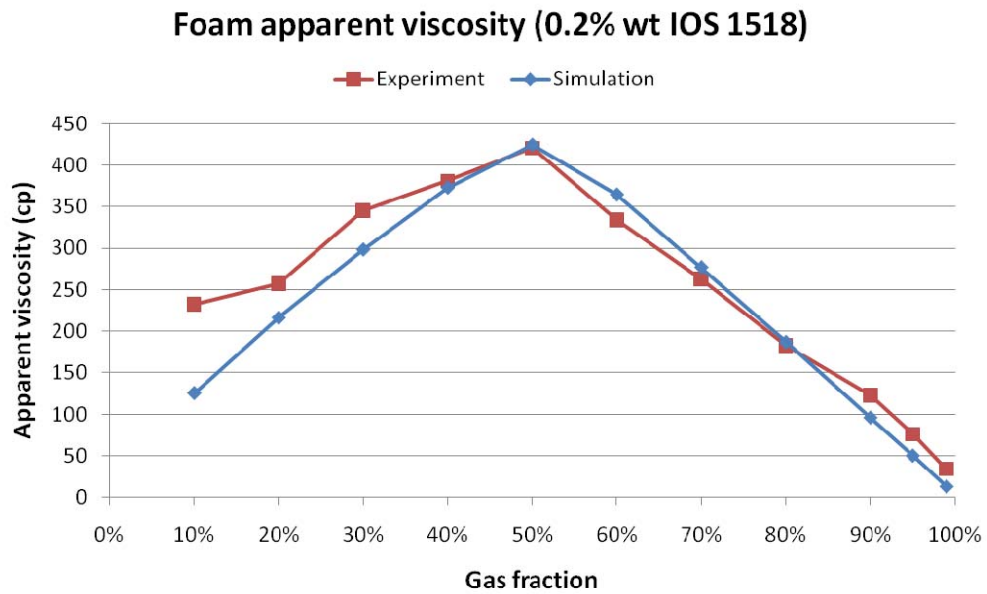
Figure 4-7: Comparison of foam apparent viscosity between simulation and experiment. $fmmob$ = 26000; $fmdry$ = 0.31.

Using the same technique, we also obtain the simulation results for 0.2% IOS1518 in **Figure 4-7**. The match between simulation and experiment is better than the case of 0.1% IOS1518, probably due to the higher foam apparent viscosities in the system with 0.2% IOS1518.

Table 4-i: _Parameters for foam simulation in this report_

Parameter	Value	Comment or reference
NX	100	
$\Delta t_D / \Delta x_D$	0.005	
$fmmob$	--	
$fmdry$	--	
$epdry$	1000	(Ashoori, van der Heijden et al. 2010)
S_{wc}	0.05	
S_{gr}	0.05	
$\mu_w (Pa \cdot s)$	0.001	
$\mu_g (Pa \cdot s)$	0.00002	
k_{rw}^0	0.2	(Ashoori, van der Heijden et al. 2010)

In the case of 0.02% IOS1518, weaker foam is observed compared with 0.1% and 0.2% IOS1518. Similar to the case of 0.1% IOS1518, foam apparent viscosity is overestimated with the simulation results in the high-quality foam region and underestimated in the low-quality foam region as indicated in **Figure 4-8**.
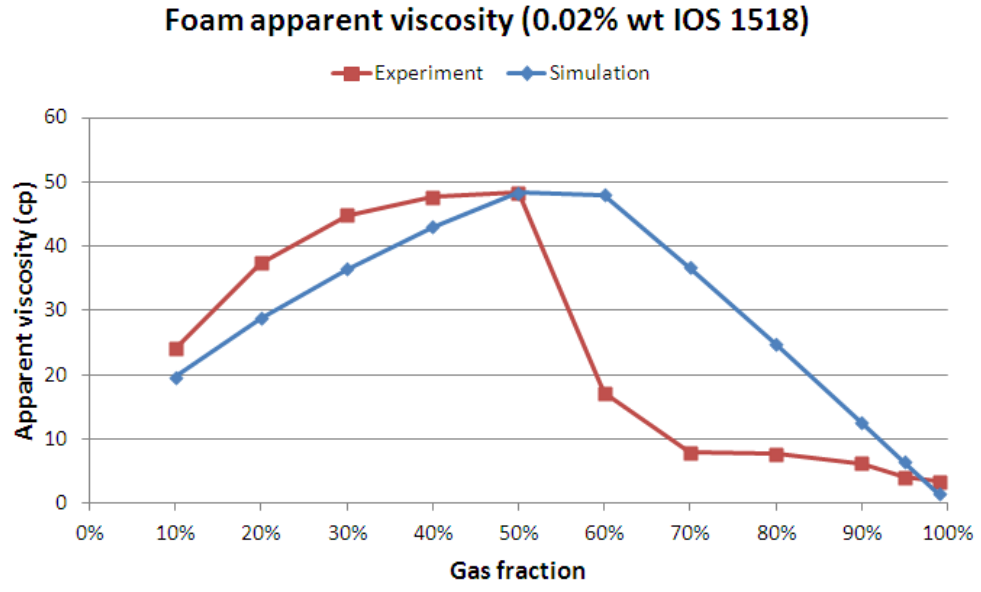
Figure 4-8: Comparison of foam apparent viscosity between simulation and experiment. $fmmob$ = 1900; $fmdry$ = 0.47.

__Table 4-ii:__ Parameters for foam simulation in this report

Parameter	Value	Comment or reference
NX	100	
$\Delta t_D / \Delta x_D$	0.005	
fmmob	--	
fmdry	--	
epdry	1000	(Ashoori, van der Heijden et al. 2010)
S_{wc}	0.05	
S_{gr}	0.05	
$\mu_w(Pa \cdot s)$	0.001	
$\mu_g(Pa \cdot s)$	0.00002	
k_{rw}^0	0.2	(Ashoori, van der Heijden et al. 2010)
k_{rg}^0	0.94	(Ashoori, van der Heijden et al. 2010)
Exponent in k_{rw} curve	4.2	(Ashoori, van der Heijden et al. 2010)
Exponent in k_{rg} curve	1.3	(Ashoori, van der Heijden et al. 2010; Zanganeh, Kam et al. 2011)
ϕ	0.36	

We list the fitting parameters in **Table 4-iii** for all three cases and the results show that *fmmob* increases and *fmdry* decreases when surfactant concentration increases.

Table 4-iii: _Parameters for foam simulation in this report_

IOS 1518 concentration (wt. %)	_fmmob_	_fmdry_
0.02	1900	0.47
0.1	12000	0.34
0.2	26000	0.31

To find a unique set of parameters for the same surfactant, it is necessary to employ the F_{surf} function:

$$F_{surf} = \begin{cases} (\dfrac{C_{sw,inj} C_{swD}}{fmsurf})^{epsurf} & \text{for } C_{swD} < (fmsurf / C_{sw,inj}) \\ 1 & \text{for } C_{swD} \geq (fmsurf / C_{sw,inj}) \end{cases}$$

Apparently the critical surfactant concentration _fmsurf_ to stabilize foam is not achieved in our case, so we need to use the function of $F_{surf} = (\dfrac{C_{sw,inj} C_{swD}}{fmsurf})^{epsurf}$. To utilize this function, a tentative assumption made here is that _fmsurf_ is equal to 1.0 % wt IOS 1518, which needs further experimental investigation. Then we should have the following set of equations to find a unique _fmmob_:

$$fmmob \cdot (\frac{0.2}{1.0})^{epsurf} = 26000 \dotfill (3.1)$$

$$fmmob \cdot (\frac{0.1}{1.0})^{epsurf} = 12000 \dotfill (3.2)$$

$$fmmob \cdot (\frac{0.02}{1.0})^{epsurf} = 1900 \dotfill (3.3)$$

By solving any pair of the above equations we can get _fmmob_ and _epsurf_:

$$\begin{cases} fmmob = 156560 \\ epsurf = 1.1155 \end{cases}$$ with Equations (3.1) and (3.2);

$$\begin{cases} fmmob = 161860 \\ epsurf = 1.1362 \end{cases}$$ with Equations (3.1) and (3.3);

$$\begin{cases} fmmob = 164220 \\ epsurf = 1.1452 \end{cases}$$ with Equations (3.2) and (3.3);

The above results give consistent estimates for $fmmob$ and $epsurf$. By taking the average, we obtain $fmmob = 160880$ and $epsurf = 1.1323$.

However, it is found in **Table 4-iii** that $fmdry$ is also dependent on surfactant concentration in a more exponential way, as shown in **Figure 4-9**.
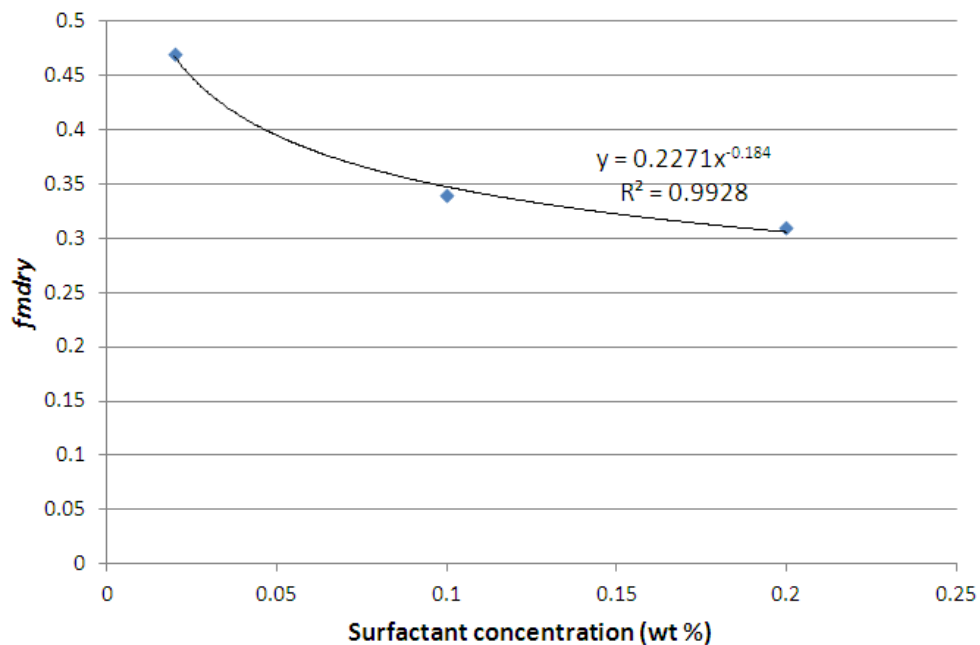
Figure 4-9: *The dependence of* $fmdry$ *on surfactant concentration.*

If an exponent $epfmdry$ is introduced into $fmdry$, one should be able to correlate $fmdry$ with surfactant concentration. Then the function $F_{water} = 0.5 + \dfrac{\arctan[epdry(S_w - fmdry)]}{\pi}$ should be modified to:

$$F_{water} = 0.5 + \frac{\arctan[epdry(S_w - fmdry(\dfrac{C_{sw,inj}C_{swD}}{fmsurf})^{epfmdry})]}{\pi}$$

where $fmdry = 0.2271$ and $epfmdry = -0.184$ according to the fit in **Figure 4-9**. Thus we obtain all the parameters in **Table 4-iv** in addition to **Table 4-ii**:

Table 4-iv: *Parameters fit for foam simulation in the case of IOS 1518*

Parameter	Value	Comment or reference
$fmmob$	160800	
$fmdry$	0.2271	
$epfmdry$	-0.184	
$fmsurf$	1.0%	hypothesized weight percentage
$epsurf$	1.1323	
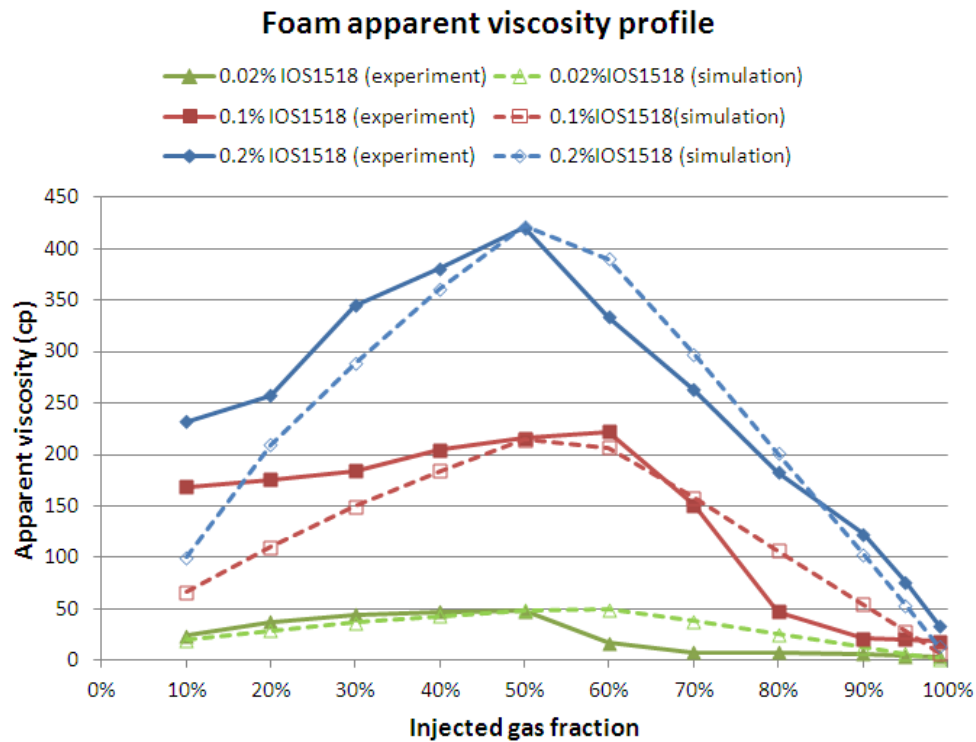
Figure 4-10: *Comparison between experimental data and simulation results of foam apparent viscosity using the parameters in Table 4-ii and Table 4-iii.*

Using the parameters in **Table 4-ii** and **Table 4-iii**, one is able to fit the experimental data with a unique set of parameters as indicated in these two tables. The results are shown in **Figure 4-10**, and a little discrepancy of the simulation results is seen compared with **Figure 4-8**.

Additionally, the surface tension of IOS 1518 is shown in **Figure 4-11**. According to the results, the CMC of this surfactant in 1.0% NaCl at room temperature is around 0.02% wt to 0.03% wt, which is close to the case of weak foam in **Figure 4-8**. Therefore, foam is stronger above the CMC as indicated in the case of 0.1% wt and 0.2% wt IOS1518 solution.
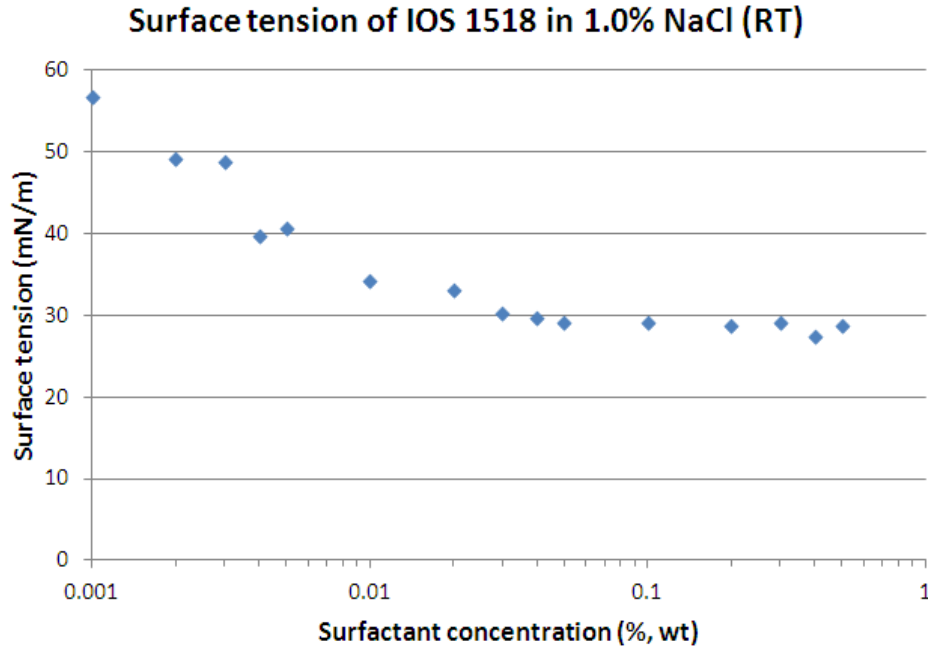
Figure 4-11: Surface tension of IOS 1518 solution with 1.0% wt NaCl at room temperature.

4.1.4. Improvement of calculation of transition foam quality at steady state

The transition foam quality f_g^* is calculated by the fractional flow theory at the critical water saturation $S_w^* = fmdry$ (Cheng et al., 2000). However, this assumption may be questionable based on the inaccurate predictions in our hybrid contour plots. In this study, we discuss what exactly S_w^* is and how to calculate it to enhance the accuracy in our proposed method to match experimental data.

Difference between S_w^* and $fmdry$

At given water saturation (S_w), foam apparent viscosity ($\mu_{foam,app}$) and gas fractional flow (f_g) can be calculated through the following equations in the

absence of capillary pressure:

$$\mu_{foam,app}(S_w) = \frac{1}{\dfrac{k_{rw}(S_w)}{\mu_w} + \dfrac{k_{rg}^f(S_w)}{\mu_g}} \quad \ldots\ldots\ldots\ldots\ldots\ldots\ldots\ldots\ldots\ldots\ldots\ldots\ldots\ldots\ldots\ldots\ldots(3\text{-}1)$$

$$f_g(S_w) = \frac{1}{1 + \dfrac{k_{rw}(S_w)}{\mu_w} \cdot \dfrac{\mu_g}{k_{rg}^f(S_w)}} \quad \ldots\ldots\ldots\ldots\ldots\ldots\ldots\ldots\ldots\ldots\ldots\ldots\ldots\ldots(3\text{-}2)$$

Then $\mu_{foam,app}$ can be plotted as a function of f_g to match experimental data if the appropriate set of parameters is used. Now, the problem is that using the assumption $S_w^* = fmdry$, the transition foam quality (f_g^*) cannot be exactly calculated with Eqn (3-2). However, we can develop an algorithm to calculate S_w^* based on Eqns (3-1) and (3-2) and compare it with $fmdry$. To describe the method, we use the simulation parameters to model the foam behavior of IOS 1518 solution as shown in **Table 4-v**.

Table 4-v: *Parameters for foam simulation in this report*

Parameter	Value	Comment or reference
epdry	1000	(Ashoori et al., 2010)
S_{wc}	0.05	
S_{gr}	0.05	
$\mu_w(Pa \cdot s)$	0.001	
$\mu_g(Pa \cdot s)$	0.00002	
k_{rw}^0	0.2	(Ashoori et al., 2010)

Based on the complete form of Eqn (3-1), we have

$$\mu_{foam,app}(S_w)$$

$$= \cfrac{1}{\cfrac{k_{rw}^0(\cfrac{S_w - S_{wc}}{1 - S_{gr} - S_{wc}})^{n_w}}{\mu_w} + \cfrac{k_{rg}^0(1 - \cfrac{S_w - S_{wc}}{1 - S_{gr} - S_{wc}})^{n_g} \cdot \cfrac{1}{1 + fmmob \times \left\{0.5 + \cfrac{\arctan[epdry(S_w - fmdry)]}{\pi}\right\}}}{\mu_g}}$$

.... (3-3)

Note that the effect of surfactant concentration is not discussed in this step. Using the parameters ($fmmob = 12000$ and $fmdry = 0.34$), the relationship between $\mu_{foam,app}$ and S_w is plotted in **Figure 4-v**.

As shown in **Figure 4-12 (a)**, near $fmdry$, $\mu_{foam,app}$ suddenly increases with S_w until reaching the maximum value, which corresponds to S_w^* and the transition foam quality f_g^* between the high quality regime and the low quality regime. After achieving the maximum apparent viscosity, $\mu_{foam,app}$ slowly decreases with the increase of S_w.

Note that the maximum foam apparent viscosity is not achieved at $S_w = fmdry = 0.3400$, but somewhere nearby ($S_w = S_w^* = 0.3461$). Since f_g changes significantly near $S_w = fmdry$ (**Figure 4-13**), a small change in S_w introduces a substantial amount of change in f_g. This result explains why we don't have the optimized pair of parameters at the cross-over point of two contour plots if $fmdry$ is used as S_w^*.
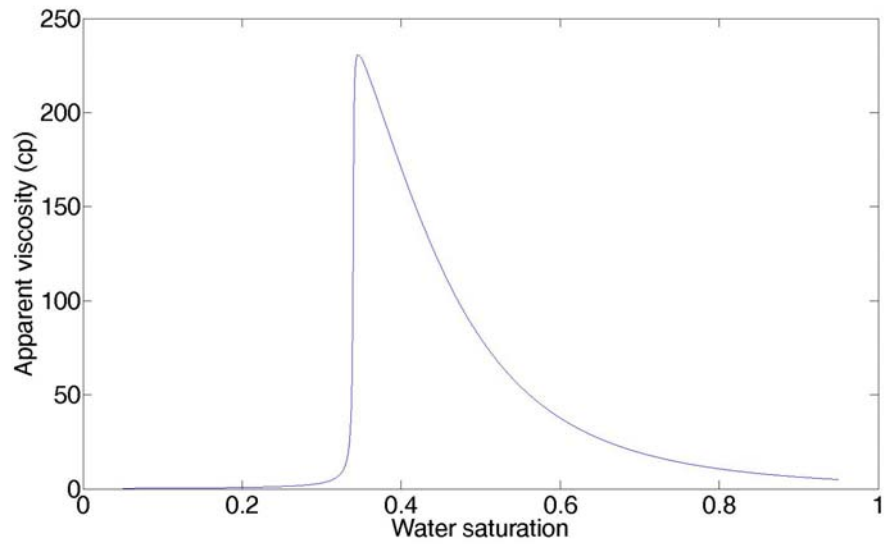
(a)
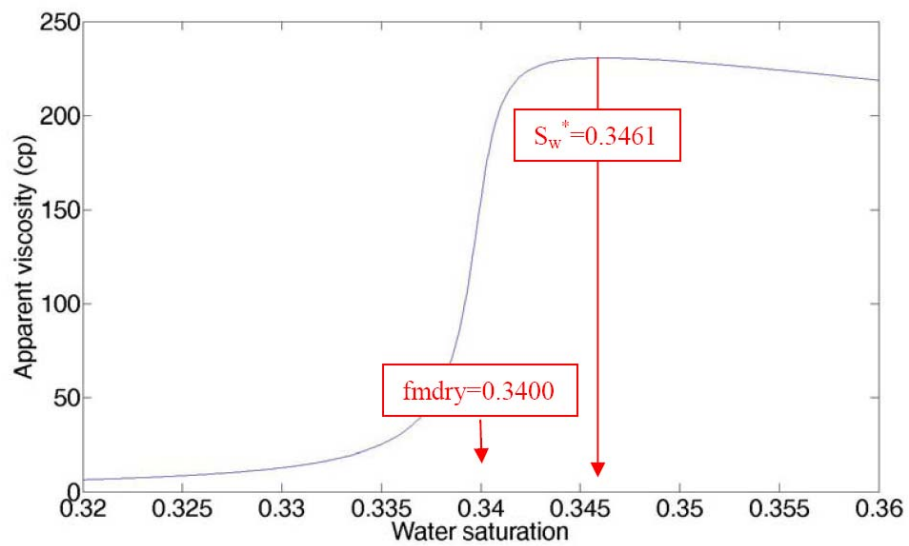
(b)

Figure 4-12: _Foam apparent viscosity as a function of water saturation using_ $fmmob = 12000$ _and_ $fmdry = 0.34$: _(a) full profile; (b) close-up profile near_ $fmdry$. _The rest of the parameters are used as shown in Table 4-v._
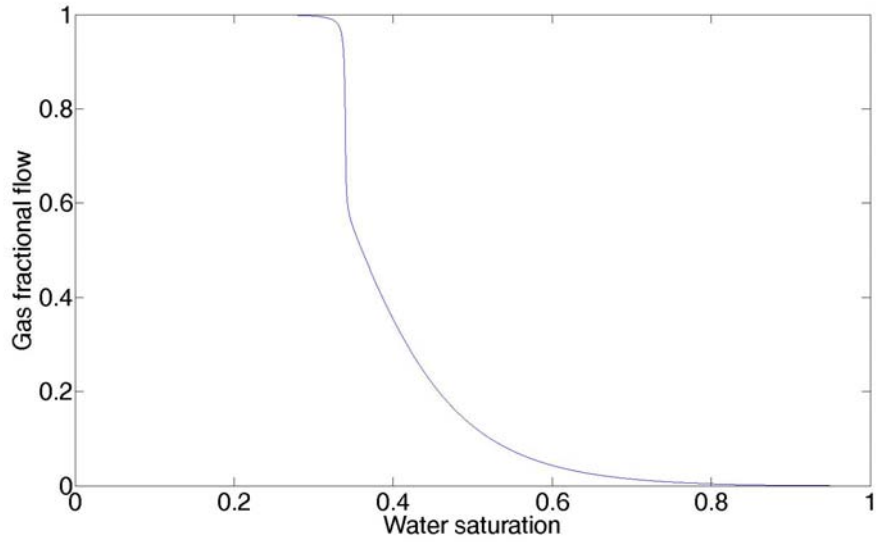
(a)
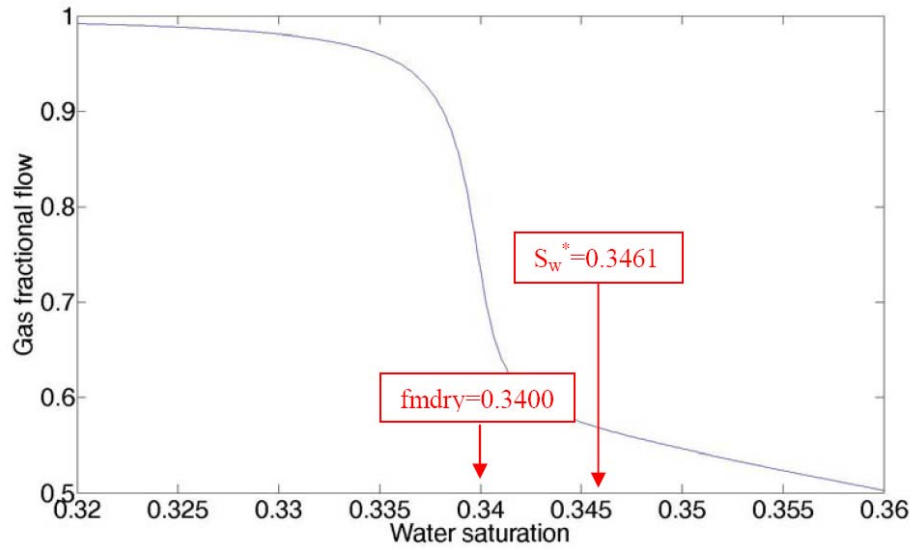
(b)

Figure 4-13: *Gas fractional flow as a function of water saturation using* $fmmob = 12000$ *and* $fmdry = 0.34$ *: (a) full profile; (b) close-up profile near* $fmdry$ *. The rest of the parameters are used as shown in Table 4-v.*

fmdry=0.34

(a)

fmdry=0.34

(b)
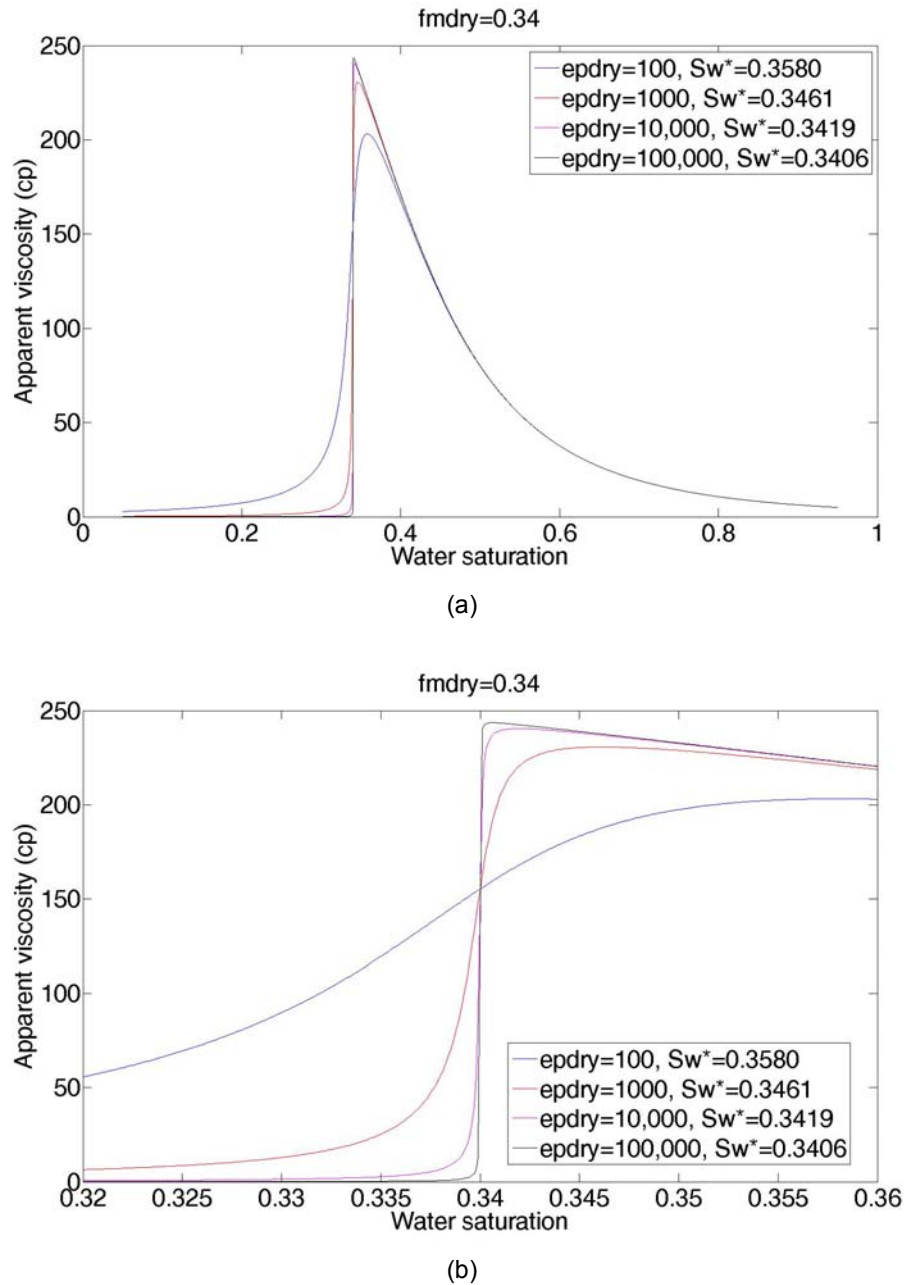
Figure 4-14: *Foam apparent viscosity as a function of water saturation using* $fmmob = 12000$ *and* $fmdry = 0.34$ *: (a) full profile; (b) close-up profile near* $fmdry$ *. Except for* $epdry$ *, the rest of the parameters are used as shown in Table 4-v.*

In fact, S_w^* is a function of $fmmob$, $fmdry$ as well as other parameters listed in **Table 4-v**. We show the change S_w^* of with the parameter $epdry$ as an example in **Figure 4-14**. $epdry$ is a parameter which tunes the slope of f-S

curve near $fmdry$ (see Eqn (3-3)), and **Figure 4-14** indicates that increasing $epdry$ leads to smaller S_w^* and makes S_w^* be closer to $fmdry$.

How to calculate S_w^*

The physical meaning of S_w^* is that at $S_w = S_w^*$, both the transition foam quality f_g^* and the maximum foam apparent viscosity $\mu_{foam,app}^*$ are achieved. The easier way to get S_w^* is to use the function "fminsearch" in MATLAB. For example, if we define the function "findSwstar2" in MATLAB which is the function Eqn (3-3), then

```
fminsearch('findSwstar2',0.05,0.95)

ans =

    0.3461
```

Therefore, when $fmmob = 12000$ and $fmdry = 0.34$ we get $S_w^* = 0.3461$. This result indicates that there is a difference between S_w^* and $fmdry$. We can also verify the above result using the derivative of Eqn (3-3):

$$\frac{d\mu_{foam,app}}{df_g}\bigg|_{f_g=f_g^*} = \frac{\dfrac{d\mu_{foam,app}}{dS_w}\bigg|_{S_w=S_w^*}}{\dfrac{df_g}{dS_w}\bigg|_{S_w=S_w^*}} = 0 \quad...\text{(3-4)}$$

According to Eqn (3-2), f_g is a monotonically decreasing function of S_w, which indicates that $\dfrac{df_g}{dS_w}\bigg|_{S_w=S_w^*} < 0$. Thus Eqn (3-4) is equivalent to Eqn (3-5):

$$\frac{d\mu_{foam,app}}{dS_w}\bigg|_{S_w=S_w^*} = 0 \quad...\text{(3-5)}$$

Since S_w^* is not equal to *fmdry*, we need to find out an way to compute S_w^*. The calculation through Eqn (3-5) is somehow tedious and we use the command "diff" in MATLAB to complete the process:

$$\frac{d\mu_{foam,app}}{dS_w}$$

$$= \{\{k_{rw}^0 \cdot n_w \cdot [-(S_w - S_{wc})/(S_{gr} + S_{wc} - 1)]^{n_w - 1}\}/[\mu_w \cdot (S_{gr} + S_{wc} - 1)] - \{k_{rg}^0 \cdot n_g \cdot [(S_w - S_{wc})$$

$$/(S_{gr} + S_{wc} - 1) + 1]^{n_g - 1}\}/\{\mu_g \cdot \{fmmob \cdot \{\arctan[epdry \cdot (S_w - fmdry)]/\pi + 1/2\} + 1\}$$

$$\cdot (S_{gr} + S_{wc} - 1)\} + \{epdry \cdot fmmob \cdot k_{rg}^0 \cdot [(S_w - S_{wc})/(S_{gr} + S_{wc} - 1) + 1]^{n_g}\}/\{\pi \cdot \mu_g \cdot \{fmmob$$

$$\cdot \{\arctan[epdry \cdot (S_w - fmdry)]/\pi + 1/2\} + 1\}^2 \cdot [epdry^2 \cdot (S_w - fmdry)^2 + 1]\}\}/\{\{k_{rw}^0 \cdot [-(S_w - S_{wc})$$

$$/(S_{gr} + S_{wc} - 1)]^{n_w}\}/\mu_w + \{k_{rg}^0 \cdot [(S_w - S_{wc})/(S_{gr} + S_{wc} - 1) + 1]^{n_g}\}/\{\mu_g \cdot \{fmmob \cdot \{\arctan[epdry$$

$$\cdot (S_w - fmdry)]/\pi + 1/2\} + 1\}\}^2$$

....(3-6)

The results based on Eqn (3-6) is shown in **Figure 4-15**. In **Figure 4-15**, $S_w^* = 0.3461$ is found according to Eqn (3-5) and it is consistent with the finding in **Figure 4-12**. Therefore, we've found a way to calculate S_w^* if other parameters are specified.
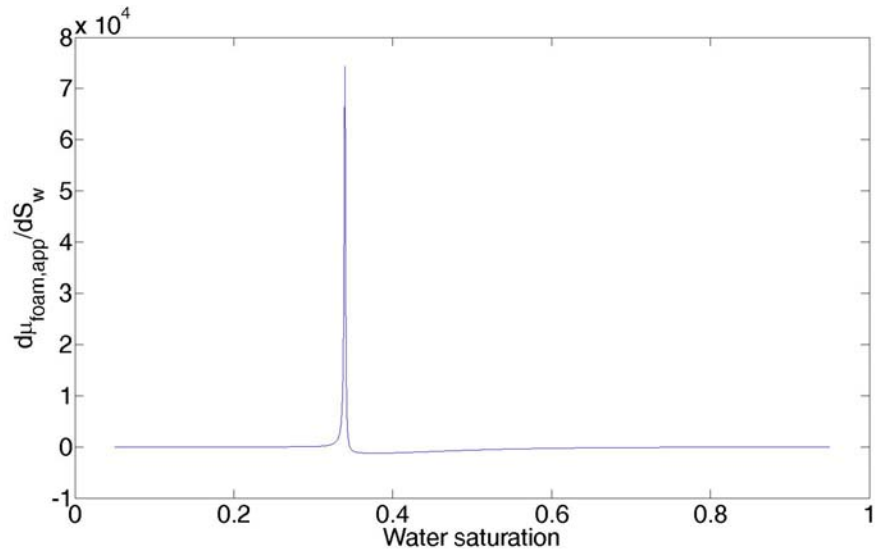
(a)
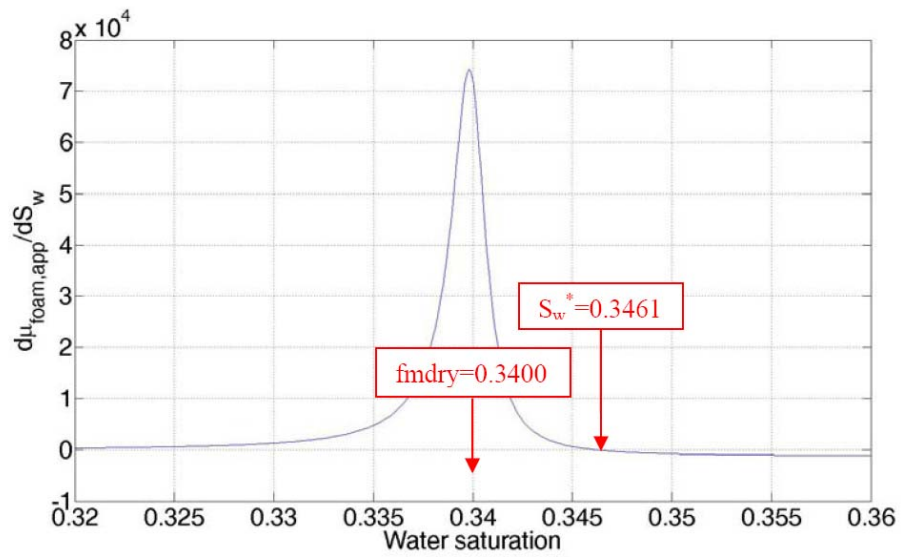
(b)

Figure 4-15: $d\mu_{foam,app}/dS_w$ as a function of water saturation using $fmmob = 12000$ and $fmdry = 0.34$: (a) full profile; (b) close-up profile near $fmdry$.

Comparing the new algorithm with the old algorithm
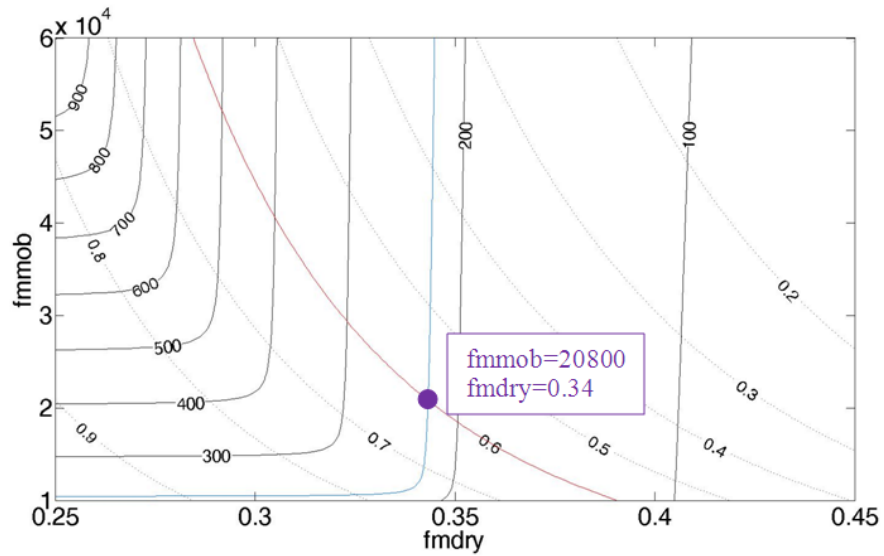
(a) old algorithm: S_w^* is assumed to be equal to $fmdry$
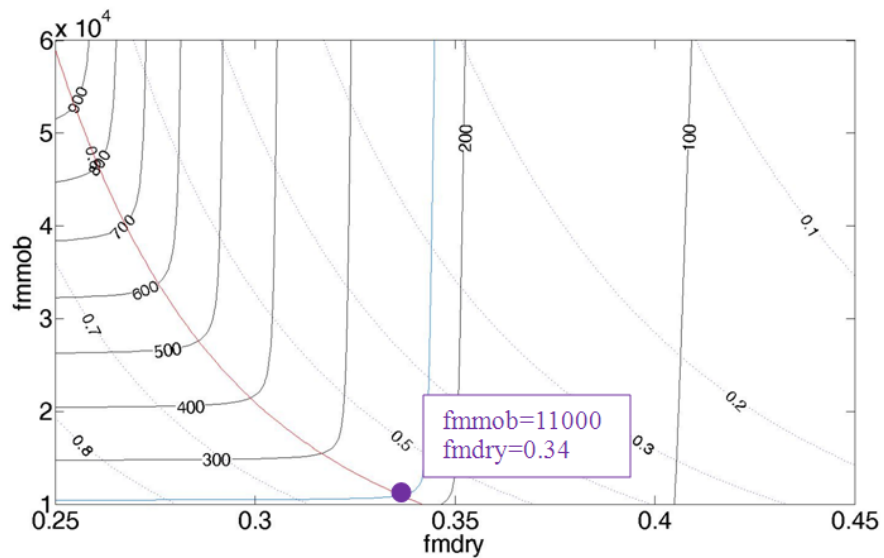
(b) new algorithm: S_w^* is calculated through Eqn (2-5)

__Figure 4-16__: Comparison of the hybrid contour plots between (a) old and (b) new algorithms. The purple point indicates where the two contour plots cross over.
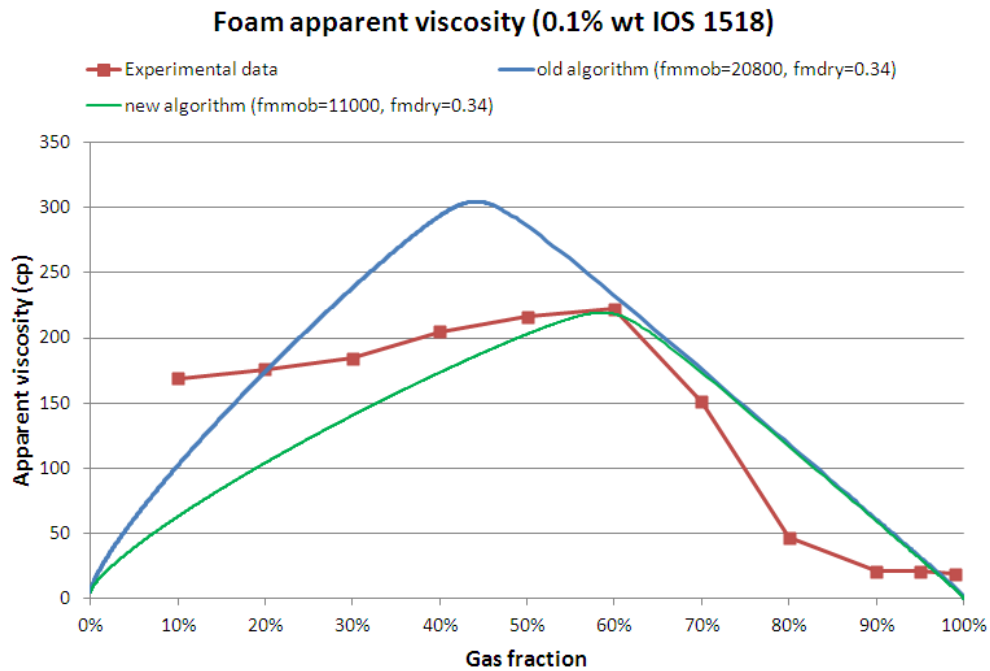
Figure 4-17: Prediction of foam apparent viscosity by the new (S_w^* is calculated through Eqn (3-5)) and old (S_w^* is assumed to be equal to *fmdry*) algorithms.

If S_w^* is calculated through Eqn (3-5) rather than assumed to be *fmdry*, the calculation of hybrid contour plot is greatly enhanced as shown in **Figure 4-16** and **Figure 4-17**.

Flow chart for matching foam flow at steady state

Now we summarize the entire procedure. The problem reduces to 3 equations with three unknown variables: S_w^*, *fmmob* and *fmdry*:

$$\mu^*_{foam,app}(measured) = \cfrac{1}{\cfrac{k_{rw}(S^*_w)}{\mu_w} + \cfrac{k^f_{rg}(S^*_w, fmmob, fmdry)}{\mu_g}} \quad\text{.....................(3-7)}$$

$$f^*_g(measured) = \cfrac{1}{1 + \cfrac{k_{rw}(S^*_w)}{\mu_w} \cdot \cfrac{\mu_g}{k^f_{rg}(S^*_w, fmmob, fmdry)}} \quad\text{.....................(3-8)}$$

$$\max \mu_{foam,app}(S_w) = \mu_{foam,app}(S^*_w) \quad\text{....................................(3-9)}$$

There is more than one way to solve Eqns (3-7) to (3-9). However, one should keep in mind that only the roots which satisfy $S_{wc} < S^*_w < 1 - S_{gr}$, $fmmob > 0$ and $S_{wc} < fmdry < 1 - S_{gr}$ are acceptable for the estimation of the parameters in the foam model. Using the hybrid contour method we proposed in **Figure 4-16**, a reasonable range of the initial guess of the parameters ($fmmob$ and $fmdry$) can be specified, which makes the problem easier to solve. The flow chart of the entire procedure is shown in **Figure 4-17**.

Obtain $f_g{}^* = f_{g,measured}{}^*$ and $\mu_{foam,app}{}^* = \mu_{foam,\,measured}{}^*$ from experimental data

Using Equations (1) and (2) to determine a contour plot 1 of $f_g{}^*$ as a function of fmmob and fmdry

$$\max \mu_{foam,app}(S_w) = \mu_{foam,app}(S_w^*) \qquad \text{Eqn (1)}$$

$$f_g^* = \frac{1}{1 + \dfrac{k_{rw}(S_w^*)}{\mu_w} \cdot \dfrac{\mu_g}{k_{rg}^f(S_w^*)}} \qquad \text{Eqn (2)}$$

Using Equations (3) and (4) to determine a contour plot 2 of $\mu_{foam,app}$ as a function of fmmob and fmdry

$$f_{g,measured}^* = \frac{1}{1 + \dfrac{k_{rw}(S_w)}{\mu_w} \cdot \dfrac{\mu_g}{k_{rg}^f(S_w)}} \qquad \text{Eqn (3)}$$

$$\mu_{foam,app}(S_w) = \frac{1}{\dfrac{k_{rw}(S_w)}{\mu_w} + \dfrac{k_{rg}^f(S_w)}{\mu_g}} \qquad \text{Eqn (4)}$$

Perform superposition of contour plots 1 and 2 and indentify the point (fmmob, fmdry) where $f_g{}^* = f_{g,measured}{}^*$ in contour plot 1 and $\mu_{foam,app} = \mu_{foam,\,measured}{}^*$ in contour plot 2 cross over

Figure 4-18: *Flow chart for matching foam flow in porous media at steady state.*

4.1.5. Estimation of parameters in STARS foam model using a non-graphical method

Description of the procedure

Table 4-vi: Parameters for foam simulation in this work

Parameter	Value	Reference
$epdry$	1000	(Ashoori, van der Heijden et al. 2010; Zanganeh, Kam et al. 2011)
S_{wc}	0.04	(Kam, Nguyen et al. 2007)
S_{gr}	0	(Kam, Nguyen et al. 2007)
$\mu_w (Pa \cdot s)$	0.0010	(Bruges, Latto et al. 1966)
$\mu_g (Pa \cdot s)$	0.00002	(Lemmon and Jacobsen 2004)
$,_0$	0.79	(Kam, Nguyen et al. 2007)

The parameters are shown in **Table 4-vi**. Note that we use a preset value of $epdry$ (1000) in this report. The effect of $epdry$ on foam modeling will be discussed in a separate later. We already learned that

$$\mu_{foam,app} = \frac{-k\nabla p}{\dfrac{-kk_{rw}\nabla p}{\mu_w} + \dfrac{-kk_{rg}^{f}\nabla p}{\mu_g}} = \frac{1}{\dfrac{k_{rw}(S_w)}{\mu_w} + \dfrac{k_{rg}^{f}(S_g)}{\mu_g}} \quad\text{.. (3-1)}$$

$$f_g = \frac{u_g}{u_w + u_g} = \frac{1}{1 + \dfrac{k_{rw}(S_w)}{\mu_w} \cdot \dfrac{\mu_g}{k_{rg}^{f}(S_g)}} \quad\text{.. (3-2)}$$

$$S_w + S_g = 1 \quad\text{.. (3-3)}$$

$$k_{rw} = k_{rw}^0 \left(\frac{S_w - S_{wc}}{1 - S_{gr} - S_{wc}}\right)^{n_w} \quad \text{..(3-4)}$$

$$k_{rg}^f = k_{rg}^0 \left(1 - \frac{S_w - S_{wc}}{1 - S_{gr} - S_{wc}}\right)^{n_g} \cdot \frac{1}{1 + fmmob \times \left\{0.5 + \dfrac{\arctan[epdry(S_w - fmdry)]}{\pi}\right\}} \quad \text{.........(3-5)}$$

Note that the definition of the transition water saturation S_w^* is:

$$\max_{S_w} \mu_{foam,app}(S_w, fmmob, fmdry) = \mu_{foam,app}(S_w^*, fmmob, fmdry) \quad \text{...............................(3-6)}$$

The goal is to solve Eqns (3-7) and (3-8) simultaneously to obtain $fmmob$ and $fmdry$ without using the hybrid contour plot method (Ma, Biswal et al. 2012).

$$\mu_{foam,app}^*(measured) = \frac{1}{\dfrac{k_{rw}(S_w^*)}{\mu_w} + \dfrac{k_{rg}^f(S_w^*, fmmob, fmdry)}{\mu_g}} \quad \text{...................................(3-7)}$$

$$f_g^*(measured) = \frac{1}{1 + \dfrac{k_{rw}(S_w^*)}{\mu_w} \cdot \dfrac{\mu_g}{k_{rg}^f(S_w^*, fmmob, fmdry)}} \quad \text{...(3-8)}$$

We show how to match the experimental data ($f_g^* = 0.5$ and $\mu_{foam,app}^* = 420.5 \ cp$) using the parameters listed in **Table 4-vi** as an example. From Eqns (3-7) and (3-8), we get

$$k_{rw}(S_w^*) = \frac{\mu_w(1 - f_g^*(measured))}{\mu_{foam,app}^*(measured)} \quad \text{..(3-9)}$$

$$k_{rg}^f(S_w^*, fmmob, fmdry) = \frac{\mu_g f_g^*(measured)}{\mu_{foam,app}^*(measured)} \quad \text{...(3-10)}$$

Based on Eqns (3-4) and (3-9) we get

$$S_w^* = S_{wc} + (1 - S_{gr} - S_{wc}) \left[\frac{\mu_w (1 - f_g^*(measured))}{k_{rw}^0 \mu_{foam,app}^*(measured)} \right]^{\frac{1}{n_w}} = 0.0749 \quad .... \text{(3-11)}$$

Thus we obtain the value of the transition water saturation $S_w^* = 0.0749$. Now only two

unknown variables, $fmmob$ and $fmdry$, need to be solved.

Based on Eqns (3-5) and (3-10) we get

$$\frac{\mu_g f_g^*(measured)}{\mu_{foam,app}^*(measured)} = k_{rg}^0 (1 - \frac{S_w^* - S_{wc}}{1 - S_{gr} - S_{wc}})^{n_g} \cdot \frac{1}{1 + fmmob \times \left\{ 0.5 + \frac{\arctan[epdry(S_w^* - fmdry)]}{\pi} \right\}}$$

Then $fmmob$ is a function of $fmdry$ only in Eqn (3-12):

$$fmmob = \frac{\frac{k_{rg}^0 \mu_{foam,app}^*(measured)}{\mu_g f_g^*(measured)} (1 - \frac{S_w^* - S_{wc}}{1 - S_{gr} - S_{wc}})^{n_g} - 1}{0.5 + \frac{\arctan[epdry(S_w^* - fmdry)]}{\pi}} \quad ....\ldots.........\text{(3-12)}$$

However, Eqn (312) only does not provide a unique solution of $fmmob$ and $fmdry$. On

the other hand, we need to make sure that the definition of the transition water saturation

S_w^* (Eqn (3-6)) is satisfied, which is

$$\max_{S_w} \mu_{foam,app}(S_w, fmmob, fmdry)$$

$$= \frac{1}{\left. \frac{k_{rw}^0 (\frac{S_w - S_{wc}}{1 - S_{gr} - S_{wc}})^{n_w}}{\mu_w} + \frac{k_{rg}^0 (1 - \frac{S_w - S_{wc}}{1 - S_{gr} - S_{wc}})^{n_g} \cdot \frac{1}{1 + fmmob \times \left\{ 0.5 + \frac{\arctan[epdry(S_w - fmdry)]}{\pi} \right\}}}{\mu_g} \right|_{S_w = S_w^*}}$$

$$\ldots\ldots\ldots\ldots\ldots\ldots\ldots\ldots\ldots\ldots\ldots\ldots\ldots\ldots\ldots\ldots\ldots\ldots\ldots\ldots.\text{(3-13)}$$

Using the symbolic algorithm "diff" in MATLAB, we obtain the derivative of the

$\mu_{foam,app}$ - S_w function and equate it to be 0 at $S_w = S_w^*$ to obtain the maximum apparent

viscosity:

$$\left. \frac{d\mu_{foam,app}}{dS_w} \right|_{S_w = S_w^*}$$

$$= \{\{k_{rw}^0 \cdot n_w \cdot [-(S_w^* - S_{wc})/(S_{gr} + S_{wc} - 1)]^{n_w - 1}\}/[\mu_w \cdot (S_{gr} + S_{wc} - 1)] - \{k_{rg}^0 \cdot n_g \cdot [(S_w^* - S_{wc})$$

$$/(S_{gr} + S_{wc} - 1) + 1]^{n_g - 1}\}/\{\mu_g \cdot \{fmmob \cdot \{\arctan[epdry \cdot (S_w^* - fmdry)]/\pi + 1/2\} + 1\}$$

$$\cdot (S_{gr} + S_{wc} - 1)\} + \{epdry \cdot fmmob \cdot k_{rg}^0 \cdot [(S_w^* - S_{wc})/(S_{gr} + S_{wc} - 1) + 1]^{n_g}\}/\{\pi \cdot \mu_g \cdot \{fmmob$$

$$\cdot \{\arctan[epdry \cdot (S_w^* - fmdry)]/\pi + 1/2\} + 1\}^2 \cdot [epdry^2 \cdot (S_w^* - fmdry)^2 + 1]\}\}/\{\{k_{rw}^0 \cdot [-(S_w^* - S_{wc})$$

$$/(S_{gr} + S_{wc} - 1)]^{n_w}\}/\mu_w + \{k_{rg}^0 \cdot [(S_w^* - S_{wc})/(S_{gr} + S_{wc} - 1) + 1]^{n_g}\}/\{\mu_g \cdot \{fmmob \cdot \{\arctan[epdry$$

$$\cdot (S_w^* - fmdry)]/\pi + 1/2\} + 1\}\}\}^2$$

$$= 0$$

………………………………………………………………………….………….(3-14)

Note that $fmmob$ in Eqn (3-14) needs to be substituted with Eqn (3-12) in order to

solve $fmdry$. Then we use the function "fzero" in MATLAB to find $fmdry = 0.0725$

through Eqn (3-14).

After getting S_w^* and $fmdry$, $fmmob$ can be easily calculated through Eqn

(3-12). Finally, we obtain $S_w^* = 0.0749$, $fmdry = 0.0725$, and $fmmob = 44182$. This

result is very close to the one obtained through the hybrid contour plot method

($fmdry = 0.072$, and $fmmob = 44200$) considering the differences in significant digits

between these two methods.

4.1.6. Discussion on selection of $epdry$ for steady state foam modeling

3-parameter estimation.

For a specific set of data, we can estimate $fmmob$, $fmdry$, and $epdry$

simultaneously using the MATLAB function "fminsearch". In this case, the objective function is:

$$\min f(fmmob, fmdry, epdry) = \sum_{i=1}^{n} \left(\frac{\mu_{i,calculated} - \mu_{i,measured}}{\mu_{i,measured}} \right)^2 \qquad \text{...............(3-1)}$$

To perform the search, we need an initial guess. Let's take the data for 0.2 wt% IOS as an example (n=11 in Eqn (3-1)). If we use a preset value of $epdry = 1000$, we can match the transition foam data ($f_g^* = 0.5$ and $\mu_{foam,app}^* = 420.5 \; cp$) using the approach proposed above and the rest of the parameters in **Table 4-vii**. We obtain $fmmob = 44282$ and $fmdry = 0.1014$ with a preset value of $epdry = 1000$.

Table 4-vii: *Parameters for foam simulation in this work*

Parameter	Value	Reference
S_{wc}	0.04	
S_{gr}	0	
$\mu_w (Pa \cdot s)$	0.0010	(Bruges et al., 1966)
$\mu_g (Pa \cdot s)$	0.00002	(Lemmon and Jacobsen, 2004)
k_{rw}^0	0.79	(Kam et al., 2007)
k_{rg}^0	1.0	(Kam et al., 2007)
n_w	1.96	(Kam et al., 2007)
n_g	2.29	(Kam et al., 2007)

Now let's use an initial value of ($fmmob = 44182$, $fmdry = 0.0725$ and $epdry = 1000$) to start the multi-dimensional search. We get the parameters ($fmmob = 61528$, $fmdry = 0.0757$ and $epdry = 576.1$) through the MATLAB algorithm. The result is shown in **Figure 4-19**. The model does provide a good fit to all the data points; however, this approach misses the fit to the transition foam quality (around 10% absolute error) as shown in **Figure 4-19**, which may be caused by the possible hysteresis due to trapped gas effect in the low-quality foam regime of the experimental data. Meanwhile, the finding of $epdry = 430.1$ indicates that a small value of $epdry$ (less than 1000) may show a good fit to this set of experimental data.
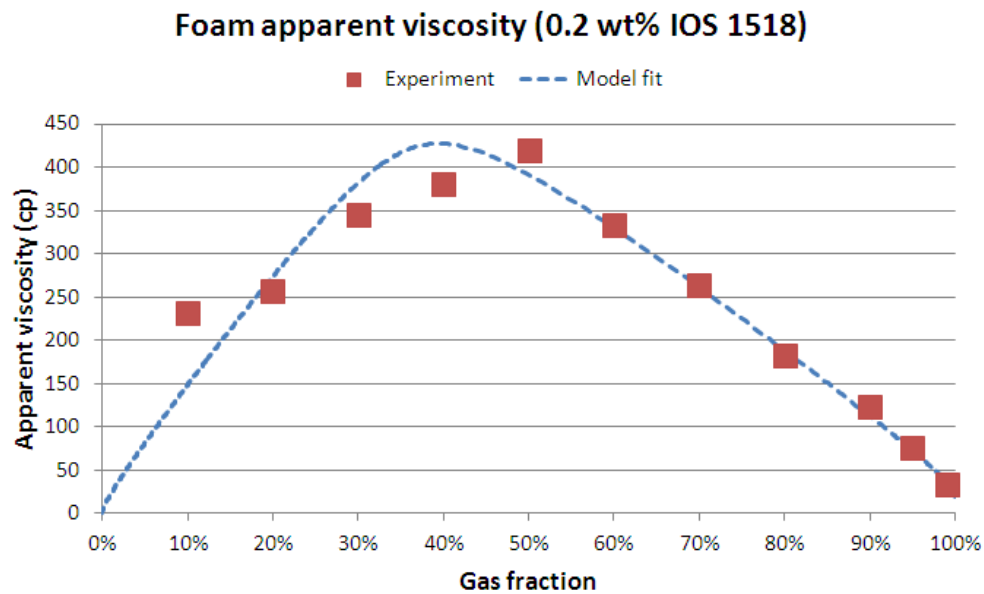
Figure 4-19: *Model fit to experimental data (0.2 wt% IOS1518) using multi-dimensional 3-parameter estimation. ($fmmob = 61528$, $fmdry = 0.0757$ and $epdry = 576.1$)*

More importantly, another problem exists in this three-parameter fitting: local minimum. **Figure 4-20** illustrates this issue. The "model fit 1" in **Figure**

4-20 is essentially the same as the fit in **Figure 4-19**. We use 3 different sets of initial data ((1) $fmmob = 44182$, $fmdry = 0.0725$ and $epdry = 1000$; (2) $fmmob = 2254600$, $fmdry = 0.093$ and $epdry = 1000$; (3) $fmmob = 38958$, $fmdry = 0.0747$ and $epdry = 1000000$) and get the same fitting results ($fmmob = 61528$, $fmdry = 0.0757$ and $epdry = 576.1$) with the function "fminsearch" in MATLAB. However, when we use ($fmmob = 2256000000$, $fmdry = 0.0934$ and $epdry = 1000000$) as the initial guess in "fminsearch" the algorithm calculated another "optimized" results: "model fit 2": ($fmmob = 405070000$, $fmdry = 0.0919$ and $epdry = 1546100$). Apparently, "model fit 2" in **Figure 4-20** is way worse than "model fit 1". Therefore, care is needed to select the appropriate initial guess in the "fminsearch" function.
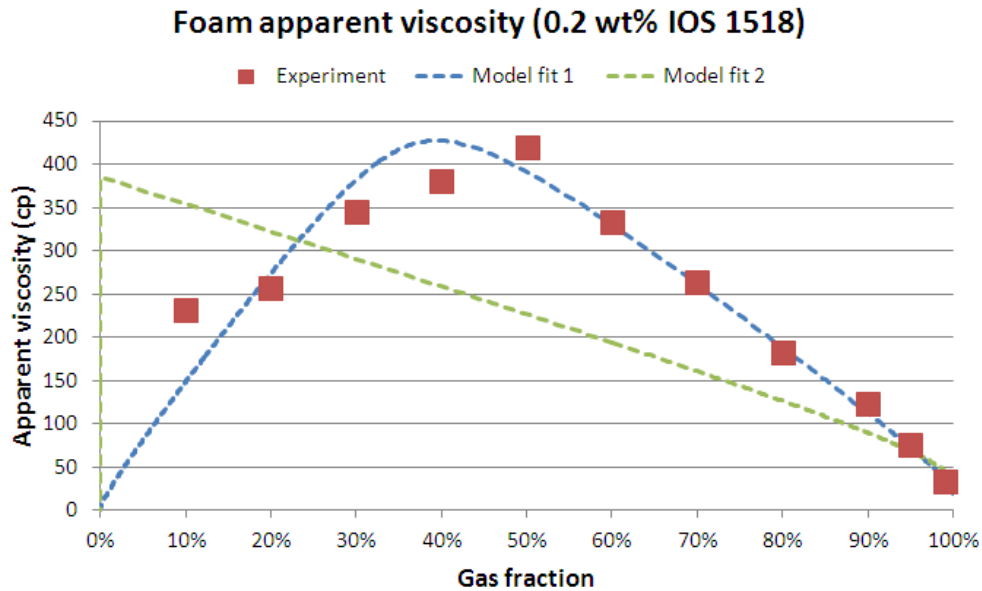
Figure 4-20: _Model fit to experimental data (0.2 wt% IOS1518) using multi-dimensional 3-parameter estimation. Model fit 1:_ $fmmob = 61528$, $fmdry = 0.0757$ _and_ $epdry = 576.1$. _Initial guess in MATLAB for Model fit 1: (1)_ $fmmob = 44182$, $fmdry = 0.0725$ _and_ $epdry = 1000$; _(2)_ $fmmob = 2254600$, $fmdry = 0.093$ _and_ $epdry = 1000$; _(3)_ $fmmob = 38958$, $fmdry = 0.0747$ _and_ $epdry = 1000000$. _Model fit 2:_ $fmmob = 405070000$, $fmdry = 0.0919$ _and_ $epdry = 1546100$. _Initial guess in MATLAB for Model fit 2:_ $fmmob = 2256000000$, $fmdry = 0.0934$ _and_ $epdry = 1000000$._

The fitting method focusing on the transition foam data is still valuable for a preliminary estimation of the parameters, as the strongest foam is possibly least affected by trapped gas, minimum pressure gradient and gravity segregation. These effects can be evaluated with additional experiments and added to the model fit if they significantly affect the model fit.

Scan *fmmob* **and** *fmdry* **at different** *epdry* **using 2-parameter estimation.**

We evaluate the model prediction using the least square method. In **Figure 4-19**, we have 11 experimental data points, and the objective is the residual sum of squares (RSS):

$$RSS = \sum_{i=1}^{11} \left(\frac{\mu_{i,calculated} - \mu_{i,measured}}{\mu_{i,measured}} \right)^2$$

Table 4-viii shows the calculation of RSS with different *epdry*. *fmmob* and *fmdry* are obtained using the 2-parameter fitting method to the peak point. As shown in **Table 4-viii**, *fmmob* increases with *epdry*, but *fmdry* does not change much.

Table 4-viii: *Calculation of parameters and RSS with preset* epdry *using the hybrid contour plot method*

epdry	fmmob	fmdry	S_W*	RSS
100	68190	0.0727	0.0748	20.8132
250	51645	0.0709	0.0749	2.0723
500	46958	0.0716	0.0748	0.4444
1,000	44202	0.0724	0.0748	0.4981
5,000	41052	0.0737	0.0748	1.0300
10,000	40381	0.0740	0.0748	1.1472
50,000	39396	0.0745	0.0748	1.2828
100,000	39245	0.0746	0.0748	1.3045
500,000	39089	0.0746	0.0747	1.3168
1,000,000	39067	0.0747	0.0748	1.3265
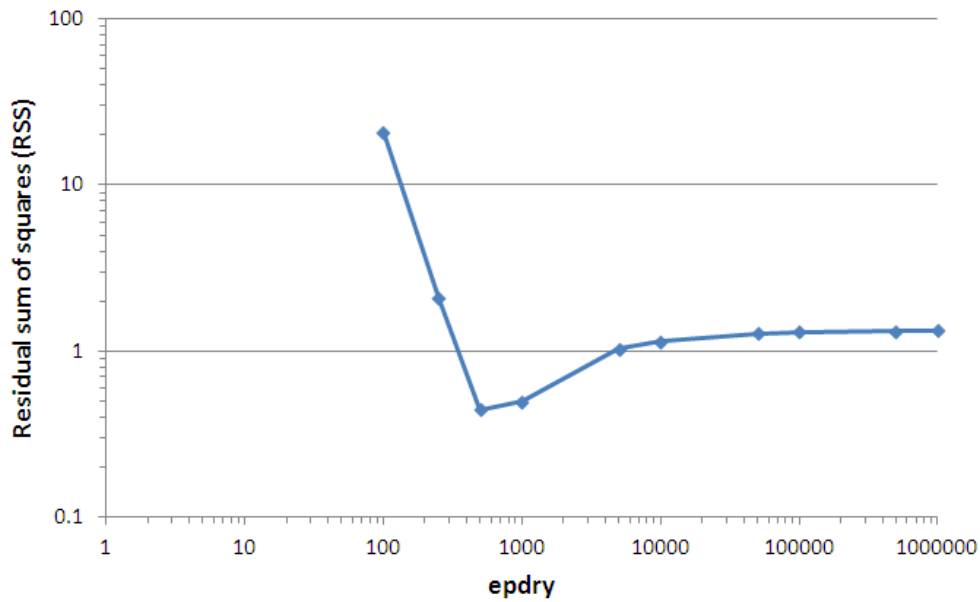
Figure 4-21: Residual sum of squares as a function of $epdry$ using the 2-parameter fitting method.

Figure 4-21 plots the data of RSS-$epdry$ in **Table 4-viii** in log-log scale. We can see from **Figure 4-21** that the optimal RSS is achieved when $epdry$ is around 500. Nevertheless, for other values of $epdry$ which is larger than 500, the fit is also reasonable as shown in **Figure 4-22**. Thus, additional transient experiments may be needed to justify which set of parameters fits the experimental data.
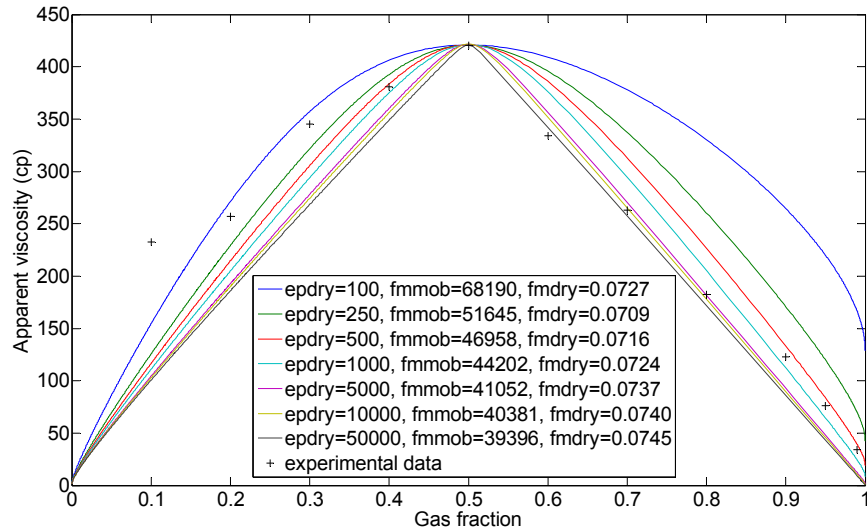
Figure 4-22: *Fit to experimental data using the parameters in* **Table 3-4**.
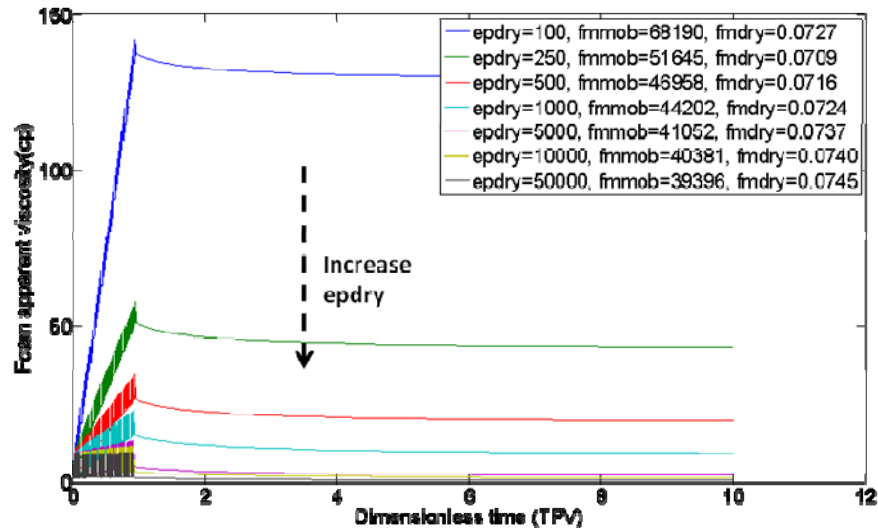
Figure 4-23: *Finite difference simulation of the transient process (gas injected to a surfactant-solution-saturated porous medium) to distinguish different set of parameters. Dimensionless time step size is $\Delta t_D=0.005\Delta x_D$.*

Figure 4-23 shows that different sets of parameters which show good fit to steady-state have very different results in transient simulation. The simulation is a case where the porous medium is previously saturated with surfactant solution and gas is injected into the system. Thus, it will be a foam generation

and dry-out process. As shown in **Figure 4-23**, an increase in $epdry$ leads to a decrease in peak foam apparent viscosity when gas breakthrough. Meanwhile, a numerical oscillation issue is observed in **Figure 4-23** when $epdry$ increases. This numerical issue is expected to be minimized by increasing the number of grid blocks and decreasing time step sizes.

4.1.7. Non-unique solutions to match the transition foam viscosity

Non-graphical solution

We introduced a hybrid contour plot method to match the transition foam viscosity between the high-quality regime and the low-quality regime. Here we discuss how to solve this problem non-graphically and how to deal with the issue of non-uniqueness.

The transition water saturation S_w^t between the high-quality and low-quality foam regimes is defined by:

$$\mu_{foam,app}(S_w^t, fmmob, fmdry) = \max_{S_w} \mu_{foam,app}(S_w, fmmob, fmdry) \ldots\ldots\ldots\ldots\ldots(3.1)$$

With a preset value of $epdry$, the goal is to solve Eqns (3.2) and (3.3) simultaneously to obtain $fmmob$ and $fmdry$.

$$\mu_{foam,app}^t = \frac{1}{\dfrac{k_{rw}(S_w^t)}{\mu_w} + \dfrac{k_{rg}^f(S_w^t, fmmob, fmdry)}{\mu_g}} \ldots\ldots\ldots\ldots\ldots\ldots\ldots\ldots\ldots\ldots\ldots\ldots(3.2)$$

$$f_g^t = \frac{1}{1 + \dfrac{k_{rw}(S_w^t)}{\mu_w} \cdot \dfrac{\mu_g}{k_{rg}^f(S_w^t, fmmob, fmdry)}} \ldots\ldots\ldots\ldots\ldots\ldots\ldots\ldots\ldots\ldots\ldots(3.3)$$

We show how to match the experimental data of 0.2 wt% IOS1518 at the transition foam quality ($f_g^t(measured) = 0.5$ and $\mu_{foam,app}^t(measured) = 421$ cp) as an example. If the solution exists, one can use the derivative method and the

root-finding algorithm to solve Eqns (3.1) to (3.3). However, a modern strategy is to use search algorithms for finding minimum without deriving the derivative. **Figure 4-24** shows the flow chart of our proposed non-graphical search method to fit experimentally measured f_g^t and $\mu_{foam,app}^t$.
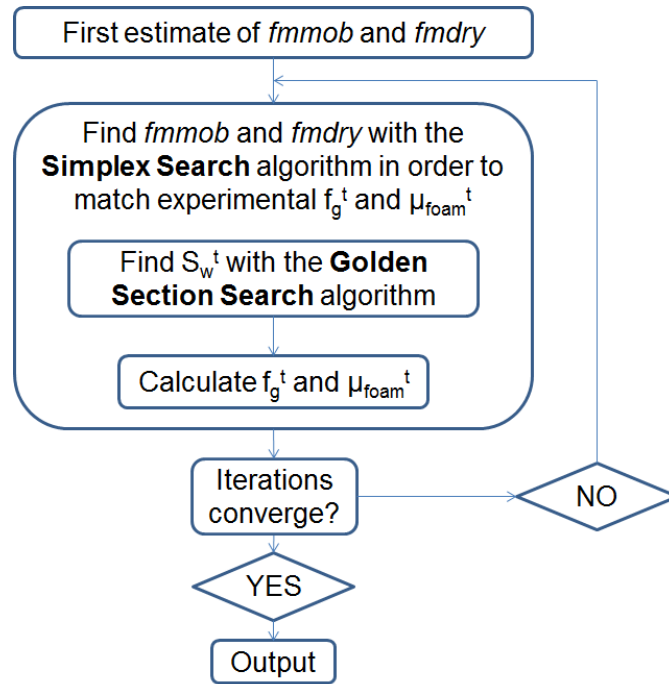
Figure 4-24: Flow chart of the non-graphical approach to match experimental data at the transition foam quality with a preset $epdry$.

As shown in **Figure 4-24**, this approach uses the simplex search method (the built-in function "fminsearch" in MATLAB (The MathWorks Inc 2012)) to find *fmmob* and *fmdry* and the golden section search method (the built-in function "fminbnd" in MATLAB (The MathWorks Inc 2012)) inside the simplex search loop to find S_w^t. The objective functions (Fun_1 and Fun_2) for minimization using the simplex search in the outer loop and the golden section search in the inner loop are shown in Eqns (3.4) and (3.5), respectively:

$$\min Fun_1(fmmob, fmdry) = \left(\frac{\mu_{foam,app}^t - \mu_{foam,app}^t(measured)}{\mu_{foam,app}^t(measured)}\right)^2 + \left(\frac{f_g^t - f_g^t(measured)}{f_g^t(measured)}\right)^2$$

.... (3.4)

$$\min Fun_2(S_w) = -\mu_{foam,app}(S_w)$$ ....(3.5)

Using an initial guess of $fmmob = 10000$ and $fmdry = 0.1$, we obtain $fmmob = 47196$ and $fmdry = 0.1006$ with a preset *epdry* of 500. This result is consistent with the solution obtained through the hybrid contour plot method (Ma, Lopez-Salinas et al.) if the difference in significant digits is considered.

Strategy to handle the non-uniqueness problem

The success using the approach proposed in Section 3.1.1.1 highly depends on the initial guess of *fmmob* and *fmdry*. For example, if we use an initial guess of $fmmob = 10^6$ and $fmdry = 0.1$, the algorithm ends up with a solution of $fmmob = 1.0897 \times 10^6$ and $fmdry = 0.1216$. This set of solution can also match the experimental data at the transition foam quality.

It is necessary to use the graphical method to investigate the existence and uniqueness of the solutions. As stated previously, the solution can be found by superimposing the contour plots of the transition foam quality and the

foam apparent viscosity (Ma, Lopez-Salinas et al.). However, only the value of 0.1006 for $fmdry$ was observed in our previous work due to the limited parameter domain which had been scanned. In **Figure 4-25(a)**, we scan the parameter domains for $fmmob$ over 4 orders of magnitude (10^3 to 10^7). Interestingly, the second solution is found as the contour of the transition foam quality (the red curve in **Figure 4-25**) forms a circuitous curve instead of a monotonic decreasing curve. These two pairs of solutions for $fmmob$ and $fmdry$, as indicated by the intersections between the blue curve and the red curve in **Figure 4-25(a)**, are consistent with the finding in **Figure 4-24** using the non-graphical method and appropriate starting values of the parameters.
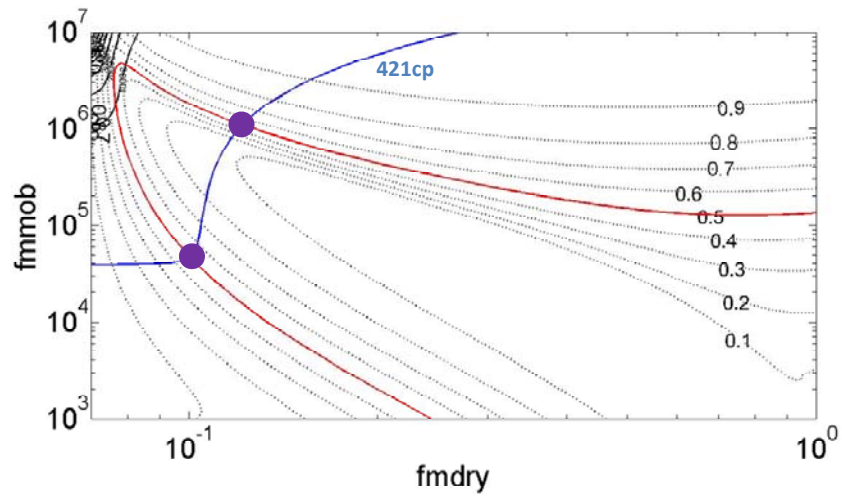
(a)
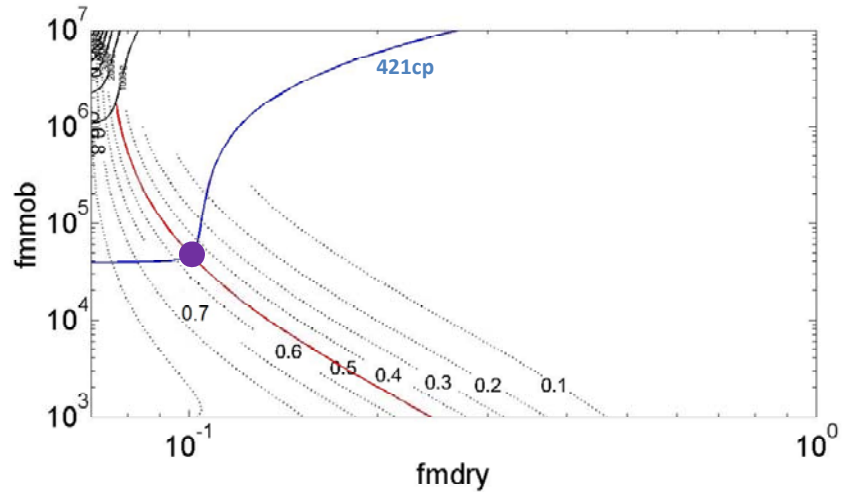
(b)

Figure 4-25: _Location of the roots which match transition foam data using the hybrid contour plot method on a log-log scale. (a) shows the parameter scan in the range of_ $10^3 < fmmob < 10^7$ _and_ $0 < fmdry < 1$; _(b) shows part of Figure 4-25(a) where_ $fmdry$ _is smaller than_ S_w^t. _The purple dots in both figures indicate where_ $f_g^t = 0.5$ _(the red curve) and_ $\mu_{foam,app}^t = 421$ cp _(the blue curve) cross over._

In order to evaluate how well these two sets of solutions fit experiments, we compare them with experimental data in **Figure 4-26**. The red curve (model fit 1) using the solution which satisfies $fmdry < S_w^t$ well fits the experimental data, while the green curve (model fit 2) does not appear to fit the experiments. Moreover, the green curve indicates a foam apparent viscosity of over 250 cp even at 100% gas injection, which is physically unreasonable. Thus, this set of non-physical solution needs to be eliminated in the algorithm. In **Figure 4-25(b)** we only display part of the hybrid contour plot which satisfies $fmdry < S_w^t$. The non-physical solution shown in the green curve in **Figure 4-26** is ruled out by limiting the solution to the one for which $fmdry < S_w^t$.

Foam apparent viscosity (0.2 wt% IOS 1518)

- ◆ Experimental data
- – – Model fit 1 (fmmob=47196, fmdry=0.1006)
- – – Model fit 2 (fmmob=1.0897E6, fmdry=0.1216)
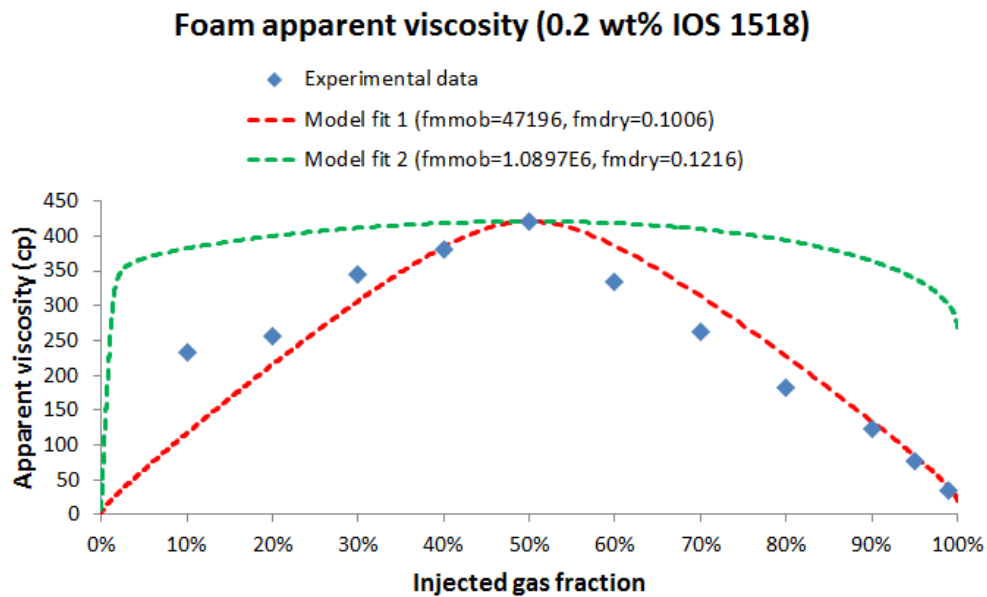
Figure 4-26: *Comparison of model fit with experimental data using two sets of parameters found in Figure 4-25, with a preset* $epdry$ *of 500. In "model fit 1",* $fmdry$ *is smaller than* S_w^t*; in "model fit 2",* $fmdry$ *is larger than* S_w^t *.*

The dry-out function in the STARS^{TM} foam model is designed to describe the effect of the limiting capillary pressure (P_c^*) on foam stability (Cheng, Reme et al. 2000). As shown in **Figure 4-27(a)**, P_c^* corresponds to a limiting

water saturation (S_w^*) for a given system. S_w^* approaches both the transition

water saturation (S_w^t) and the parameter *fmdry* in the STARS^{TM} foam model

if a sufficiently large *epdry* is used (Cheng, Reme et al. 2000). However, a

smaller *epdry* may be needed for matching transient (continuous gas

injection) experiments (Ma, Lopez-Salinas et al.). In this case, there is a

substantial difference between *fmdry* and S_w^t. Foam should not dry out in

the low-quality regime (right-hand side of S_w^t in **Figure 4-27(b)**) as bubble

trapping and mobilization rather than coalescence dominates foam mobility.

Therefore, one should pick the value of *fmdry* in the high-quality regime

(left-hand side of S_w^t in **Figure 4-27(b)**) and exclude the root in the low quality

regime from this point of view.

(a)

220
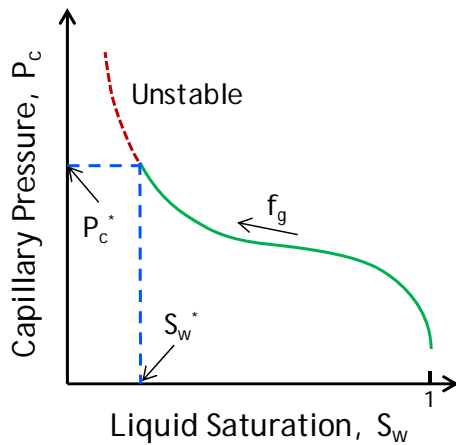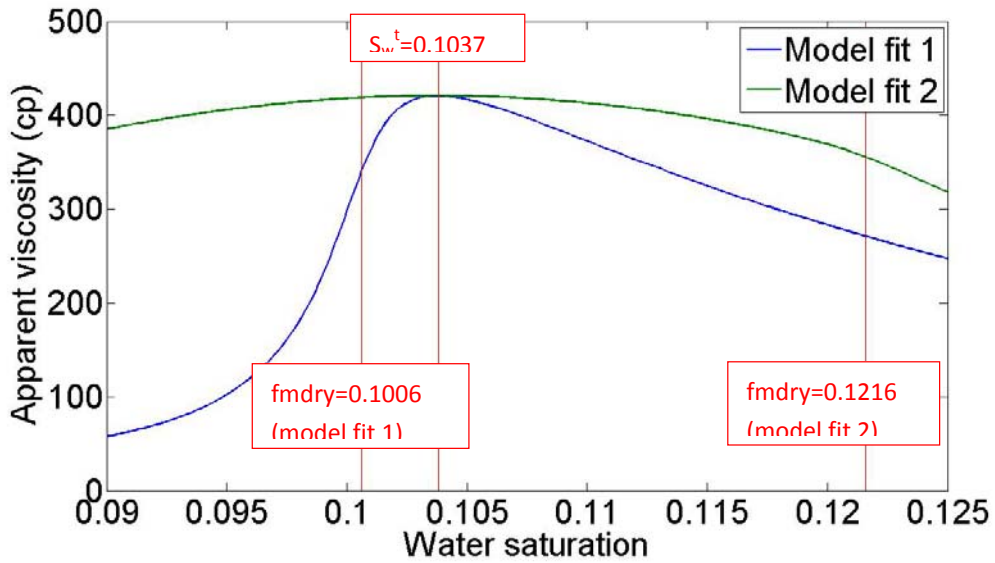
(b)

Figure 4-27: Graphical illustration of S_w^*, S_w^t, and $fmdry$. (a) The concept of the limiting capillary pressure (P_c^*) and the limiting water saturation (S_w^*), adapted from literature (Khatib, Hirasaki et al. 1988; Farajzadeh, Andrianov et al. 2012); (b) Comparison of $\mu_{foam,app} - S_w$ curves in the vicinity of S_w^t between model fit 1 and 2.

Discussion on multi-variable multi-dimensional search

We showed that care was needed to select the appropriate initial guess in the "fminsearch" function. The problem is stated as:

$$\min f(fmmob, fmdry, epdry) = \sum_{i=1}^{n} \omega_i \left(\frac{\mu_{foam,i,calculated} - \mu_{foam,i,measured}}{\mu_{foam,i,measured}} \right)^2 \dots\dots\dots(3.6)$$

$s.t.$ $fmmob > 0$, $S_{wc} \leq fmdry \leq 1 - S_{gr}$, and $epdry > 0$

where $\mu_{foam,i,calculated}$ is the calculated foam apparent viscosity at the corresponding gas fractional flow $f_{g,i,measured}$. The value of $\mu_{foam,i,calculated}$ is computed through Eqns (A.4) and (A.5) and the value of $\mu_{foam,i,measured}$ is taken from all experimental data, not just the transition value. A set of weighting

parameters, denoted as ω_i in Eqn (2.6), is usually employed to indicate expected standard deviation of each experimental point. In the following analysis we hypothesize that the weighting parameters are all equal to unity except for a value of 5 for the transition value ($\omega_i = 5$ when $\mu_{foam,i,measured} = \mu^t_{foam}$).

This problem is essentially a search for a constrained 3-variable optimization. If appropriate initial values are chosen, unconstrained optimization can be implemented to perform the search. The built-in simplex search function "fminsearch" in MATLAB begins with an initial estimate and attempt to finds a local minimum of a scalar function of several variables (The MathWorks Inc 2012). For a specific set of experimental data, we can estimate $fmmob$, $fmdry$, and $epdry$ simultaneously using this function. However, inappropriate initial values may lead to failure using the simplex search. For example, if we use an initial guess of ($fmmob = 1$, $fmdry = S_{wc}$ and $epdry = 1$) for matching all experimental data points in **Figure 4-26**, the unconstrained search provides a set of non-physical results ($fmmob = 3018.9$, $fmdry = -81.67$ and $epdry = 316.5$) with a negative $fmdry$. In order to have a wider range of initial guesses applicable to search the global minimum, a feasible way to add the constraints to unconstrained optimization is to use the penalty function (Avriel 1976; Bazaraa, Sherali et al. 2006). We use the constraint $fmdry \geq S_{wc}$ as a penalty function and construct a new objective function in Eqn (3.7):

$$\min f(fmmob, fmdry, epdry) = \sum_{i=1}^{n} \omega_i \left(\frac{\mu_{foam,i,calculated} - \mu_{foam,i,measured}}{\mu_{foam,i,measured}} \right)^2 + (fmdry - S_{wc})^2 \cdot \Theta$$

$$\Theta = \begin{cases} 0, & when \quad fmdry \geq S_{wc} \\ \sigma_k, & when \quad fmdry < S_{wc} \end{cases} \quad\dots\dots\dots\dots\dots\dots\dots\dots\dots\dots\dots\dots\dots\dots\dots\dots\dots\dots(3.7)$$

In Eqn (3.7), Θ is the penalty function and σ_k is the penalty coefficient. Several iterations may be needed to implement the penalty function method if the solution does not converge quickly. The solution from the previous iteration is used as the initial guess and the penalty coefficient is increased in each iteration to solve the unconstrained problem (Avriel 1976; Bazaraa, Sherali et al. 2006). Specifically for the experimental data in **Figure 4-26**, we start with an initial guess of ($fmmob = 1$, $fmdry = S_{wc}$ and $epdry = 1$) and a penalty coefficient of $\sigma_k = 0.1$. The solution quickly converges to ($fmmob = 60873$, $fmdry = 0.1039$ and $epdry = 629.2$) using the "fminsearch" function in MATLAB without the need of increasing σ_k . The result is shown in **Figure 4-28**.
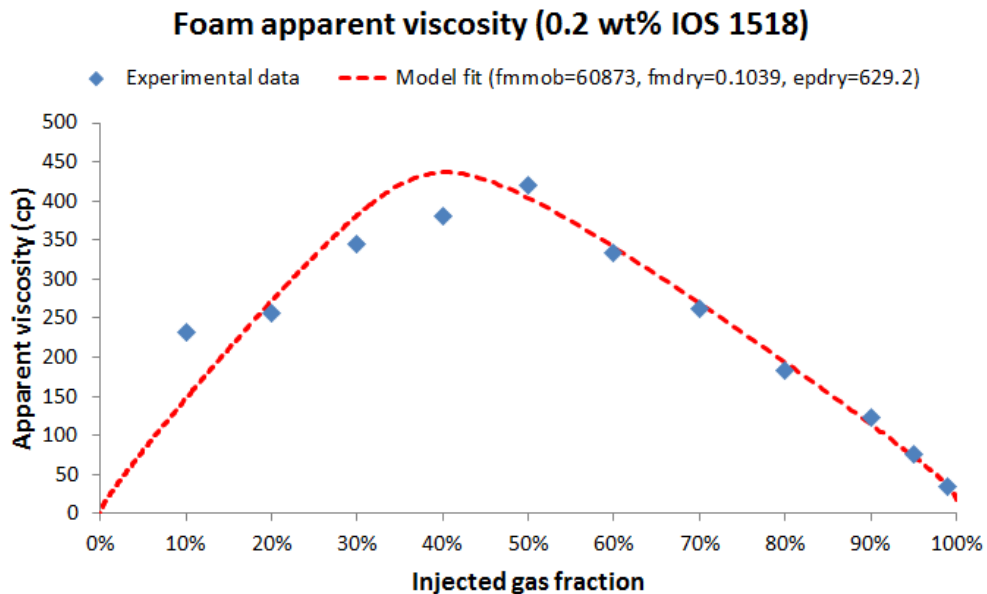
Figure 4-28: *Comparison of model fit with experimental data using the multi-dimensional 3-parameter estimation.*

Compared with the 2-parameter model fit in **Figure 4-26** which exactly fit the transition fractional flow and viscosity, this unconstrained optimization method provides a good fit to all the data points. The results obtained here indicate that the use of a penalty function is helpful to have a wider range of initial guess.

Numerical oscillation in transient foam simulation

It has been noted that $epdry$ should not be too large in order to have acceptable stability and run time in simulators using the finite difference algorithm (Cheng, Reme et al. 2000; Zanganeh, Kraaijevanger et al. 2012). In previous work, we simulated the transient foam process of continuous gas injection to 100% surfactant-solution-saturated porous media. Now we compare the result of finite difference simulation (FD) with the method of characteristics (MOC) and investigate how significant the numerical artifact is in the finite difference simulation. We discuss the case with the dry-out function in the foam model only. In order to compare the MOC solution with the FD simulation, we use the same set of foam parameters ($fmmob = 47196$, $fmdry = 0.1006$ and $epdry = 500$) in the following computation. The FD algorithm with a standard IMPES (implicit in pressure and explicit in saturation) formulation is used to simulate the transient foam process in which 100% gas displaces 100% surfactant solution.

The local foam apparent viscosity ($\mu_{foam,app}$) and the average foam apparent viscosity ($\overline{\mu}_{foam,app}$) are defined in Eqns (3.8) and (3.9), respectively. $\mu_{foam,app}$ is a function of time and distance, which reflects the local normalized pressure gradient as foam advances in porous media. $\overline{\mu}_{foam,app}$ is a function of time, which reflects the averaged, overall normalized pressure gradient in the system.

$$\mu_{foam,app} = \cfrac{1}{\cfrac{k_{rw}}{\mu_w} + \cfrac{k_{rg}^f}{\mu_g}} \quad\text{..} \quad (3.8)$$

$$\overline{\mu}_{foam,app} = -\frac{k(p_{out} - p_{in})}{(u_w + u_g)L} \quad\text{..}\quad(3.9)$$

Figure 4-29 shows the apparent viscosity history of the transient foam process in which 100% gas displaces 100% surfactant solution. According to **Figure 4-29**, these two methods are consistent with each other after gas breakthrough where the foam starts drying out and the apparent viscosity decreases when time increases. However, the result using the FD simulation exhibits some oscillations before gas breakthrough. A zoom-in investigation reveals that this oscillation is periodic and the apparent viscosity is consistently overshot compared with the result obtained with the MOC approach.
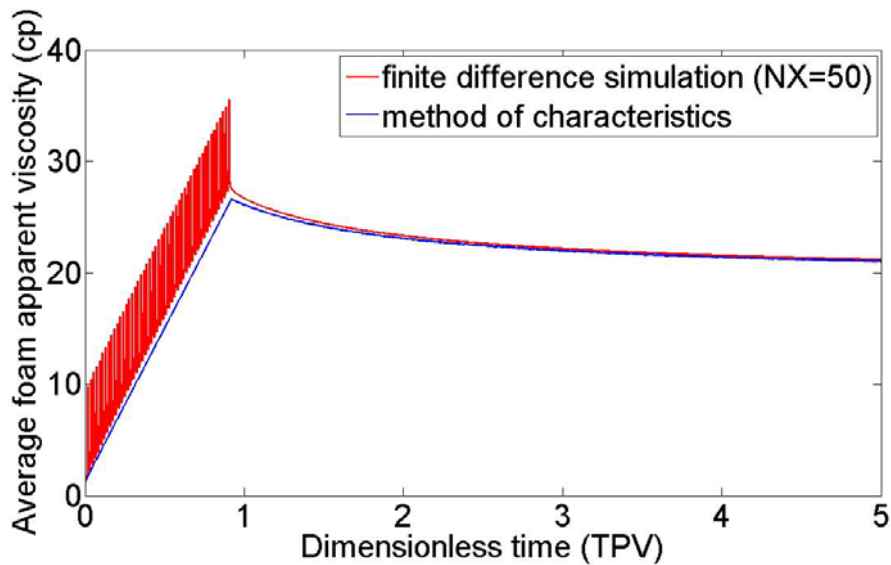
Figure 4-29: Comparison of foam apparent viscosity history between finite difference method and method of characteristics. $NX = 50$ and $\Delta t_D = 0.005 \Delta x_D$ (in finite difference simulation), $fmmob = 47094$, $fmdry = 0.1006$ and $epdry = 500$.

Figure 4-30(a) shows the zoom-in details in the periodic oscillation in the case shown in **Figure 4-29** with a period of about 0.02 TPV. The saturation profiles at 0.5100 TPV and 0.5162 TPV are plotted in **Figure 4-30 (b)** and **(c)**, which represent small and large deviations of foam apparent viscosity history using the FD simulation from using MOC, respectively. The local foam apparent viscosity profiles at 0.5100 TPV and 0.5162 TPV are shown in **Figure 4-30 (d)** and **(e)**, respectively. One can find that significant deviations of the FD solution from the MOC solution occur near the foam displacement front. The MOC solution assumes a discontinuous change in saturation across the front while the FD solution has intermediate values of saturation change. The gas saturation in the 28th grid block at 0.5162 TPV (**Figure 4-30 (c)**) is 0.8975 using the finite difference method, which is very close to the transition gas saturation ($S_g^t = 1 - S_w^t = 0.8963$) shown as a spike in **Figure 4-30 (g)**. Therefore, a substantially higher local foam apparent viscosity results in the 28th grid block at 0.5162 TPV in **Figure 4-30 (e)**.This fact leads to a pressure discontinuity at the foam displacement front in FD simulation. **Figure 4-30 (f)** shows the flow potential (dimensionless gas pressure, $\Phi_D = (p_g - p_g{}^{BC})kk_{rg}^0/u^{BC}\mu_g L$) at 0.5100 TPV and 0.5162 TPV, respectively. The flow potential at 0.5162 TPV shows a large discontinuity between the 28th and the 29th grid blocks, indicating an overshoot in pressure in the 28th grid block; while the flow potential at 0.5100 TPV does not indicate a significant overshooting issue.
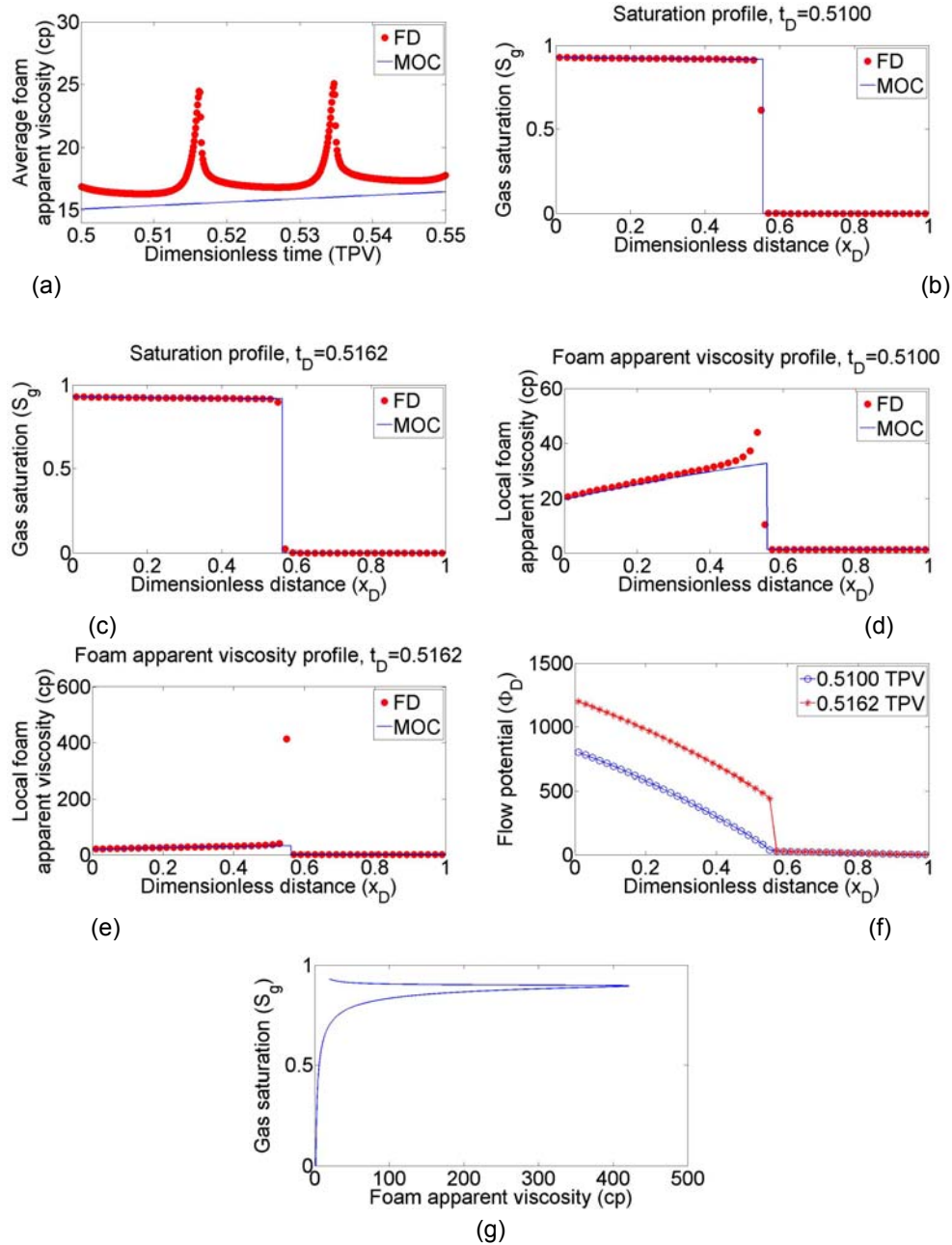
Figure 4-30: Investigation of numerical oscillation in FD simulation in which 100% gas displaces surfactant solution at 100% water saturation: (a) average foam apparent viscosity history from 0.50 to 0.55 TPV; (b) saturation profile at 0.5100 TPV; (c) saturation profile at 0.5162 TPV; (d) local foam apparent viscosity profile at 0.5100 TPV; (e) local foam apparent viscosity profile at 0.5162 TPV; (f) flow potential profiles at 0.5100 TPV and 0.5162 TPV; (g) the relationship between gas saturation and foam apparent viscosity.

$NX = 50$, $\Delta t_D = 0.005\Delta x_D$, $fmmob = 47196$, $fmdry = 0.1006$ and $epdry = 500$.

In order to understand the main factors in finite difference simulation which contribute to this numerical artifact observed in **Figure 4-29** and **4-30**, we simulate five cases of the transient foam simulation in which 100% gas displaces 100% surfactant solution. The parameters that are altered among different cases are shown in **Table 4-ix** in bold.

Table 4-ix: Parameters for the simulation of transient foam in Figure 4-31.

Parameter	Case 1	Case 2	Case 3	Case 4	Case 5
$\Delta t_D / \Delta x_D$	0.005	**0.0005**	0.005	0.005	0.005
NX	50	50	**200**	50	50
epdry	500	500	500	500	**100**
fmmob	47196	47196	47196	**28479**	69618
fmdry	0.1006	0.1006	0.1006	**0.2473**	**0.1020**
	1.96	1.96	1.96	**4.0**	1.96

Cases 1, 2 and 3 share the same set of foam modeling parameters. The parameter sets in all five cases in **Table 4-ix** exhibit good fit to steady-state data at the transition foam quality ($f_g^t = 0.5$ and $\mu_{foam,app}^t = 421$ cp) as shown in **Figure 4-31(a)**. **Figure 4-31(b)** shows the base case (Case 1) using a total grid block numbers of $NX = 50$ and a time step size of $\Delta t_D = 0.005 \Delta x_D$, Which is essentially the same as that in **Figure 4-29**. In Case 2 (**Figure 4-31(c)**) we decrease the time step size to 1/10 of the one in the base case, however, no significant change is observed in the numerical oscillations. This result reveals that the IMPES simulator is numerically stable in terms of selection of time step size in the base case. The total grid blocks are increased to $NX = 200$ in Case 3 (**Figure 4-31(d)**) and significant reduction in the amplitude of numerical oscillation is observed compared with the base case. Also, it is observed that

the frequency of the oscillation is proportional to the number of grid blocks. This observation indicates that an increase in total grid block numbers in the FD simulation leads to a better approximation to the solution using the MOC approach, at the cost of increasing computational time during the simulation. The reason behind this is that the contribution of the pressure drop in the grid block exactly at foam displacement front is smaller when the size of the grid block is smaller.

The parameters used in relative permeability curves and the foam modeling parameters also affects the numerical oscillation. They can change the shape of foam apparent viscosity as a function of saturation (**Figure 4-30(g)**), and a less sharp peak in **Figure 4-30(g)** will result a less significant oscillation. The increase in the exponent of the water relative permeability curve (Case 4, **Figure 4-31(e)**) from 1.96 to 4.0 does not help reduce numerical oscillation because the steady-state $\mu_{foam,app}$ - f_g curve in Case 4 does not differ much from that in Case 1 as shown in **Figure 4-31(a)**. As indicated in Case 5 (**Figure 4-31(f)**), a decrease in $epdry$ causes a decrease in the amplitude of numerical oscillation in foam apparent viscosity history before gas breakthrough. This result indicates that a more gradual transition between the high-quality and low-quality regimes reduces numerical oscillation. Additionally, a weaker foam, which requires a smaller $fmmob$, can also lead to a smaller amplitude in numerical oscillation. This is consistent with the practice of most foam simulation studies using a small $fmmob$ and a small $epdry$ in order to avoid numerical issues (Farajzadeh, Andrianov et al. 2012).
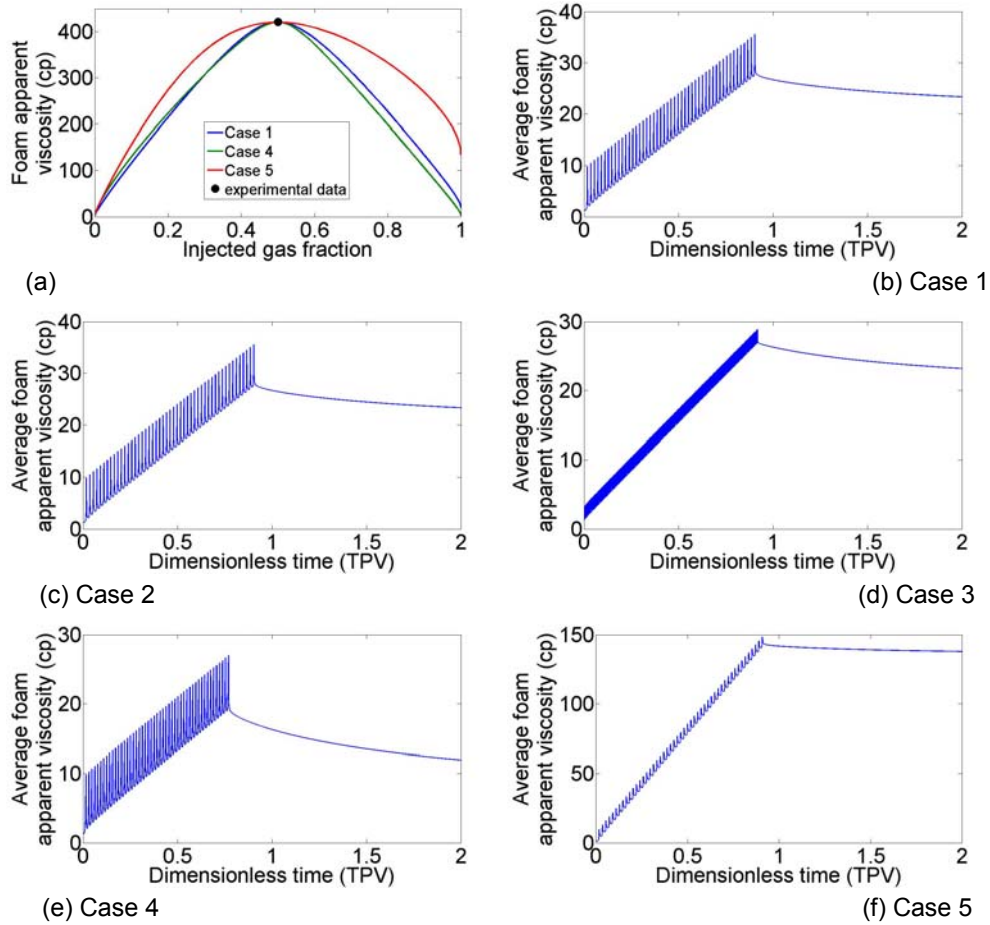
Figure 4-31: Investigations of factors which may affect numerical oscillation in the FD simulation of 100% gas displacing 100% surfactant solution. (a). Model fit to transition steady-state experimental data. (b) to (f). Transient simulation of Cases 1 to 5. The parameters in Cases 1 to 5 are listed in Table 4-ix.

Therefore, only strong foams with an abrupt transition between the high-quality and low-quality regimes may exhibit significant numerical oscillation. Since foam modeling parameters can be estimated by a combination of matching both steady-state and transient experiments, a practical way to minimize this numerical oscillation issue is to select an acceptable number of total grid blocks and a large time step which does not affect the numerical stability in the FD simulation. The crux to reduce the numerical oscillation in foam apparent viscosity history is to smear out the foam displacement front and to avoid the sharp change in local apparent viscosity at the foam front in the FD simulation. For applications such as co-injecting gas and surfactant solution into the system which has not been previously filled with surfactant solution, the local apparent viscosity at the foam front is control by both water saturation and surfactant concentration if one uses the dry-out function and the surfactant-concentration-dependent function simultaneously in the foam model. If a dispersive surfactant front exists at the foam front (assuming no chromatographic retardation), a weaker foam front can result compared with the full-strength foam at the foam bank, leading to lower amplitude in numerical oscillation (data not shown).

Sensitivity of foam parameters

Parameters in the STARS^{TM} foam model are sensitive to the estimation of the parameters which are used to model gas-water flow in porous media in the absence of foam. It was found that in general k_{rw} functions were more nonlinear for consolidated sandstones than for sandpacks and that an increase in the nonlinearity of k_{rw} could benefit the Surfactant-Alternating-Gas (SAG) process (Ashoori and Rossen 2012). It is important to recognize that one cannot apply the same set of foam parameters to different porous media without experimental verification. For example, the transition foam quality (f_g^t)

was shown to decrease significantly when permeability decreased from a sandpack to a Berea core using the same surfactant formulation (Bio-Terge AS-40 surfactant supplied by Stepan, a C14-16 sodium alpha-olefin sulfonate) (Alvarez, Rivas et al. 2001). In order to demonstrate the sensitivity of foam modeling parameters with respect to two-phase flow parameters, we match the experimental data ($f_g^t(measured) = 0.5$ and $\mu_{foam,app}^t(measured) = 421\ cp$) using the dry-out function in the STARS^{TM} foam model with changes in the parameters of the exponent in the k_{rw} function (n_w) and connate water saturation (S_{wc}) shown in **Figure 4-32** and **4-33**.

The nonlinearity of the k_{rw} function is controlled by the exponent n_w as shown in **Figure 4-32(a)**. An increase in n_w leads to a more curved k_{rw} curve. It is found that the experimental data ($f_g^t(measured) = 0.5$ and $\mu_{foam,app}^t(measured) = 421\ cp$) in **Figure 4-32(b)** cannot be fit with the STARS^{TM} foam model if n_w is equal to 1. We fit the experimental data at the transition foam quality using values of n_w from 1.5 to 4.0. The model fit appears similar in the low-quality regime and distinguishable differences in the high-quality-regime with higher predicted apparent viscosity using lower value of n_w. Moreover, **Figure 4-32(c)** and **(d)** show strong dependence of the foam modeling parameters *fmmob* and *fmdry* on the exponent n_w of the k_{rw} curve with a preset *epdry* of 500. *fmmob* decreases by about one-half when n_w increases from 1.5 to 4.0, while *fmdry* increases significantly with n_w.
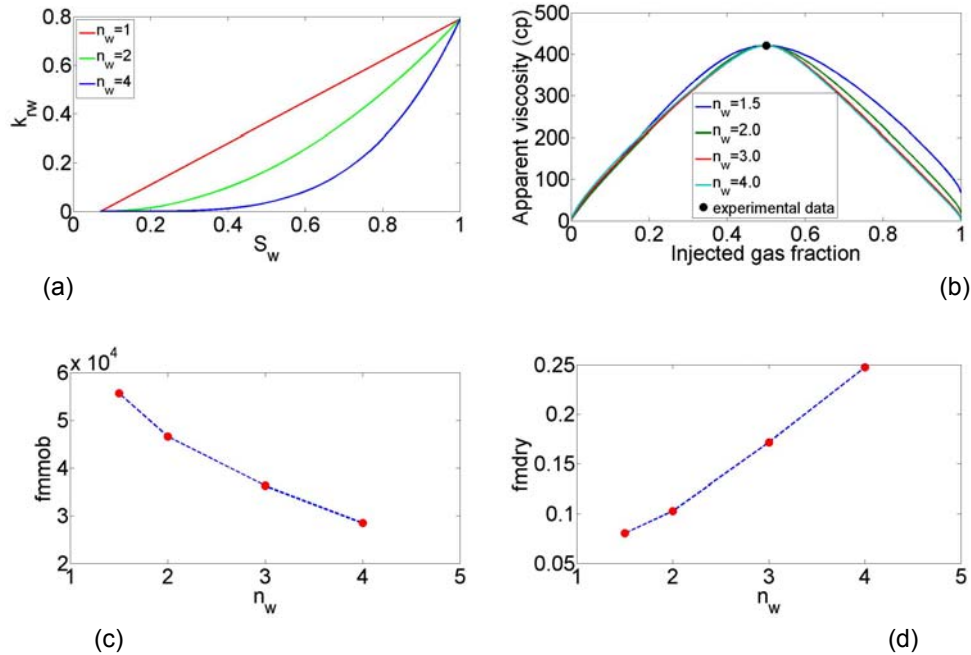
Figure 4-32: *The influence of changing the exponent n_w in the k_{rw} function on foam modeling parameters, with a preset $epdry$ of 500. (a) The k_{rw} curve with different exponent n_w; (b) model fit to the steady-state transition foam data with different exponent n_w; (c) change of $fmmob$ with the exponent n_w in the model fit of Figure 4-32(b); (d) change of $fmdry$ with the exponent n_w in the model fit of Figure 4-32(b).*

The connate water saturation S_{wc} is another important parameter that can affects the estimation of foam modeling parameters. **Figure 4-33(a)** shows indistinguishable model fit to experimental data using different values of S_{wc} (0.05, 0.10, and 0.15). The influence of S_{wc} on $fmmob$ is weak as shown in **Figure 4-33(c)**, however, S_{wc} significantly affects the estimation of $fmdry$ and a quasilinear monotonic increasing relationship with a slope close to 1 in observed **Figure 4-33(d)**. The way to estimate S_{wc} in the presence of foam is

233

to match experimental measured fractional flow curve **(Figure 4-33(b))** as discussed previously.

(a)　　　　　　　　　　　　　　　　　(b)

(c)　　　　　　　　　　　　　　　　　(d)
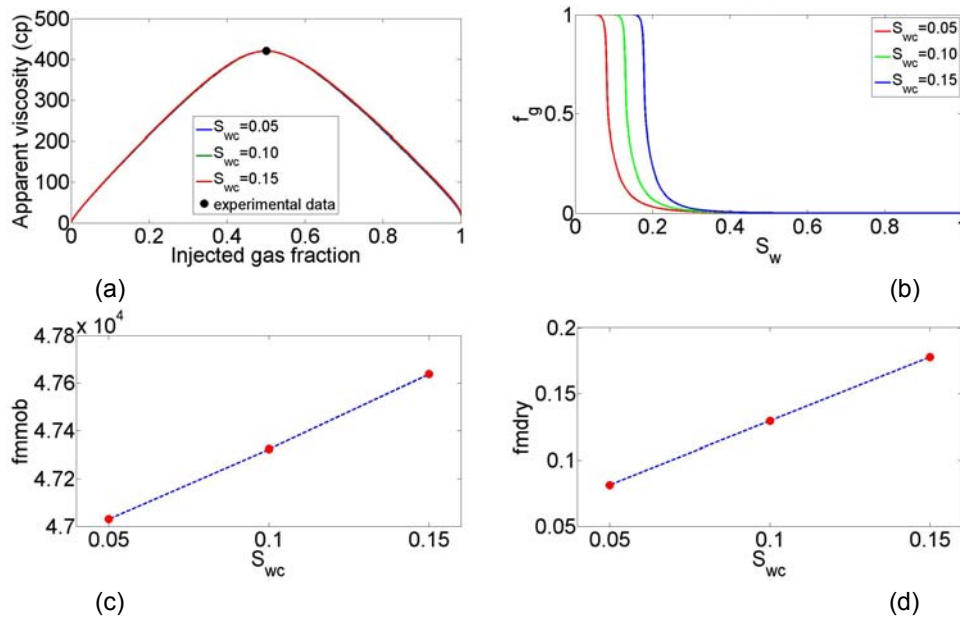
__Figure 4-33:__ The influence of changing the connate water saturation S_{wc} on foam modeling parameters. The rest of the parameters are used as shown in Table A1 with a preset $epdry$ of 500. (a) Model fit to the steady-state transition foam data with different S_{wc}; (b) fractional flow curve with different S_{wc}; (c) change of $fmmob$ with S_{wc} in the model fit of Figure 4-33(a); (d) change of $fmdry$ with S_{wc} in the model fit of Figure 4-33(a).

We showed a wide range of $epdry$ could be used to estimate $fmmob$ and $fmdry$ at the transition foam quality in steady-state experiments. We verify the results here in **Figure 4-34** with the numerical method proposed in **Figure 4-24** and show the parameter sensitivity to $epdry$. **Figure 4-34(a)** showed that different preset $epdry$ ranging from 500 to 500,000 can fit the

transition experimental data using the non-graphical approach proposed in **Figure 4-34**. *fmmob* decreases when *epdry* increases (**Figure 4-34 (b)**) till *fmmob* approaches a plateau value, while *fmdry* only exhibits a subtle change in the third significant digit in response to *epdry* (**Figure 4-34 (c)**). This is because *fmdry* asymptotically approaches S_w^t when *epdry* is sufficiently large. In the case of $f_g^t = 0.5$ and $\mu_{foam,app}^t = 421 \ cp$, S_w^t is 0.1037.

(a)

(b)

(c)
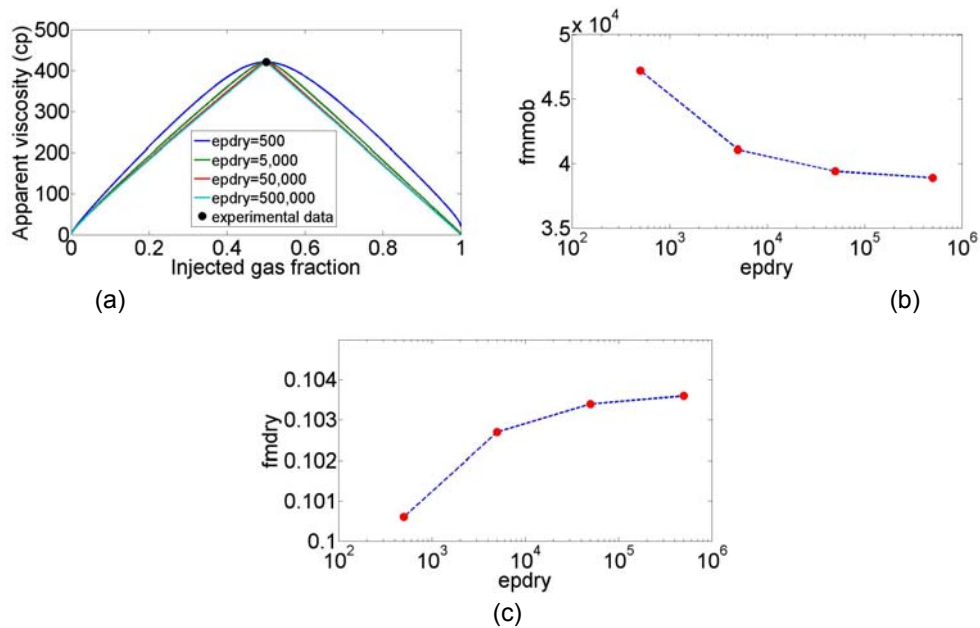
Figure 4-34: *The influence of changing the parameter* $epdry$ *on other foam modeling parameters. (a) Model fit to the steady-state transition foam data with different* $epdry$*; (b) change of* $fmmob$ *with* $epdry$ *in the model fit of Figure 3-11(a); (c) change of* $fmdry$ *with* $epdry$ *in the model fit of Figure 3.11(a).*

4.2. Mechanistic Foam Modeling Approach

4.2.1. Modeling of Gas Trapping Based on Pore Network Approach

4.2.1.1. Network Model Generation

We utilize network models mapped from two different types of porous media: computer-generated sphere pack and sandstones digitized from real media. The sphere packs are obtained using a collective rearrangement algorithm (Jodrey and Tory,1985) and have the advantage of fast generation and the ability to easily vary grain-size distribution and porosity. Network models of sandstones are more difficult to extract and pore-level properties are fixed, but they represent naturally-occurring, real media.

Regardless of the medium used, it is mapped to a 3D, physically-representative network model using a modified Delaunay tessellation (Al-Raoushet al., 2003). The resulting network captures the inherent heterogeneity and consists of pores (containing the pore volume) and connecting throats (accounting for resistance to flow). In addition, we use a network model constructed from a real, naturally-occurring sandstone (Thompson et al., 2008) that was imaged using X-ray computed microtomography (Al-Raoush et al., 2003; Liang et al., 2000; Lindquist et al., 2000). **Figure 4-35** illustrates the two porous media and the resulting transformed network models. Dimensionless properties of the networks are described in **Table 4-x**. The permeability of each network can be varied through scaling (where the grain diameters are increased to increase permeability). Simulations were conducted using an average grain diameter, rg, of 0.00017 cm (k = 10 mD) for the sphere pack and, for the sandstone, 0.001 cm (k = 10 mD). However, all results presented are dimensionless.
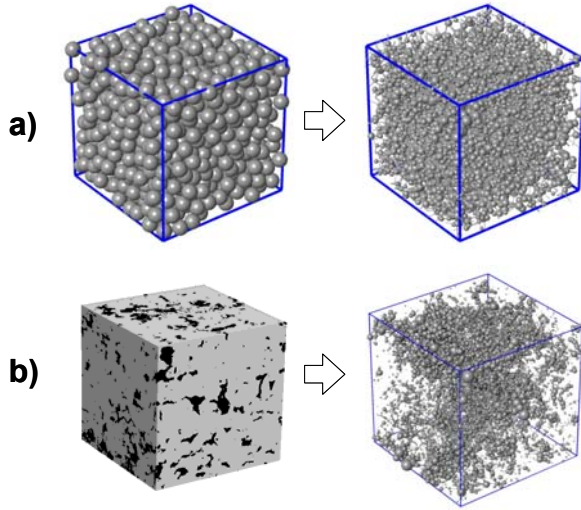
Figure 4-35:. (a) Packed bed of 1000 uniform spheres with 38% porosity and the resulting network model and (b) Sample sandstone structure from the Frontier Formation in Wyoming, USA with 17% porosity and the resulting network model (Gani and Bhattacharya, 2003).

Table 4-x: Statistics of sample porous media and corresponding network model.

Medium	# grains	ϕ	# Pores	k_D	$\bar{r}_{t,D}$	$\sigma^2_{t,D}$
Sphere Pack	1000	38	4070	3.38E-03	2.66E-01	8.69E-03
Sandstone	2487	17	4991	9.68E-05	2.87E-01	1.68E-02

$$k_D = \frac{k}{\bar{r}_g^2}; \quad r_{t,D} = \frac{\bar{R}}{\bar{r}_g}; \quad \sigma^2_{t,D} = \frac{\sigma_t^2}{\bar{r}_g^2}$$

4.2.1.2. Modeling of Flow Equations

Fluids that exhibit a yield stress require a minimum pressure gradient to initiate flow; the shear stress at the wall ($\intercal_w$ = $\Delta PR/2L$) must exceed the fluid yield stress ($\intercal_0$). Two constitutive equations often used to describe yield stress fluids are the Bingham and Herschel-Bulkley model. Analytical expressions for flow rate as a function of pressure drop can be derived for a Bingham (Equation

237

3.4) and Herschel-Bulkley (Equation 3.5) fluid in a cylindrical tube starting from the constitutive equation for stress (Skelland, 1967).

$$Q = \frac{\pi R^4}{8m\,L}\Delta P\left[1 - \frac{4}{3}\left(\frac{2L\tau_0}{\Delta PR}\right) + \frac{1}{3}\left(\frac{2L\tau_0}{\Delta PR}\right)^4\right] \quad if\,\Delta P > \Delta P_m \equiv \frac{2L\tau_0}{R}$$

……………….. (3.4)

$$Q = \frac{\pi R^3}{m^{1/n}\tau_w^{\;3}}\left(\tau_w - \tau_0\right)^{1/n+1}\left[\frac{\left(\tau_w - \tau_0\right)^2}{1/n + 3} + \frac{2\tau_0\left(\tau_w - \tau_0\right)}{1/n + 2} + \frac{\tau_0^{\;2}}{1/n + 1}\right] \quad if\,\Delta P > \Delta P_m \equiv \frac{2L\tau_0}{R}$$

……………………………………………………………………(3.5)

The Herschel-Bulkley model reduces to Bingham in the limiting case of n = 1. In these equations, flow is zero below a critical pressure drop and is finite above it. The no-flow region causes numerical difficulties in solution of the non-linear system of equations. Here, we use the approach described by Balhoff and Thompson (2004) to solve the nonlinear system of equations.

4.2.1.3. Modeling of Foam Fluids

Foams exhibit similar behavior to yield-stress fluids in that a minimum pressure gradient is required to initiate flow. However, foam flow is governed by different physics than traditional yield-stress fluids. In the case of foam, the "yield stress" is not a fluid rheological property, but rather derives from the surface tension between surfactant solution and gas and is inversely related to pore-throat radius (Rossen, 1990). The functional relationship between threshold pressure drop for flow across one pore and pore geometry is based on the Young–Laplace relation for static pressure drop over a curved lamella, which scales inversely with pore-throat radius (Falls et al., 1989; Rossen, 1990; Nguyen et al., 2004):

$$\Delta P_m \sim \frac{4\gamma}{R}$$

……………………………………………………………(3.6)

In the context of continuum fluid models like Equations 3.4 and 3.5, where ΔPm scales with $2L\tau_o/R$, this implies that the apparent yield stress τ_o is a constant. We neglect the influence of dynamic surface-tension effects such as

the surface elasticity and surface viscosity during the motion of foam films in diverging–converging conical channels (Nguyen et al., 2004).

In addition to the Bingham (Equation 3.4) and Herschel-Bulkley (Equation 3.5) relationships, we test two simpler equations, which we call the linear foam model (Equation 3.7) and power-law foam model (Equation 3.8)

$$Q = \frac{\pi R^4}{8m\,L}\left[\Delta P - \Delta P_m\right] \quad if \ \Delta P > \Delta P_m \equiv \frac{2L\tau_0}{R}$$ ………………………………...(3.7)

$$Q = \frac{\pi R^{3+\frac{1}{n}}}{4(2mL)^{\frac{1}{n}}}\left(\frac{4n}{3n+1}\right)\left[\Delta P - \Delta P_m\right]^{\frac{1}{n}} \quad if \ \Delta P > \Delta P_m \equiv \frac{2L\tau_0}{R}$$ …………………. (3.8)

In this case the apparent yield stress τ_0 of the foam incorporates the capillary resistance to displacement of lamellae rather than a yield-stress condition at the pore wall. The power-law foam model reduces to the linear model when n = 1. These equations have the advantage that scaling of flow rate with ∇P is simple above the threshold for flow in one tube, which makes it easier to distinguish viscosity effects (that control scaling of flow along one path with ∇P) and relative-permeability effects in our network model.

Figure 4-36 compares the relationships of flow rate as a function of pressure drop for the foam models and traditional yield-stress fluids.

239
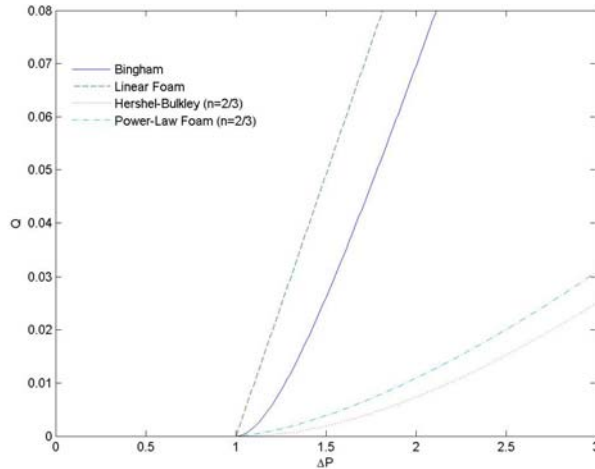
Figure 4-36: _Flow rate versus pressure drop in a dimensionless capillary tube (R = 0.5; L= 1) for (a) linear foam, (b) power-law foam (n = 0.67), (c) Bingham fluid, and (d) Herschel-Bulkley fluid (n = 0.67). All fluids have the same viscosity (m = 1) and yield stress, T_0 = 0.25._

Most network modeling studies assume throats are simple capillary tubes; however, porous media are converging/diverging and the pore throats should capture this behavior. Balhoff and Thompson[42,60] conducted Finite Element simulations of yield-stress and other non-Newtonian fluids in converging/diverging throats. They used the results to develop new closed-form expressions for flow rate versus pressure drop valid in those geometries. They concluded the capillary-tube equation could be used for a Bingham fluid if the geometric parameters of the throat (R and L) are converted using results from the FEM simulation. They also showed [60] that, to be rigorous, the capillary tube equation cannot be used exactly for a Herschel-Bulkley fluid, but a good approximation can still be obtained. Therefore, the approach used in those works to convert converging/diverging throats to capillary tubes is used here for all four models (Bingham, Herschel-Bulkley, linear foam, and power-law foam).

Below a threshold pressure gradient, no flow occurs because there is no connecting path of throats that have pressure drops in excess of the local,

throat mobilization pressure drop ΔP_m. In fact, below the threshold gradient, no throats are open because this would violate mass conservation. At the threshold gradient, a single percolating path exists which connects one end of the network to the other. This threshold pressure gradient is exactly equal to the sum of the local mobilization pressure drops in the percolation path across the network.

$$L_{pm} \cdot \nabla P_T = \sum_i \Delta P_{m,i}$$ …………………………………………………………………..(9)

There are two ways to determine the percolating path and threshold gradient. The first involves a search algorithm to determine the minimum sum of mobilization pressure drops across the network. Sochi and Blunt[50] compared two algorithms, Invasion Percolation with Memory (IPM)[51] and their algorithm, Path of Minimum Pressure (PMP), to determine the percolation path and obtained similar results. A second method simply involves solving the nonlinear system of flow equations at various applied pressure gradients and identifying the first pathway that forms. This approach can be numerically challenging, but successful techniques for solution are discussed by Balhoff and Thompson[42]. Regardless of the technique used, the same threshold gradient and percolation path should be obtained.

Here, we are also concerned with the opening of pores above the threshold pressure gradient and, therefore, we solve the nonlinear flow equations for an applied pressure gradient. (IMP and PMP are useful only for finding the threshold gradient.) Solution of the nonlinear system of equations results in flow rates in each throat and the pathway of pores that are open to flow can be easily determined. Convergence of the numerical solution occurs when the mass balance reaches a pre-defined tolerance. The Balhoff and Thompson[42] approach involves imposing a large, but finite, viscosity in throats that are closed to find a solution for the pressure field, which may otherwise be indeterminate. The algorithm iterates, opening and closing bonds as the pressure field varies from iteration to iteration, until it converges. However, the solution may occasionally lead to isolated clusters of pores that appear to be

open (material balance at each pore is below the tolerance) but do not form a connecting path in the network. The flow rates in these pores are so small that they do not significantly affect numerical results for flow rate (i.e. Darcy velocity), but they can give inaccurate results for open pore volume. Therefore, once the numerical solution is complete, a "breadth-first search" is used to determine the open pores that form a connecting path(s) in the network and any isolated clusters are discarded. The algorithm also ensures that the pressure drop across each throat in the connecting path(s) exceeds the local throat threshold.

4.2.1.4. Percolation Patterns for different rheological models

The flow model (Bingham, Herschel-Bulkley, and the two foam models) is varied to investigate yield behavior. One goal of this work is to determine if universal relationships can be developed to describe the velocity and trapping of foam fluids. Here, we introduce dimensionless parameters for pressure gradient and velocity in order to develop these universal models. These dimensionless parameters are consistent with a bundle-of-tubes derivation of flow of shear-thinning fluids with a yield stress in porous media:

$$\nabla P_D = \frac{\Delta P}{L_{pm}\tau_0}\sqrt{\frac{2k}{\phi}}$$
………………………………………………………….(3.10)

$$u_D = \frac{u^n}{\left(\frac{k}{H}\sqrt{\frac{\phi}{2k}}\tau_0\right)}$$
………………………………………………………..(3.11)

All results presented are for m = 0.01 cp-sn and τ_0 = 0.7 dynes/cm2. The permeability in all cases is 9.88×10-11 cm2 (10 mD). However, results are presented in dimensionless form.

Flow simulations were conducted by imposing various pressure differences across the network model and investigating the resulting percolation path. At low pressure gradients, fluid does not yield and no pores are open to flow. The

threshold pressure gradient is the minimum pressure gradient required to induce flow.

Figure 4-37(A) shows the percolation path at the threshold gradient (∇PD = 0.35) in the uniform sphere packing for the four fluids: linear foam, power-law foam (n = 0.67), Bingham, and Herschel-Bulkley (n = 0.67). All simulations were performed in 3D, but the figure is collapsed into 2D for clarity. At the threshold gradient, 16 connected pores (out of 4070 total) open simultaneously. The percolation path is identical for all four fluids despite the flow equations being very different (**Figure 4-36**). For all fluids, the local mobilization pressure drop in a throat is equal to ΔPm. The disparities in flow behavior (**Figure 4-36**) above the mobilization pressure drop in a pore throat are irrelevant; at this threshold gradient Q = 0 in all throats except those on the percolating path, where the flow rates are infinitesimally small.
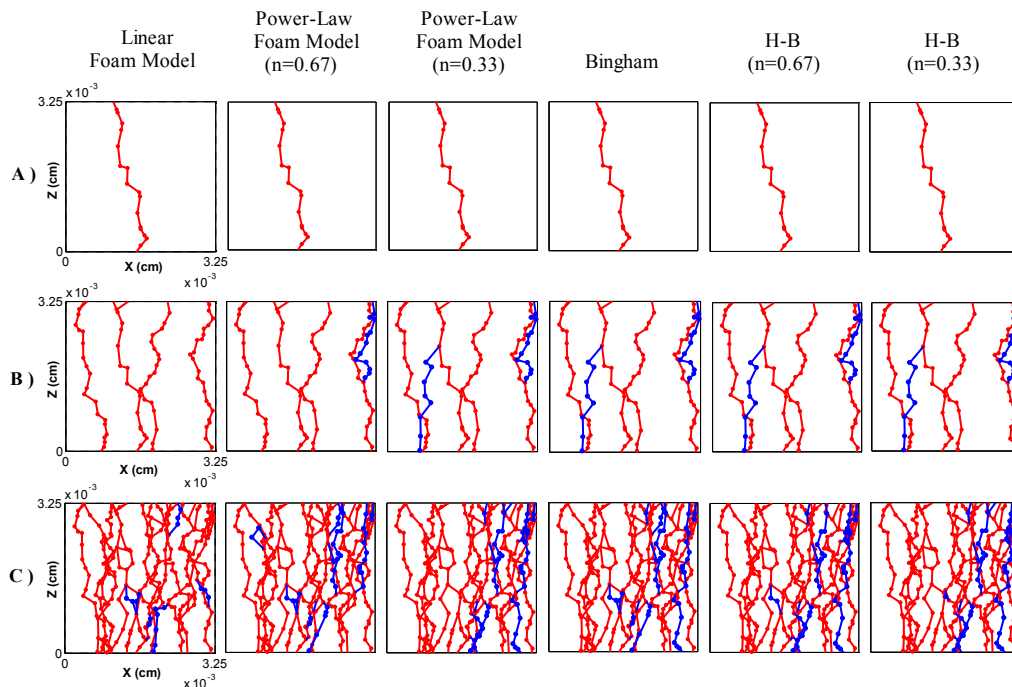
Figure 4-37: *Percolation patterns in grain packing for Bingham, Hershel-Bulkely, and Foam fluids (A) at the threshold (∇PD =0.35), (B) just above the threshold (∇PD =0.41), and (C) at high pressure gradients (∇PD = 0.49). Pathways in red are shared by all four*

fluid models and pathways in blue are specific to a particular model. All simulations were conducted by imposing a pressure gradient in the Z-direction.

The percolating path shown in **Figure 4-37(A)** is different from what would be obtained in classical percolation theory. In classical theory, the percolating path would correspond to the set of connected pores/throats that were all above some critical radius. It does not allow for small pores/throats on the connected path. Here, the percolation path is simply the minimum sum of local mobilization pressure drops (Equation 3.9). It is very possible to have throats with a small radius on that path (Rossen and Mamun, 1993). **Figure 4-38** compares the initial flow path at the threshold pressure gradient to the percolation cluster from classical percolation theory for the same sphere pack. The initial pathway for flow in this case is not even part of the percolation cluster from classical percolation theory.

(A)   (B)
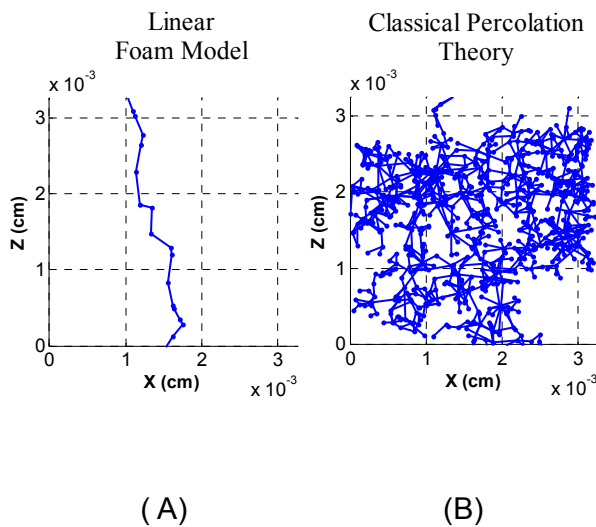
Figure 4-38: *Flow path (A) at the threshold pressure gradient obtained from flow modeling and (B) percolation cluster at the percolation threshold obtained from classical percolation theory, both for the sphere pack.*

Figure 4-37 (B) shows the percolation paths at a pressure gradient just above the threshold (∇PD = 0.41) where 77-97 pores are open. More than one percolation pathway has formed but these individual paths are in general not

connected to each other. Once again, these paths are nearly identical for the four fluid models despite the fact that the overall Darcy velocity and pressure distributions are (slightly) different. Evidently flow is dominated by yield-stress effects and not viscous effects at this pressure gradient. The pressure field in the open pores is different in the four simulations, but not enough to cause significant differences in trapping.

Figure 4-37 (C) shows the open pores at a higher pressure gradient ($\nabla PD = 0.49$): 282-313 pores are open. Individual percolating pathways have merged and formed branches. The pore pressures reflect both yield stress and viscous effects. As a result, pores/throats open in different sequences for the different fluid models (i.e. the pressure drop across a particular throat may be large enough to open for a simulation with one fluid model, but not another). The threshold percolation path is independent of the fluid model, but the flow backbone at higher pressure gradients is dependent on the fluid model.

4.2.1.5. Key differences between the curves are observed for the sphere pack and the sandstone:

The dimensionless threshold gradient for the sandstone ($\nabla PT = 0.07$) is lower than the sphere pack ($\nabla PT = 0.35$). The sandstone has a broader pore-size distribution. It is more likely that the percolation path is formed with connected wide pores. Also, there can be spatial correlation in pore size in the sandstone, since it is imaged from a real, natural medium; large pores tend to be connected to large pores and small pores to small pores.

Scaling of open volume fraction with pressure gradient is distinctly different from that for the sphere pack. Given the magnitude of this difference, it seems unlikely that any model like Equation 3.2 could work for the range of porous media encountered in foam EOR in the field with a single scaling exponent.
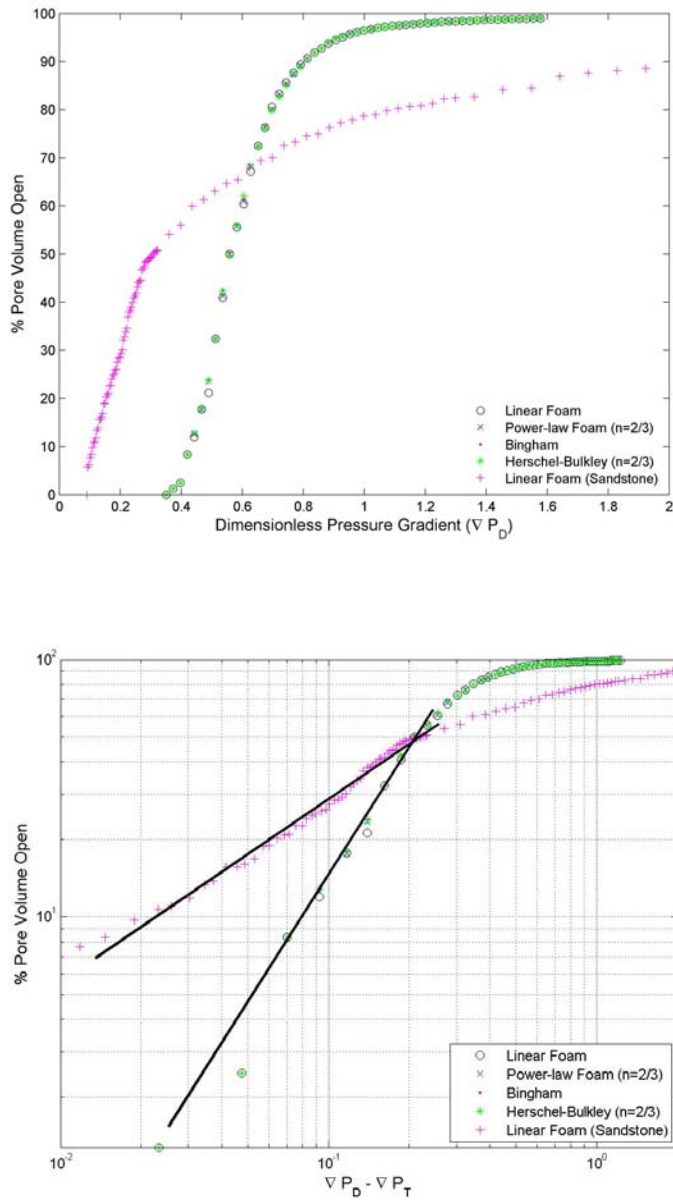
Figure 4-39: (top) Percent pore volume open (flowing) versus dimensionless pressure gradient for Bingham, Herschel-Bulkley (n = 0.67), and foam fluids in a packing of uniform spheres, and the linear foam model (n = 1) in the sandstone and (bottom) open volume fraction plotted on a log-log scale v. (∇PD-∇PT) for the given network. Straight lines are merely trends lines through the results.

Despite the smaller dimensionless threshold pressure gradient for flow, a larger dimensionless pressure gradient is needed to mobilize gas in all pores in the sandstone than in the sphere pack. The wide pore size distribution means that there is a wide difference between the pressure gradient required to open the first path for flow and to open the smallest pores in the network.

The percolation path at the threshold gradient represents a larger pore volume for the sandstone than for the sphere pack. The large fraction of pore volume in the initial path is largely due to the large number of pores in the connecting path for the sandstone (40 pores out of 4991) which contain 2.4% pore volume at the threshold. In the sphere pack, fewer pores open at the threshold (16 out of 4070) which contain only 1.3% of the pore volume. In the sandstone, the throats connecting pores are relatively short. Moreover, the more heterogeneous and lower-porosity medium requires a more tortuous path to connect at the edges.

4.2.2. Dimensionless Velocity/Relative Permeability

One goal of this work is to develop a macroscopic, closed-form model for Darcy velocity of foam. We take two approaches to develop such a model. The first involves adapting existing models for yield stress flow in porous media which are valid at large pressure gradients (but fail near the threshold). The second approach builds on existing scaling theories for foam flow.

Yield Stress Model. The Al-Farris and Pinder model for flow of Herschel-Bulkely fluids in porous media (represented as a bundle of uniform tubes) can be written in dimensionless form as:

$$u_D = \nabla P_D - \nabla P_T$$ ……………………………………………………………………(4.1)

The model was derived under several limiting assumptions (Balhoff and Thompson, 2004). In fact, the model is invalid for Bingham and Herschel-Bulkley fluids near the threshold gradient even in a uniform bundle of

tubes because it ignores additional nonlinearities in the flow equations. The model is better suited for the foam models presented in this paper that do not have these nonlinearities.
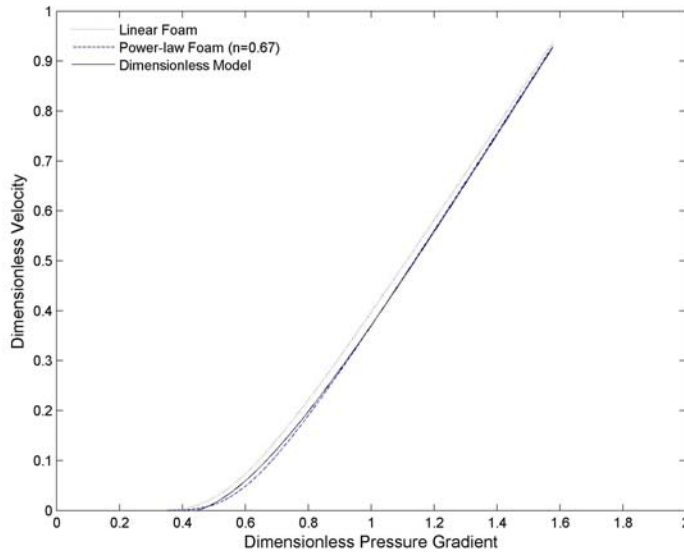
Figure 4-40: Dimensionless velocity versus dimensionless pressure gradient for the two foam models in sphere pack. The numerical results are compared to the theoretical model (Equations 4.2 and 4.3).

For the foam models a linear relationship analogous to Equation 4.1 is correct for $\nabla PD \gg \nabla PT$ because all pores are open, but is inaccurate near the threshold gradient in real porous media. **Figure 4-40** shows the dimensionless velocity versus dimensionless pressure gradient for the linear and power-law foam fluid models. Plotted on this figure, Equation 4.1 is a straight line. The superficial velocity is nonlinear near the threshold pressure gradient, however, as pores open. The curve approaches a straight line (with slope one) at higher pressure gradients. Equation 4.1 is not useful for foam flow, where we are concerned with relatively low pressure gradients. Here we attempt to correct the equation to account for foam trapping behavior.

The linear relationship between dimensionless velocity and pressure gradient as proposed in Equation 4.1 would be correct if the open fraction of

pores were to remain constant. However, pores open in a very nonlinear fashion as pressure gradient is increased. We propose a dimensionless, modified form or Darcy's law for foam that is based on our pore-network results. The expression includes threshold pressure gradient but the curve is nonlinear near the threshold gradient. **Figure 4-40** shows that the curve approaches a straight line with a new x-intercept shifted ~85% to the right. This is accounted for in Equation 4.2 with the variable "D".

$$u_D = \nabla P_D - \nabla P_T \left(1 + D\right) \quad (4.2)$$

where

$$D = D_0 \left\{ 1 - \exp\left[-4\left(\nabla P_D - \nabla P_T \right) \right] \right\} \quad (4.3)$$

D evolves from 0 at the threshold gradient to D0=0.85 at high pressure gradients. **Figure 4-40** shows the relationship between D and pressure gradient for the linear foam model and power-law foam model (n=0.67) in the sphere pack. The curves follow similar trajectories and can be approximately described by Equation 4.4. However, the curves are different and Equation 4.4 still results in error near the threshold gradient.
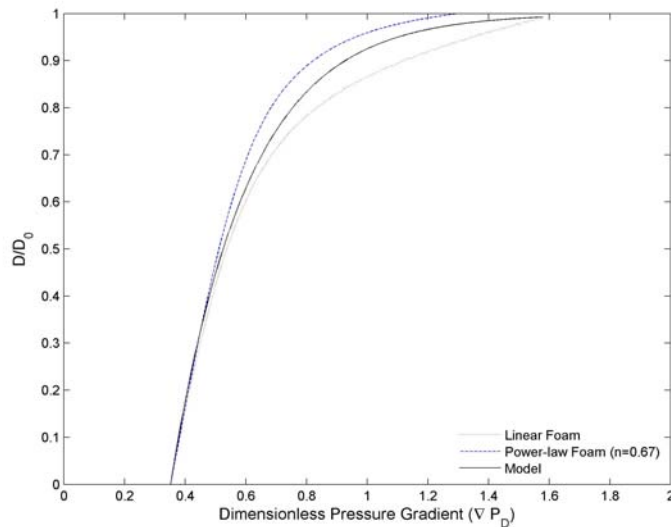
Equations 4.4 and 4.5 represent a first step toward a model for all fluids in all media, but here are based on results from two fluids in the sphere pack. For other media, such as sandstone, Equation 4.5 may not suffice for all fluids (or at least different fitting constants would need to be needed).

A plot of uD versus (∇PD-∇PT) (**Figure 4-41**) illustrates the challenges in developing a universal model for foam flow. For the sandstone there is no single linear trend through the data, but a continuously decreasing slope throughout. For the sphere pack, behavior is markedly different. For both foam fluids, there is a distinct change in trend at a dimensionless pressure gradient (∇PD-∇PT) ~ 0.06. At this ∇P, less than 10% of the foam is flowing (**Figure 4-39 (b)**). For smaller pressure gradient, the dimensionless superficial velocity scales with about the 1.1 power of (∇PD-∇PT). Above this transition, dimensionless superficial velocity rises with different scaling for the two foam models. An additional complication for real foams is that the relation between flow rate and ∇P along one pathway may be much more complex, and harder to unravel, than for the simple model fluids considered here (Xu and Rossen, 2003).
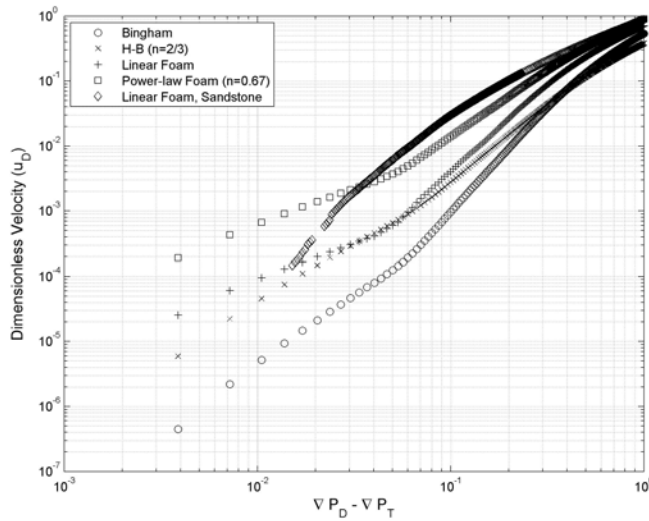
__Figure 4-42:__ Log-log plot of dimensionless velocity versus (∇PD-∇PT) for the two foam models in the sphere pack and the foam model with n=1 in the sandstone.

4.2.3. Modeling trapped gas as a function of lamella density

4.2.3.1. Fluid Models

We test three different continuum fluid models to represent the lamella flow through a pore throat: linear, power-law, and Hirasaki-Lawson apparent gas (lamella) viscosity models. Although the flow equation is different for each fluid model because of the different definitions of apparent gas viscosity as shown in **Table 4-xi**, all the flow equations share the same form as follows:

$$q = \frac{g}{\mu_{app}}\left[\Delta P - \Delta P_m\right] \quad ; \quad \Delta P \geq \Delta P_m \ldots\ldots\ldots\ldots\ldots\ldots\ldots\ldots\ldots\ldots\ldots\ldots\ldots\ldots\ldots(4.1)$$

where q is the flow rate in a pore throat, g is the hydraulic conductivity of a pore throat, μ_{app} is the pore-scale apparent gas viscosity, ΔP is the pressure drop in a pore throat, and ΔP_m is the mobilization pressure difference across a pore throat.

The use of the linear model reflects the approximation of the viscous drag force on the shape of the surface region tangential to the aqueous film wetting the pore surface (Nguyen et al., 2004). Due to the continuity of the liquid within the Plateau border and the wetting film, the motion of the Plateau border as a whole must be resisted by a certain viscous stress of the order of ($\mu_{liq} v_g^f / \delta$), where δ is the wetting layer thickness, μ_{liq} is the liquid viscosity, and v_g^f interstitial gas velocity with foam lamella. In this sense, since no mass transfer is taken into account, it is assumed the viscous drag force exerted by the wetting layer on the moving Plateau border is proportional to the shear rate at the wetting film-Plateau border contact (film velocity) for a given wetting layer thickness.

However, the above approximation is not very accurate when the effect of the viscous drag force on the shape of the surface region tangential to the wetting film becomes significant. This effect was first theoretically described by Bretherton (1961) and then extended by Hirasaki and Lawson (1985) to the motion of lamellas separated gas. In the latter study, the apparent gas viscosity was found to be proportional to $(v_g^f)^{-1/3}$ suggesting a shear thinning behavior of lamella flow in a straight capillary tube. In this work, we compare the mechanistic Hirasaki-Lawson model with the empirical power-law model. Since the power-law model reduces to the linear model when $n = 1$, these two simple foam models have the advantage that scaling of flow rate with pressure gradient is much simpler above the threshold for flow in one tube, which makes it easier to distinguish viscosity effects and relative-permeability effects in our network model. They also allow one to test a range of shear-thinning and yield-stress behavior in a simple format.

Table 4-xi: _Fluid models representing the lamella flow through a pore throat._

Fluid Model	General Form	Apparent Gas Viscosity	Flow Equations
Linear	$q = \dfrac{g}{\mu_{app}}\left[\Delta P - \Delta P_m\right]$ $\Delta P \geq \Delta P_m$ $g = \dfrac{\pi R^4}{8L}$	$\mu_{app} = \mu$	$q = \dfrac{g}{\mu}\left[\Delta P - \Delta P_m\right]$
Power-law		$\mu_{app} = \mu_o\left(\dfrac{3n+1}{4n}\right)^n\left(\dfrac{R}{4v_g^f}\right)^{(1-n)}$	$q = \dfrac{g}{\mu_o^{1/n}}\left(\dfrac{4n}{3n+1}\right)\left(\dfrac{R}{2L}\right)^{(1/n)-1}\left(\Delta P - \Delta P_m\right)^{1/n}$
Hirasaki-Lawson (1985)		$\mu_{app} = 0.85\dfrac{\mu_w(R/L)}{(r_c/R)}\left(\dfrac{\gamma}{3\mu_w v_g^f}\right)^{1/3}\left[\left(\dfrac{r_c}{R}\right)^2+1\right]$	$q = \dfrac{g}{\dfrac{3\mu_w R^2}{8\gamma L}\left(2.26\dfrac{\gamma}{r_c}\left[\left(\dfrac{r_c}{R}\right)^2+1\right]\right)^{3/2}}\left[\Delta P - \Delta P_m\right]^{3/2}$

Gas trapping is mainly governed by either entry capillary pressure or resilience of lamellae. The former even occurs in a non-dispersed two-phase system during drainage, where gas cannot invade some liquid-filled pore throats of high entry capillary pressure (sometime called dead-ends to the invading fluid). The latter, which is most important in steady-state foam flow, or imbibition following steady-state foam, relates to the inherent yield property of lamellas in divergent flow channels. Like bulk foam – where Bingham plastic behavior is expressed through the deformation of a foam interface before either its rupture or mobilization (Princen, 1983; Prud'homme, 1981; Heller and Kuntamukkula, 1987), the yield stress of a curved lamella in a divergent pore is nothing but the imposed pressure gradient that is counterbalanced by the equilibrium lamella tension (γ). Therefore, it may scale as

$$\Delta P_m \sim \frac{\gamma}{R} \dots\dots\dots\dots\dots\dots\dots\dots\dots\dots\dots\dots\dots\dots\dots\dots\dots\dots\dots\dots\dots(4.2)$$

where R is pore-throat radius and ΔP_m is mobilization pressure difference across a pore throat.

Note that this static yield stress can be significantly modified during the stretching-contracting motion of the lamella because of surface elasticity and viscosity (Schramm, 1994; Schramm and Green, 1995). As a result, besides pore radius (frequently taken as pore throat radius), the dynamic lamella tension also determines the magnitude of the yield pressure gradient (Xu and Rossen, 2000; Falls et al., 1989) under dynamic condition. However, this effect will be addressed in our future work.

In general, the flow equations in **Table 4-xi** are only applicable for flow in a straight capillary tube and need some modifications to capture the effect of converging and diverging structure of real porous media on fluid flow. Balhoff and Thompson (2004, 2006) developed a function to convert the geometric parameters of a real pore throat to an equivalent capillary by performing finite element simulations of power-law and yield stress fluids. This conversion helps to make better predictions of threshold pressure gradient at the macro scale, and it is employed here due to the similarity between the flow of yield-stress fluids and the flow of a foam lamella through a pore throat.

4.2.3.2. Definition of Lamella Density

Lamella density is a good measure of foam strength. It is believed that stronger foam in a porous medium exhibits finer bubbles whose sizes are limited by pore sizes (Rossen, 1996). Weak foam has coarse texture with lamella spacing of several pore lengths. In this sense, we investigate the effect of lamella density in the pore network by specifying the number of lamellas and then distributing them over the pore throats. Different realizations of spatial lamella distribution are used in favor of the fact that exact location of each lamella during flow in porous media is unknown. Therefore, our model does not explicitly simulate the movement of one lamella from one pore to another. Instead, it captures the lamella moving process by performing simulations for different lamella distributions in the network at constant total lamella density

and constant pressure gradient. Each realization represents a snapshot of the lamella flowing process.
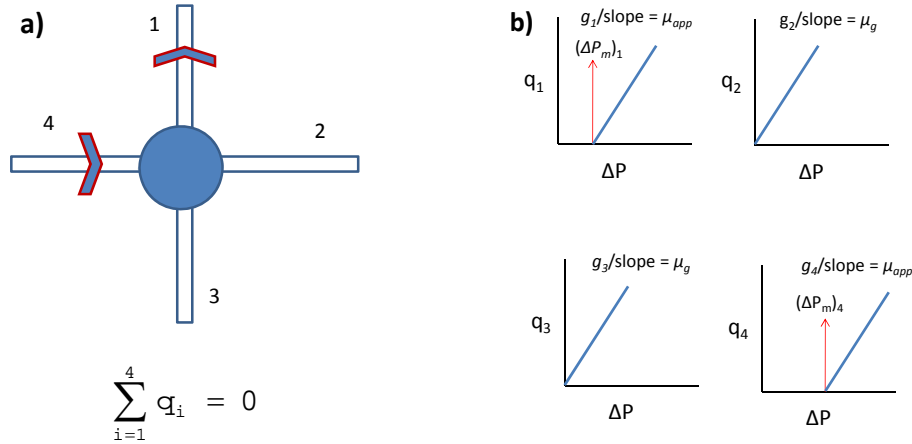
Figure 4-43: *(a) A sketch of the proposed model for a representative pore and its throats and (b) the respective plots of flow equations at each pore throat.*

A sketch of the proposed model is shown in **Figure 4-43 (a)**. Consider a pore with four throats; two (pore throats #1 and #4) have one lamella, while the other two (#2 and #3) do not have lamella. If the linear model (**Table 4-xi**) is employed to represent gas flow with lamella through the pore throats, the respective plots of the flow equations for each throat are depicted in **Figure 4-43 (b)**. Gas flow through a pore throat without a lamella (throats #2 and #3) is represented by the Newtonian flow equation with an assumption that gas compressibility is negligible. This assumption is valid for small pressure gradient as compared to the system pressure. Modeling flow in the network requires ensuring mass balance at every pore; this leads to a system of N equations (N being the number of pores), where the pore pressures are the unknowns. The resulting system of equations can be solved to determine the pore pressures in the network and the total flow rate (or velocity) for an applied pressure gradient in one direction. The fluid flow equations representing lamella flow through a capillary tube in **Table 4-xi** are nonlinear and therefore a multidimensional Newton-Raphson scheme is used to solve a system of these equations.

We use two different lamella density definitions in **Table 4-xii** to make comparisons between our results and the theoretical studies in literature. In the first definition, flowing lamella density is defined as the number of flowing lamellas divided by the number of pore throats in the flowing gas domain, while total lamella density is defined as the total number of lamellas in the pore-network divided by the total number of pore throats. In the second definition, the number of flowing lamellas is normalized to the flowing gas volume and the number of total lamellas to the total gas volume (pore volume in our case). The first definition of lamella density is used throughout the paper unless otherwise specified.

__Table 4-xii:__ *Different definitions of lamella density.*

	Flowing Lamella Density	**Trapped Lamella Density**	**Total Lamella Density**
ef. 1	$\rho_{fg}^{L} = N_{fg}^{L} \big/ N_{fg}^{T}$	$\rho_{tg}^{L} = N_{tg}^{L} \big/ N_{tg}^{T}$	$\rho_{t}^{L} = N^{L} \big/ N^{T}$
ef. 2	$n_{fg}^{L} = N_{fg}^{L} \big/ V_{fg}$	$n_{tg}^{L} = N_{tg}^{L} \big/ V_{tg}$	$n_{t}^{L} = N^{L} \big/ V_{g}$

4.2.3.3. Calculation of trapped Gas fraction

Gas trapping is driven by the pore-scale differential pressure relative to the mobilization pressure drop (ΔP_{m}) across each pore throat occupied by a lamella. The latter depends on the lamella interfacial tension and pore geometry. The local pressure field in a pore network with N pores could be obtained from the solution of Eq. 4.1**.**

$$
\underbrace{\begin{bmatrix} -\left(\sum_{j=1}^{t1}\dfrac{g_{1j}}{\left(\mu_{1j}\right)_z}\right) & \cdots & \left(\dfrac{g_{1j}}{\left(\mu_{1j}\right)_z}\right)_z \\ \vdots & \ddots & \vdots \\ \left(\dfrac{g_{Nj}}{\left(\mu_{Nj}\right)_z}\right)_z & \cdots & -\left(\sum_{j=1}^{tN}\dfrac{g_{Nj}}{\left(\mu_{Nj}\right)_z}\right) \end{bmatrix}}_{\text{Matrix A} \qquad N\times N} \begin{bmatrix} P_1 \\ \vdots \\ P_N \end{bmatrix}_{N\times 1} = \underbrace{\begin{bmatrix} \left(\sum_{j=1}^{t1}\left(\dfrac{g_{1j}\left(\Delta P_m\right)_{1j}}{\left(\mu_{app}\right)_{1j}}\right)_z - \left(\dfrac{g_{1j}}{\left(\mu_{1j}\right)_z}P_b\right)_z\right) \\ \vdots \\ \left(\sum_{j=1}^{tN}\left(\dfrac{g_{Nj}\left(\Delta P_m\right)_{Nj}}{\left(\mu_{app}\right)_{Nj}}\right)_z - \left(\dfrac{g_{Nj}}{\left(\mu_{Nj}\right)_z}P_b\right)_z\right) \end{bmatrix}}_{\text{Vector B} \qquad N\times 1}
$$
(4.1a)

$$
\left(\frac{g_{Nj}}{\left(\mu_{Nj}\right)_z}\right)_z = \begin{cases} \dfrac{g_{Nj}}{\left(\mu_{Nj}\right)_z} & \text{, with pore throat} \\ 0 & \text{, no pore throat} \end{cases} ; \qquad \left(\mu_{Nj}\right)_z = \begin{cases} \left(\mu_{app}\right)_{Nj} & \text{, with lamella} \\ \mu_g & \text{, no lamella} \end{cases}
$$
(4.1b)

$$
\left(\frac{g_{Nj}}{\left(\mu_{Nj}\right)_z}P_b\right)_z = \begin{cases} \dfrac{g_{Nj}}{\left(\mu_{Nj}\right)_z}P_b & \text{, with constant pressure boundary} \\ 0 & \text{, no boundary} \end{cases} ; \qquad P_b = \begin{cases} P_{in} & \text{, inlet boundary} \\ P_{out} & \text{, outlet boundary} \end{cases}
$$
(4.1c)

$$
\left(\frac{g_{Nj}\left(\Delta P_m\right)_{Nj}}{\left(\mu_{app}\right)_{Nj}}\right)_z = \begin{cases} \dfrac{g_{Nj}\left(\Delta P_m\right)_{Nj}}{\left(\mu_{app}\right)_{Nj}} & \text{, with lamella} \\ 0 & \text{, no lamella} \end{cases} ; \qquad \left(\mu_{app}\right)_{Nj} = \begin{cases} \text{Linear} \\ \text{Power-law} \\ \text{Hirasaki-Lawson (1985)} \end{cases}
$$
(4.1d)

where g_{Nj} is the hydraulic conductivity of a pore throat, μ_{Nj} is the apparent gas viscosity (μ_{app}) or gas viscosity (μ_g) depending on the distribution of lamellas in the network, P_b is inlet or outlet boundary pressure of the pore-network. Moreover, the subscript Nj is the pore throat j connected to pore N, and the upper bound of summation tN is the number of pore throats connected to pore N. Eq. 4.1a shows that the local differential pressure distribution is determined by total lamella density, spatial lamella distribution in the network, the contrast between the apparent and ordinary gas viscosities, and the shear thinning effect of moving lamellas.

For the purpose of scaling trapped gas fraction with the characteristics of permeable medium, fluids, and flow, we use the following dimensionless macroscopic pressure gradient (Balan et al., 2011a, 2011b).

$$\nabla P_D = \frac{\nabla P}{(2\gamma/L_c)}\sqrt{\frac{2k}{\phi}} \quad \text{...(4.2)}$$

Where γ is interfacial tension between surfactant solution and gas, L_c is characteristic pore-throat length of the pore network, k is absolute permeability, Φ is porosity, ∇P is pressure gradient, and ∇P_D is dimensionless pressure gradient.

Unless otherwise specified, permeability and $(2\gamma/L_c)$ ratio used in all cases are 9.88×10^{-15} m^2 (10 mD) and 6.89×10^{-2} Pa, respectively. Moreover, the interfacial tension between water and gas (γ) is 72×10^{-3} N/m for Hirasaki-Lawson model, and shear-thinning index for power-law model (n) is (2/3). Since there are only gas and lamellae in the network, total gas saturation is equal to one and thus the flowing gas fraction is defined as flowing gas saturation, S_{fg} in Eq. 4.3.

$$X_{fg} \equiv S_{fg} \quad \text{with} \quad S_g = 1.0 \quad \text{...(4.3)}$$

4.2.3.4. Flowing gas fraction versus pressure gradient

Figure 4-45 (a) shows the relationship between flowing gas fraction (X_{fg}) and dimensionless pressure gradient for different total lamella densities and zero viscosity contrast between lamellas and gas. X_{fg} increases with decreasing total lamella density (ρ_t^L) in the pore network at fixed pressure gradient. Therefore, it is easier to open flow paths at lower total lamella density. It is also found that there exists a threshold pressure gradient (∇P_T) as total lamella density increases above 0.6 and that the threshold pressure gradient nonlinearly increases with total lamella density. **Figure 4-44 (b)** shows the gas relative permeability with foam as a function of flowing gas fraction for different total lamella densities, compared with the theoretical correlations proposed by Falls et al. (1988, 1989), Friedmann et al. (1991), Kovscek and Radke (1994). It could be observed from this figure that the effect of total lamella density on the

gas relative permeability with foam is not very significant. Therefore, flowing gas fraction mainly determines the relative permeability of the flowing gas. In addition, our results indicate that the gas relative permeability increases nonlinearly with the flowing gas fraction, which is qualitatively consistent with Kovscek and Radke (1994). Note that the gas relative permeability curves in **Figure 4-45 (b)** have different end points because of the difference in total lamella density used in these cases.
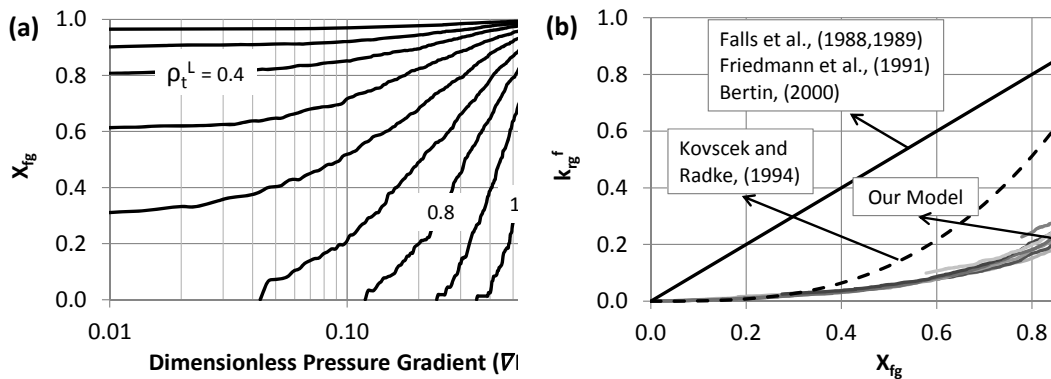
Figure 4-44: *(a) Flowing gas fraction vs. dimensionless pressure gradient, ∇P_D for different total lamella densities in the pore network, and (b) gas relative permeability with foam vs. flowing gas fraction. The linear model is used for our results.*

  Figure 4-45 (a) shows that flowing lamella density is zero at low pressure gradient when total lamella density is lower than 0.7, consistent with zero threshold pressure gradient observed in **Figure 4-44 (a)**. Flowing phase prefers the least resistant pathways at a specific pressure gradient. Total lamella densities lower than 0.7 enables gas to flow through lamella unoccupied paths at low pressure gradient and to mobilize lamella at elevated pressure gradient, resulting an increase in flowing lamella density (ρ_{fg}^{L}) within the flowing gas domain. The flowing lamella density converges to the total lamella density as pressure gradient is high enough to open all pores in the network to flow. As demonstrated in **Figure 4-45 (b)** flowing lamella density converges to the total lamella density of 0.8 while trapped lamella density converges to 1.0 when pressure gradient increases. This important result opposes one of the main

259

assumptions underlying the population balance based foam modeling approaches (Kovscek et al., 1995, 1997) that is flowing lamella density is equal to trapped lamella density.
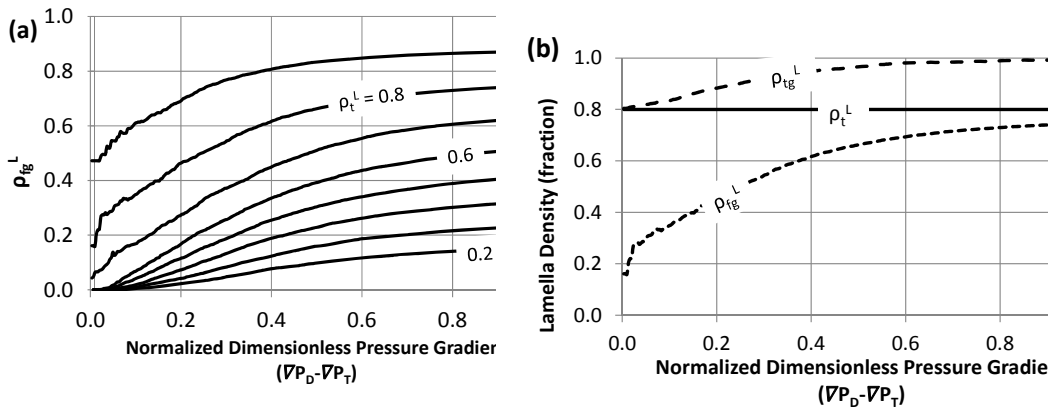
__Figure 4-45:__ (a) Flowing lamella density vs. normalized dimensionless pressure gradient for different total lamella densities in the pore network, and (b) flowing and trapped lamella density vs. normalized dimensionless pressure gradient at a constant total lamella density of 0.8. The linear model is used in these simulations.

Note that the above results are based on one realization of spatial lamella distribution in the network. Different patterns of lamella distribution may modify the functional relationships between the gas relative permeability, trapped gas fraction, and pressure gradient. This hypothesis could be tested by evaluating the variation of these relationships for multiple realizations. More than 50 different realizations for each total lamella density have been tested and the test results for two different total lamella densities (0.4 and 0.8) and 6 distributions of lamellas in the pore network are shown in **Figure 4-46**. These six realizations represent both "heterogeneous" and "homogeneous" type distribution of lamella in the network. The former means that the lamellas are mixed well with all the pore throats in the network. For low total lamella density (**Figure 4-46 (a)**), the heterogeneity of lamella distribution does have an obvious influence on flowing gas fraction. However, this influence is significantly reduced for high total lamella density as shown in **Figure 4-46 (b)**. It is also found that the relationship between gas relative permeability and

flowing gas fraction (**Figure 4-44 (b)**) is not modified by the variation of lamella distribution over a wide range of lamella density. This suggests that modeling of the movement of lamellae from one pore to another may be unnecessary to obtain macroscopic rheological foam properties at a constant total lamella density.
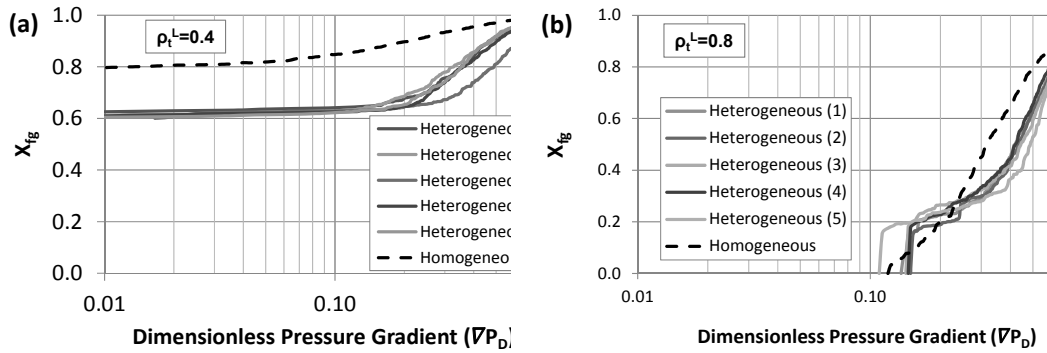
Figure 4-46: *Comparison of the effect of different spatial lamella distributions on flowing gas fraction as function of dimensionless pressure gradient at constant total lamella densities: $\rho_t^L = 0.4$ (a) and 0.8 (b). The linear model is used in these simulations.*

Due to significant lamella resistance to flow, one may suspect that the viscosity contrast between gas and lamella would influence trapped gas fraction through modifying the local pressure field at fixed pressure gradient. To quantify this effect, four different hypothetical viscosity contrasts are investigated for two different total lamella densities and the results are shown in **Figure 4-47**. It is interesting to observe from this figure that pore-scale viscosity contrast is not an important factor controlling flowing gas fraction and thus gas relative permeability with foam on a macroscopic scale over a wide range of total lamella density. Since the viscosity contrast is both affecting the matrix *A* and vector *B* in Eq. 4.1, its effect on the pressure field, and thus gas trapping is reduced.
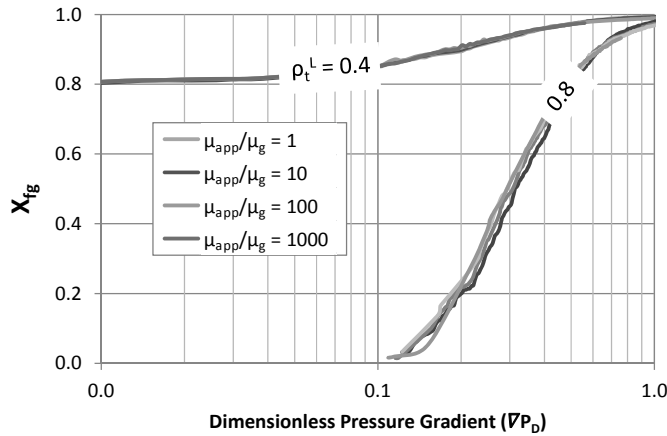
Figure 4-47: *Flowing gas fraction X_{fg} vs. dimensionless pressure gradient ∇P_D for different viscosity contrasts and two total lamella densities, $\rho_t^L = 0.4$ and 0.8. The legend shows the ratio of pore-scale apparent gas viscosity to ordinary gas viscosity at standard conditions. The linear model is used in these simulations.*

The non-Newtonian effect of lamella flow on gas trapping is evaluated through the power-law and Hirasaki-Lawson models and the results are shown in **Figure 4-48**. It is obvious from this figure that the variation of rheological behavior from Newtonian to shear thinning does not influence the flowing gas fraction over a wide range of total lamella density.
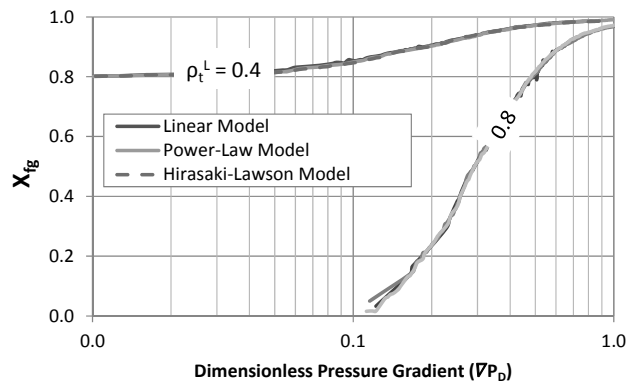
Figure 4-48: *Flowing gas fraction vs. dimensionless pressure gradient for the linear, power law, and Hirasaki-Lawson models for two different total lamella densities, $\rho_t^L = 0.4$ and 0.8.*

4.2.4. Scaling of TRAPPED GAS FRACTION

We have establish that the relationship between flowing gas fraction and dimensionless pressure gradient is not dependent on the viscosity contrast between lamella and gas, and the viscosity models over a wide range of overall lamella density. For numerical simplicity, the lamella flow equation with the constant viscosity model is used in here, and the apparent gas (lamella) viscosity is equal to regular gas viscosity.

Figure 4-49 (a) shows the relationship between flowing gas fraction (X_{fg}) and dimensionless pressure gradient ($\nabla P_D = \dfrac{\nabla P}{\left(2\gamma/L_c\right)}\sqrt{\dfrac{2k}{\phi}}$) for an overall lamella density (ρ_t^L) of 1.0 in the grain pack and the sandstone (overall lamella density is defined as the total number of lamellas in the pore-network divided by the total number of pore throats). Note that the percent pore volume open for sandstone does not reach to 100% at very high pressure gradients due to presence of the dead-end pores in the network, where fluid flow does not occur. In fact, removing these dead-end pores from the network does not change the absolute permeability of sandstone. Therefore, the flowing gas fraction for sandstone in **Figure 4-49 (a)** is a normalized version of the percent pore volume open. **Figure 4-49 (a)** shows that the dimensionless threshold pressure gradient, ∇P_T, for the sandstone is smaller than that for the grain pack.

Moreover, the sandstone requires more (∇P_D -∇P_T) to open all pores in the network than the grain pack does. The physical meaning of these results can only be understood if the pore-throat radius distributions of each pore-network having the same permeability are plotted (**Figure 4-49 (b)**). Log-normal mean of the pore-throat radius distribution for the sandstone is greater than that for the grain pack. The larger the mean pore-throat radius, the easier the foam flow initiates and therefore, the smaller the ∇P_T. Furthermore, the variance of pore-throat radius for sandstone is greater than that for the grain pack. The higher the variance of pore-throat radius, the more pressure gradient

above the threshold pressure gradient (∇P_D -∇P_T) is required to open all pores in the network.

Flowing gas fraction vs. dimensionless pressure gradient is plotted for different overall lamella densities for the grain pack and the sandstone in **Figure 4-50**. Although it seems that X_{fg} curves for the sandstone are different than those for the grain pack, there are some important similarities between them that need to be highlighted. For both networks, X_{fg} increases with decreasing ρ_t^L at a fixed ∇P_D. Therefore, it is easier to open flow paths at lower ρ_t^L. Moreover, ∇P_T for both networks increases with ρ_t^L if ρ_t^L is above 0.65.
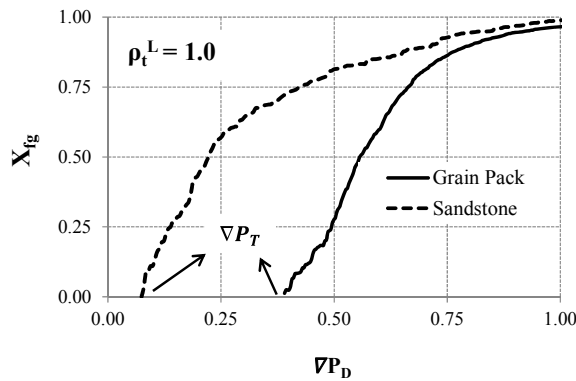
(a)
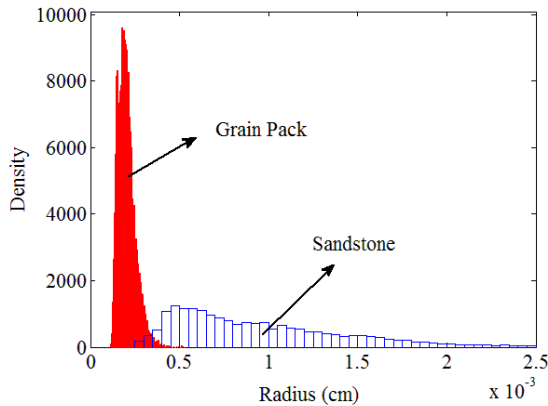
(b)

Figure 4-49: (a) Flowing gas fraction (X_{fg}) vs. dimensionless pressure gradient (∇P_D) for an overall lamella density (ρ_t^L) of 1.0 in the grain pack and the sandstone. (b) Pore-throat radius distribution for the grain pack and the sandstone having a permeability of 9.88 10^{-10} cm^2 (100mD).
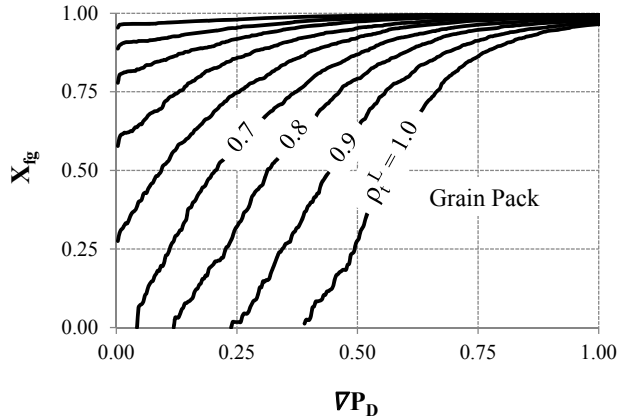
(a)
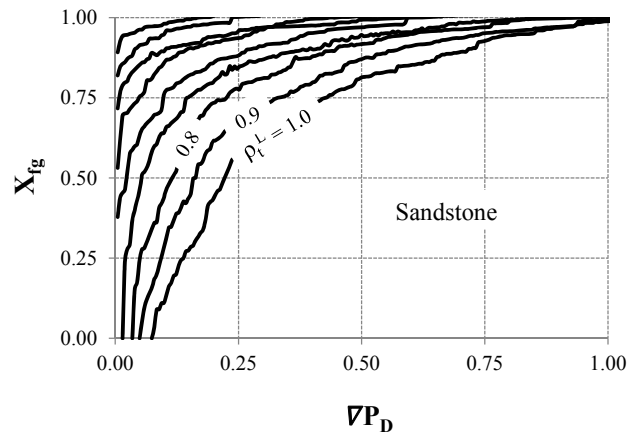
(b)

Figure 4-50: Flowing gas fraction (X_{fg}) vs. dimensionless pressure gradient (∇P_D) for different overall lamella densities (ρ_t^L) in (a) the grain pack and (b) the sandstone.

It is important to note that the definition of the ∇P_D (Eq. 3.1) does not include the log-normal mean and variance of the pore-throat radius distribution for each network. This explains why X_{fg} curves for sandstone and grain pack look different in **Figure 4-50**.

$$\nabla P_D = \frac{\nabla P}{\left(2\gamma/L_c\right)}\sqrt{\frac{2k}{\phi}} \quad \text{...(3.1)}$$

Therefore, including the characteristic pore-network parameters into the definition of dimensionless pressure gradient would generate X_{fg} curves

independent of the pore-network type. For this purpose, the following dimensionless pressure gradient $(\nabla P_D)_A$ is proposed:

$$\left(\nabla P_D\right)_A = \frac{\nabla P}{\left(2\gamma/L_c\right)}\sqrt{\frac{2\left(\bar{R}\right)^2}{\phi}}\frac{\bar{R}}{\sigma_R} \quad\text{..(3.2)}$$

where $\bar{R}$ and σ_R are log-normal mean and standard deviation of the pore-throat radius distribution for a pore-network. The permeability term in Eq. 3.1 is replaced by $\bar{R}^2$ in Eq. 3.2. Moreover, the ratio of $(\bar{R}/\sigma_R)$ is included as a multiplier (Eq. 3.2).

Plotting X_{fg} as a function of $(\nabla P_D)_A$ instead of ∇P_D overlaps the dimensionless threshold pressure gradients $(\nabla P_T)_A$ for the grain pack and the sandstone for the overall lamella densities, ρ_t^L above 0.65 (**Figure 4-51**). Moreover, there exists a linear relationship between $(\nabla P_T)_A$ and ρ_t^L, which is independent of the pore-network type (**Figure 4-52**).
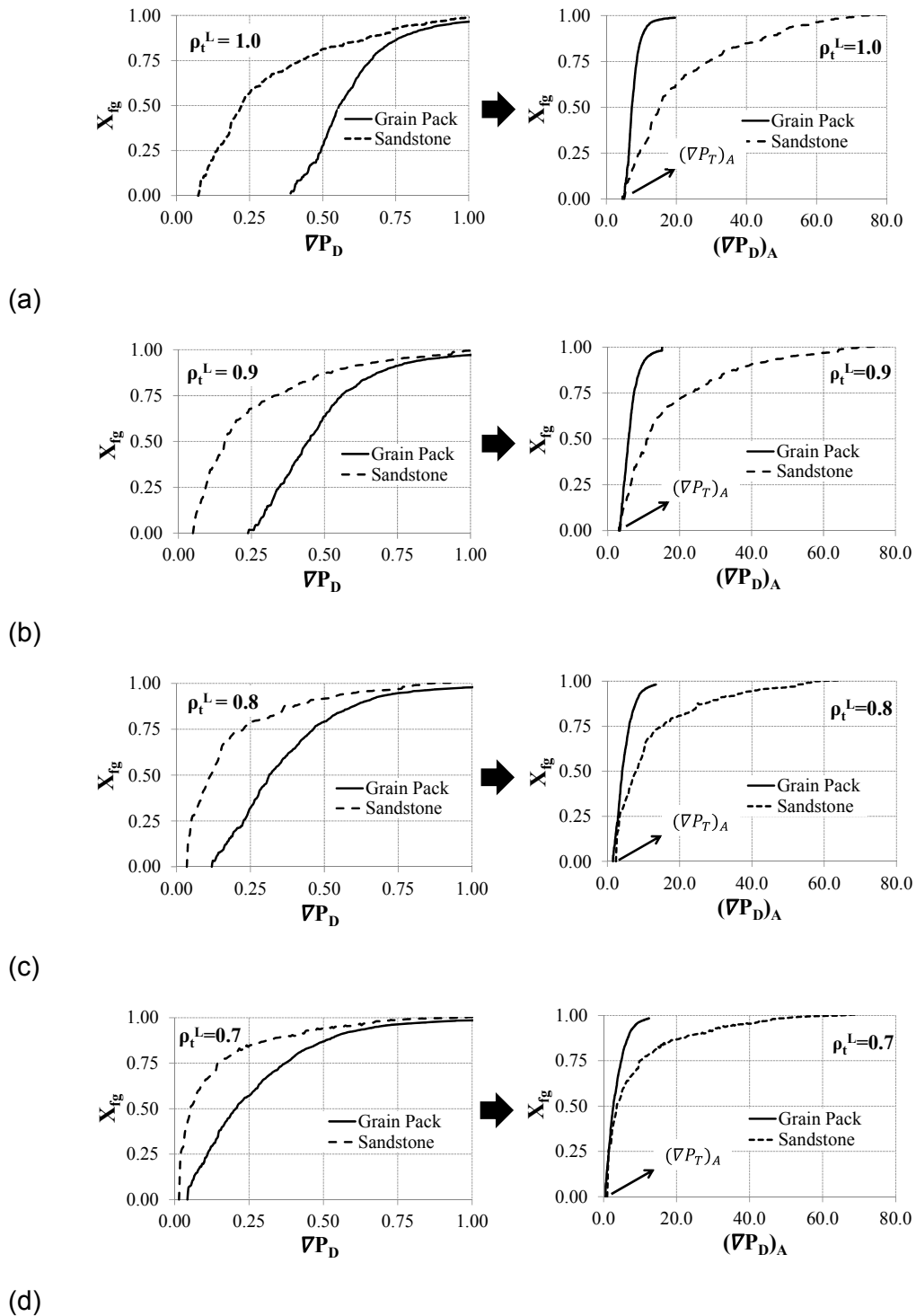
Figure 4-51: _Plotting flowing gas fraction (X_{fg}) as a function of (∇P_D)$_A$ instead of (∇P_D)_
overlaps the dimensionless threshold pressure gradients (∇P_T)$_A$ for the grain pack and the
sandstone for different overall lamella densities (ρ_t^L) in the discontinuous-gas foam flow
regime: (a) ρ_t^L =1.0, (b) 0.9, (c) 0.8, and (d)0.7.
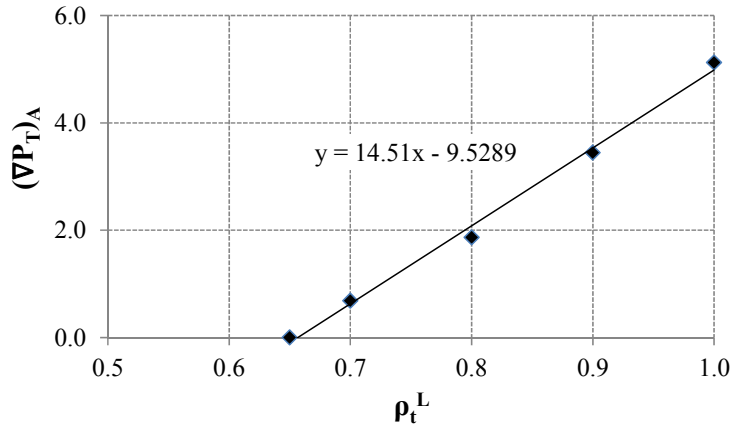
**Figure 4-52:** _The linear relationship between the dimensionless threshold pressure gradient ($\nabla P_T)_A$ and overall lamella density (ρ_t^L), which is independent of pore-network type._

Figure 4-51 shows that the sandstone requires more $(\nabla P_D)_A$ to open all the pores than the grain pack does, which results from the differences in the variance of pore-throat radius distribution $(\sigma_R)^2$ for each pore-network. $(\nabla P_D)_A$ has already a multiplier, which is $(1/\sigma_R)$, to represent standard deviation of the pore-throat radius distribution (σ_R) (Eq. 3.2), so the following modification on $(\nabla P_D)_A$ is proposed :

$$\left(\nabla P_D\right)_B = \left[\left(\nabla P_D\right)_A - \left(\nabla P_T\right)_A\right]\left(\frac{\sqrt{k}}{\sigma_R}\right)^{f_1} \quad \dots\dots\dots\dots\dots\dots\dots\dots\dots\dots\dots\dots\dots\dots(3.3)$$

Where f_1 is a matching parameter, which is defined as a function of ρ_t^L in **Figure 4-53**, to overlap X_{fg} curves for the sandstone and the grain pack at different ρ_t^L (**Figures 4-54** and **4-55**). Moreover, the two distinct foam flow regimes, which are continuous-gas ($\rho_t^L < 0.65$) and discontinuous-gas ($\rho_t^L > 0.65$) foam, can easily be identified in **Figure 4-53**. f_1 has a constant value of 0.35, if ($\rho_t^L < 0.65$) and it is an increasing linear function of ρ_t^L, if ($\rho_t^L > 0.65$).
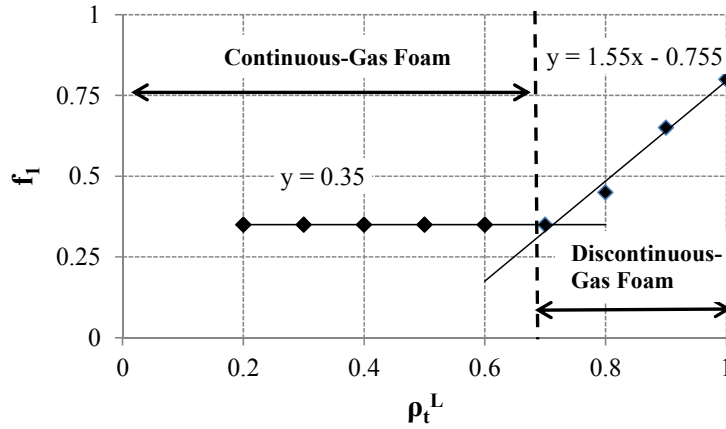
Figure 4-53: *The matching parameter f_1 as a function of overall lamella density (ρ_t^L).*

In **Figures 4-54** and **4-55**, the cumulative log-normal distribution function (Eq. 3.4) is successfully matched with the X_{fg} curves for different overall lamella densities. To improve these matches 0.35 is added to the values of the $(\nabla P_D)_B$ in Eq. 3.4a.

$$\left(\nabla P_D\right)_{B'} = \left(\nabla P_D\right)_B + 0.35 \quad\text{...(3.4a)}$$

$$X_{fg} = \frac{1}{2}\left[erfc\left(\frac{x_1 - \ln\left[\left(\nabla P_D\right)_{B'}\right]}{x_2\sqrt{2}} \right) \right] \quad\text{..(3.4b)}$$

The matching parameters x_1 and x_2 are defined as a function of overall lamella density, ρ_t^L in **Figure 4-56**.
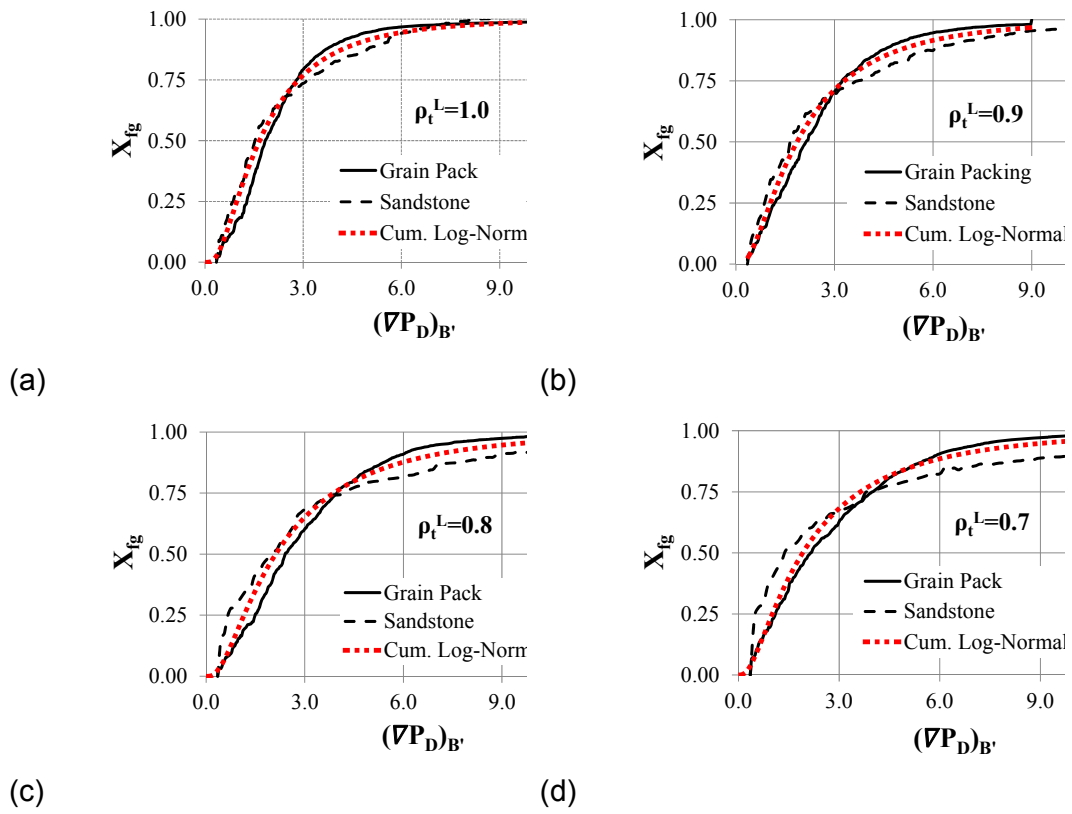
Figure 4-54: *Plotting flowing gas fraction (X_{fg}) as a function of ($\nabla P_D)_{B'}$ overlaps X_{fg} curves for the grain pack and the sandstone for different overall lamella densities (ρ_t^L) in the discontinuous-gas foam flow regime: (a) ρ_t^L=1.0, (b) 0.9, (c) 0.8, and (d)0.7. Moreover, cumulative log-normal distribution functions are successfully fitted to these curves.*

(a)

(b)

(c)

(d)

(e)
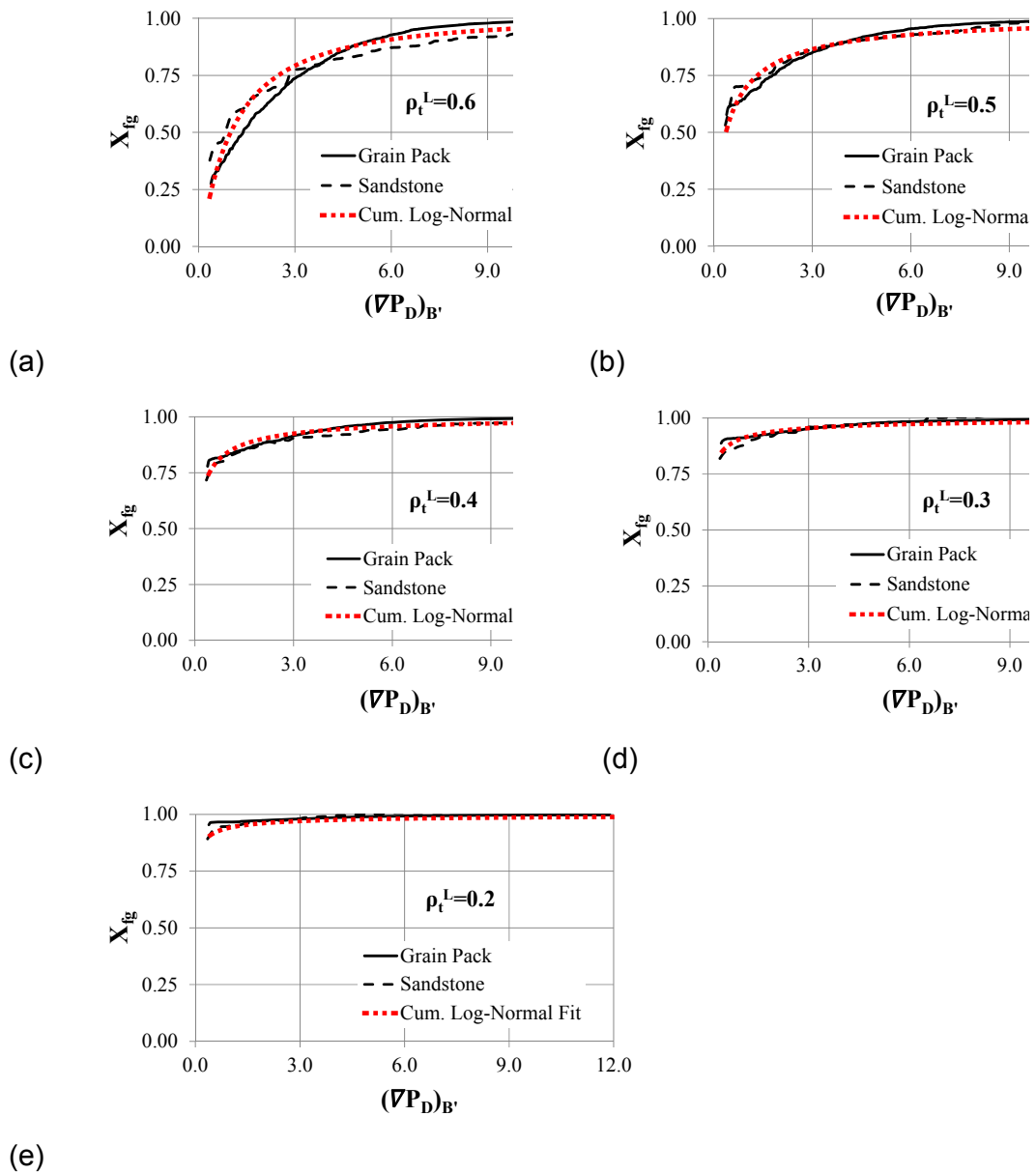
Figure 4-55: _Plotting flowing gas fraction (X_{fg}) as a function of ($\nabla P_D)_{B'}$ overlaps X_{fg} curves for the grain pack and the sandstone for different overall lamella densities (ρ_t^L) in the continuous-gas foam flow regime(a) ρ_t^L=0.6, (b) 0.5, (c) 0.4, (d) 0.3, and e) 0.2. Moreover, cumulative log-normal distribution functions are successfully fitted to these curves._
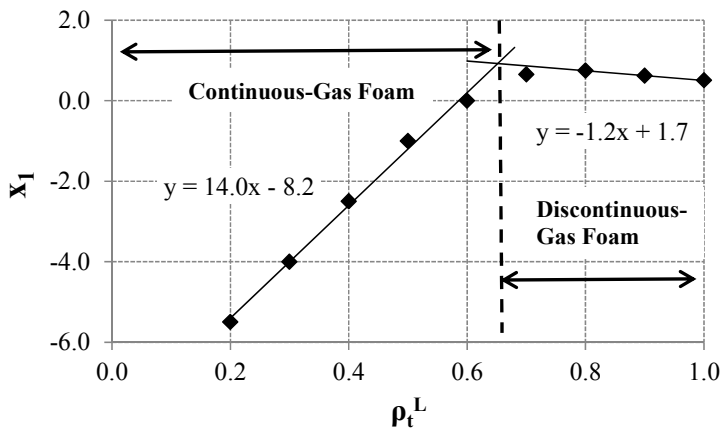
(a)
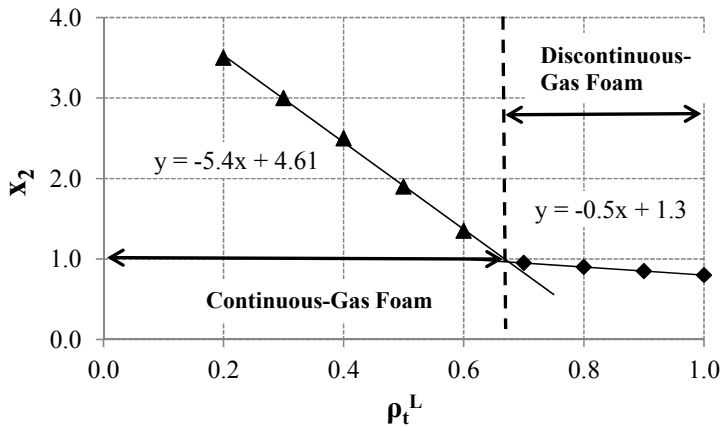
(b)

Figure 4-56: *The matching parameters x_1 and x_2 as a function of overall lamella density (ρ_t^L).*

4.2.5 Modeling effective Gas Viscosity

To distinguish the contribution of effective gas viscosity (μ_g^f) from that of gas relative permeability to foam mobility, the effective viscosity is evaluated at sufficiently high pressure gradient such that all lamellas in the network are mobilized. For simplicity, the lamella flow equation with the constant viscosity model is chosen to perform this evaluation whose result is shown in **Figure 4-57**. In this simulation, the ratio μ_{app}/μ_g is set to 100. The effective gas viscosity normalized to the ordinary gas viscosity increases exponentially with flowing

lamella density ($\rho_{fg}{}^{\perp}$). A sharp increase in the effective gas viscosity as $\rho_{fg}{}^{\perp}$ approaches 0.65 is due to the change of foam regime from continuous-gas to discontinuous-gas foam when $\rho_{fg}{}^{\perp}$ is around 0.65. This finding is striking as it indicates much higher sensitivity of effective gas viscosity to flowing lamella density in porous media than the Hirasaki-Lawson based foam viscosity model commonly used in all population balance based approaches where effective gas viscosity is proportional to flowing lamella density. This implies that volume averaging of the pore-scale apparent gas viscosity should reflect the characteristics that could not be captured by a bundle of capillary tubes model. Another important implication of this result is that the kinetics of gas trapping and remobilization is more influenced by the lamella density contrast between the flowing and trapped gas domains. Our result above shows that this contrast could be significant, making the assumption that flowing and trapped lamella densities are equal, which was employed in several population balance models (Kovscek et al., 1995, 1997), problematic.

Furthermore, when the exchange of lamella between the trapped and flowing gas domains occurs, spatial redistribution of lamella may modify the effective gas viscosity. To verify this effect, several simulations with different realizations of lamella distribution are performed. The results shown in **Figure 4-58** confirm that the effective gas viscosity is poorly sensitive to the spatial distribution of lamella for a wide range of flowing lamella density in the pore network.
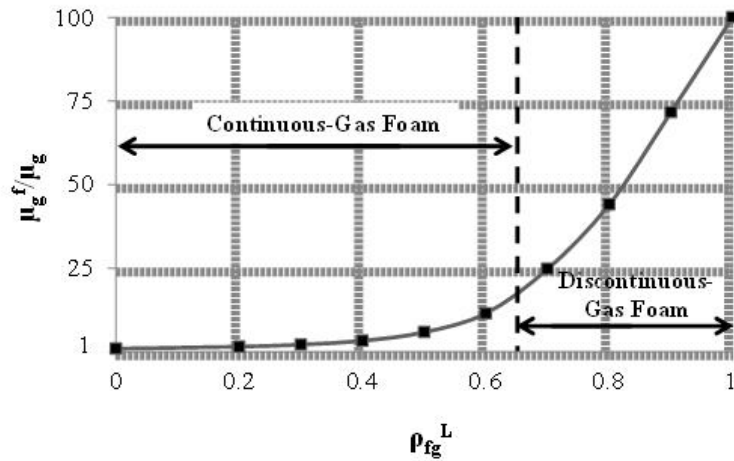
Figure 4-57: *Normalized effective gas viscosity (μgf/μg) as a function of flowing lamella density (ρfgL) for a high pressure gradient (all pores are open). The lamella flow equation with the constant viscosity model is used in these simulations with μapp/μg = 100.*
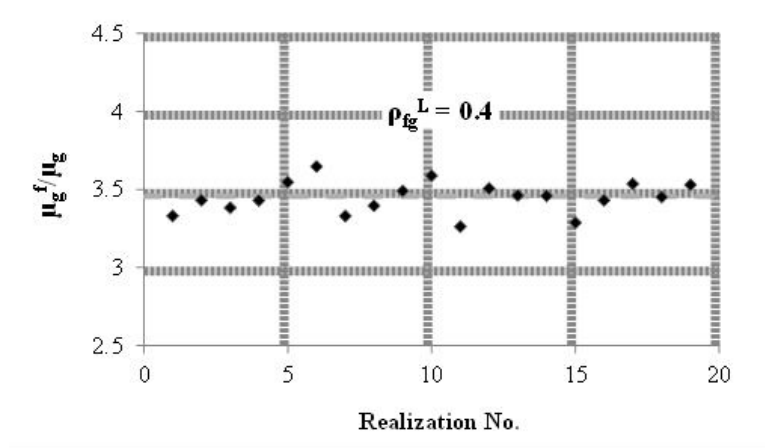
(a)
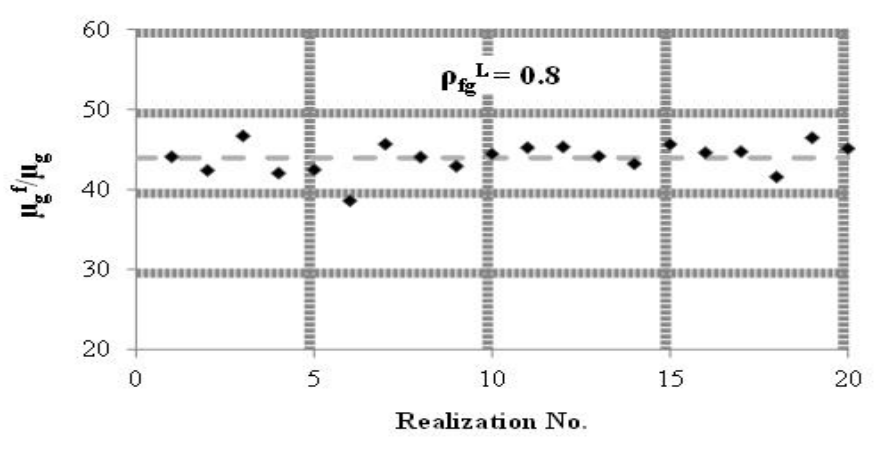
(b)

Figure 4-58: _Influence of different spatial lamella distribution on normalized effective gas viscosity (μgf/μg) for two flowing lamella densities (a) ρfgL = 0.4 and (b) 0.8. All pores are open to flow. The lamella flow equation with the constant viscosity model is used in these simulations with μapp/μg = 100._

The effect of pore-scale shear thinning behavior of flowing lamellas on the effective gas viscosity could be quantified using the Hirasaki-Lawson viscosity model. In this model, pore-scale apparent gas viscosity, μ_{app} scales with $(N_c)^{-1/3}$, where N_c is the capillary number defined by Eq. 4.4.

$$N_c = \frac{\mu_w v_g^f}{\gamma}$$ ……………………………………………………………………..……

(4.4)

The resulting normalized effective gas viscosity as a function of N_c are given for different flowing lamella densities, ρ_{fg}^L in **Figure 4-59 (a)**. Effective gas viscosity decreases with increasing capillary number, which is the characteristic flow behavior of shear-thinning fluids. Moreover, effective gas viscosity increases non-linearly with flowing lamella density at a constant N_c (**Figure 4-59(b)**). Comparing **Figures 4-57** and **4-59 (b)** reveals that the fluid types do not modify the nonlinear relationship between flowing lamella density and effective gas viscosity.
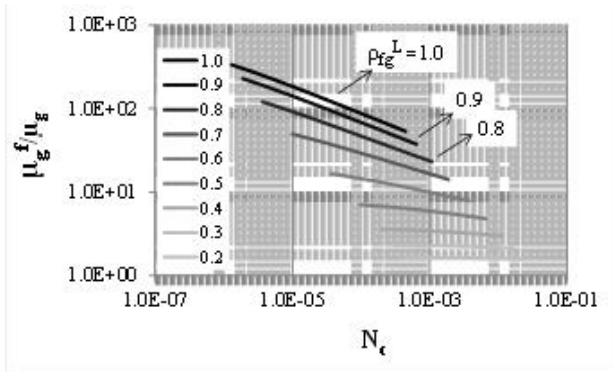
(a)
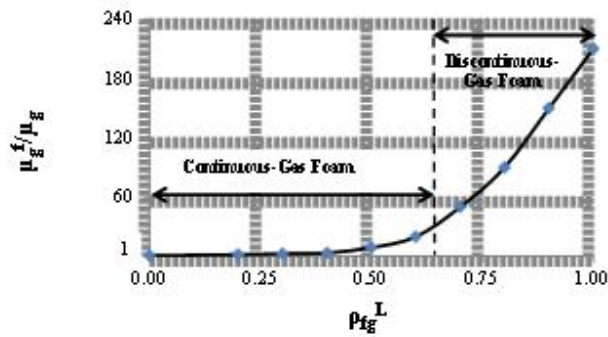
(b)

__Figure 4-59:__ (a) Normalized effective gas viscosity (µgf/µg) as a function of capillary number (Nc) for different flowing lamella densities (ρfgL). (b) Normalized effective gas viscosity (µgf/µg) as a function of flowing lamella density (ρfgL) at a constant capillary number (Nc) of 1.0×10-5 based on the Hirasaki-Lawson viscosity model. All the pores are open to flow

We further investigated the effect of permeability on the effective gas viscosity. The results are shown in **Figure 4-60**. In this figure, the normalized effective gas viscosity increases with permeability at a constant capillary number, which is consistent with the relationship between Hirasaki-Lawson pore-scale apparent gas viscosity.
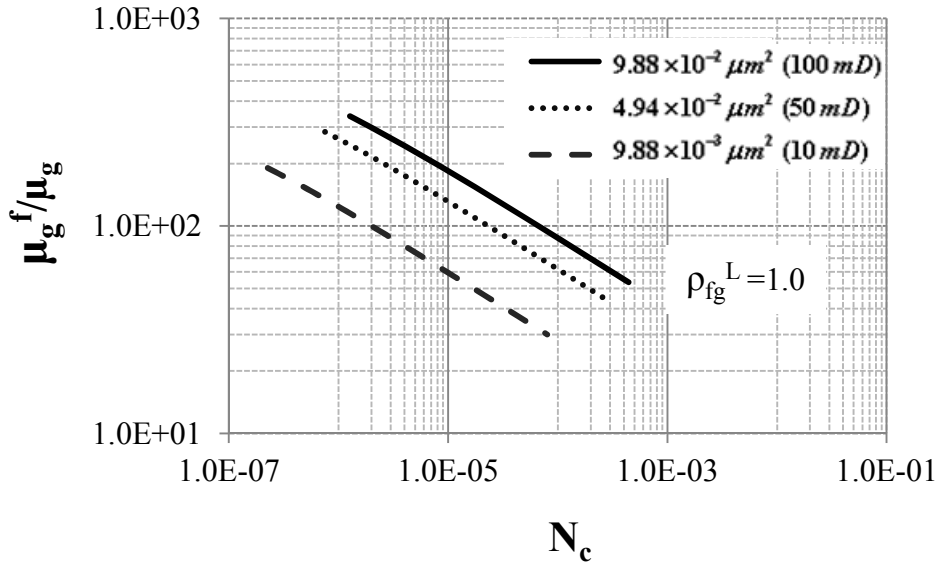
Figure 4-60: Normalized effective gas viscosity (μ_{gf}/μ_g) as a function of capillary number (Nc) for different permeabilities at a flowing lamella density (ρ_{fg}^L) of 1.0 based on the lamella flow equation with the Hirasaki-Lawson viscosity model. All the pores are open to flow.
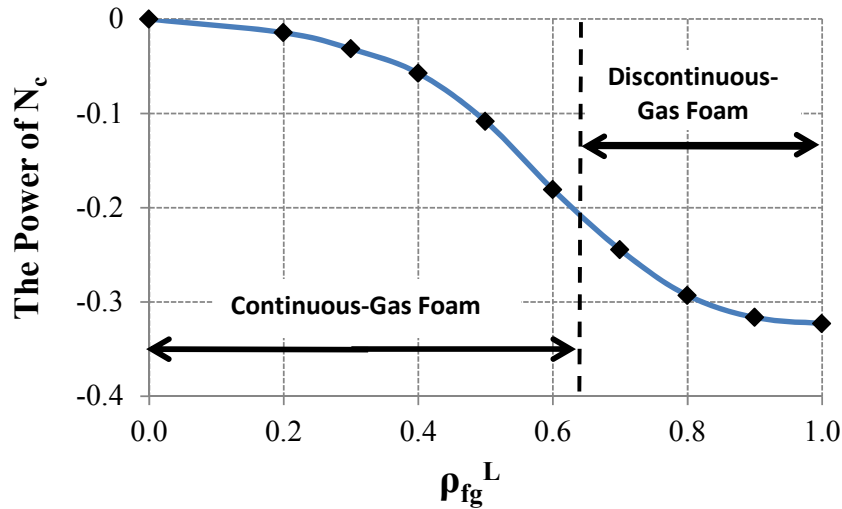
Figure 4-61: The power of capillary number as a function of flowing lamella density (ρ_{fg}^L) based on the lamella flow equation with the Hirasaki-Lawson viscosity model. All the pores are open to flow.

The power of capillary number decreases nonlinearly with increasing flowing lamella density and approaches a constant value of -1/3 for $\rho_{fg}^L > 0.8$ (**Figure 4-61**), which is consistent with the scaling of pore-scale apparent gas

viscosity, μapp with capillary number. When flowing lamella density is below 0.4, effective gas viscosity is a very weak function of capillary number, so the Newtonian flow behavior becomes more obvious. However, shear thinning of foam flow in straight capillary tubes is expected to be dominant at high flowing lamella density.

4.2.6. Effective Gas Viscosity with Trapped Gas

The nonlinear functional relationship between effective gas viscosity and flowing lamella density is based on high pressure gradient at which all the pores are open to flow. Since the effect of spatial lamella distribution on effective gas viscosity is almost negligible, this relationship is expected to be also valid for foam flow at low pressure gradient. Indeed, **Figure 4-62** shows a single trend for effective gas viscosity at both low and high pressure gradients regardless of the presence of trapped gas at low pressure gradient. This is particularly true if flowing lamella density is defined as the number of flowing lamellas divided by the number of pore throats in the flowing gas domain (ρ_{fg}^{L}), while overall lamella density is defined as the total number of lamellas in the pore network divided by the total number of pore throats (ρ_{t}^{L}). Since the flowing gas fraction curve is not influenced by spatial lamella distributions, viscosity contrast between lamella and gas, and the viscosity models over a wide range of overall lamella density, the gas relative permeability curves for non-foamed gas are used to calculate effective gas viscosity at low pressure gradient (in the presence of trapped gas).
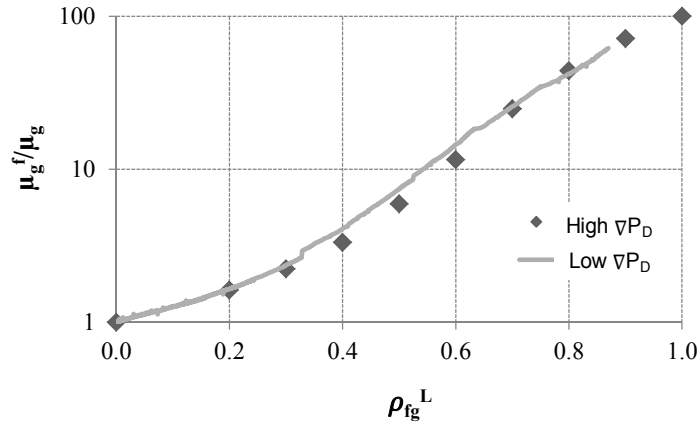
Figure 4-62: _Comparison of normalized effective gas viscosity (μ_{gf}/μ_g) vs. flowing lamella density ($\rho_{fg}{}^L$) at low and high dimensionless pressure gradients. Trapped gas is present at low dimensionless pressure gradient. The lamella flow equation with the constant viscosity model is used in these simulations with $\mu_{app}/\mu_g = 100$._

Even though the use of $\rho_{fg}{}^L$ allows evaluating separately contribution of relative gas permeability and effective gas viscosity to foam mobility, this specific definition of flowing lamella density may not be convenient for scaling up these two rheological properties of foam flow. One reason is that it is difficult to define the number of pore throats in natural rocks. This may also account for the fact that the existing population balance based foam use an alternate definition of flowing lamella density in terms of the number of flowing lamellas normalized to the flowing gas volume. Based on our simulations, it is found that these two definitions of flowing lamella density are actually related for the grain pack as shown in Eq.4.1 below.

$$\rho_{fg}^{L} \;\propto\; n_{fg}^{L} k^{3/2}$$

……………………………..(4.1)

However, the use of $n_{fg}{}^L$ may cause difficulties in obtaining a universal correlation for effective gas viscosity (**Figure 4-62**) regardless of gas trapping. This is due primarily to the fact that the number of flowing lamellas may vary proportionally with flowing gas saturation during the dynamic process of lamella trapping and remobilization. As a result, different effective gas viscosity may be

observed at a constant n_{fg}^L. This could be verified by plotting normalized effective gas viscosity versus n_{fg}^L for different pressure gradients and overall lamella densities (n_t^L) as shown in **Figure 4-63**. It can be clearly observed from this figure that effective gas viscosity is a function of not only n_{fg}^L but also overall lamella density.
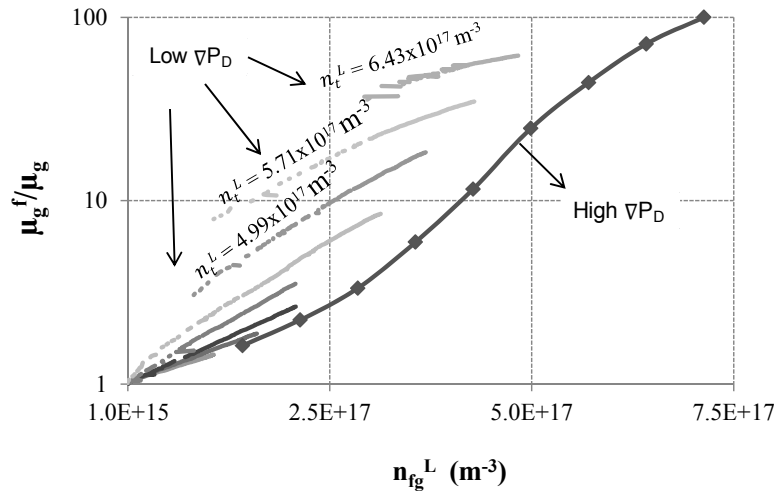
Figure 4-63: *Normalized effective gas viscosity (μ_{gf}/μ_g) as a function of flowing lamella density (n_{fg}^L) at both high and low dimensionless pressure gradients.*

Key findings from scaling trapped gas and apparent gas viscosity

A 3D pore-network model of computer-generated sphere packs coupled with fluid models that represent a lamella flow through a pore throat has been successfully used to quantify two key rheological features of foam mobility (i.e. gas relative permeability and effective gas viscosity) and their influencing factors.

Flowing gas fraction increases as the overall lamella density in the pore network decreases at a constant pressure gradient. This results in a significant variation of the threshold pressure gradients at high overall lamella density. Relative gas permeability is a strong non-linear function of flowing gas fraction. This observation disagrees with most of the existing theoretical models for the effect of gas trapping on relative gas permeability in which a linear relationship

is commonly assumed. Moreover, the shape of the relative gas permeability curve is poorly sensitive to overall lamella density.

The findings on the dynamics of foam trapping and remobilization indicate that both flowing and trapped lamella densities vary with pressure gradient, but are not necessarily the same. This preliminary result provides insight into the least explored aspect of population balance based modeling approaches, that is the kinetics of gas trapping. It is also relevant to understanding phase trapping during multi-phase flow.

Empirical and mechanistic pore-scale apparent gas viscosity models are evaluated and compared. It is found that all the models give almost the same functional relationship between flowing gas fraction and pressure gradient. This would facilitate scaling of flow rate with pressure gradient and testing a range of shear-thinning and yield-stress behavior in a simple format.

Effective gas viscosity is a strong function of flowing lamella density. The nonlinearity of this function is opposed to the existing foam viscosity models developed for foam flow in porous media and reported here for the first time. In addition, shear thinning foam flow is more obvious at high flowing lamella density while Newtonian flow becomes significant at relatively low flowing lamella density.

Scaling of effective gas viscosity with flowing lamella density depends on how the later quantity is defined. Effective gas viscosity is a unique function of the number of flowing lamellas normalized to the total number of pore throats open to flow. However, it also scales with overall lamella density if the number of flowing lamellas is normalized to the flowing gas volume. This issue has not been addressed in the literature of modeling of foam in porous media because the dynamics of gas trapping and remobilization and its effect on foam mobility has been neglected.

4.3. Foam process upscaling

4.3.1. Simulation Description

A 15° sector of a cylindrical homogenous reservoir 100 ft thick and 440 ft in radius was used for all simulations in this work. Porosity is 20%. The vertical and horizontal permeabilities are 400 md and 200 md, respectively. The reservoir model was numerically constructed using 100 grid blocks in radial direction and 20 grid blocks in vertical direction. A vertical injector is placed at the center of the reservoir and fully completed over 100 ft along, while a parallel fully penetrating producer is placed in the outer boundary grids whose permeability is set to 10000 Darcy to simulate an open boundary reservoir. The radial grid size increases from 3 ft for the first 30 grids from the injector to 5 ft for the remaining grid blocks. All simulations were conducted with the Computer Modelling Group's STARS simulator.

4.3.2. Injection scheme

Previous studies of injection strategies have focused on conventional CO_2 *insoluble* surfactants (Rossen et al. 2006). This focus has been expanded into this work where the influences of surfactant partitioning between CO_2 and water phases on field-scale foam performance were numerically evaluated through three different injection strategies.

The first strategy is the alternating injection of surfactant solution and gas (Surfactant-Alternating-Gas, SAG) at constant respective rates. This most commonly used strategy, also known as foam improved water-alternating gas (WAG) process, is appropriate for reservoirs with limited well injectivity.

If the injectivity is not a main concern in a reservoir, simultaneous injection of gas and surfactant solution at respective fixed rates either into the lower part of the reservoir (Simultaneous Injection Same Interval, SISI) or water into the upper part while gas into the lower part (Simultaneous Injection Different Interval, SIDI) may be more favorable for far-field foam propagation. A schematic of the two strategies is shown in **Figure. 4-64**. The main goal of

these two particular injection strategies is to reduce the effect of gravity segregation commonly encountered in gas-liquid flow in reservoirs with high vertical communication (Rossen et al. 2006). For the simulation presented in this work, the bottom half of the reservoir thickness was used to SISI, while the top half was used only for water injection in SIDI.

Then, the novel mode, CO_2 continuous injection with dissolved surfactant without any water injection, was examined with three CO_2 soluble surfactants for only uniform perforation in all layers, where partial perforation has been proven to present almost exactly same foam performance. We emphasize again that to perform a fair comparison, time line was 8 years and surfactant concentration declined to keep the same amount of surfactant injection because the CO_2 rate was the summary of above two phases.

Table 4-xiii summarizes the design parameters for the three injection strategies described above. Note that the total injected pore volumes are not the same for all the strategies because the total amount of injected surfactant was fixed, and that except for the CGI, all the surfactants were injected in water for the purpose of comparing foam performance by the conventional and novel CO_2 soluble surfactants.
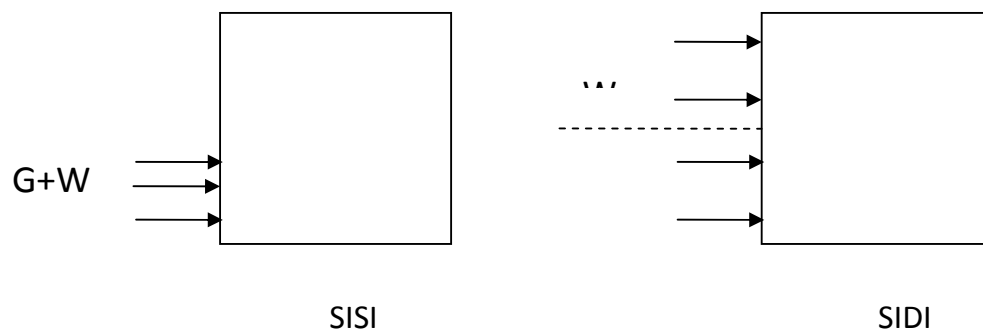
Figure 4-64: Two different injection strategies for simultaneous injection of surfactant solution and CO_2: SISI and SIDI

Table 4-xiii: Design parameters for different injection strategies.

Injection Strategies	Water/CO_2 Cycle Ratio	Water Cycle (day)	Water Rate (bbl/d)	CO_2 Rate (SCF/d)	Total Injected PV/time
SAG	1:1	36,5, 182.5 and 365	45	90000 90000	5.76/16 years
SISI	-	-	45	90000	5.76/8 years
SIDI	-	-	45	115714.	5.76/8 years
Novel CO_2	-	-	-	3	5.76/8 years

4.3.3 Surfactant-alternating-gas (SAG)

Figure 4-65 shows the respective gas production rate profiles for the four surfactants (CD1045, S, 4S, and 15S). Early CO_2 breakthrough due to gravity segregation can be clearly observed at almost the same time (about 138 days) for all the surfactants. However, gas production rates differ significantly between these cases after the breakthrough. For the case of zero partition coefficient (CD1045), the gas rate abruptly increases and almost levels off after 600 days. It significantly decreases as the surfactant partition coefficient increases (S, 4S, and 15S). In particular, the highest partition coefficient (15S) yields the lowest gas production rate, but only for a shortest period of time (about 300 days) before rapidly converging to the gas rate profile for the absence of surfactant partitioning. Therefore, surfactants with relatively lower partition coefficients (e.g. S and 4S) can improve better vertical sweep efficiency.
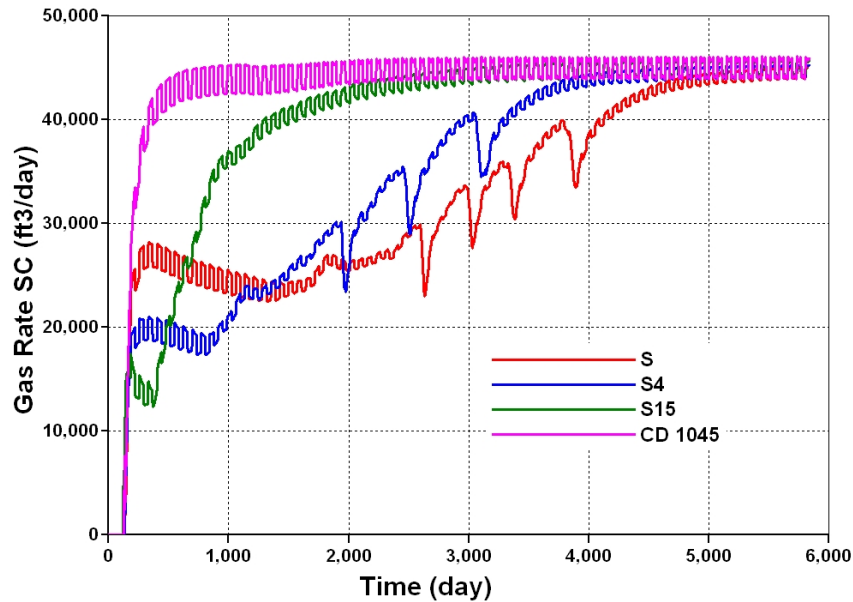
Figure 4-65: Gas production rates for four surfactants with different partition coefficients during alternating injection of CO_2 and surfactant solution.

The early-time production behavior (before 300 days) is due primarily to deeper surfactant and foam propagation into the reservoir with higher partition coefficient. This is qualitatively consistent with our experimental observations that the pressure and water saturation responses were significantly faster for 15S than CD1045. However, the early-time production behavior dramatically changes at later time (after about 300 days), that is the gas production rate increases with surfactant partitioning. This is because of the effect of surfactant concentration on the reduction of gas relative permeability. An increase in surfactant partition coefficient leads to a more spreading of surfactant concentration distribution towards the producer, enhancing the significance of surfactant concentration effect. This late-time behavior is analogous to the experimentally observed delay of strong foam propagation as the surfactant partition coefficient increases. **Figure 4-66** shows the respective gas saturations in the reservoir at the end of the last injection cycle for the four surfactants. It can be clearly observed that the override zones first increases and then decreases with increasing surfactant partition coefficient, which is

similar to the trend of core-flood pressure responses for the four surfactants. Furthermore, this particular effect of surfactant partitioning improves not only sweep efficiency but also well injectivity. Indeed, **Figure 4-67** shows the respective well bottomhole pressures during the injection of CO_2 and surfactant cycles. The average well bottomhole pressure decreases with increasing surfactant partition coefficient. Note that the regular fluctuation of the well pressure observed for all the surfactant is due to the alternation of CO_2 and surfactant cycles.

(a)

(b)

(c)

(d)
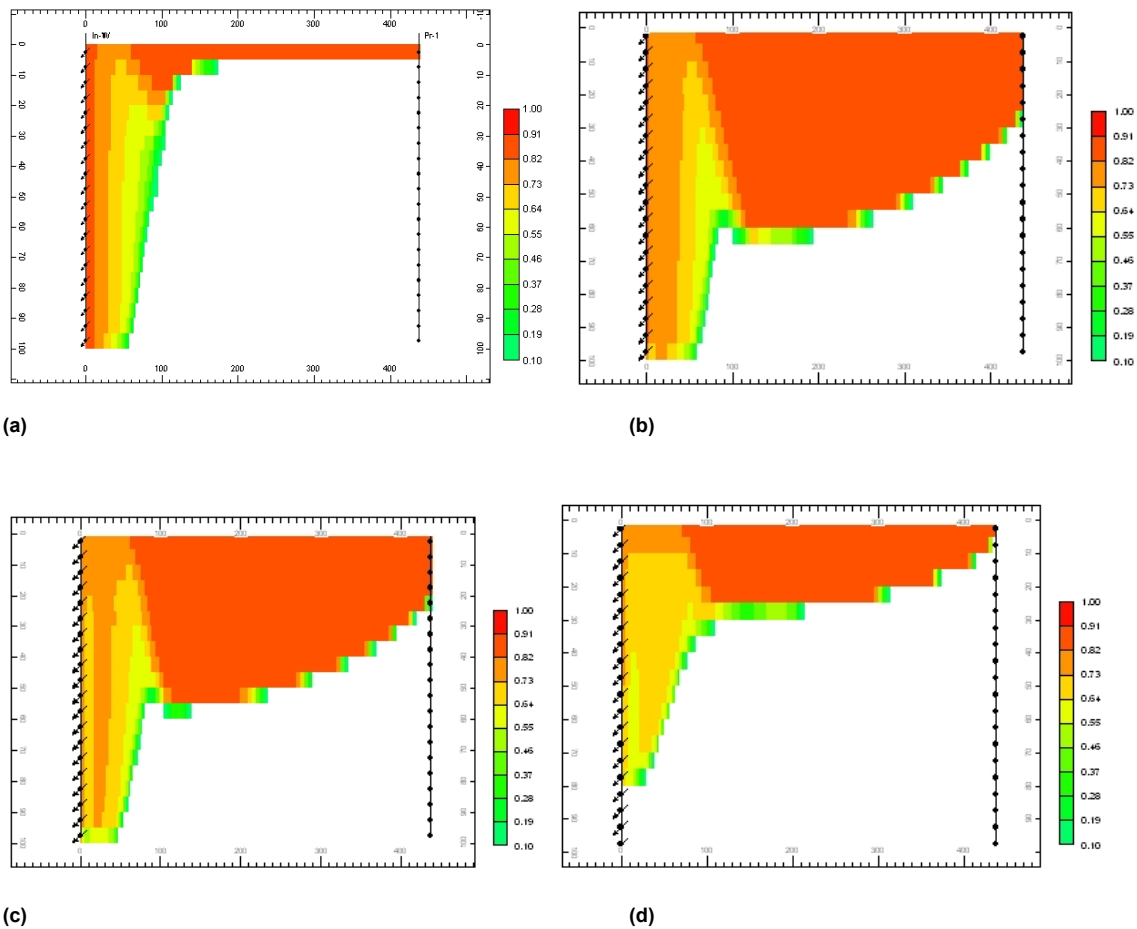
Figure 4-66: *Gas saturations for (a) CD1045, (b) S, (c) 4S, and (d) 15S at the end of CO_2 alternating surfactant solution injection.*

(a)

(b)

(c)

(d)
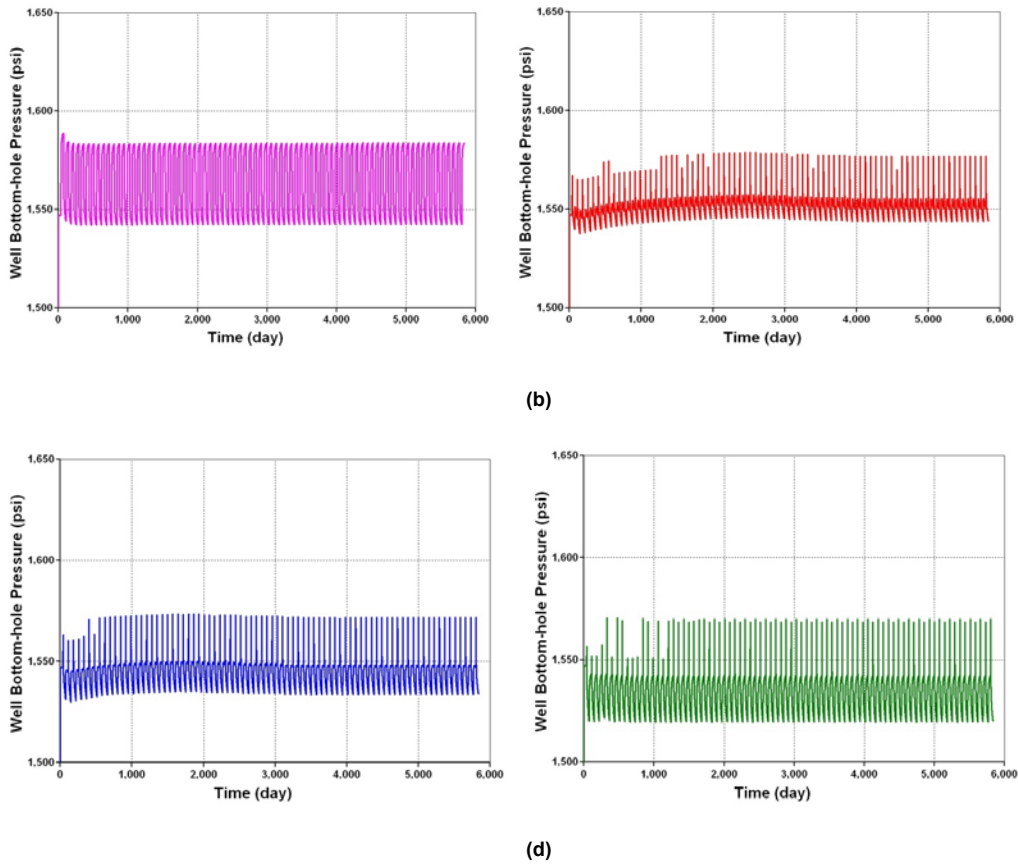
Figure 4-67: *Well bottomhole pressure for (a) CD1045, (b) S, (c) 4S, and (d) 15S during CO_2 alternating surfactant solution injection.*

Figure 4-68 shows the gas saturation at the end of the last injection cycle for the four surfactants with larger injection cycles (182.5 days). For the conventional foam with CD 1045 (**Figures. 4-66(a)** and **4-68(a)**), an increase in slug size significantly improves vertical sweep efficiency by extending the distance R_g that the injected gas-water mixture flows before complete segregation. It has been established that R_g increases with foam strength (i.e. reduced total relative fluid mobility, λ_{rt}). Therefore, the larger slug size yields stronger foam because of the ensuing larger contact between the injected CO_2 and surfactant slugs. However, comparing **Figures 4-66(b)-(d)** and **4-68(b)-(d)** reveals that foam is actually weaker as the water-CO_2 cycle increases for all

the CO_2 soluble surfactants as indicated by the overall reduction of gas saturation. The effect of cycle size is more pronounced at higher partition coefficient as demonstrated by the case of 15S (**Figures. 4-66(d)** and **4-68(d)**). In this case, an increase in cycle size by a factor of 3 reduces R_g to the distance near wellbore region where vertical flow becomes important. This can be explained by the fact that surfactant concentration is lowest around the middle of a CO_2 cycle due to the partitioning of surfactant into the CO_2 phase during SAG injection. The gradient of surfactant concentration is dependent on the cycle size and the magnitude of partition coefficient. If the latter is fixed, an increase of water-CO_2 cycle reduces surfactant concentration gradient that may impair the continuation of strong foam propagation which is observed from our simulation results (e.g. Figures 3-3(b) and 3-5(b)). In addition, an increase in surfactant partitioning leads to spreading of surfactant concentration distribution as discussed earlier. This enhances the effect of reduced surfactant concentration gradient on gravity segregation that is associated with foam propagation (e.g. **Figures 4-66(d)** and **4-68(d)**).

$$R_g = \sqrt{\frac{Q}{\pi k_z (\rho_w - \rho_g) g \lambda_{rt}{}^m}} \qquad \ldots\ldots\ldots\ldots\ldots\ldots\ldots\ldots\ldots\ldots\ldots\ldots\ldots\ldots\ldots\ldots\ldots\ldots(4.1)$$

(c)   (d)
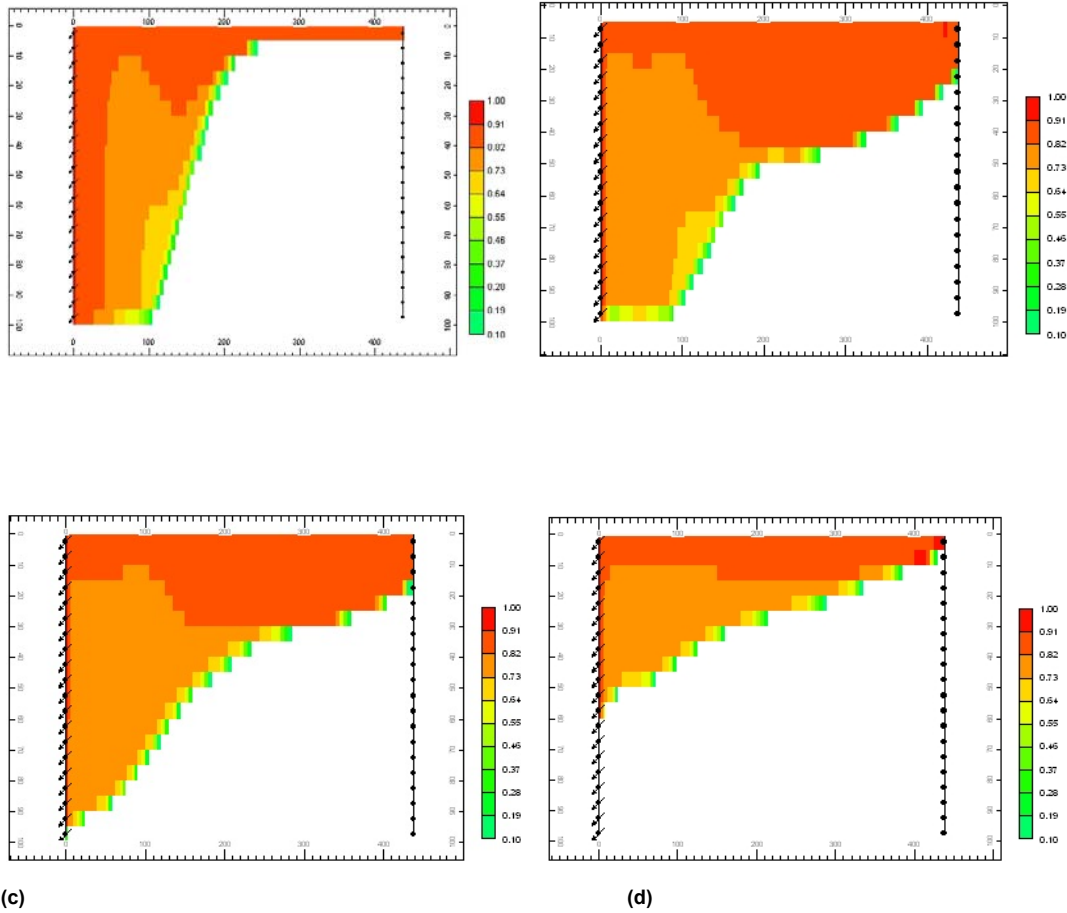
Figure 4-68: *Gas saturations for larger injected cycle size (182.5 days) for (a) CD1045, (b) S, (c) 4S, and (d) 15S during CO_2 alternating surfactant solution injection.*

Reservoir pressure distribution as shown in **Figure 4-69** can be a more direct way to correlate surfactant transport with foam propagation and foam induced fluid redistribution. For the conventional surfactant CD1045, high pressure gradient is concentrated only within the near wellbore region and expands somewhat from the wellbore as the fluid cycle increases (**Figure. 4-69(a)** top and bottom). However, it spreads much further into the reservoir for CO_2 soluble surfactants with small cycle size or low surfactant partition coefficient (**Figure. 4-69(b) top and bottom**). The pressure field approaches the hydrostatic pressure distribution for the highly partitioning 15S with large cycle size (**Figure. 4-69(d) bottom**).
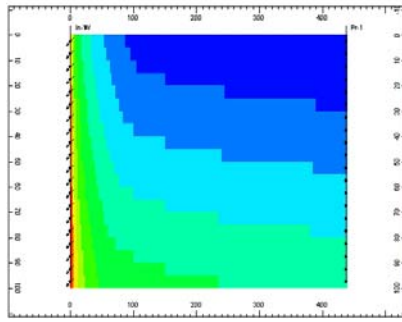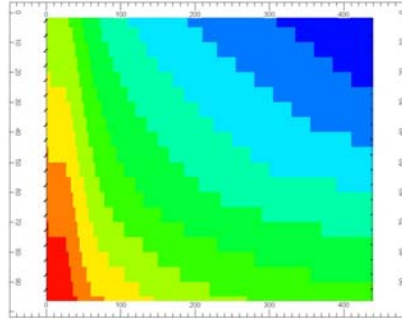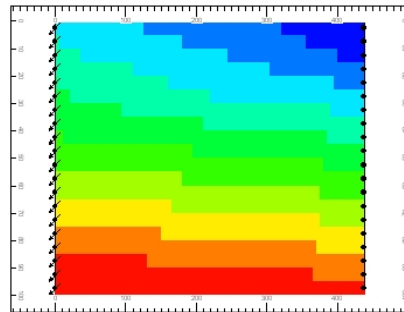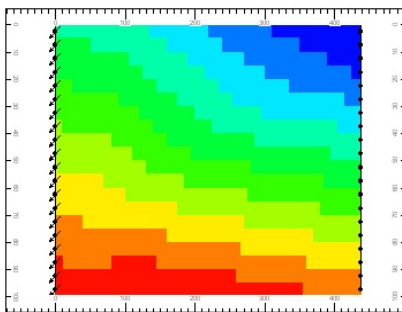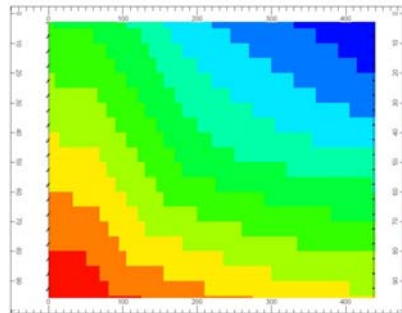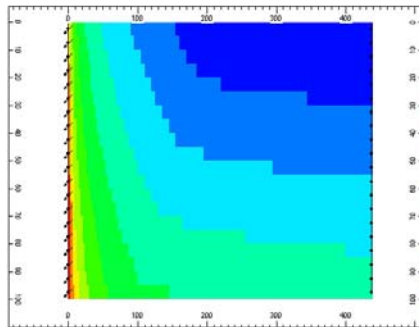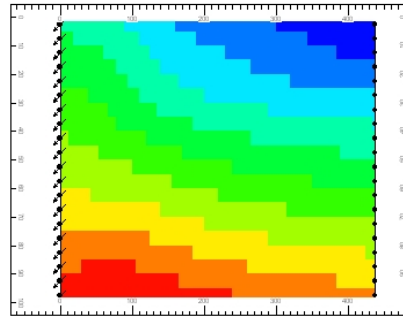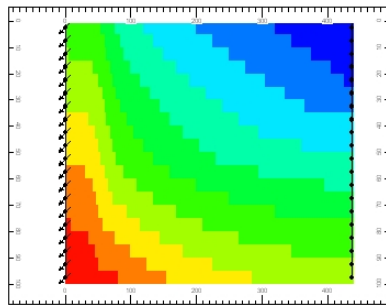
Figure 4-69: *Reservoir pressure distribution for (top two) 36.5 day cycle and (bottom two) 182.5 day cycle for (a) CD1045, (b) S, (c) 4S, and (d) 15S during CO$_2$ alternating surfactant solution injection.*

With further increasing of slug size to 365 days, gas saturation and reservoir pressure distribution, shown in **Figure 4-70**, prove our interpretation above.
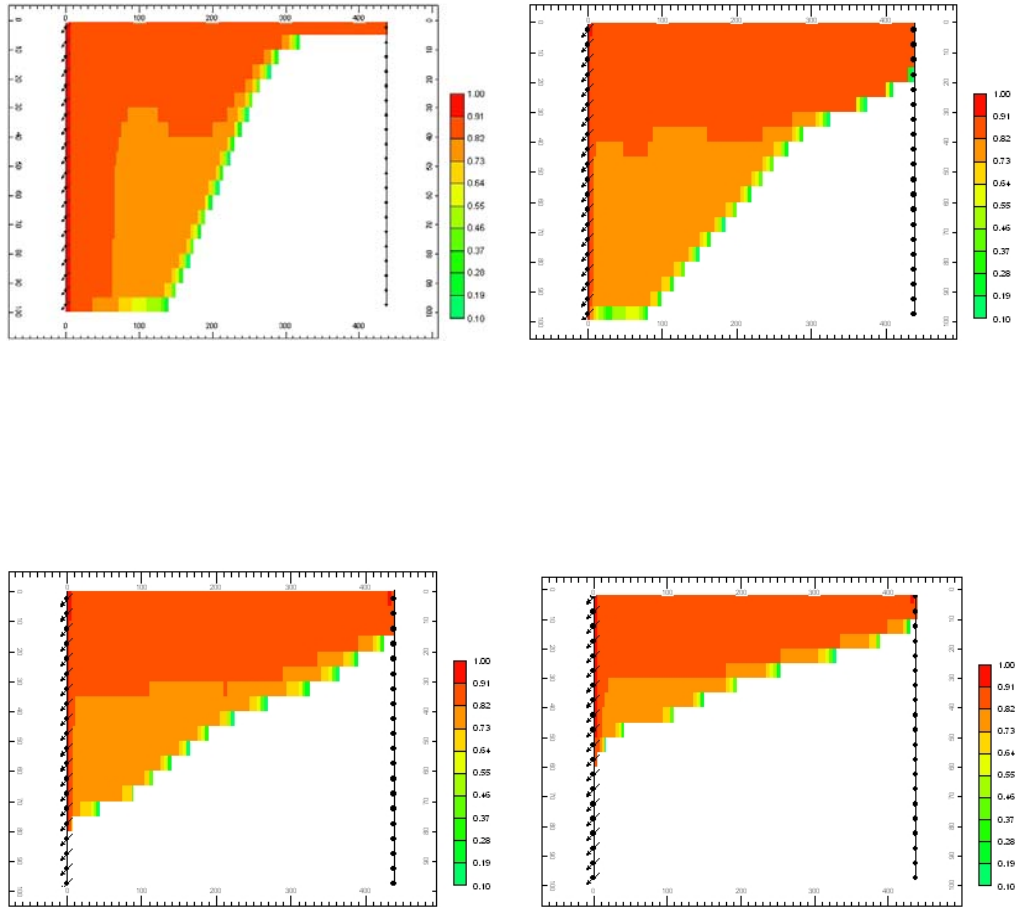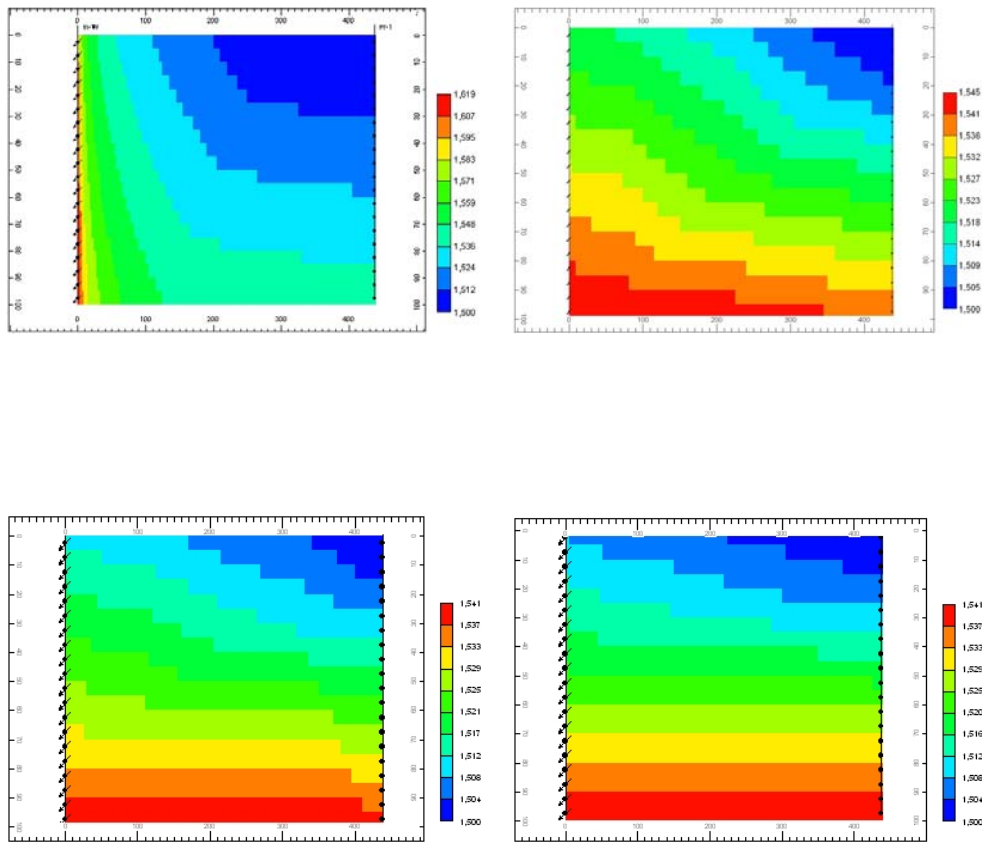
Figure 4-70: *Gas saturations (top four) and Reservoir pressure distribution (bottom four) for 365 day cycle for (a) CD1045, (b) S, (c) 4S, and (d) 15S during CO_2 alternating surfactant solution injection.*

However, the cycle size does not modify the pattern of surfactant partition coefficient effect on well injectivity and sweep efficiency. The former is evidenced by comparing the well bottomhole pressures for two different cycle sizes **(Figures. 4-67 and 4-71).** The bottomhole pressure decreases with increasing surfactant partitioning regardless of cycle size. The latter can be clearly observed from the plot of vertical sweep efficiency in terms of the amount CO_2 stored in the reservoir at the end of fluid injection versus partition coefficient, shown **Figure 4-72**. The level of CO_2 storage exhibits a maximum as the partition coefficient increases. **Figure 4-72** also confirms that increasing slug size improves vertical sweep efficiency only for the conventional CO_2

292

insoluble surfactant at the expense of well injectivity. If water and/or CO_2 are injected at constant pressure, the incremental CO_2 storage at elevated cycle size may be marginal for a substantial reduction of well injectivity.
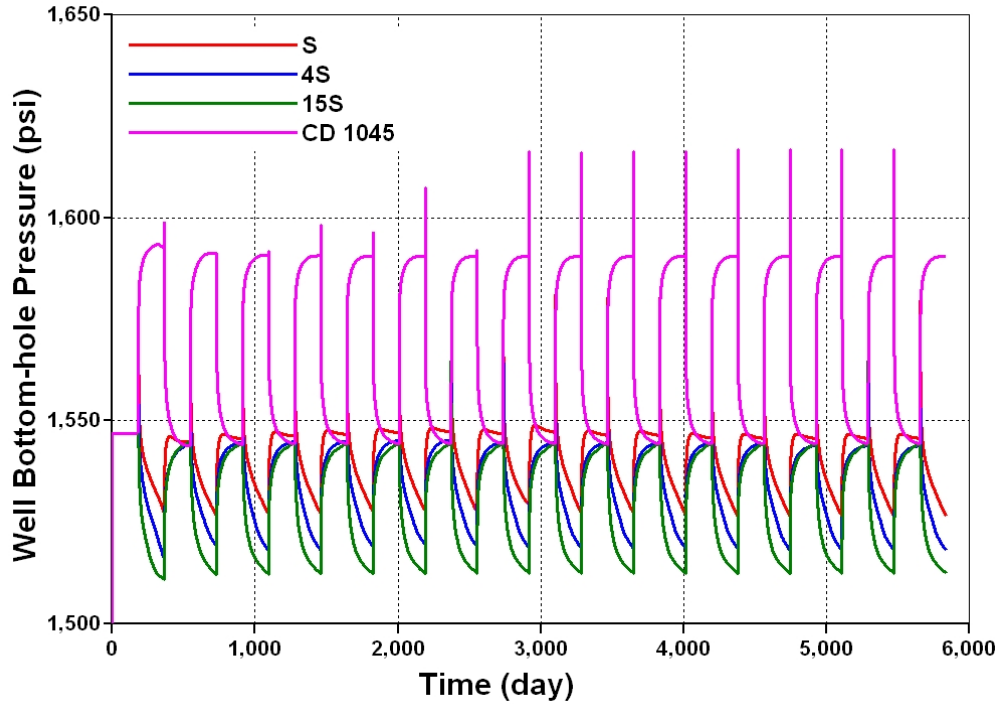
Figure 4-71: *Well bottomhole pressures for CD1045, S, 4S, and 15S during CO_2 alternating surfactant solution injection with 182.5 day cycle*
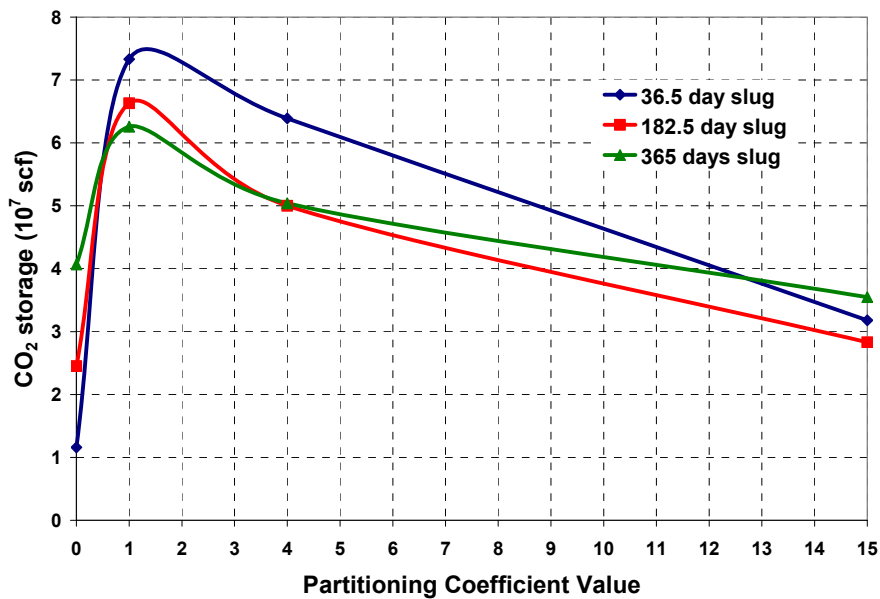
Figure 4-72: *CO_2 storage at the end of fluid injection for CD1045, S, 4S, and 15S during CO_2 alternating surfactant solution injection.*

4.3.4. Simultaneous Injection of CO_2 and Surfactant Solution

We have expanded our investigation on the injection strategies for CO2 soluble surfactants with focus on the influences of surfactant partitioning between CO2 and water phases on field-scale foam performance. Two different injection strategies have been investigated. The first strategy is the alternating injection of surfactant solution and gas (Surfactant-Alternating-Gas, SAG) at constant respective rates. This most commonly used strategy, also known as foam improved water-alternating gas (WAG) process, is appropriate for reservoirs with limited well injectivity. We present the second injection strategy that is simultaneous injection of gas and surfactant solution at respective fixed rates either into the lower part of the reservoir (Simultaneous Injection Same Interval, SISI) or water into the upper part while gas into the lower part (Simultaneous Injection Different Interval, SIDI). A schematic of the two strategies is shown in **Figure 4-73**. The main goal of these two particular injection strategies is to reduce the effect of gravity segregation commonly encountered in gas-liquid flow in reservoirs with high vertical communication (Rossen et al. 2006). For the simulation presented in this work, the bottom half of the reservoir thickness was used to SISI, while the top half was used only for water injection in SIDI.

Table 4-73 summarizes the design parameters for the two injection strategies described above. Note that the total injected pore volumes are not the same for all the strategies because the total amount of injected surfactant was fixed, and that all the surfactants were injected in water for the purpose of comparing foam performance by the conventional and novel CO2 soluble surfactants
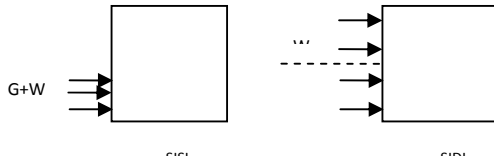
Figure 4-73: Two different injection strategies for simultaneous injection of surfactant solution and CO_2: SISI and SIDI

Table 4-xiv: Design parameters for different injection strategies

Injection Strategies	Water/CO₂ Cycle Ratio	Water Cycle (day)	Water Rate (bbl/d)	CO₂ Rate (SCF/d)	Total Injected PV/time
SISI	-	-	45	90000	55.76/8 years
SIDI	-	-	45	90000	5.76/8 years

Figure 4-74 shows the gas production rates for two different simultaneous injection strategies (SISI and SIDI). For SISI, the production profiles for all the surfactants (**Figure 4-74 (a)**) are quite similar to those observed with SAG injection. This is quite expected because the behavior of SAG process approaches that of SIDI processes as the cycle size decreases. In addition, a simulation study from Rossen et al (2006) has shown that the point of gravity segregation (Rg) for constant-rate injection is not sensitive to the simultaneous injection of gas and water into either a partially or a fully completed well. However, injection of water on top of gas (SIDI) exhibits a distinct feature; that is all the gas production rates for the CO2 soluble surfactants converge soon after the end of the early-time production behavior (about 300 days, **Figure 4-74 (b)**) regardless of the variation of surfactant partition coefficient. This is consistent with the pattern of gas saturation that is almost the same for the three CO2 soluble surfactants (S, 4S, and 15S), shown in **Figure 4-75**-bottom.
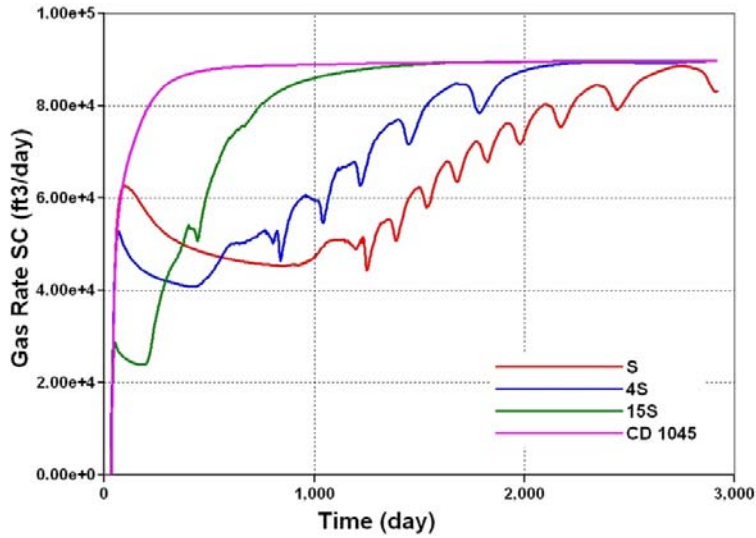
(a)
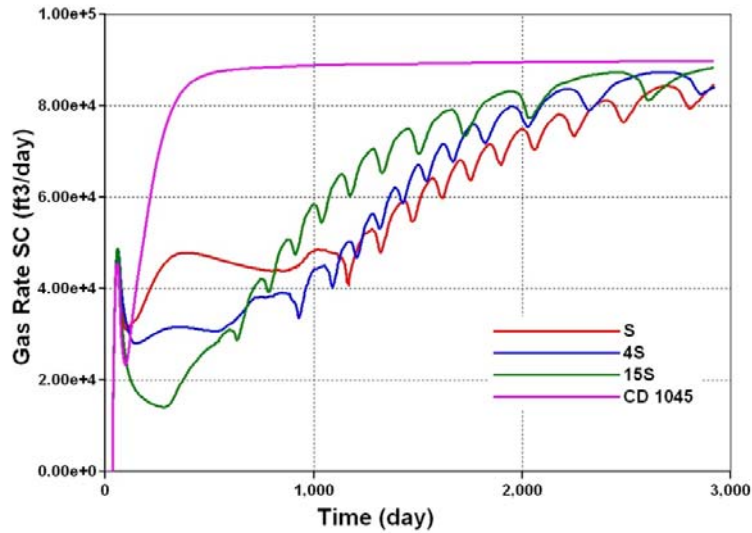
(b)

Figure 4-74: Gas production rate for simultaneous injection of CO2 and surfactant solution (a) into the same lower interval-SISI, and (b) with the surfactant solution into the top part and CO2 the bottom part-SIDI.

Examining the gas-water mixing zones for all the surfactants shown in **Figure 4-75** indicates that the distance to point of complete segregation Rg increases by a factor of about 2. This result agrees with the theoretical prediction of Rg as a function of water fractional flow reported by Rossen et al (2006). The injection of water above gas increases the travel distance for both gas and water in the vertical countercurrent flow which is in turn resisted by

foam formation. Note that in spite of the increase in Rg the override zone for the conventional surfactant (CD1045) does not vertically expand, as opposed to CO_2 soluble surfactants. The advantage of SIDI is further enhanced with CO_2 soluble surfactant as this injection strategy allows more surfactant to be carried with CO_2 into the override zone by CO_2 due to a better contact between the injected CO_2 and surfactant solution. As a result, better foam propagation in the upper part of the reservoir can be achieved. This is evidenced by the pressure distribution in the reservoir shown in **Figure 4-76**. High pressure gradient extends much further into the reservoir for SIDI than SISI. Moreover, the extension of high pressure gradient field does not impair well injectivity. Indeed, the bottomhole pressure (**Figure 4-77**) is higher for SISI than that for SIDI for all surfactant. In addition, it increases with the decreasing surfactant partitioning coefficient for SISI while almost the same for all the CO_2 soluble surfactants for SIDI.

Figure 4-75*: Gas saturation for simultaneous injection of CO2 and surfactant solution (top four) into the same lower interval-SISI, and (bottom four) with the surfactant solution into the top part and CO2 the bottom part-SIDI*
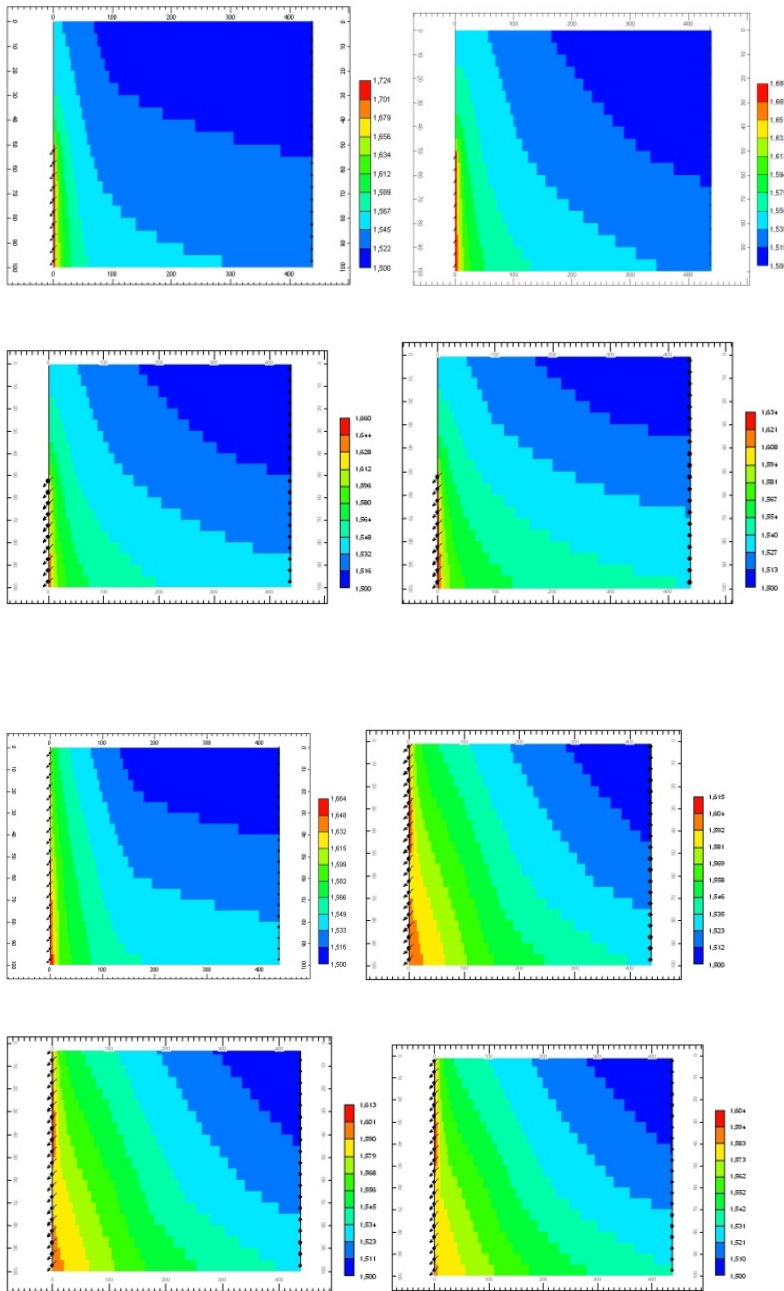
Figure 4-76: Pressure distribution for simultaneous injection of CO2 and surfactant solution (top four) into the same lower interval-SISI, and (bottom four) with the surfactant solution into the top part and CO2 the bottom part-SISI
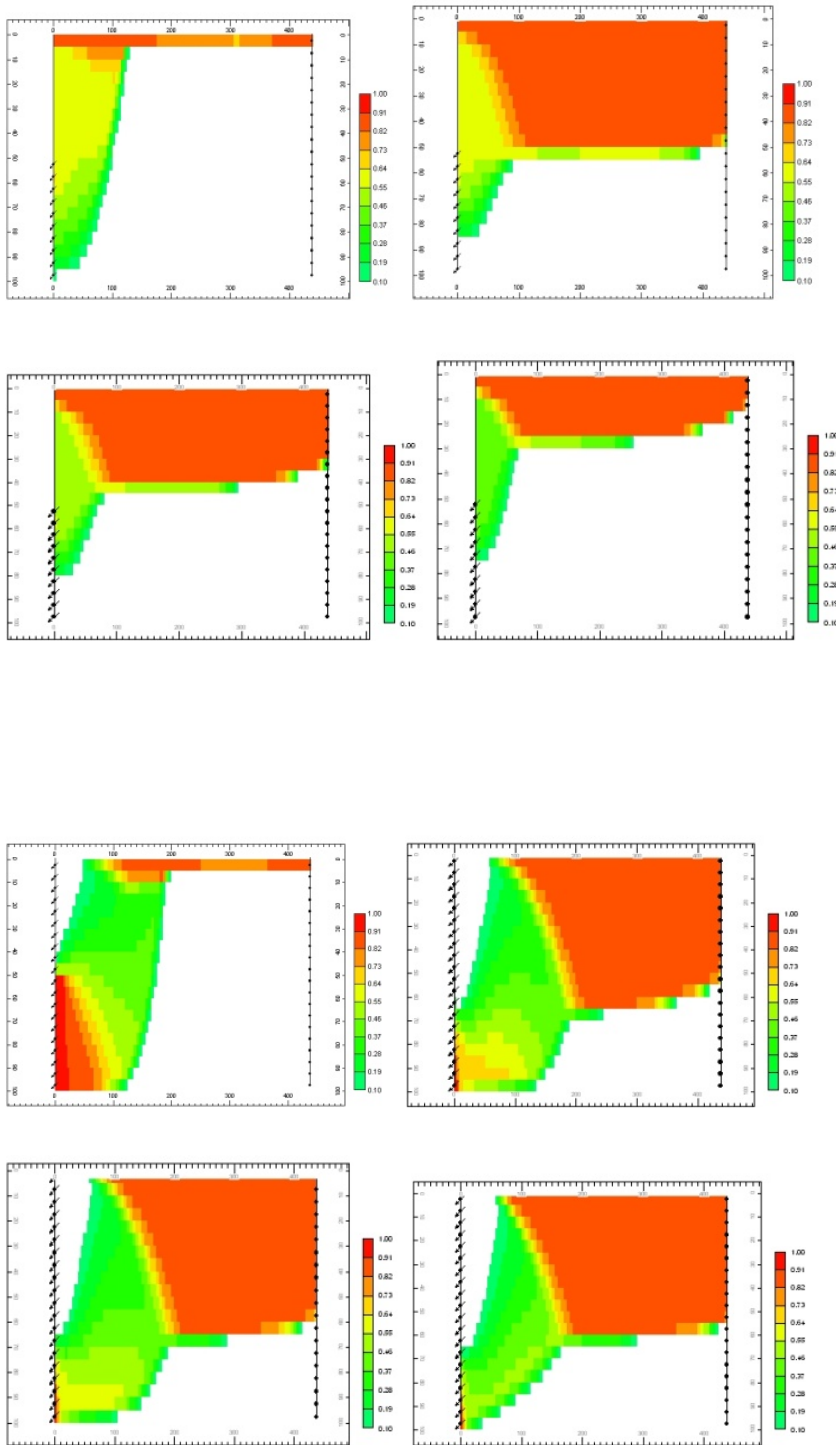
(a)

(b)
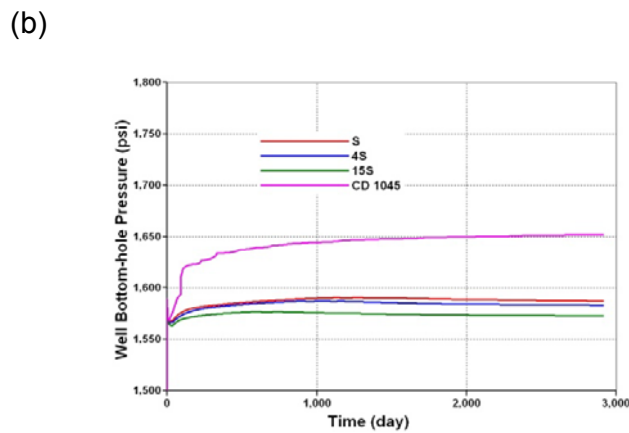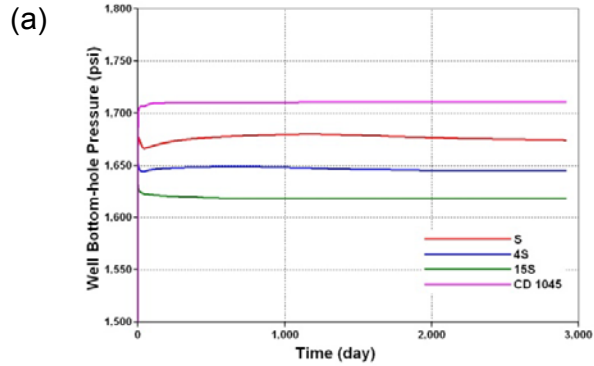
Figure 4-77: *Well bottomhole pressure for simultaneous injection of CO2 and surfactant solution (a) into the same lower interval-SISI, and (b) with the surfactant solution into the top part and the CO2 the bottom part-SIDI.*

4.3.5. Continuous Injection of CO_2 with Dissolved Surfactant

Figures 4-78(a) and **(b)** show the effect of surfactant partitioning on gas production rate and bottom pressure of the injection well, respectively. These results clearly show that an increase in surfactant partitioning coefficient significantly reduces both CO2 production rate only at the early stage of injection and injection pressure. The relationship between CO2 production rate and surfactant partition is reversed at later injection stage while the injectivity still remains highest for the highest surfactant partition.

(a)

(b)
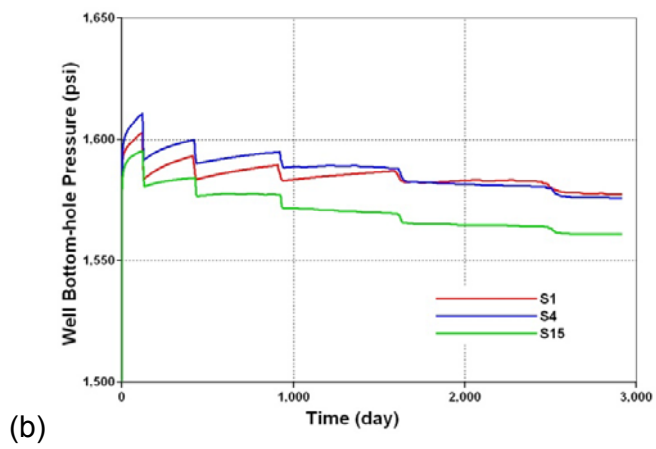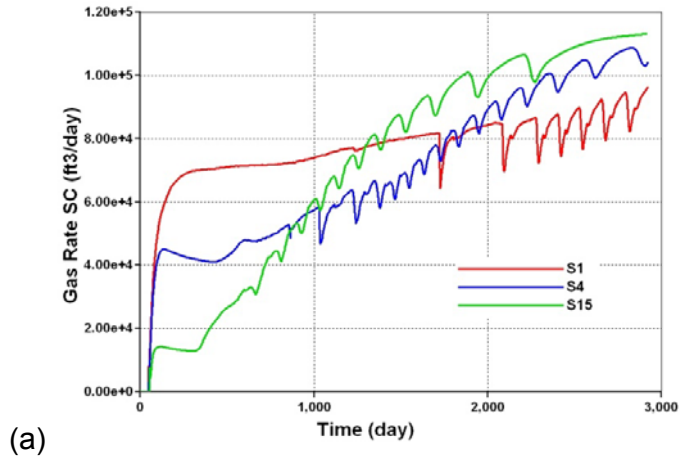
Figure 4-78: *(a) Gas production rate and (b) well bottomhole pressure for continuous injection of CO2 with dissolved surfactant*

PART V- RESERVOIR CANDIDATE FOR FOAM TRIAL

5.1. Brief description of East Seminole Field

The East Seminole field (**Figure 5.1**) is a San Andres dolomite reservoir that exhibits a classic shallowing upward sequence of depositional facies, recording the regression of Guadalupian seas eastward across the Central Basin Platform and into the Midland Basin. The reservoir is at a depth of approximately 5400 feet, with a temperature of 110 °F, and produces at a fairly low GOR of around 350 SCF/BO. Reservoir rock is composed of subtidal and intertidal facies. The supratidal facies acts as a cap or seal. The maximum thickness of the gross pay interval exceeds 200 feet. The oil/water contact at East Seminole is essentially a planar surface at an average depth of 2200 ft. The observed oil/water contact tilts from west to east approximately 40 ft/mile.

The field can be divided into four distinct flow zones separated by permeability barriers based on the core analysis:

Flow zone 1   5364-5393 ft

       Barrier   5394-5411 ft

Flow zone 2   5412-5427 ft

       Barrier   5428-5433 ft

Flow zone 3   5435-5450 ft

       Barrier   5451-5456 ft

Flow zone 4   5458-5529 ft

       Barrier   5530-5535 ft

The zonation based on permeability and porosity correlates directly to the depositional cycles recorded in the core description. Four shallowing upward cycles translate into four flow zones separated by permeability barriers. Overall, reservoir quality increases with depth corresponding to deeper water deposition. Flow zone 1 consists of intertidal pelleted wacke/packstones. Flow zone 2 consists of subtidal mud/wackestones. Flow zones 3 and 4 consist of

subtidal fusulinid. All four permeability barriers are composed of intertidal shaly laminated mudstone.

Pay zones typically have the following characteristics:

Porosity   8-l2%

Permeability (k)   1-10 md.

Barriers typically have these characteristics:

Porosity   8-12%

Permeability   0.1-1 md

The East Seminole reservoir is highly heterogeneous. Permeability-porosity correlation is shown in **Figure 5.2**. The reservoir can be divided into four zones of high sweep efficiency separated by four zones of low sweep. The breakdown of sweep efficiency by zone is as follows:

Zone 1   Poor floodability

Zone 2,3   Good floodability

Zone 4   Possible early breakthrough.

Flow zone 1 (intertidal) will be more difficult to flood than flow zones 2 and 3 (subtidal). Flow zone 4 (deeper subtidal) will breakthrough first.

The San Andres exhibits a regressive, shallowing upward sequence of rock composed of the following supratidal, intertidal and subtidal facies. Intercrystal porosity and permeability were developed by fresh water leaching (diagenesis) of the formation (**Figure 5.1**). Extensively burrowed facies were leached to form reservoir rock. Burrowing destroys impermeable shale laminations that impede fluid flow. Facies lacking burrows (laminations preserved) were not leached and act as permeability barriers separating

hydrocarbon flow zones. Grains and mud were deposited as high magnesium calcite and aragonite. Hypersaline brines converted the unstable limestone to dolomite. The conversion of $CaCO_3$ needles to $CaMgCO_3$ rhoms can create approximately 13% intercrystal porosity. The reservoir rock is quite oil wet, as indicated by the water-oil relative permeability curves shown in **Figure 5.3**.
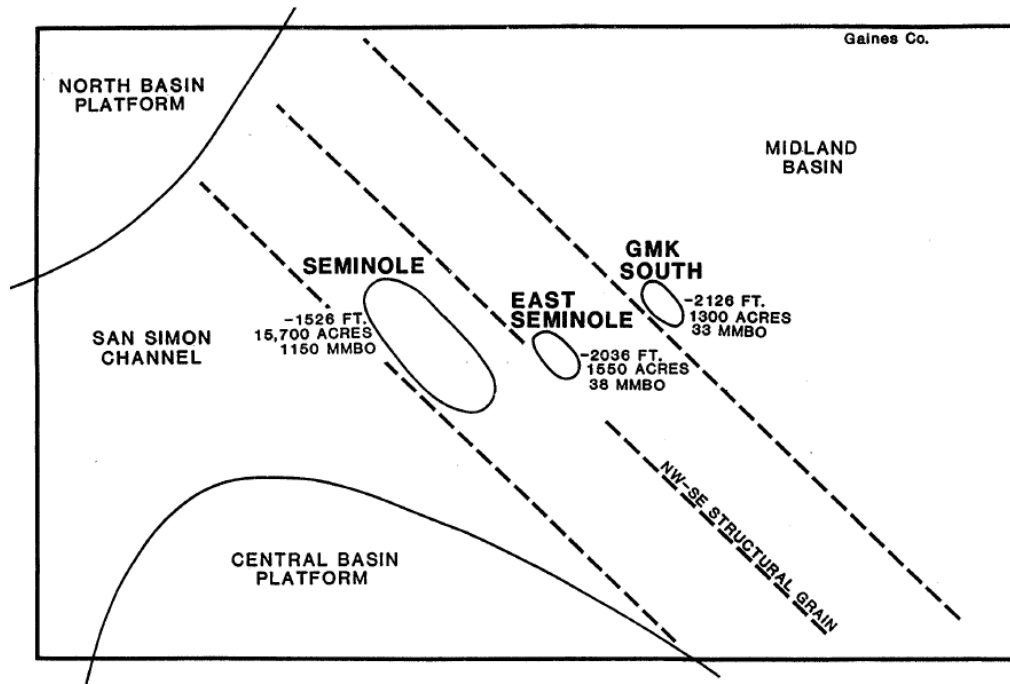
Figure 5.1. East Seminole location map
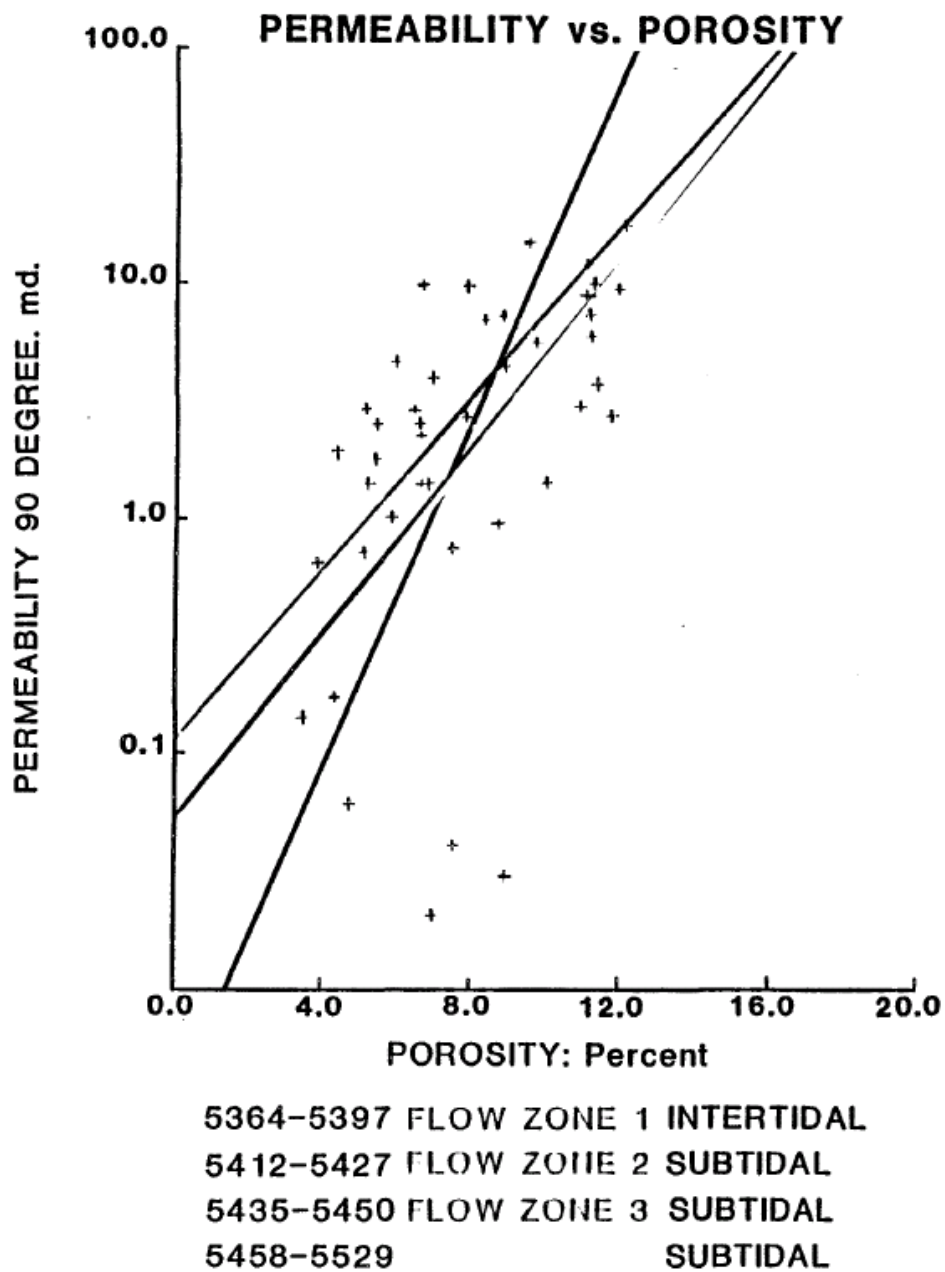
Figure 5.2. Porosity versus permeability in East Seminole reservoir
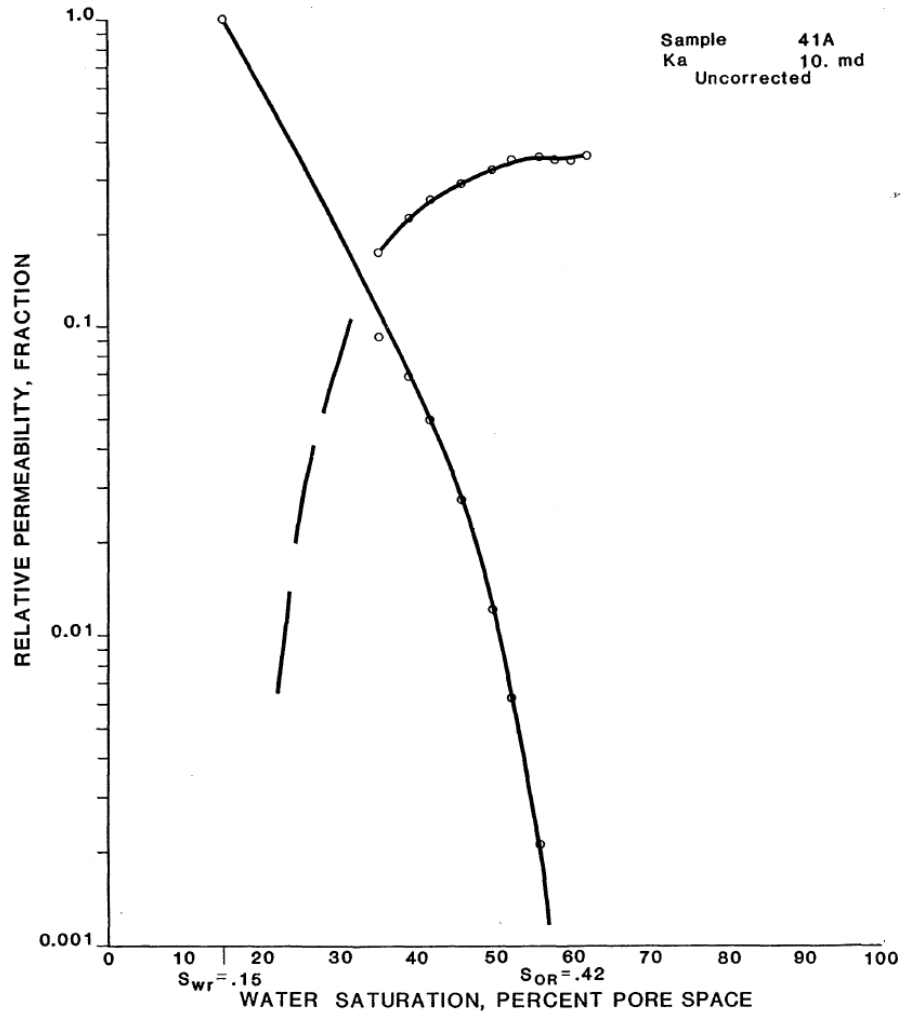
Figure 5.3. Water-oil relative permeabilities from East Seminole cores

5.2. Status of CO2 flood in East Seminole Field

Tabula Rasa (TR) continues to inject at East Seminole in five injection wells and roughly a field total of 14,000 MCFPD. They have been injecting since October of 2013 so they are closing in on one year of injection. Since May 2014 TR has seen some significant oil response. TR average 515 BOPD for June and should be ahead of that for July. The field was producing 250-275 BOPD when we began injection.

One of the five patterns has shown significant gas breakthrough as shown in Figure 5.4. The red is sale gas so that's why it no longer has a gas stream on the plot. The well continues to make 80-100 MCFPD but has kept its oil production in line. The well was offline for a few months with ESP issues and a severed flow line that occurred in some trenching operations.

Tabula Rasa has planned to start water-alternating-gas injection for these patterns in early 2016 for about 9 months to establish the injection and production base lines for a foam trial. A foam pilot design will be developed based on the injection/production base lines the results of all lab tests from this project.
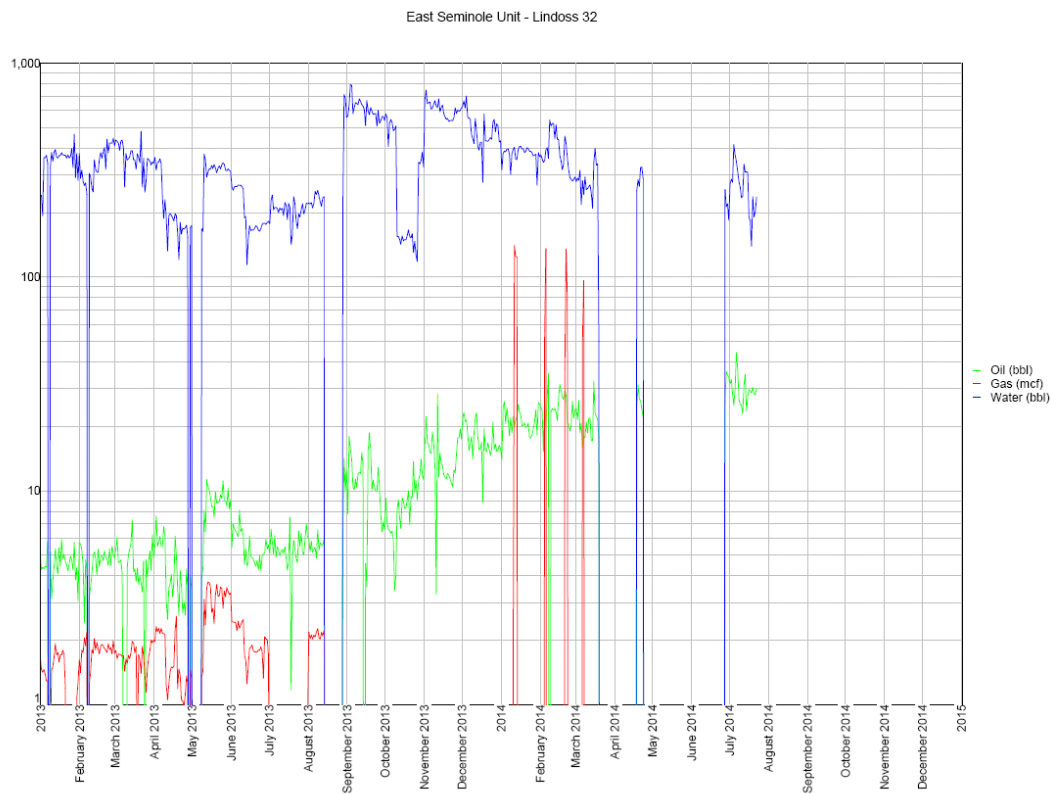
Figure 5.3. Production data from a producer that shows early CO2 breakthrough.

References and Publications

Part 1:

Adkins, et al., Langmuir 2010, 26(8), 5335–5348

Adkins, S. S., X. Chen, et al., Journal of Colloid and Interface Science 2010, 346, 455-463.

Adkins, S. S., X. Chen, et al., Langmuir 2010, 26(8), 5335-5348.

Fenghour, A.; Wakeham, W.A.; Vesovic, V., J. Phys. Chem. Ref. Data, 1998, 27, 31-44

Friedmann, F.; Jensen, J. A. In SPE California Regional Meeting; Society of Petroleum Engineers, Inc.: Oakland, CA, 1986.

Friedmann, F.; Jensen, J. A. In SPE California Regional Meeting; Society of Petroleum Engineers, Inc.: Oakland, CA, 1986.

Harris, P. C,. SPE Production Engineering 1989, 4, 249-257.

Lemert, R. M., Fuller, R. A., et al, J. Phys. Chem. 1990, 94, 6021.

O'Neill, M. L., Q. Cao, et al., Ind. Eng. Chem. Res. 1998, 37, 3067-3079.

Verbist, G.; Weaire, D.; Phelan, R. In Foams and Emulsions; Sadoc, J. F.,Rivier, N., Eds.; Kluwer Academic Publishers: Dordrecht, Netherlands, 1999, 354, 303-314.

Verbist, G.; Weaire, D.; Phelan, R. In Foams and Emulsions; Sadoc, J. F.,Rivier, N., Eds.; Kluwer Academic Publishers: Dordrecht, Netherlands, 1999, 354, 303-314.

Yunshen Chen, et al., DOE report, September 2011

Part 2:

Alvarez, J. M., H. J. Rivas, et al. (2001). Unified model for steady-state foam behavior at high and low foam qualities. SPE Journal 6(3): 325-333.

Ashoori, E. and W. R. Rossen (2012). Can Formation Relative Permeabilities Rule Out a Foam EOR Process? SPE Journal 17(2): 340-351.

Ashoori, E., van der Heijden, T. L. M., et al. (2010). Fractional-Flow Theory of Foam Displacements With Oil. Spe Journal 15(2): 260-273.

Ashoori, E., van der Heijden, T.L.M. and Rossen, W.R., 2010. Fractional-Flow Theory of Foam Displacements With Oil. *SPE Journal*, 15(2): 260-273.

Ashoori, E., van der Heijden, T.L.M. and Rossen, W.R., 2010. Fractional-Flow Theory of Foam Displacements with Oil. SPE Journal, 15(2): 260-273.

Aster, R. C., C. H. Thurber, et al. (2005). Parameter estimation and inverse problems. Amsterdam ; Boston, Elsevier Academic Press.

Avriel, M. (1976). Nonlinear programming : analysis and methods. Englewood Cliffs, Prentice-Hall.

Bazaraa, M. S., H. D. Sherali, et al. (2006). Nonlinear programming : theory and algorithms. New York, NY ; Chichester, Wiley.

Bruges, E. A., B. Latto, et al. (1966). New correlations and tables of coefficient of viscosity of water and steam up to 1000 bar and 1000 degrees C. International Journal of Heat and Mass Transfer 9(5): 465-480.

Bruges, E. A., Latto, B., et al. (1966). New Correlations and Tables of Coefficient of Viscosity of Water and Steam up to 1000 Bar and 1000 Degrees C. International Journal of Heat and Mass Transfer 9(5): 465-&.

Bruges, E.A., Latto, B. and Ray, A.K., 1966. New Correlations and Tables of Coefficient of Viscosity of Water and Steam up to 1000 Bar and 1000 Degrees C. International Journal of Heat and Mass Transfer, 9(5): 465-&.

Chalbaud, C. A., Moreno, R. A., et al. (2002). Simulating Foam Process for a Venezuelan Pilot Test. SPE Annual Technical Conference and Exhibition. San Antonio, Texas.

Cheng, L., Reme, A. B., et al. (2000). Simulating Foam Processes at High and Low Foam Qualities. SPE/DOE Improved Oil Recovery Symposium. Tulsa, Oklahoma.

Cheng, L., Reme, A.B., Shan, D., Coombe, D.A. and Rossen, W.R., 2000. Simulating Foam Processes at High and Low Foam Qualities, SPE/DOE Improved Oil Recovery Symposium, Tulsa, Oklahoma.

Computer Modeling Group (2007). STARSTM User's Guide. Calgary, Alberta, Canada.

Critical Cleaning Process Applications Management Safety and Environmental Concerns [M]. CRC press, 2011. Page 399

Farajzadeh, R., A. Andrianov, et al. (2012). Foam-oil interaction in porous media: Implications for foam assisted enhanced oil recovery. Advances in Colloid and Interface Science 183: 1-13.

Fletcher, R. (1987). Practical methods of optimization. Chichester ; New York, Wiley.

Kam, S.I., Nguyen, Q.P., Li, Q. and Rossen, W.R., 2007. Dynamic simulations with an improved model for foam generation. SPE Journal, 12(1): 35-48.

Khatib, Z. I., G. J. Hirasaki, et al. (1988). Effects of capillary pressure on coalescence and phase mobilities in foams flowing through porous media. SPE Reservoir Engineering 3(3): 919-926.

309

Kim, J. S., Dong, Y., et al. (2005). Steady-state flow behavior of CO2 foam. Spe Journal 10(4): 405-415.

Kovscek, A. R. and Apaydin, O. G. (2001). Surfactant concentration and end effects on foam flow in porous media. Transport in Porous Media 43(3): 511-536.

L. A. Verkruyse and S.J. Salter (1985). Potential Use of Nonionic Surfactants in Micellar Flooding. SPE Oilfield and Geothermal Chemistry Symposium, 9-11 March 1985, Phoenix, Arizona

Lemmon, E. W. and R. T. Jacobsen (2004). Viscosity and thermal conductivity equations for nitrogen, oxygen, argon, and air. International Journal of Thermophysics 25(1): 21-69.

Liu, M., Andrianov, A., et al. (2011). Sweep Efficiency in CO2 Foam Simulations With Oil. SPE EUROPEC/EAGE Annual Conference and Exhibition. Vienna, Austria.

Lopez-Salinas, J. L., Hirasaki, G. J., & Miller, C. A. Determination of Anhydrite in Reservoirs for EOR. SPE141420

Ma, K., Biswal, S. L., et al. (2012). Estimation of parameters for simulation of steady state foam flow in porous media. The 2012 AIChE Spring Meeting & 8th Global Congress on Process Safety, Houston, U.S.A.

Ma, K., J. L. Lopez-Salinas, et al. Estimation of parameters for the simulation of foam flow through porous media: Part 1; the dry-out effect. Energy & Fuels: Submitted.

Masalmeh, S. K., Wei, L., et al. (2011). Mobility Control for Gas Injection in Heterogeneous Carbonate reservoirs: Comparison of Foams versus Polymers. SPE Middle East Oil and Gas Show and Conference. Manama, Bahrain.

Methohm (2011). Potentiometric titration of surfactants and pharmaceutical compounds. Application Bulletin 268.

Mukerjee, P. and Mysels, K. J. (1971). Critical Micelle Concentrations of Aqueous Surfactant Systems. US. Government Printing Office, Washington,.D.C. NSRDS-NBS 36.

Osterloh, W. T. and Jante Jr, M. J. (1992). Effects of Gas and Liquid Velocity on Steady-State Foam Flow at High Temperature. SPE/DOE Enhanced Oil Recovery Symposium. Tulsa, Oklahoma.

Renkema, W. J. and Rossen, W. R. (2007). Success of Foam SAG Processes in Heterogeneous Reservoirs. SPE Annual Technical Conference and Exhibition. Anaheim, California, U.S.A.

Seethepalli, A., Adibhatla, B., et al. (2004). Physicochemical interactions during surfactant flooding of fractured carbonate reservoirs. *SPE Journal* 9(4): 411-418.

Skauge, A., Aarra, M. G., et al. (2002). Foam-Assisted WAG: Experience from the Snorre Field. SPE/DOE Improved Oil Recovery Symposium. Tulsa, Oklahoma.

Stumm, W. and Morgan, J. J. (1996). Aquatic chemistry : chemical equilibria and rates in natural waters. New York, Wiley.

Tabatabai, A., Gonzalez, M. V., et al. (1993). Reducing Surfactant Adsorption in Carbonate Reservoirs. Spe Reservoir Engineering 8(2): 117-122.

The MathWorks Inc (2012). MATLAB User's Guide. Natick, MA, USA.

Vassendan, F., Holt, T., et al. (1999). Foam propagation on semi-reservoir scale. Spe Reservoir Evaluation & Engineering 2(5): 436-441.

Wu, Y. F., Shuler, P. J., et al. (2008). An experimental study of wetting behavior and surfactant EOR in carbonates with model compounds. *SPE Journal* 13(1): 26-34.

Zanganeh, M. N., J. F. B. M. Kraaijevanger, et al. (2012). Adjoint-Based Optimization of a Foam EOR Process. 13th European Conference on the Mathematics of Oil Recovery. Biarritz, France.

Zanganeh, M. N., Kam, S. I., et al. (2011). The Method of Characteristics Applied to Oil Displacement by Foam. Spe Journal 16(1): 8-23.

Zanganeh, M.N., Kam, S.I., LaForce, T.C. and Rossen, W.R., 2011. The Method of Characteristics Applied to Oil Displacement by Foam. *SPE Journal*, 16(1): 8-23.

Part 4:

Alvarez, J. M., H. J. Rivas, et al. (2001). Unified model for steady-state foam behavior at high and low foam qualities. SPE Journal 6(3): 325-333.

Ashoori, E. and W. R. Rossen (2012). Can Formation Relative Permeabilities Rule Out a Foam EOR Process? SPE Journal 17(2): 340-351.

Ashoori, E., van der Heijden, T.L.M. and Rossen, W.R., 2010. Fractional-Flow Theory of Foam Displacements With Oil. *SPE Journal*, 15(2): 260-273.

Aster, R. C., C. H. Thurber, et al. (2005). Parameter estimation and inverse problems. Amsterdam ; Boston, Elsevier Academic Press.

Avriel, M. (1976). Nonlinear programming : analysis and methods. Englewood Cliffs, Prentice-Hall.

Bazaraa, M. S., H. D. Sherali, et al. (2006). Nonlinear programming : theory and algorithms. New York, NY ; Chichester, Wiley.

Bruges, E. A., B. Latto, et al. (1966). New correlations and tables of coefficient of viscosity of water and steam up to 1000 bar and 1000 degrees C. International Journal of Heat and Mass Transfer 9(5): 465-480.

311

Chalbaud, C. A., Moreno, R. A., et al. (2002). Simulating Foam Process for a Venezuelan Pilot Test. SPE Annual Technical Conference and Exhibition. San Antonio, Texas.

Cheng, L., Reme, A.B., Shan, D., Coombe, D.A. and Rossen, W.R., 2000. Simulating Foam Processes at High and Low Foam Qualities, SPE/DOE Improved Oil Recovery Symposium, Tulsa, Oklahoma.

Computer Modeling Group (2007). STARS^{TM} User's Guide. Calgary, Alberta, Canada.

Farajzadeh, R., A. Andrianov, et al. (2012). Foam-oil interaction in porous media: Implications for foam assisted enhanced oil recovery. Advances in Colloid and Interface Science 183: 1-13.

Fletcher, R. (1987). Practical methods of optimization. Chichester ; New York, Wiley.

Kam, S. I., Q. P. Nguyen, et al. (2007). Dynamic simulations with an improved model for foam generation. SPE Journal 12(1): 35-48.

Khatib, Z. I., G. J. Hirasaki, et al. (1988). Effects of capillary pressure on coalescence and phase mobilities in foams flowing through porous media. SPE Reservoir Engineering 3(3): 919-926.

Kim, J. S., Dong, Y., et al. (2005). Steady-state flow behavior of CO2 foam. Spe Journal 10(4): 405-415.

Kovscek, A. R. and Apaydin, O. G. (2001). Surfactant concentration and end effects on foam flow in porous media. Transport in Porous Media 43(3): 511-536.

L. A. Verkruyse and S.J. Salter (1985). Potential Use of Nonionic Surfactants in Micellar Flooding. SPE Oilfield and Geothermal Chemistry Symposium, 9-11 March 1985, Phoenix, Arizona

Lemmon, E. W. and R. T. Jacobsen (2004). Viscosity and thermal conductivity equations for nitrogen, oxygen, argon, and air. International Journal of Thermophysics 25(1): 21-69.

Liu, M., Andrianov, A., et al. (2011). Sweep Efficiency in CO2 Foam Simulations With Oil. SPE EUROPEC/EAGE Annual Conference and Exhibition. Vienna, Austria.

Ma, K., J. L. Lopez-Salinas, et al. Estimation of parameters for the simulation of foam flow through porous media: Part 1; the dry-out effect. Energy & Fuels: Submitted.

Masalmeh, S. K., Wei, L., et al. (2011). Mobility Control for Gas Injection in Heterogeneous Carbonate reservoirs: Comparison of Foams versus Polymers. SPE Middle East Oil and Gas Show and Conference. Manama, Bahrain.

Methohm (2011). Potentiometric titration of surfactants and pharmaceutical compounds. Application Bulletin 268.

Osterloh, W. T. and Jante Jr, M. J. (1992). Effects of Gas and Liquid Velocity on Steady-State Foam Flow at High Temperature. SPE/DOE Enhanced Oil Recovery Symposium. Tulsa, Oklahoma.

Renkema, W. J. and Rossen, W. R. (2007). Success of Foam SAG Processes in Heterogeneous Reservoirs. SPE Annual Technical Conference and Exhibition. Anaheim, California, U.S.A.

Seethepalli, A., Adibhatla, B., et al. (2004). Physicochemical interactions during surfactant flooding of fractured carbonate reservoirs. *SPE Journal* 9(4): 411-418.

Skauge, A., Aarra, M. G., et al. (2002). Foam-Assisted WAG: Experience from the Snorre Field. SPE/DOE Improved Oil Recovery Symposium. Tulsa, Oklahoma.

Stumm, W. and Morgan, J. J. (1996). Aquatic chemistry : chemical equilibria and rates in natural waters. New York, Wiley.

The MathWorks Inc (2012). MATLAB User's Guide. Natick, MA, USA.

Vassendan, F., Holt, T., et al. (1999). Foam propagation on semi-reservoir scale. Spe Reservoir Evaluation & Engineering 2(5): 436-441.

W.R. Rossen, C.J. van Duijn, Q.P.Nguyen and C.Chen, Injection Strategies to Overcome Gravity Segregation in Simultaneous Gas and Water Injection into Homogeneous Reservoirs, paper SPE 99794 presented at the 2006 SPE/DOE IOR symposium, Tulsa, OK, Apr. 22-26.

Wu, Y. F., Shuler, P. J., et al. (2008). An experimental study of wetting behavior and surfactant EOR in carbonates with model compounds. *SPE Journal* 13(1): 26-34.

Zanganeh, M. N., J. F. B. M. Kraaijevanger, et al. (2012). Adjoint-Based Optimization of a Foam EOR Process. 13th European Conference on the Mathematics of Oil Recovery. Biarritz, France.

Zanganeh, M. N., Kam, S. I., et al. (2011). The Method of Characteristics Applied to Oil Displacement by Foam. Spe Journal 16(1): 8-23.

Zanganeh, M.N., Kam, S.I., LaForce, T.C. and Rossen, W.R., 2011. The Method of Characteristics Applied to Oil Displacement by Foam. *SPE Journal*, 16(1): 8-23.

Publications:

Elhag, Amro S.; Chen, Yunshen; Chen, Hao; Reddy, Prathima P.; Cui, Leyu; Worthen, Andrew J.; Ma, Kun; Hirasaki, George J.; Nguyen, Quoc P.; Biswal, Sibani L.; Johnston, Keith P.: "Switchable Amine Surfactants for Stable CO2/Brine Foams in High Temperature, High Salinity Reservoirs", SPE paper 169041 presented at 2014 SPE Improved Oil Recovery Symposium, 12-16 April, Tulsa, Oklahoma, USA.

Yunshen Chen Amro S. Elhag, Benjamin M. Poon, Leyu Cui, Kun Ma, Sonia Y. Liao, Prathima P. Reddy, Andrew J. Worthen, George J. Hirasaki, Quoc P. Nguyen, Sibani L. Biswal, and Keith P. Johnston: "Switchable Nonionic to Cationic Ethoxylated Amine Surfactants for CO2 Enhanced Oil Recovery in High Temperature, High Salinity Carbonate Reservoirs," SPEJ, 19 (2): 249-259, 2014.

Yunshen Chen, Amro S. Elhag, Benjamin M. Poon, Leyu Cui, Kun Ma, Sonia Y. Liao, Amr Omar, Andrew J. Worthen, George J. Hirasaki, Quoc P. Nguyen, and Keith P. Johnston: "Ethoxylated Cationic Surfactants for CO2 EOR in High Temperature, High Salinity Reservoirs," SPE paper 154222 presented at the Eighteenth SPE Improved Oil Recovery Symposium held in Tulsa, Oklahoma, USA, 14–18 April 2012.

Guanwei Ren, Aaron W. Sanders, Quoc P. Nguyen: "New Method for the Determination of Surfactant Solubility and Partitioning Between CO2 and Brine," The Journal of Supercritical Fluids, 91: 77-83, 2014.

Ren, G., Zhang, H., and Nguyen, Q.P. 2013. Effect of Surfactant Partitioning on Mobility Control during Carbon-Dioxide Flooding. SPE J.; 18 (4): 752-765

Balan, H.O., Balhoff, M.T., Nguyen, Q.P., 2012. Modeling of Foamed Gas Mobility in Porous Media. Presented at the 18th SPE Improved Oil Recovery Symposium in Tulsa, OK, 14-18 April.

Ma, K., Biswal, S. L., Hirasaki, G. J.: "Experimental and Simulation Studies of Foam in Porous Media At Steady State," presented at the 1st International Conference on Upstream Engineering and Flow Assurance, Houston, Texas, 2012.

Charles A. Conn, Kun Ma, George J. Hirasaki and Sibani Lisa Biswal: "Visualizing oil displacement with foam in a microfluidic device with permeability contrast," Lab Chip, 2014,14, 3968-3977.

Rice University. "Foam favorable for oil extraction: Experiments visualize methods for enhanced recovery from wells." ScienceDaily. ScienceDaily, 12 August 2014. <www.sciencedaily.com/releases/2014/08/140812163800.htm>.

Kun Ma, Leyu Cui, Yezi Dong, Tianlong Wang, Chang Da, George J. Hirasaki, , Sibani Lisa Biswal: Adsorption of cationic and anionic surfactants on natural and synthetic carbonate materials," Journal of Colloid and Interface Science, 408, 15 October 2013, Pages 164–172.